Mathematical Modelling of Microcirculation in a Poroelastic Model of the Liver, and its Application to the Study of Ascites

Maryam Argungu

A thesis submitted for the degree of Doctor of Philosophy
and for the Diploma of Imperial College London

Department of Bioengineering
Imperial College London

June 2018

Copyright Declaration

The copyright of this thesis rests with the author and is made available under a Creative Commons Attribution Non-Commercial No Derivatives licence. Researchers are free to copy, distribute or transmit the thesis on the condition that they attribute it, that they do not use it for commercial purposes and that they do not alter, transform or build upon it. For any reuse or redistribution, researchers must make clear to others the licence terms of this work.

Declaration of Originality

I declare that this submission is my own work and that it contains no material previously published or written by another person, nor material which to a substantial extent has been accepted for the award of any other degree or diploma of the university or other institute of higher learning, except where due acknowledgment has been made in the text.

Abstract

The liver performs many vital functions in the body and has a natural ability to regenerate itself, except in the case of repeated or severe damage often caused by liver diseases. Damage due to liver disease occurs in the form of scarring of healthy liver tissue, a process known as fibrosis. Chronic fibrosis can lead to liver cirrhosis, a condition that is irreversible and often requires liver transplantation. Cirrhosis manifests itself in the form of increased tissue stiffness and decreased tissue permeability, which then leads to a marked decrease in blood perfusion and functioning of the liver tissue. As a homeostatic response, hepatic portal blood pressure also increases, which then leads to an increased outflow of excess interstitial fluid across the surface of the liver and into the surrounding peritoneal cavity. The abnormal accumulation of fluid in the peritoneal cavity is known as ascites and is characterised by large abdominal girth, abdominal pain and discomfort.

The aim of this thesis was to model the microcirculation of blood and interstitial fluid in the liver, so as to investigate the changes in vasculature that lead to impaired blood perfusion and the formation of ascites. To that end, we have developed a dual-porosity, dual-permeability deformable model of the liver tissue using the Biot theory of poroelasticity. We then used the model as part of a compartmental model of the peritoneal cavity and investigated the effect of liver disease (fibrosis/cirrhosis) on the accumulation of fluid in the peritoneal cavity. By varying the degree of liver tissue stiffness, we simulated and compared different stages of liver fibrosis, as well as predicted the severity of the resulting ascites. This makes our model an improvement on the current literature, with the aim of future use in informing and improving disease treatment strategies.

To my loving family,

for their continuous support and infinite belief in my capabilities.

Acknowledgements

Alhamdulillah for this personal journey of learning and growth that has been my PhD. I would like to take this opportunity to thank a number of people that in one way or the other have made a significant impact on my studies along the way.

Firstly, I would like to thank my supervisor and mentor, Dr. Jennifer Tweedy (neé Siggers), without whom none of this would have been possible. Thank you, Jennifer, for your continued guidance and support. You have made such a big impact on my life and I hope to continue following in your footsteps.

A special thanks to Professor Kim Parker, who stepped in often in a supervisory role, for being a great source of knowledge and wisdom. The conversations we had were always enlightening, and I am really grateful for them. Thank you also to Dr. Rodolfo Repetto for hosting me in Genoa, and to the other group members, Amabile and Filippo, for sharing their knowledge on COMSOL and solid mechanics. I look forward to our continued collaboration on the work already started.

I am also grateful to the staff at the Bioengineering Department for all their help over the years, especially Britta. Thank you to the lecturers who gave me the opportunity to teach their students and develop as a tutor - Jennifer, Warren, Chiu Fan, Reiko, James. To members of the Tweedy group, past and present, who have been sources of support and friendship over the years. To Karla, whom I look up to, for always knowing the right words to say. To Naima, a true friend, for being with me every step of the way. I would also like to give credit to all the mathematics tutors I have had over the years, from secondary school to college and university, who have had such a big impact on my learning, especially Julian Chapman, my A-levels tutor. Julian made me promise to acknowledge him when I write my big research "paper". Even as a teenager, he clearly saw a path for me that I was yet to see for myself.

Thank you to my dad, who was my first mathematics tutor, and my mum for always being there for me. You have given me everything a daughter could ever ask for and more. Thank to Maama and Daddy, for your continued support and prayers. I can only pray that God blesses you all for all you have done for me. To the rest of my family and friends, I thank you for your words of encouragement along the way. For those no longer with us, you will always be in our hearts.

My final (and most special) thanks goes to Mansur, my husband. You have been my source of strength and my inspiration. This achievement is ours, together, and I will forever be grateful for you being in my life.

Contents

Copyright **2**

Declaration of Originality **3**

Abstract **4**

Acknowledgements **6**

List of Tables **14**

List of Figures **15**

List of Symbols **28**

I Background 33

1 Introduction **34**

1.1 Overview of Research 34

1.1.1 Motivation 34

1.1.2 Research Aim and Objectives 37

1.1.3 Structure of Thesis 38

1.1.3.1 Published Work in this Thesis 39

1.2 Biological Background 40

1.2.1 The Liver 40

1.2.1.1 Anatomy and Physiology 40

1.2.1.2 Functions of the Liver 45

1.2.2 The Peritoneal Cavity 46

1.2.2.1 Anatomy and Physiology . . . 46
1.2.2.2 Surrounding organs . . . 47
1.3 Literature Review . . . 51
1.3.1 Mathematical Models of Physiological Fluid Flow in the Liver . . . 51
1.3.1.1 Electrical Analogue Models . . . 51
1.3.1.2 3D CFD Models . . . 53
1.3.1.3 Biphasic Model . . . 54
1.3.1.4 Porous Media Models . . . 54
1.3.2 Mathematical Models of Physiological Fluid Flow Across the Peritoneal Membrane . . . 56
1.4 Mathematical Background: Introduction to Poroelasticity . . . 58
1.4.1 Fluid Flow in Porous Media . . . 58
1.4.1.1 Darcy's Law . . . 58
1.4.1.2 Modified Carmen–Kozeny Equation . . . 60
1.4.2 Mechanics of Elastic Solid Deformation . . . 61
1.4.2.1 Introduction . . . 62
1.4.2.2 Small Deformation Theory . . . 63
1.4.2.3 Cauchy Stress Tensor for Linear Elastic Materials . . . 64
1.4.2.4 Large Deformation Theory . . . 64
1.4.2.5 Cauchy Stress Tensor for Hyperelastic Materials . . . 65
1.4.2.6 Material Vs Geometric Nonlinearities . . . 67
1.4.3 Fluid Flow in Poroelastic Media . . . 68

II Microcirculation in a Poroelastic Model of the Liver 69

2 Linear Elastic Deformation Model 70

2.1 Introduction . . . 70
2.2 Modelling Assumptions . . . 70
2.2.1 Physiological Fluids . . . 70
2.2.2 Liver Tissue . . . 71
2.2.3 Geometry . . . 72

2.3 Equations Governing Fluid Flow . . . 73
2.3.1 Undeformed Liver Lobule . . . 73
2.3.2 Deformed Liver Lobule . . . 75
2.4 Equations Governing Tissue Deformation . . . 76
2.4.1 Stress–Strain Relationship . . . 76
2.5 Hydraulic Conductivity of Pore Networks . . . 77
2.5.1 Tissue Porosity . . . 77
2.5.2 Tissue Permeability . . . 79
2.6 Summary of Governing Equations . . . 81
2.6.1 Weak Formulation of Governing Equations . . . 81
2.7 Boundary Conditions . . . 82
2.7.1 Fluid Flow Boundary Conditions . . . 82
2.7.2 Tissue Deformation Boundary Conditions . . . 83
2.8 Derived Values . . . 84
2.8.1 Total Blood Flux . . . 84
2.8.2 Total Lymphatic Uptake . . . 85
2.8.3 Fluid Loss via Liver Surface . . . 85
2.9 Physiological Parameter Values . . . 86
2.10 Results and Discussion . . . 86
2.10.1 Domain Mesh . . . 86
2.10.2 Single Lobule . . . 89
2.10.2.1 Blood Pressure and Velocity . . . 89
2.10.2.2 Interstitial Fluid Pressure and Velocity . . . 93
2.10.2.3 Fluid Exchange Across Sinusoidal Vessels . . . 97
2.10.2.4 Deformation Profile . . . 99
2.10.3 Multiple Lobules . . . 100
2.10.3.1 Blood Pressure and Velocity . . . 100
2.10.3.2 Interstitial Fluid Pressure and Velocity . . . 104
2.10.3.3 Fluid Exchange Across Sinusoidal Vessels . . . 108
2.10.3.4 Deformation Profile . . . 110

2.10.4 Effect of Portal Pressure Variation on Tissue Expansion . . . 111
2.10.5 Derived Values . . . 113
2.10.5.1 Total Blood Flux . . . 113
2.10.5.2 Lymphatic Uptake Rate . . . 113
2.10.5.3 Fluid Loss into the Peritoneal Cavity . . . 115
2.11 Summary and Conclusion . . . 116

3 Hyperelastic Deformation Model 119

3.1 Introduction . . . 119
3.2 Modelling Assumptions . . . 119
3.3 Equations Governing Fluid Flow . . . 119
3.3.1 Blood and Interstitial Fluid Volumes . . . 120
3.3.2 Tissue Porosity . . . 120
3.3.3 Tissue Hydraulic Conductivity . . . 121
3.4 Equations Governing Tissue Deformation . . . 122
3.4.1 Stress–Strain Relationship . . . 122
3.4.2 Choice of Strain Energy Function . . . 123
3.4.2.1 Isochoric Elastic Response . . . 123
3.4.2.2 Volumetric Elastic Response . . . 123
3.4.2.3 Strain Energy Function . . . 124
3.5 Summary of Governing Equations . . . 125
3.5.1 Weak Formulation of Governing Equations . . . 126
3.5.2 Change of Reference Frame: Balance Principle for a Cauchy Continuum . 127
3.6 Boundary Conditions . . . 132
3.6.1 Top and Bottom Surface of the 3D lobule . . . 132
3.6.2 Change of Reference Frame . . . 133
3.7 Derived Values . . . 134
3.7.1 Total Blood Flux . . . 134
3.7.2 Total Lymphatic Uptake . . . 135
3.7.3 Total Fluid Loss into the Peritoneal Cavity . . . 135
3.8 Physiological Parameter Values . . . 136

3.9 Results and Discussion . . . 137
3.9.1 Domain Mesh . . . 137
3.9.2 Single Lobule . . . 138
3.9.2.1 Blood and Interstitial Fluid Pressure and Velocity Profiles . . . 139
3.9.2.2 Deformation Profile . . . 143
3.9.3 Multiple Lobules . . . 144
3.9.3.1 Blood and Interstitial Fluid Pressure and Velocity Profiles . . . 144
3.9.3.2 Deformation Profile . . . 149
3.9.4 Comparison with Linear Elasticity Model . . . 149
3.9.4.1 Tissue Expansion . . . 149
3.9.4.2 Liver Porosity . . . 150
3.9.4.3 Total Blood Flux . . . 151
3.9.4.4 Lymphatic Uptake Rate . . . 153
3.9.4.5 Fluid Loss into the Peritoneal Cavity . . . 154
3.9.5 Variation of Boundary Conditions . . . 155
3.9.5.1 Change in Lobule Height . . . 155
3.9.5.2 Non-uniform Pressure Change Across Portal Tracts . . . 157
3.9.5.3 Pressure Drop Across Portal Tracts and Central Vein . . . 159
3.10 Summary and Conclusion . . . 164

4 Liver Cirrhosis **165**

4.1 Introduction . . . 165
4.2 Portal Hypertension . . . 165
4.3 Tissue Fibrosis . . . 166
4.3.1 Tissue Stiffness . . . 166
4.3.2 Changes in Tissue Permeability . . . 170
4.3.3 Conductivity of the Glissonian–Peritoneal Membrane . . . 172
4.4 Combined Portal Hypertension and Tissue Fibrosis . . . 174
4.5 Summary and Conclusion . . . 180

III Development of Ascites **181**

5 Mathematical Model of the Peritoneal Cavity **182**

5.1 Introduction . . . 182

5.2 Volume–Pressure Relationship . . . 182

5.2.1 Experimental Data From Literature . . . 182

5.2.2 Constant Compliance Model . . . 184

5.2.3 Combination Model: Linear and Nonlinear Behaviour . . . 185

5.2.3.1 Parameter Estimation . . . 187

5.2.4 Results and Discussion . . . 188

5.3 Fluid Exchange in the Peritoneal Cavity . . . 189

5.3.1 Absorption Rate Coefficient of the Peritoneal Cavity . . . 189

5.3.1.1 Parameter Estimation . . . 190

5.3.1.2 Timescale to Equilibrium Fluid Volume . . . 191

5.3.2 Compartmental Model of Fluid Exchange . . . 191

5.3.3 Fluid Flux Across Individual Organs/Tissue Adjacent to the Peritoneal Cavity . . . 192

5.3.3.1 Liver Flux . . . 192

5.3.3.2 Spleen Flux . . . 193

5.3.3.3 Diaphragm Flux . . . 193

5.3.3.4 Abdominal Wall . . . 194

5.3.4 Results and Discussion . . . 197

5.3.4.1 Fluid Contributions to the Peritoneal Cavity . . . 197

5.3.4.2 Parameter Estimates . . . 199

5.4 Development of Ascites due to Liver Disease . . . 206

5.4.1 Predicting Severity of Ascites . . . 208

5.5 Summary and Conclusion . . . 209

IV Conclusion **211**

6 Thesis Summary and Conclusion **212**

6.1 General Summary/Discussion . . . 212

6.2 Future Work . . . 214
6.2.1 3D Hyperelastic Liver Model . . . 214
6.2.2 Peritoneal Cavity Model . . . 216

A Parameter Sensitivity Analysis **218**
A.1 Geometrical Parameters . . . 218
A.2 Fluid Flow Parameters . . . 221
A.2.1 Permeabilities of Pore Spaces . . . 221
A.2.2 Effective Dynamic Viscosities . . . 222
A.2.3 Hepatic Filtration Coefficient . . . 223
A.2.4 Conductance of Lymphatic Vessels . . . 224
A.2.5 Pressure Within Flowing Lymphatic Vessels . . . 225
A.3 Solid Material Parameters . . . 226
A.3.1 Porosity Constants . . . 226
A.3.2 Shear Deformation Constants . . . 227

Bibliography **228**

List of Tables

2.1 List of parameter values used for the lobule geometry in the 2D linear elasticity model, together with references. 117

2.2 List of parameter values used for fluid flow in the 2D linear elasticity model, together with references. 117

2.3 List of parameter values used for tissue deformation in the linear elasticity model, together with references. 118

3.1 Boundary conditions used in the deformed liver lobule and the corresponding change of reference frame from the current domain $\mathcal{D}$ to the fixed domain $\mathcal{D}_0$. . 134

3.2 Parameters of the 5-constant Mooney–Rivlin polynomial (3.18) used to describe the shear behaviour of the liver tissue obtained from the experimental studies by Fu and Chui (2014). 137

4.1 Categorisation of liver tissue stiffness at different stages of tissue fibrosis by Mueller and Sandrin (2010). 166

5.1 List of parameter values used for the volume–pressure equations in peritoneal cavity model, together with references. 188

5.2 List of parameter values used to estimate fluid flux from the spleen, together with references. 204

5.3 List of parameter values used to estimate fluid flux through the diaphragm, together with references. 204

5.4 List of parameter values used in the abdominal wall model, together with references. 205

5.5 Classification of the severity of ascites by the International Ascites Club (Moore et al., 2003). 209

List of Figures

1.1 Realistic illustration of a comparison between healthy and cirrhotic human livers. 35

1.2 Photograph of an ascites patient. 36

1.3 Illustration of the location of the human liver within the abdomen. 40

1.4 Illustration of the human liver showing the major blood vessels - hepatic artery, portal vein and hepatic vein, as well as some of their bifurcations into smaller blood vessels. 41

1.5 Illustration showing: (A) the human liver and (B) a hexagonal representation of the liver lobule showing the 6 portal tracts (triad) and central vein. 42

1.6 Histological slides of the human liver tissue vs pig liver tissue. The boundaries between lobules (vascular septa) can be clearly seen in the pig liver tissue but not in the human liver tissue. 43

1.7 Illustrative diagram of a portion (1/6) of the lobule showing the blood vessels, bile and lymphatic ducts, cells, and interstitial space (space of Disse). 44

1.8 Lateral cross-section of the abdomen showing the peritoneal cavity (white space) and the surrounding tissues and organs. Note that the amount of white space in this image has been exaggerated for illustrative purposes only. 46

1.9 Comparison of human liver tissue vs spleen tissue. 48

1.10 A: Electronic micrograph image of a rat diaphragm showing a stoma (S) nestled between mesothelial cells (MC). B: Partial cross–section of a rat diaphragm showing the mesothelial and muscle layers. Within them, the lacuna, muscle fibres, blood and lymphatic vessels. C: Full cross–section of a rat diaphragm showing both the pleural (PL) and peritoneal (PE) sides. Lymphatic vessels carry fluid from the lacuna, through the muscle fibres, and into the lymphatic collectors. 49

1.11 Schematic diagram of the electrical analog model of the liver showing the two inlets of the portal vein and hepatic artery, P_{PV} and P_{HA}, respectively, and the outlet via the hepatic vein P_{HV}. Each generation of blood vessels is represented by one π-filter with blood inertia L, vascular resistance R_s, vessel wall viscoelasticity R_p and vessel compliance C. The generations of the portal vein, hepatic artery and hepatic vein are numbered from $1, \cdots, m$, $1, \cdots, n$ and $1, \cdots, p$, respectively. 52

1.12 3D replica of the vasculature of a human liver showing: (a) all 3 networks of blood vessels (b) the hepatic artery network with 6 generations (c) the portal vein network with 6 generations (d) the hepatic venous network with 5 generations. 53

1.13 Sketch of a cross–section of the domain used by Bonfiglio et al. (2010), showing: (a) single hexagonal lobule with side length L, six portal tracts of diameter D_p and a central vein of diameter D_v (b) hypothetical lobule lattice highlighting the sinusoidal space and vascular septa. 55

1.14 Illustration of fluid transport across a peritoneal tissue space of thickness x_1 by Flessner et al. (1984). The tissue is assumed to be evenly distributed with blood capillaries. Fluid drainage is through blood capillaries in the tissue and lymphatic uptake from the peritoneal cavity. 56

1.15 Hypothetical block of porous medium of volume $\mathcal{V}$, end area A, and length L in the third direction, containing N idealised cylindrical capillaries. 60

1.16 Movement of material particle from reference configuration $\mathcal{D}_0$ to current configuration $\mathcal{D}$ during deformation. 62

2.1 Illustration of the lattice arrangement of the liver lobules used to model the liver. The diagram shows both the interior lobules, located within the tissue, and the exterior lobules located next to the outer surface of the liver. Each lobule has one central vein surrounded by five or six portal tracts. 72

2.2 Illustration of (a) Interior lobule and (b) Exterior lobule. Interior lobules are located within the liver tissue and have six portal tracts surrounding a central vein. Exterior lobules are located next to the outer surface of the liver and have five portal tracts surrounding a central vein. 73

2.3 COMSOL Multiphysics mesh distribution used in the 2D linear elastic liver model to obtain numerical solutions. 88

2.4 Blood pressure distribution in 2D: (a) undeformed liver lobule and (b) deformed linearly elastic liver lobule following a 10% increase in sinusoidal blood portal pressure. Colour bars show pressure magnitude and have the same range in both subfigures. Pressure contours at intervals of 0.15 mmHg are also plotted in both subfigures. 90

2.5 Blood Darcy velocity in 2D: (a) undeformed liver lobule and (b) deformed linearly elastic liver lobule following a 10% increase in sinusoidal blood portal pressure. In both subfigures, arrows show the direction of flow and are proportional to the magnitude of flow velocity. Colour bars show velocity magnitude and are of the same range for both subfigures. 91

2.6 Average blood pore velocity in 2D: (a) undeformed liver lobule and (b) deformed linearly elastic liver lobule following a 10% increase in sinusoidal blood portal pressure. In both subfigures, arrows show the direction of flow and are proportional to the magnitude of flow velocity. Colour bars show velocity magnitude and are of the same range for both subfigures. 92

2.7 Interstitial fluid pressure distribution in 2D: (a) undeformed liver lobule and (b) deformed linearly elastic liver lobule following a 10% increase in sinusoidal blood portal pressure. Colour bars show pressure magnitude and have different ranges in each subfigure. Pressure contours are at intervals of 0.02 mmHg in both subfigures. 94

2.8 Interstitial fluid Darcy velocity in 2D: (a) undeformed liver lobule and (b) deformed linearly elastic liver lobule following a 10% increase in sinusoidal blood portal pressure. In both subfigures, arrows show the direction of flow and are proportional to the magnitude of flow velocity. Colour bars show velocity magnitude and are of the same range for both subfigures. 95

2.9 Average interstitial fluid pore velocity in 2D: (a) undeformed liver lobule and (b) deformed linearly elastic liver lobule following a 10% increase in sinusoidal blood portal pressure. Arrows show the direction of flow and are proportional to the magnitude of flow velocity. Colour bars show velocity magnitude and are of the same range for both subfigures. 96

2.10 Plasma flux per unit volume into the interstitial space q_{plasma} in 2D: (a) undeformed liver lobule and (b) deformed linearly elastic liver lobule following a 10% increase in sinusoidal blood portal pressure. Colour bars show the magnitude of plasma exchange and are of the same range for both subfigures. Contours are of intervals of $1\,\text{s}^{-1}$ in both subfigures. 98

2.11 Displacement of a 2D linear elastic lobule following a 10% increase in blood sinusoidal portal pressure, referenced against the undeformed lobule (black line). Colour bar shows displacement magnitude $|\mathbf{u}|$. 99

2.12 Displacement contours of a 2D linearly elastic lobule following a 10% increase in blood sinusoidal portal pressure, referenced against the undeformed lobule. The contours are at intervals of $0.5\,\mu$m. Arrows show the direction of displacement and are proportional to the magnitude of displacement. 100

2.13 Blood pressure distribution in 2D: (a) undeformed liver lobule lattice and (b) deformed linearly elastic liver lobule lattice following a 10% increase in sinusoidal blood portal pressure. Colour bars show pressure magnitude and have the same range in both subfigures. 101

2.14 Blood Darcy velocity in 2D: (a) undeformed liver lobule lattice and (b) deformed linearly elastic liver lobule lattice following a 10% increase in sinusoidal blood portal pressure. In both subfigures, arrows show the direction of flow and are normalised to the magnitude of flow velocity. Colour bars show velocity magnitude and are of the same range for both subfigures. 102

2.15 Average blood pore velocity in 2D: (a) undeformed liver lobule lattice and (b) deformed linearly elastic liver lobule lattice following a 10% increase in sinusoidal blood portal pressure. In both subfigures, arrows show the direction of flow and are normalised to the magnitude of flow velocity. Colour bars show velocity magnitude and are of the same range for both subfigures. 103

2.16 Interstitial fluid pressure distribution in 2D: (a) undeformed liver lobule lattice and (b) deformed linearly elastic liver lobule following a 10% increase in sinusoidal blood portal pressure. Colour bars show pressure magnitude and have the same range in each subfigure. 105

2.17 Interstitial fluid Darcy velocity in 2D: (a) undeformed liver lobule lattice and (b) deformed linearly elastic liver lobule lattice following a 10% increase in sinusoidal blood portal pressure. In both subfigures, arrows show the direction of flow and are normalised to the magnitude of flow velocity. Colour bars show velocity magnitude and are of the same range for both subfigures. 106

2.18 Average interstitial fluid pore velocity in 2D: (a) undeformed liver lobule lattice and (b) deformed linearly elastic liver lobule lattice following a 10% increase in sinusoidal blood portal pressure. Arrows show the direction of flow and are normalised to the magnitude of flow velocity. Colour bars show velocity magnitude and are of the same range for both subfigures. 107

2.19 Plasma flux per unit volume into the interstitial space q_{plasma} in 2D: (a) undeformed liver lobule lattice and (b) deformed linearly elastic liver lobule lattice following a 10% increase in sinusoidal blood portal pressure. Colour bars show the magnitude of plasma exchange and are of the same range for both subfigures. 109

2.20 Displacement magnitude of a 2D linearly elastic lobule lattice following a 10% increase in blood sinusoidal portal pressure, referenced against the undeformed lobule. 110

2.21 Displacement contours of a 2D linearly elastic lobule lattice following a 10% increase in blood sinusoidal portal pressure, referenced against the undeformed lobule. The contours are at intervals of 1 μm. Arrows show the direction of displacement and are proportional to the magnitude of displacement. 111

2.22 Surface averaged increase in liver volume $\mathcal{V}/\mathcal{V}_{\text{ref}}$ and cross–sectional stretch λ against increase in sinusoidal blood pressure at the portal tracts, using the 2D linear elastic liver model. 112

2.23 Surface averaged liver porosity against increase in sinusoidal blood pressure at the portal tracts, using the 2D linear elastic liver model. 112

2.24 Total volume flux of blood in the linearly elastic liver model versus the rigid liver model by Siggers et al. (2014), for different percentage increase in blood sinusoidal portal pressure. 114

2.25 Total lymphatic uptake within the linearly elastic liver model versus the rigid liver model by Siggers et al. (2014), for different percentage increase in blood sinusoidal portal pressure. 114

2.26 Fluid loss into the peritoneal cavity using the linearly elastic liver model versus the rigid liver model by Siggers et al. (2014), for different percentage increase in blood sinusoidal portal pressure. 115

3.1 Constrained lateral surfaces (in blue) on the 3D deformed liver lobule in: (a) single lobule case and (b) lobule lattice case. 133

3.2 COMSOL Multiphysics mesh distribution used in the 3D hyperelastic liver model to obtain numerical solutions. 138

3.3 Blood pressure distribution in 3D: (a) undeformed liver lobule and (b) deformed hyperelastic liver lobule following a 10% increase in sinusoidal blood portal pressure. Colour bars show pressure magnitude and have the same range in both subfigures. Pressure contours at intervals of 0.15 mmHg are also plotted in both subfigures. 139

3.4 Average blood pore velocity in 3D: (a) undeformed liver lobule and (b) deformed hyperelastic liver lobule following a 10% increase in sinusoidal blood portal pressure. In both subfigures, arrows show the direction of flow and are proportional to the magnitude of flow velocity. Colour bars show velocity magnitude and are of the same range for both subfigures. 140

3.5 Interstitial fluid pressure distribution in 3D: (a) undeformed liver lobule and (b) deformed hyperelastic liver lobule following a 10% increase in sinusoidal blood portal pressure. Colour bars show pressure magnitude and have different ranges in each subfigure. Pressure contours are at intervals of 0.02 mmHg in both subfigures. 141

3.6 Average interstitial fluid pore velocity in 3D: (a) undeformed liver lobule and (b) deformed hyperelastic liver lobule following a 10% increase in sinusoidal blood portal pressure. Arrows show the direction of flow and are proportional to the magnitude of flow velocity. Colour bars show velocity magnitude and are of the same range for both subfigures. 142

3.7 Solid deformation of a 3D hyperelastic lobule following a 10% increase in blood sinusoidal portal pressure, referenced against the undeformed lobule. Colour bar shows displacement magnitude $|\mathbf{u}|$, and is the same for all 3 subfigures. 143

3.8 Blood pressure distribution in 3D: (a) undeformed liver lobule lattice and (b) deformed hyperelastic liver lobule lattice following a 10% increase in sinusoidal blood portal pressure. Colour bars show pressure magnitude and have the same range in both subfigures. 145

3.9 Average blood pore velocity in 3D: (a) undeformed liver lobule lattice and (b) deformed hyperelastic liver lobule lattice following a 10% increase in sinusoidal blood portal pressure. In both subfigures, arrows show the direction of flow and are normalised to the magnitude of flow velocity. Colour bars show velocity magnitude and are of the same range for both subfigures. 146

3.10 Interstitial fluid pressure distribution in 3D: (a) undeformed liver lobule lattice and (b) deformed hyperelastic liver lobule following a 10% increase in sinusoidal blood portal pressure. Colour bars show pressure magnitude and have the same range in each subfigure. 147

3.11 Average interstitial fluid pore velocity in 3D: (a) undeformed liver lobule lattice and (b) deformed hyperelastic liver lobule lattice following a 10% increase in sinusoidal blood portal pressure. Arrows show the direction of flow and are proportional to the magnitude of flow velocity. Colour bars show velocity magnitude and are of the same range for both subfigures. 148

3.12 Displacement of a 3D hyperelastic lobule lattice following a 10% increase in blood sinusoidal portal pressure, referenced against the undeformed lobule. Colour bar shows displacement magnitude $|\mathbf{u}|$. 149

3.13 Comparison of the volume averaged increase in liver volume J (solid lines) and tissue stretch λ (dotted lines) against increase in sinusoidal blood pressure at the portal tracts between the 3D hyperelastic model (red lines) and 2D linear elastic model (black lines). 150

3.14 Comparison of the volume averaged liver porosity against increase in sinusoidal blood pressure at the portal tracts between the 3D hyperelastic model (solid line) and 2D linear elastic model (dashed line). 151

3.15 Comparison of the total volume flux of blood into the liver against blood sinusoidal portal pressure increase in the 3D hyperelastic model (red, solid line) with the 2D linear elastic model (red, dashed line) and the liver models by Siggers et al. (2014) (black, dotted line) and Bonfiglio et al. (2010) (black, solid and dashed line) 152

3.16 Comparison of the total volume flux of blood into the liver against blood sinusoidal portal pressure increase estimated from the 3D hyperelastic model (red, solid line), the 2D linear elastic model (red, dashed line) and the 2D rigid model by Siggers et al. (2014) (black, dotted line), with the experimental data of portal vein volume flux by Dahmen et al. (2007) (blue circles) 153

3.17 Comparison of the total lymphatic uptake within the liver against blood sinusoidal portal pressure between the 3D hyperelastic model (solid line), the 2D linear elastic model (dashed line) and the 2D rigid model by Siggers et al. (2014) (dotted line). 154

3.18 Comparison of fluid loss from the liver into the peritoneal cavity between the 3D hyperelastic model (solid line), the 2D linear elastic liver model (dashed line) and the rigid liver model by Siggers et al. (2014) (dotted line), for different percentage increases in blood sinusoidal portal pressure. 155

3.19 Displacement profile of the 3D hyperelastic liver lobule, with average volume change ratio J, for different heights, $h_{\text{lob}} = 25\,\mu\text{m}, 50\,\mu\text{m}$ and $250\,\mu\text{m}$, following a 10% increase in sinusoidal blood portal pressure. Colour bars show the displacement magnitude $|\mathbf{u}|$ and have different ranges in all subfigures. 156

3.20 Displacement profile of the 3D hyperelastic liver lobule, with average volume change ratio J, for different cases of non-linear pressure increase. Sinusoidal blood portal pressure is increased by 50% in (a) one portal tract (b) two portal tracts and (c) three portal tracts, while the rest of the portal tracts have a 10% increase in pressure. Colour bars show the displacement magnitude and have different ranges in all subfigures. 158

3.21 (a) Blood pressure distribution and (b) average pore velocity in a 3D deformed hyperelastic liver lobule following a 10% increase in sinusoidal blood portal pressure with a 1 mmHg pressure gradient along the portal tracts and central vein. Blood flows in opposite directions along the portal tracts and central vein. Colour bar shows (a) pressure magnitude and (b) pore velocity magnitude. Pressure contours at intervals of 0.1 mmHg are also plotted in (a), while (b) has arrows that show the direction of flow, proportional to the magnitude of velocity. 160

3.22 (a) Blood pressure distribution and (b) average pore velocity in a 3D deformed hyperelastic liver lobule following a 10% increase in sinusoidal blood portal pressure with a 1 mmHg pressure gradient along the portal tracts and central vein. Blood flows in a parallel direction along the portal tracts and central vein. Colour bar shows (a) pressure magnitude and (b) pore velocity magnitude. Pressure contours at intervals of 0.2 mmHg are also plotted in (a), while (b) has arrows that show the direction of flow, proportional to the magnitude of velocity. 162

3.23 Cut surface of the 3D hyperelastic lobule along the x–y plane going from portal tract (left-hand side edge), across the central vein (space in the middle) and to another portal tract (right-hand side egde) showing the (a) blood pressure and (c) blood pore velocity distribution assuming opposite flow directions in the portal tracts and central vein and (b) blood pressure and (d) blood pore velocity distribution assuming parallel flow directions in the portal tracts and central vein. The results shown have a 1 mmHg pressure gradient along the portal tracts and central vein, following a 10% increase in sinusoidal blood portal pressure. Colour bars in (a) and (b) are the same and show pressure magnitude while those in (c) and (d) are the same and show pore velocity magnitude. Pressure contours are at intervals of 0.2 mmHg in both (a) and (b) while (c) and (d) have arrows that show the direction of flow and are proportional to the magnitude of pore velocity. 163

4.1 Effect of change of bulk modulus E_{bulk} on volume change ratio J in the 3D hyperelastic liver lobule, following a 10% increase in blood sinusoidal portal tract pressure. The *white* shade denotes normal tissue, *light grey* shade denotes mild fibrosis and *medium grey* shade denotes severe fibrosis and *dark grey* shade denotes advanced fibrosis/cirrhosis. 167

4.2 Effect of change of bulk modulus E_{bulk} on average blood Darcy velocity $\mathbf{v}_s$ in the 3D hyperelastic liver, following a 10% increase in blood sinusoidal portal tract pressure. The *white* shade denotes normal tissue, *light grey* shade denotes mild fibrosis and *medium grey* shade denotes severe fibrosis and *dark grey* shade denotes advanced fibrosis/cirrhosis. 167

4.3 Effect of change of bulk modulus E_{bulk} on average interstitial fluid Darcy velocity $\mathbf{v}_i$ in the 3D hyperelastic liver, following a 10% increase in blood sinusoidal portal tract pressure. The *white* shade denotes normal tissue, *light grey* shade denotes mild fibrosis and *medium grey* shade denotes severe fibrosis and *dark grey* shade denotes advanced fibrosis/cirrhosis. 168

4.4 Effect of change of bulk modulus E_{bulk} on the total blood flux Q_{blood} in the 3D hyperelastic liver, following a 10% increase in blood sinusoidal portal tract pressure. The *white* shade denotes normal tissue, *light grey* shade denotes mild fibrosis and *medium grey* shade denotes severe fibrosis and *dark grey* shade denotes advanced fibrosis/cirrhosis. 168

4.5 Effect of change of bulk modulus E_{bulk} on the lymphatic uptake Q_{lymph} in the 3D hyperelastic liver, following a 10% increase in blood sinusoidal portal tract pressure. The *white* shade denotes normal tissue, *light grey* shade denotes mild fibrosis and *medium grey* shade denotes severe fibrosis and *dark grey* shade denotes advanced fibrosis/cirrhosis. 169

4.6 Effect of change of bulk modulus E_{bulk} on the fluid loss into the peritoneal cavity $Q_{\text{L,PC}}$ in the 3D hyperelastic liver, following a 10% increase in blood sinusoidal portal tract pressure. The *white* shade denotes normal tissue, *light grey* shade denotes mild fibrosis and *medium grey* shade denotes severe fibrosis and *dark grey* shade denotes advanced fibrosis/cirrhosis. 169

4.7 Effect of change of reference permeability of the interstitial space $\kappa_{i,\text{ref}}$ on average interstitial fluid Darcy velocity $\mathbf{v}_i$ in the 3D hyperelastic liver, following a 10% increase in blood sinusoidal portal tract pressure. The asterisk $*$ marks the physiological value. 170

4.8 Effect of change of reference permeability of the interstitial space $\kappa_{i,\text{ref}}$ on the lymphatic uptake Q_{lymph} in the 3D hyperelastic liver, following a 10% increase in blood sinusoidal portal tract pressure. The asterisk $*$ marks the physiological value. 171

4.9 Effect of change of reference permeability of the interstitial space $\kappa_{i,\text{ref}}$ on the fluid loss into the peritoneal cavity $Q_{\text{L,PC}}$ in the 3D hyperelastic liver, following a 10% increase in blood sinusoidal portal tract pressure. The asterisk $*$ marks the physiological value. 171

4.10 Effect of change of conductivity of the Glissonian–peritoneal membrane M_{GP} on average interstitial fluid Darcy velocity $\mathbf{v}_i$ in the 3D hyperelastic liver, following a 10% increase in blood sinusoidal portal tract pressure. The asterisk $*$ marks the physiological value. 172

4.11 Effect of change of conductivity of the Glissonian–peritoneal membrane M_{GP} on the lymphatic uptake Q_{lymph} in the 3D hyperelastic liver, following a 10% increase in blood sinusoidal portal tract pressure. The asterisk $*$ marks the physiological value. 173

4.12 Effect of change of conductivity of the Glissonian–peritoneal membrane M_{GP} on the fluid loss into the peritoneal cavity $Q_{\mathrm{L,PC}}$ in the 3D hyperelastic liver, following a 10% increase in blood sinusoidal portal tract pressure. The asterisk $*$ marks the physiological value. 173

4.13 Effect of increased blood portal tract pressure p_s^{pt} (portal hypertension) on the average volume change ratio J in a healthy liver, mild fibrotic liver, severe fibrotic liver and cirrhotic liver. 175

4.14 Effect of increased blood portal tract pressure p_s^{pt} (portal hypertension) on the average sinusoidal blood Darcy velocity $\mathbf{v}_s$ in a healthy liver, mild fibrotic liver, severe fibrotic liver and cirrhotic liver. 176

4.15 Effect of increased blood portal tract pressure p_s^{pt} (portal hypertension) on the average interstitial fluid Darcy velocity $\mathbf{v}_i$ in a healthy liver, mild fibrotic liver, severe fibrotic liver and cirrhotic liver. 176

4.16 Effect of increased blood portal tract pressure p_s^{pt} (portal hypertension) on the total blood flux Q_{blood} in a healthy liver, mild fibrotic liver, severe fibrotic liver and cirrhotic liver. 177

4.17 Effect of increased blood portal tract pressure p_s^{pt} (portal hypertension) on the lymphatic uptake rate Q_{lymph} in a healthy liver, mild fibrotic liver, severe fibrotic liver and cirrhotic liver. 177

4.18 Effect of increased blood portal tract pressure p_s^{pt} (portal hypertension) on the fluid loss from the liver into the peritoneal cavity $Q_{\mathrm{L,PC}}$ in the healthy case, mild fibrotic case, severe fibrotic case and cirrhotic case. 179

4.19 Effect of increased blood portal tract pressure p_s^{pt} (portal hypertension) on the fluid loss from the liver into the peritoneal cavity $Q_{\mathrm{L,PC}}$ in the healthy case, mild fibrotic case, severe fibrotic case (with high $M_{GP} = 5M_{GP,0}$ and moderate $M_{GP} = 1.5M_{GP,0}$) and cirrhotic case. $M_{GP,0}$ is the physiological conductivity of the Glissonian–peritoneal membrane. 179

5.1 Graphs of intra-peritoneal pressure (IAP) measured against intra-peritoneal fluid volume (IVP) of 1.5% and 4.25% glucose solutions from the experiments by Twardowski et al. (1983). Results show an approximate linear relation between pressure and volume obtained in supine, upright and sitting patient positions. . 184

5.2 Schematic diagram of a linearly elastic peritoneal cavity. Left: Spherical, inflated peritoneal cavity with radius, r_{PC}, and membrane thickness, h_{PC}; Right: Cross section of inflated cavity with internal and external pressures, P_{PC} and $P_{PC,\mathrm{ext}}$, respectively, and membrane stress T_{PC}. 185

5.3 Graph of steady state pressure in the peritoneal cavity P_{PC} against fluid volume V_{PC} for the constant compliance model (dotted red line), linearly elastic Hooke's law model (dotted green line) and combination model (dashed blue line). 189

5.4 Graph of pressure in the peritoneal cavity, P_{PC}, against change in fluid volume, V_{PC}, at steady state for different values of the critical volume $V_{PC,\text{crit}}$. 190

5.5 Schematic diagram of the compartment model of fluid exchange in the peritoneal cavity, where $Q_{i,PC}$ ($Q_{PC,i}$) denotes fluid flux from (into) tissue i into (from) the peritoneal cavity. 192

5.6 Schematic diagram of abdominal wall cross section showing the 3 layers: muscle; subcutaneous tissue and skin. Arrows show the direction of fluid flow, i.e. from the peritoneal cavity into the abdominal wall, in the normal physiological case. . 195

5.7 Volumetric fluxes from each organ into the peritoneal cavity. Dark blue: liver, $Q_{L,PC}$; Light blue: spleen, $Q_{Sp,PC}$; Black: abdominal wall, $-Q_{PC,AW}$; Red: diaphragm, $-Q_{PC,D}$. In the case of the abdominal wall, the dashed line shows the case with constant hydraulic conductivity and the solid line indicates the case with pressure-dependent hydraulic conductivity given by Equation (5.28). . 198

5.8 Total fluid absorption rate from the peritoneal cavity $\mathrm{d}V_{PC}/\mathrm{d}t$ given by Equation (5.17), against change in intraperitoneal pressure. The dashed line shows the case with constant hydraulic conductivity and the solid line indicates the case with pressure-dependent hydraulic conductivity given by (5.28). 198

5.9 Graph of volumetric flux from the peritoneal cavity into the abdominal wall against change in abdominal muscle thickness for different values of peritoneal cavity pressure. The dashed lines show the case with constant hydraulic conductivity and the solid lines indicate the case with pressure-dependent hydraulic conductivity given by Equation (5.28). The thicknesses of the subcutaneous tissue and skin layers, as well as all the other parameters except x_m and P_{PC}, are held fixed at the values in Table 5.4. The black solid line overlaps the black dashed line since the pressure-dependent hydraulic conductivity is constant for pressures ≤ 1.2 mmHg. 202

5.10 Graph of volumetric flux from the spleen into the peritoneal cavity $Q_{Sp,PC}$ against change in peritoneal cavity pressure for different values of the membrane conductivity of the spleen M_{Sp}. 203

5.11 Graph of volumetric flux from the peritoneal cavity into the diaphragm $Q_{PC,D}$ against change in peritoneal cavity pressure for different values of the membrane conductivity of the spleen M_{Sp}. 203

5.12 Fluid pressure in the peritoneal cavity against increase in blood pressure in the portal tracts of the liver for the different liver tissue types, as defined in Section 4.4.207

5.13 Fluid volume accumulation in the peritoneal cavity against increase in blood pressure in the portal tracts of the liver for the different liver tissue types, as defined in Section 4.4. 208

A.1 Effect of changes in geometrical parameters: side length of lobule (l_{lob}), diameter of central vein (d_{cv}) and diameter of portal tracts (d_{pt}) on the average displacement magnitude of the lobule $|\mathbf{u}|$. Black lines denote the 2D linear elastic model (LEM) while blue lines denote the 3D hyperelastic model (HEM). 219

A.2 Effect of changes in geometrical parameters: side length of lobule (l_{lob}), diameter of central vein (d_{cv}) and diameter of portal tracts (d_{pt}), on the average blood Darcy velocity within the lobule $\mathbf{v}_s$. Black lines denote the 2D linear elastic model (LEM), blue lines denote the 3D hyperelastic model (HEM), while green lines denote the rigid model by Siggers et al. (2014). 220

A.3 Effect of changes in geometrical parameters: side length of lobule (l_{lob}), diameter of central vein (d_{cv}) and diameter of portal tracts (d_{pt}), on the average interstitial fluid Darcy velocity within the lobule $\mathbf{v}_i$. Black lines denote the 2D linear elastic model (LEM), blue lines denote the 3D hyperelastic model (HEM), while green lines denote the 2D rigid model by Siggers et al. (2014). 220

A.4 Effect of variation of the reference sinusoidal space permeability $\kappa_{s,\text{ref}}$ on the average blood Darcy velocity within the lobule $\mathbf{v}_s$. Dashed line denotes the 2D linear elastic model (LEM), solid line denotes the 3D hyperelastic model (HEM), while dotted line denotes the 2D rigid model by Siggers et al. (2014). 222

A.5 Effect of variation of the effective dynamic viscosity of blood μ_s on the average blood Darcy velocity within the lobule $\mathbf{v}_s$. Dashed line denotes the 2D linear elastic model (LEM), solid line denotes the 3D hyperelastic model (HEM), while dotted line denotes the 2D rigid model by Siggers et al. (2014). 223

A.6 Effect of variation of the hepatic filtration coefficient C_f on the average interstitial fluid Darcy velocity within the lobule $\mathbf{v}_i$. Dashed line denotes the 2D linear elastic model (LEM), solid line denotes the 3D hyperelastic model (HEM), while dotted line denotes the 2D rigid model by Siggers et al. (2014). 224

A.7 Effect of variation of the conductance of lymphatic vessels C_l on the total lymphatic fluid uptake of the liver Q_{lymph}. Dashed line denotes the 2D linear elastic model (LEM), solid line denotes the 3D hyperelastic model (HEM), while dotted line denotes the 2D rigid model by Siggers et al. (2014). 225

A.8 Effect of variation of the pressure within flowing lymphatic vessels p_0 on the total lymphatic fluid uptake of the liver Q_{lymph}. Dashed line denotes the 2D linear elastic model (LEM), solid line denotes the 3D hyperelastic model (HEM), while dotted line denotes the 2D rigid model by Siggers et al. (2014). 226

A.9 Effect of the variation of the 5-constant Mooney–Rivlin polynomial constants by ±20% on the experimental stress-strain behaviour of the liver paranchyma. . . . 227

List of Symbols

A. Liver Model

l_{lob}	Side length of hexagonal lobule
t_{lob}	Thickness of hexagonal lobule
h_{lob}	Height of hexagonal lobule
d_{pt}	Diameter of portal tract
d_{cv}	Diameter of central vein
$p_{s,\text{ref}}$	Sinusoidal blood pressure in the undeformed liver lobule (reference case)
$p_{i,\text{ref}}$	Interstitial fluid pressure in the undeformed liver lobule (reference case)
$\kappa_{s,\text{ref}}$	Sinusoidal space permeability in the undeformed liver lobule (reference case)
$\kappa_{i,\text{ref}}$	Interstitial space permeability in the undeformed liver lobule (reference case)
$\mathbf{K}_{s,\text{ref}}$	Sinusoidal space hydraulic conductivity in the undeformed liver lobule (reference case)
$\mathbf{K}_{i,\text{ref}}$	Interstitial space hydraulic conductivity in the undeformed liver lobule (reference case)
μ_s	Blood effective dynamic viscosity
μ_i	Interstitial fluid effective dynamic viscosity
$\mathbf{v}_{s,\text{ref}}$	Blood Darcy's velocity in the undeformed liver lobule (reference case)
$\mathbf{v}_{i,\text{ref}}$	Interstitial fluid Darcy's velocity in the undeformed liver lobule (reference case)
q_{plasma}	Plasma flux per unit volume of the liver
q_{lymph}	Lymph uptake per unit volume of the liver
C_f	Filtration coefficient of liver sinusoids
C_l	Conductance of lymphatic vessels in liver lobule
p_0	Average pressure within flowing lymphatic vessels
p_s	Sinusoidal blood pressure in the deformed liver lobule
p_i	Interstitial fluid pressure in the deformed liver lobule
κ_s	Sinusoidal space permeability in the deformed liver lobule
κ_i	Interstitial space permeability in the deformed liver lobule
$\mathbf{K}_s$	Sinusoidal space hydraulic conductivity in the deformed liver lobule
$\mathbf{K}_i$	Interstitial space hydraulic conductivity in the deformed liver lobule
$\mathbf{v}_s$	Blood Darcy's velocity in the deformed liver lobule
$\mathbf{v}_i$	Interstitial fluid Darcy's velocity in the deformed liver lobule

$\boldsymbol{\sigma}$	Hookean Cauchy stress tensor
$\boldsymbol{\sigma}_e$	Hyperelastic Cauchy stress tensor
$\tilde{\boldsymbol{\sigma}}$	Modified Cauchy stress tensor
p_f	Net increase in referenced blood and interstitial fluid pressures
$\mathbf{I}$	Identity tensor
$\boldsymbol{\varepsilon}$	Strain tensor
$\mathbf{u}$	Displacement vector
E_L	Elastic constant of liver tissue
ν_L	Poisson ratio of the liver tissue
$\mathcal{V}$	Control volume of liver tissue in the deformed case
$\mathcal{V}_{\text{ref}}$	Control volume of liver tissue in the undeformed (reference) case
$\mathcal{V}_{\text{tissue}}$	Volume of tissue in $\mathcal{V}$
$\mathcal{V}_{\text{blood}}$	Volume of blood in $\mathcal{V}$
$\mathcal{V}_{\text{blood,ref}}$	Volume of blood in $\mathcal{V}_{\text{ref}}$
$\mathcal{V}_{\text{ifluid}}$	Volume of interstitial fluid in $\mathcal{V}$
$\mathcal{V}_{\text{ifluid,ref}}$	Volume of interstitial fluid in $\mathcal{V}_{\text{ref}}$
$\mathcal{L}$	Length of $\mathcal{V}$ in the third direction
$\mathcal{L}_{\text{ref}}$	Length of $\mathcal{V}_{\text{ref}}$ in the third direction
J	Volume change ratio
λ	Stretch of the domain $\mathcal{V}$ in the third direction
φ_L	Total liver porosity in the deformed case
φ_s	Porosity of sinusoidal space in the deformed case
φ_i	Porosity of interstitial space in the deformed case
$\varphi_{L,\text{ref}}$	Total liver porosity in the undeformed (reference) case
$\varphi_{s,\text{ref}}$	Porosity of sinusoidal space in the undeformed (reference) case
$\varphi_{i,\text{ref}}$	Porosity of interstitial space in the undeformed (reference) case
β_s	Coefficient of pressure ratio for blood
β_i	Coefficient of pressure ratio for interstitial fluid
$\mathcal{D}$	Deformed (current) domain
$\mathcal{D}_0$	Undeformed (reference) domain
$\partial\mathcal{D}$	Boundary of $\mathcal{D}$
$\partial\mathcal{D}_0$	Boundary of $\mathcal{D}_0$
$\mathbf{w}$	Test function of $\tilde{\boldsymbol{\sigma}}$ in $\mathcal{D}$
$\tilde{\mathbf{w}}_0$	Test function of $\tilde{\boldsymbol{\sigma}}$ in $\mathcal{D}_0$
$\check{p}_s$	Test function of p_s in $\mathcal{D}$
$\check{p}_i$	Test function of p_i in $\mathcal{D}$
$\hat{p}_s$	Test function of p_s in $\mathcal{D}_0$
$\hat{p}_i$	Test function of p_i in $\mathcal{D}_0$
$\check{p}_{s,\text{ref}}$	Test function of $p_{s,\text{ref}}$ in $\mathcal{D}_0$
$\check{p}_{i,\text{ref}}$	Test function of $p_{i,\text{ref}}$ in $\mathcal{D}_0$

$\mathbf{n}$	Unit normal vector on $\partial\mathcal{D}$
$\mathbf{n}_0$	Unit normal vector in $\partial\mathcal{D}_0$
$\mathbf{m}$	Unit tangent vector on $\partial\mathcal{D}$
$\mathbf{m}_0$	Unit tangent vector in $\partial\mathcal{D}_0$
$p^{pt}_{s,\mathrm{ref}}$	Blood portal tract pressure in the undeformed (reference) case
p^{pt}_{s}	Blood portal tract pressure in the deformed case
$p^{cv}_{s,\mathrm{ref}}$	Blood central vein pressure in the undeformed (reference) case
p^{cv}_{s}	Blood central vein pressure in the deformed case
M_{GP}	Hydraulic conductivity of Glissonian–peritoneal membrane
M_{BA}	Hydraulic conductivity of bare area
P_{BA}	Pressure adjacent to the outer surface of the bare area
V_{liv}	Total volume of liver
V_{lob}	Volume of single lobule
A_{lob}	Area of single lobule
N_{lob}	Average number of lobules in the liver
$\mathcal{N}_{\mathrm{lob}}$	Average number of lobules in the liver times height of a lobule
$A_{\mathrm{L,GP}}$	Surface area of the Glissonian–peritoneal membrane
$A_{\mathrm{L,BA}}$	Surface area of the bare area
$Q_{\mathrm{blood,ref}}$	Total volume flux of blood into undeformed liver
Q_{blood}	Total volume flux of blood into deformed liver
$Q_{\mathrm{lymph,ref}}$	Total lymphatic uptake rate in undeformed liver
Q_{lymph}	Total lymphatic uptake rate in deformed liver
$Q_{\mathrm{L_{ref},PC}}$	Fluid loss from the liver into the peritoneal cavity in the undeformed (reference) case
$Q_{\mathrm{L,PC}}$	Fluid loss from the liver into the peritoneal cavity in the deformed case
$Q_{\mathrm{L_{ref},BA}}$	Fluid loss across the bare area of the liver in the undeformed (reference) case
$Q_{\mathrm{L,BA}}$	Fluid loss across the bare area of the liver in the deformed case
$\mathbf{F}$	Deformation gradient tensor
$\mathbf{B}$	Left Cauchy–Green tensor
I_1	First invariant of $\mathbf{B}$
I_2	Second invariant of $\mathbf{B}$
W	Strain energy function of liver
W_{vol}	Volumetric component of W
W_{iso}	Isochoric component of W
E_{bulk}	Bulk modulus of the liver
$\boldsymbol{\nabla}$	Gradient tensor in $\mathcal{D}$
$\overline{\boldsymbol{\nabla}}$	Gradient tensor in $\mathcal{D}_0$
$\tilde{\mathbf{S}}_0$	1st Piola–Kirchhoff tensor of $\tilde{\boldsymbol{\sigma}}$
$\tilde{\mathbf{s}}_0$	Surface force distribution on $\mathcal{D}_0$
$\mathbf{t}$	Surface force distribution on $\mathcal{D}$

B. Peritoneal Cavity Model

P_{PC}	Pressure in the peritoneal cavity
V_{PC}	Fluid volume in the peritoneal cavity
C_{PC}	Compliance of the peritoneal cavity
C_0	Compliance constant in linear model of the peritoneal cavity
$V_{PC,\text{ref}}$	Measured reference fluid volume in the peritoneal cavity
$P_{PC,\text{ref}}$	Measured reference pressure of the peritoneal cavity
$V_{PC,\text{crit}}$	Critical fluid volume in the peritoneal cavity over which volume–pressure behaviour becomes non-linear
$P_{PC,\text{crit}}$	Critical pressure in the peritoneal cavity over which volume–pressure behaviour becomes non-linear
r_{PC}	Radius of peritoneal cavity
h_{PC}	Thickness of peritoneal membrane
$r_{PC,\text{crit}}$	Radius of peritoneal cavity at $V_{PC,\text{crit}}$
$h_{PC,\text{crit}}$	Thickness of peritoneal membrane at $V_{PC,\text{crit}}$
T_{PC}	Normal stress in the peritoneal membrane
$P_{PC,\text{ext}}$	Uniform pressure outside the peritoneal cavity
V_0	Volume of peritoneal cavity at which the transmural pressure would be zero under Hooke's law
r_0	Radius of peritoneal cavity at V_0
V_{membrane}	Volume of peritoneal membrane
E_{PC}	Young's modulus of peritoneal membrane
ν_{PC}	Poisson's ration of peritoneal membrane
ϵ_{PC}	Strain of peritoneal membrane
k_{PC}	Fluid absorption rate coefficient in the peritoneal cavity
$P_{PC,0}$	Steady state pressure in the peritoneal cavity
$Q_{Sp,PC}$	Net volumetric fluid flux from the spleen into the peritoneal cavity
A_{Sp}	Surface area of the spleen adjacent to the peritoneal cavity
M_{Sp}	Hydraulic conductivity of the spleen outer membrane
P_{Sp}	Average interstitial fluid pressure within the interior surface of the spleen
$Q_{PC,D}$	Net volumetric fluid flux from the peritoneal cavity into the diaphragm
A_D	Surface area of the diaphragm adjacent to the peritoneal cavity
D_{stoma}	Average density of a stoma
G_{stoma}	Average hydraulic conductivity of a stoma
M_{stoma}	Total hydraulic conductivity of the stomata
P_{stoma}	Average pressure within the stomata
$Q_{PC,AW}$	Net volumetric fluid flux from the peritoneal cavity into the abdominal wall
A_{AW}	Surface area of the abdominal wall adjacent to the peritoneal cavity
M_{AW}	Net hydraulic conductivity of the abdominal wall

C. Abdominal Wall Model

θ	Interstitial fluid volume fraction in the abdominal wall
p_{aw}	Interstitial fluid pressure in the abdominal wall
$p_{aw,0}$	Steady state interstitial pressure in the abdominal wall
j_{aw}	Volumetric flux per unit area into the abdominal wall
$q_{c,aw}$	Net fluid absorption from the abdominal wall tissue into the blood capillaries
L_p	Hydraulic conductivity of the capillary wall
a	Surface area of capillaries per unit volume of tissue
p_b	Blood mechanical pressure
Π_b	Blood oncotic pressures
σ_Π	Capillary wall reflection coefficient
Π_i	Local oncotic pressure in the interstitium of the abdominal wall
$q_{l,aw}$	Net fluid uptake by lymphatics in the abdominal wall
$q_{l0,aw}$	Rate of lymphatic absorption in the steady state
$q_{l1,aw}$	Sensitivity of lymphatic absorption to increase in pressure
K_{aw}	Hydraulic conductivity of the abdominal tissue
x_m	Boundary between the muscle and subcutaneous tissue layers
x_f	Boundary between the subcutaneous and skin layers
x_s	Outer boundary of the skin

Part I

Background

Chapter 1

Introduction

1.1 Overview of Research

The liver is a vital organ that plays key roles in the normal functioning of the human body, including the processing of digested food and detoxification of blood. It has a specialised tissue that is capable of expanding to accommodate changes in blood volume and pressure, following digestion of foods, and also regenerating itself following damage to its tissue structure. However, extreme liver damage is irreversible, often occurring as a result of liver diseases and could lead to liver failure. The primary goal of this research is to make use of mathematical modelling to gain more insight into the physiology of the liver and the changes that occur during liver diseases. To that end, we will study the dynamics of blood flow at the microcirculation level, i.e. within the smallest blood vessels of the liver, and the filtration of blood plasma into the surrounding extracellular space. This process is key to the effective perfusion of blood in the liver and vital to the normal functioning of the organ. Once we develop a mathematical model of microcirculation in the liver, we will apply the model to study the development of a secondary condition known as ascites, which is the abnormal accumulation of fluid in the peritoneal cavity and generally occurs as a consequence of liver diseases. First, we present our motivation for this research in Section 1.1.1 below.

1.1.1 Motivation

The UK National Health Service (NHS) estimates that there are over 100 types of liver diseases, ranging from viral to hereditary, alcohol and obesity related, affecting at least 2 million people in the UK. Public Health England (PHE) records also show that liver diseases are one of the major causes of death in UK, next to heart, cancer, age-related (dementia and Alzheimer's) and respiratory diseases, thereby highlighting their severity and prevalence within our society.

Aside from obesity related liver diseases, which are characterised by the formation of fat globules (a process known as steatosis), many other types of liver diseases result in liver damage

through scarring of the tissue. The condition in which healthy liver tissue is gradually and continuously replaced by scar tissue is known as fibrosis. Fibrosis causes an increase in the global stiffness of the liver tissue, which hinders its "sponge-like" ability to expand and accommodate changes in blood volume. Most liver diseases are not detectable in the early stages, as symptoms only occur once fibrosis has reached the terminal stage of cirrhosis. Cirrhosis is characterised by the formation of regenerative nodules (see Figure 1.1 [a]), irreversible and has no cure. The current medical response is to manage its symptoms to prevent further progression and, in the worst case, liver transplantation (Guyton and Hall, 2015; Keeffe and Friedman, 2004).

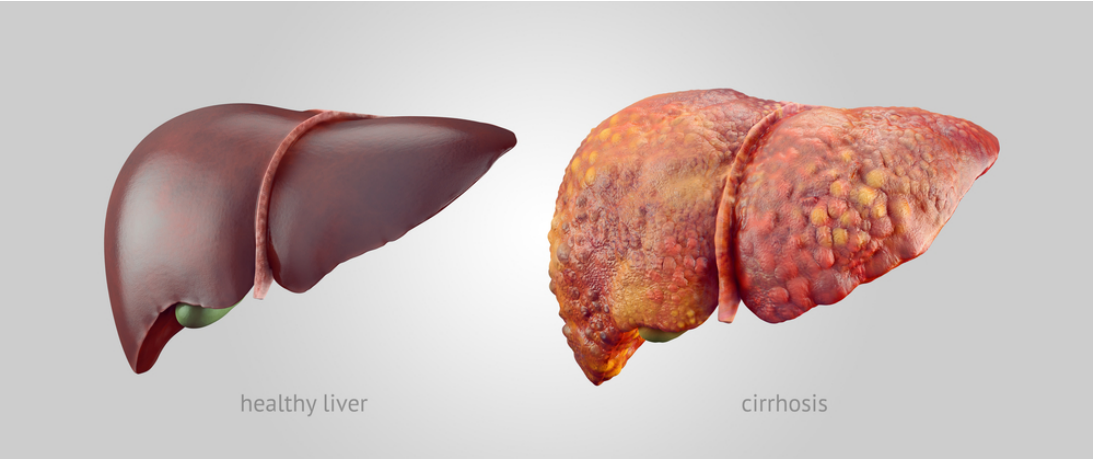


Figure 1.1: Realistic illustration of a comparison between healthy and cirrhotic human livers.

Among other things, cirrhosis disrupts the normal functioning of the liver by causing an increase in the resistance of the liver tissue to blood flow. This necessitates higher blood pressures to overcome it, which, together with changes in the membrane surrounding the liver, leads to an increasing volume of fluid collecting in the adjacent peritoneal cavity. This accumulation of fluid in the peritoneal cavity is known as ascites. Under normal physiological conditions, the peritoneal cavity contains very little amount of fluid - negligible in men and up to 20 mL in women (Shah, 2016). However, in patients with ascites, a fluid increase of up to 10 L can be observed (Dykes and Jones, 1968), leading to an increased pressure and expansion of the cavity (see Figure 1.2[b]). About 10% of cirrhosis patients develop ascites, 44% of which die within 3 years of onset (Gordon, 2012). During that time, their physical appearance, mobility and nutrition is affected, as well as an increased risk of infection possibly due to the migration of bacteria from the intestinal lumen or an impaired immune system (Shah, 2016). Depending on the severity, low-sodium diets and diuretics may be used to control further accumulation of fluid. However, effective treatment usually requires some form of external drainage (dialysis) using a catheter tube (Alpers et al., 2011).

[a] Image by Eranicle, with copyright license obtained from Shutterstock, `https://www.shutterstock.com`
[b] Photo by Donikz, with copyright license obtained from Shutterstock, `https://www.shutterstock.com`



Figure 1.2: Photograph of an ascites patient.

There are of course other conditions that can lead to the development of ascites. However, about 75% of patients with ascites have underlying liver cirrhosis, with the remaining being 10% due to malignancy, 3% due to heart failure, 2% due to tuberculosis, 1% due to pancreatitis and the rest due to other rare causes (Moore and Aithal, 2006). This is why we are most interested in the role played by the cirrhotic liver on the development of ascites.

The use of mathematical modelling has been previously employed to investigate other medical problems regarding the liver, including finding optimal conditions to preserve and perfuse donor livers for patients awaiting liver transplant (Debbaut et al., 2011, 2012; Van Der Plaats et al., 2004) and addressing the issue of tissue remodelling following a hepatic outflow obstruction, as observed after a liver resection and split liver transplantation (Ho et al., 2013a; Ricken et al., 2010). It is our hope that our research will give us further insight into the cirrhosis of the liver and the consequent development of ascites, with the aim of predicting the severity of the conditions and informing and improving treatment strategies.

1.1.2 Research Aim and Objectives

The main aim of this research is to develop a mathematical model of blood and interstitial fluid flow, at the microcirculation level, within a liver tissue capable of expanding to accommodate physiological changes in blood volume and pressure. This involves extending the current liver models of Bonfiglio et al. (2010) and Siggers et al. (2014) to include tissue compliance, which has not yet been properly accounted for. As it stands, the models are not accurate enough to model patients in pathological or non-physiological conditions. By incorporating tissue compliance, we aim to develop a more robust model of hepatic microcirculation, which in turn will be used to model progressive stages of fibrosis within the diseased liver. Furthermore, we will investigate the role played by the diseased liver in the abnormal accumulation of fluid in the peritoneal cavity. This would require us to develop a model of the peritoneal cavity itself, taking into account its sources and drains, which is yet to be done mathematically. To that end, we set ourselves the following research objectives:

1. To extend the mathematical models of microcirculation in the liver developed by Bonfiglio et al. (2010) and Siggers et al. (2014) to include tissue compliance. This involves coupling the equations of blood and interstitial fluid developed by Siggers et al. (2014) with that of solid tissue deformation.

    (a) As a first approximation, the liver tissue is modelled as a 2D linearly elastic solid, i.e. assuming a linear stress–strain behaviour, which would give us deformation profiles under small strains. This would follow the methods of Bonfiglio et al. (2010), but with a double-pore network of blood and interstitial fluid, modified permeability equations and for the whole liver tissue rather than a single subunit of the liver known as the lobule.

    (b) The 2D linear elastic model is then extended to a 3D hyperelastic model, i.e. with a non-linear stress–strain behaviour, which is more representative of the liver tissue under large strains.

2. To make use of the newly developed 3D hyperelastic model of liver microcirculation to simulate diseased states of the liver. This involves modelling tissue fibrosis, represented by an increase in global tissue stiffness and decrease in interstitial fluid permeability, and portal hypertension, which are both indicators of liver diseases. It will also allow us to compare changes in fluid flow profiles and deformation observed in the diseased liver with respect to the healthy liver.

3. To develop a mathematical model of the peritoneal cavity that can be used to study the development of ascites due to liver disease. This requires:

    (a) Investigating the physiological fluid volume–pressure behaviour within the peritoneal cavity.

(b) Investigating the sources and drains of fluid in the peritoneal cavity and quantifying their respective fluid volume flux under normal physiological and pathological peritoneal pressure conditions.

(c) Developing a compartmental model of fluid exchange in the peritoneal cavity and using it to predict the abnormal accumulation of fluid volumes in the cavity as a result of liver disease, modelled using fibrosis and portal hypertension.

In the next section, we provide a guideline to the structure of our thesis in which the objectives set out above are addressed.

1.1.3 Structure of Thesis

In the rest of this introductory chapter of the thesis (Part I), we will provide background descriptions on the anatomy and physiology of both the human liver and the peritoneal cavity in relation to physiological fluid flow. We will then present a literature review of mathematical models describing blood flow and microcirculation in the liver, as well as fluid transport across the peritoneal cavity. This will set the scene for current research and where our thesis aims to fill in gaps. Finally, we will give brief introductions to the mathematical equations used in this thesis, namely the theory of poroelasticity.

The remainder of the thesis is further split into Part II, Part III and Part IV. Part II details the development of the poroelastic model of liver microcirculation and constitutes Chapters 2–4. In Chapter 2, we present the development of the 2D linear elastic model, including modelling assumptions and equations governing blood flow, interstitial fluid flow and tissue deformation. Using prescribed boundary conditions, we solve the governing equations using the COMSOL Multiphysics software and present the numerical results at the end of the chapter.

In Chapter 3, we extend the governing equations for the 2D linear elastic liver developed in Chapter 2 into that of a 3D hyperelastic liver. Again, using prescribed boundary conditions, we solve the resultant governing equations using COMSOL Multiphysics and present the numerical solutions towards the end of the chapter. We also compare results obtained from the two models and discuss the differences between them.

In Chapter 4, we make use of the 3D hyperelastic model to study the effect of tissue fibrosis and portal hypertension on fluid flow and deformation of the liver tissue. To that end, we investigate different degrees of tissue damage, including mild fibrosis, severe fibrosis and cirrhosis, and compare the results against that of a healthy liver tissue.

Having developed a mathematical model of the liver capable of simulating liver disease, we move onto Part III of the thesis, which details the development of the mathematical model of the peritoneal cavity and constitutes Chapters 5. In the latter, we develop a mathematical model of the peritoneal cavity, including the fluid volume–pressure relationship and a compartmental

model of fluid exchange in the peritoneal cavity. We then make use of the model to investigate the role played by the diseased liver in the development of ascites and predict its severity.

Finally, in Chapter 6 of Part IV, we conclude this thesis by summarising what we have achieved so far, what the limitations of our models are and what possible extensions can be done to improve them in the future.

A complete list of mathematical symbols used in Chapters 2–6 is also given on pages 24–28 of this thesis for reference.

1.1.3.1 Published Work in this Thesis

Preliminary work on the 2D linear elastic liver model (Chapter 2) has been published in a book of proceedings for the Sixth Biot Conference on Poromechanics, held in Paris, France, July 9–13, 2017. Details of this can be found in the paper "Microcirculation of Blood and Interstitial Fluid in a Poroelastic Model of the Liver" (Argungu and Tweedy, 2017).

The mathematical model of the peritoneal cavity and development of ascites (Chapter 5) developed using the rigid liver model by Siggers et al. (2014), and not the poroelastic liver model developed in this research, has been submitted for publication to the Journal of Mathematical Medicine and Biology under the title "A Mathematical Model of Fluid Exchange in the Peritoneal Cavity and the Role Played by Liver Cirrhosis in the Development of Ascites" and is currently under its second review.

1.2 Biological Background

1.2.1 The Liver

1.2.1.1 Anatomy and Physiology

The human liver is made up of soft, brownish parenchyma enclosed within a thin collagenous capsule, also known as the Glisson's capsule. On average, it weighs between 1.3 kg – 1.5 kg (Dancygier, 2009), and lies in the upper right quadrant of the abdomen, underneath the diaphragm and above the stomach, duodenum, colon and right kidney (see Figure 1.3[c]). The surface of the liver next to the diaphragm is referred to as the diaphragmatic surface while that adjacent to the abdominal organs is referred to as the visceral surface.

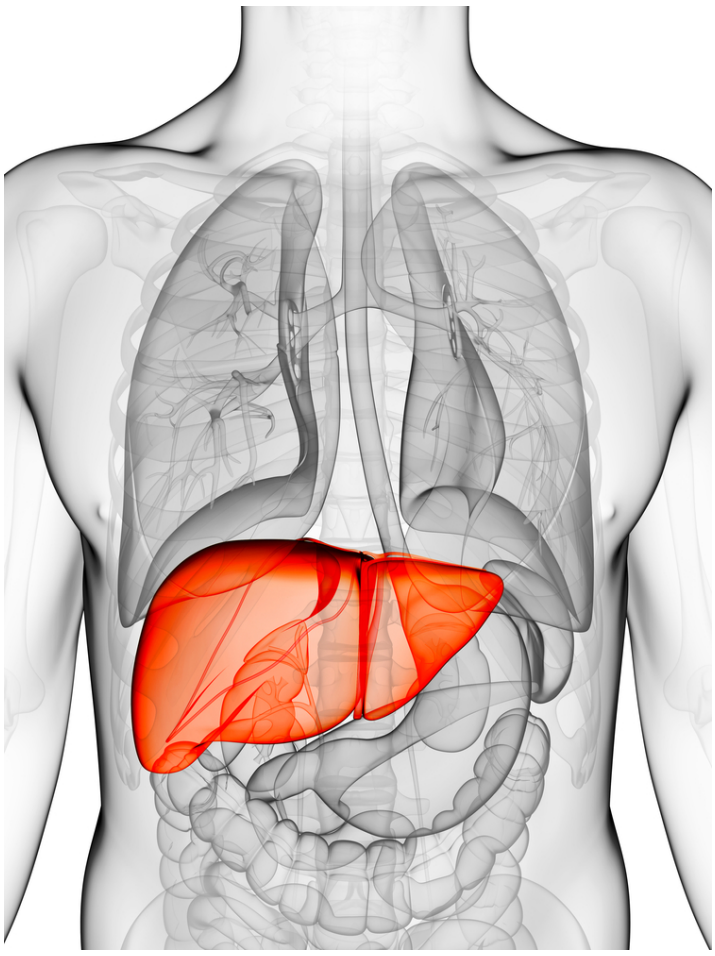


Figure 1.3: Illustration of the location of the human liver within the abdomen.

[c]Image by Sebastian Kaulitzki, with copyright license obtained from Shutterstock, `https://www.shutterstock.com/`

Blood Supply

On average, the liver filters about 1350 ml of blood per minute (Guyton and Hall, 2015). Blood supply to the liver is via two major blood vessels: 25% via the hepatic artery and 75% via the portal vein (Dancygier, 2009). The hepatic artery supplies fully oxygenated blood from the heart, while the portal vein supplies partially deoxygenated and nutrient-rich blood from the stomach, the intestines (small and large), the spleen, the gall bladder and the pancreas. These blood vessels undergo several bifurcations to form two networks of micro-vessels, which lie next to each other. Bifurcations from the hepatic artery and portal vein have terminal endings at portal tracts within the liver, which feed into the sinusoids (the smallest blood vessels in the liver). Blood flows across the sinusoids and into the central vein, which then feeds into a network of venous vessels that drain blood from the liver through the hepatic veins. The hepatic veins then return the blood to the heart via the inferior vena cava (see Figure 1.4[d]).

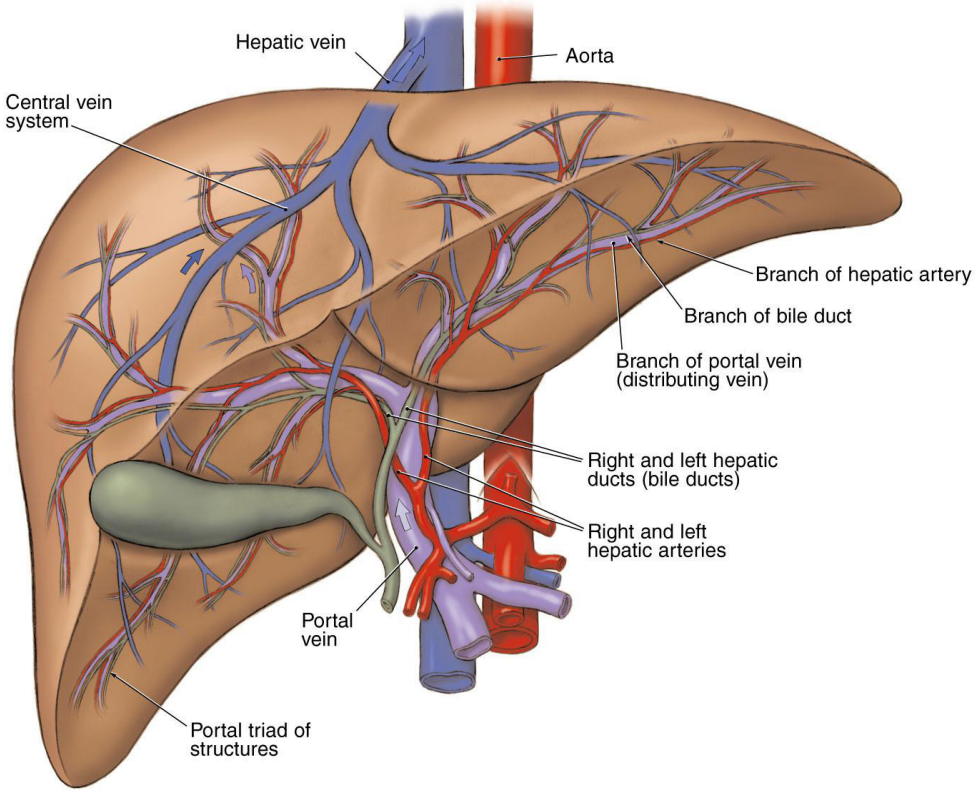


Figure 1.4: Illustration of the human liver showing the major blood vessels - hepatic artery, portal vein and hepatic vein, as well as some of their bifurcations into smaller blood vessels.

[d]Original image by MediVisuals, Inc. (2007).

Based on arterial and portal venous blood supply, biliary drainage, and hepatic venous drainage, the liver can be divided into 8 functional lobes and segments. This is particularly useful for liver resection and transplantation, since each segment has its own blood supply (Skandalakis et al., 2004b). The liver tissue itself comprises of functional units called lobules. Each lobule consists of a central vein, surrounded by an average of five to seven portal tracts. Each portal tract consists of a venule, an arteriole and a bile duct. The hepatic lobule is most commonly approximated into the hexagonal shape shown in Figure 1.5[e] for modelling purposes, also known as the classical lobule. The boundaries between neighbouring classical lobules are known as vascular septa. These can be clearly seen in some organisms e.g. pigs, but not in the human liver (see Figure 1.6[f]).

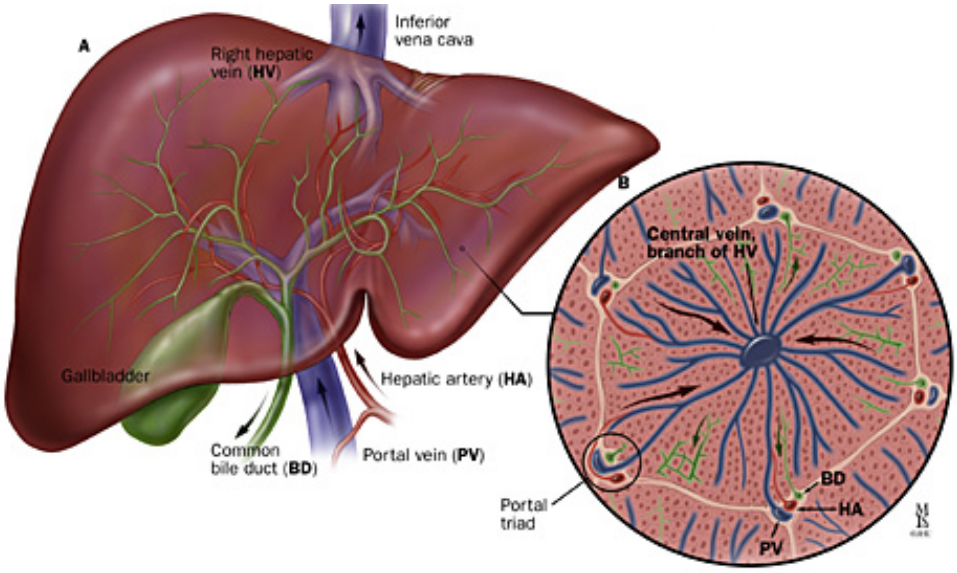


Figure 1.5: Illustration showing: (A) the human liver and (B) a hexagonal representation of the liver lobule showing the 6 portal tracts (triad) and central vein.

Two other classifications of the liver lobule include the portal lobule and the acinus. The portal lobule is a sixth of the classical lobule (triangular in shape), going from a single portal tract to the central vein, and most commonly used in modelling bile formation and flow. The liver acinus is elliptical in shape and goes from one central vein to another central vein of a neighbouring lobule, across the vascular septa. It is divided into 3 zones that correspond to distance from arterial blood supply. The liver acinus is most commonly used for modelling oxygen and glucose metabolism. For the purpose of this thesis, we shall make use of the classical hexagonal lobule and simply refer to it as the "lobule".

[e]Image obtained from the website of John Hopkins Medicine, Gastroenterology and Hepatology, `https://www.halstedsurgery.org/JHGI_Home.aspx?CurrentUDV=31`

[f]Original image by Kateryna Kon, with copyright license obtained from Shutterstock, `https://www.shutterstock.com/`

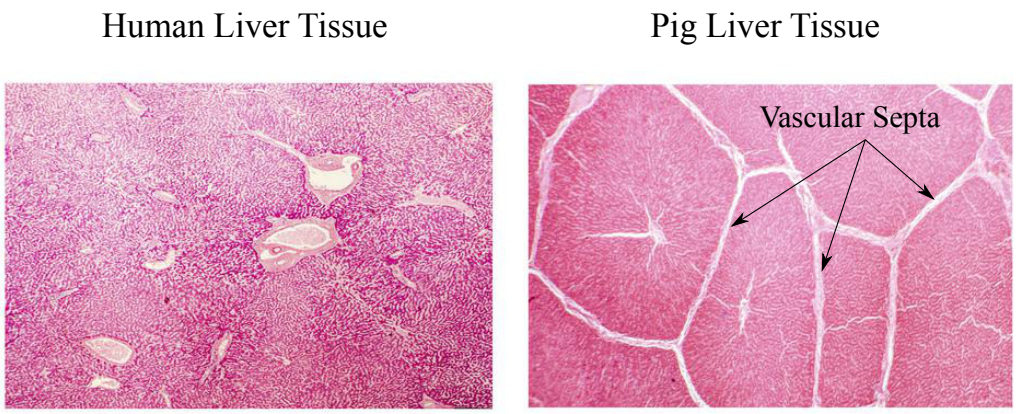


Figure 1.6: Histological slides of the human liver tissue vs pig liver tissue. The boundaries between lobules (vascular septa) can be clearly seen in the pig liver tissue but not in the human liver tissue.

Microcirculation

Sinusoids have wide endothelial gaps, known as fenestrations, and discontinuities in their basement membranes that allow the free flow of fluid and plasma proteins from blood, as it passes from the portal tracts to the central vein, into the surrounding interstitial space known as the space of Disse. This makes them considerably more permeable than capillary vessels found in other tissues, such as the skeletal muscle (Guyton and Hall, 2015). The space of Disse lies between sinusoids and the hepatocyte cells of the liver. Hepatocytes have specialised microvilli that project into the space of Disse for increased absorption of interstitial fluid and small solutes.

Excess interstitial fluid within the space of Disse can leave the liver either via the initial lymphatics within the liver lobule or the liver surface. Initial lymphatics have primary valves to prevent the backward flow of interstitial fluid and drain into larger collecting lymphatics around the liver (Ohtani and Ohtani, 2008). In addition to the Glisson's capsule, the majority of the liver surface is covered by another thin membrane known as the peritoneum or peritoneal membrane, which also encloses the peritoneal cavity. Fluid leaving through this part of the liver surface passes through this membrane and enters the peritoneal cavity. The double membrane formed by the Glisson's capsule and the peritoneum is referred to as the Glissonian–peritoneal membrane in this thesis, as in Siggers et al. (2014). The remaining part of the liver not covered by the peritoneum is at the site of attachment of the gallbladder and a small area on the diaphragmatic surface known as the bare area. It lies directly next to the diaphragm, and thus all fluid leaving via the bare area gets taken up by the diaphragmatic lymphatics (Dancygier, 2009).

Bile fluid formed by the hepatocyte cells of the liver are collected by thin vessels known as bile canaliculi. Bile canaliculi lie between adjacent hepatocytes and empty into bile ducts, which are then connected to the common hepatic duct. From there, bile is emptied into the gall bladder where it is stored before being released into the small intestine to aid in the digestion of fat lipids (Boyer, 2013).

Figure 1.7[g] gives an illustration of the vessels involved in microcirculation in the liver discussed above. Note however, that as mentioned previously, we will only focus on the flow of blood and interstitial fluid at the micro-scale and neglect the flow of blood and lymph fluid in the larger blood vessels, as well as the production and flow of bile in the liver.

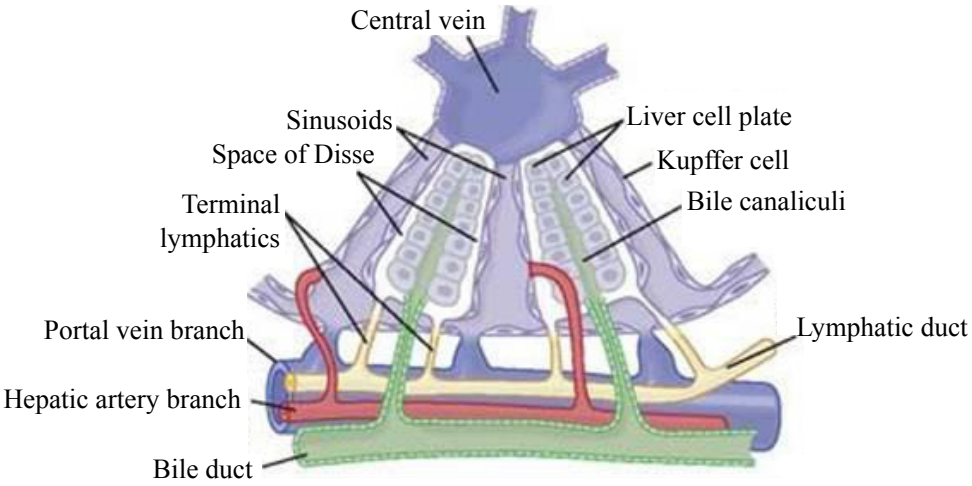


Figure 1.7: Illustrative diagram of a portion (1/6) of the lobule showing the blood vessels, bile and lymphatic ducts, cells, and interstitial space (space of Disse).

[g]Image obtained and adapted from Guyton and Hall (2015).

1.2.1.2 Functions of the Liver

Hepatocyte cells account for 80% of the volume of the liver and are responsible for the majority of the liver functions, including:

- **Metabolism**: The conversion of carbohydrates, fatty acids and amino acids into glucose or energy in the form of ATP. Glucose is also converted and stored in the form of glycogen within the liver.
- **Detoxification**: Toxic substances such as alcohol and drugs are removed and destroyed. The breakdown of amino acids produces ammonia as a by-product, which is further converted into urea and excreted in urine by the kidneys.
- **Storage**: Vitamins A, D, E, K, and B12, as well as the minerals iron and copper.
- **Homeostasis**: Regulation of blood glucose, as well as certain body hormones.
- **Protein Synthesis**: Production of vital plasma proteins involved in blood clotting (prothrombin and fibrinogen) and the maintenance of blood tonicity (albumins).

Within the lining of the sinusoid walls are also specialised macrophages known as Kupffer cells. Kupffer cells are responsible for destroying worn-out white and red blood cells, bacteria and other foreign bodies within the blood, hence providing an immune function to the body (Grabowski and Tortora, 2003). Stellate cells are another small class of cells that exist in the liver within the space of Disse. Under normal physiological conditions, stellate cells are dormant. The functional aspect of the cells are activated following liver damage through the formation of scar tissue, which can lead to cirrhosis (Grabowski and Tortora, 2003).

1.2.2 The Peritoneal Cavity

1.2.2.1 Anatomy and Physiology

The peritoneal cavity is a potential space which lies within the abdominal cavity (see Figure 1.8[h]). As mentioned previously, it is lined by a thin membrane known as the peritoneum or peritoneal membrane. The peritoneum consists of a single layer of mesothelium and a layer of connective tissue, which together provide a barrier between the abdominal organs and the abdominal wall. The small amount of transcellular fluid normally present in the peritoneal cavity acts as a lubricant, ensuring smooth movement of the organs against one another, especially during digestion (Gokal, 2000). It also contains leukocytes and antibodies that provide immunity against infection (Moore et al., 2002).

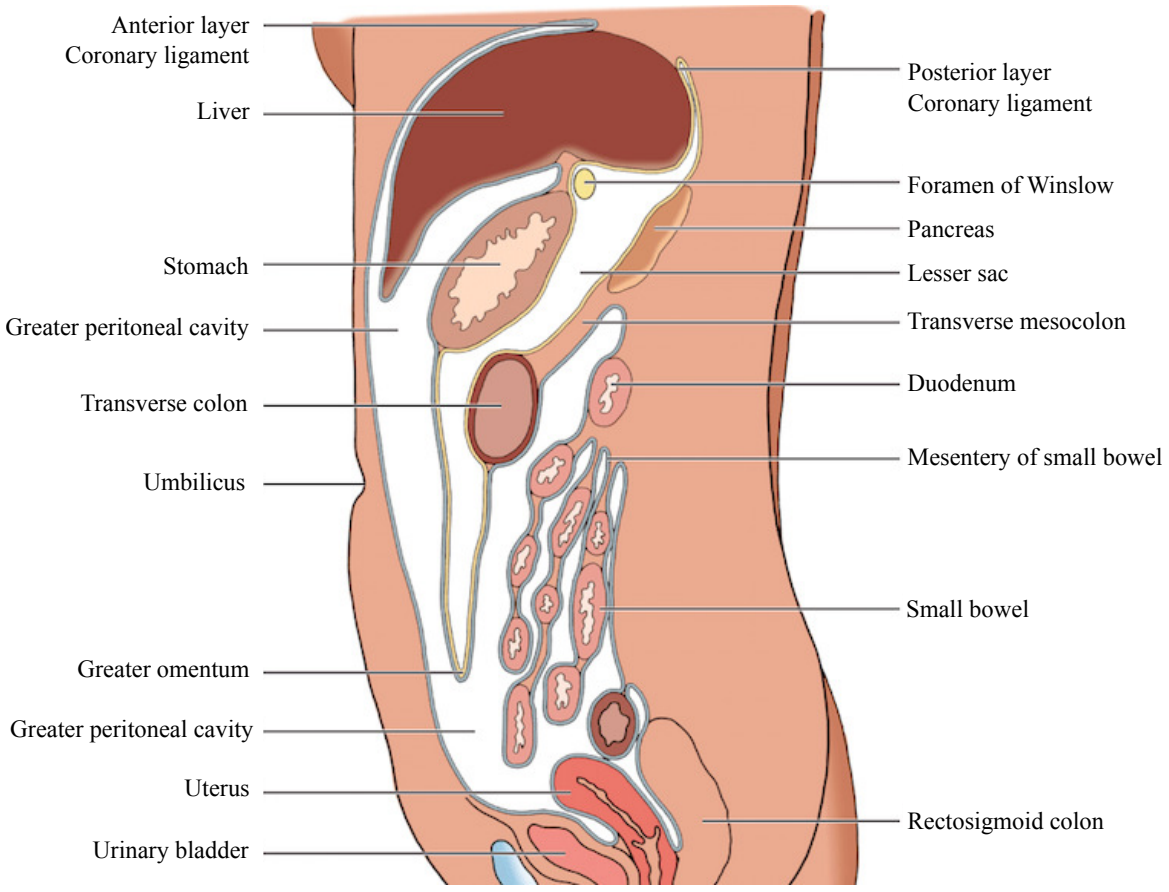


Figure 1.8: Lateral cross-section of the abdomen showing the peritoneal cavity (white space) and the surrounding tissues and organs. Note that the amount of white space in this image has been exaggerated for illustrative purposes only.

[h]Image obtained from Skandalakis et al. (2004a).

1.2.2.2 Surrounding organs

The peritoneum covers the surface of the abdominal wall and most of the organs within the abdominal cavity. The section of the peritoneal membrane that lines the abdominal wall is known as the parietal peritoneum while the other section that lines the abdominal organs is known as the visceral peritoneum. The abdominal organs can be categorised depending on their location within, behind or below the peritoneal cavity (Alpers et al., 2011). Organs lying within the peritoneal cavity are referred to as intraperitoneal organs and include the liver, spleen, stomach, parts of the small and large intestines and ovaries (in women). Organs located behind the peritoneal cavity are referred to as retroperitoneal organs and include the rest of the small and large intestines, pancreas and kidneys, while those below the peritoneal cavity are referred to as subperitoneal organs and include the bladder, uterus (in women) and lower part of the rectum (Alpers et al., 2011). In front of the peritoneal cavity lies the abdominal wall and above it lies a section of the diaphragm.

For the purpose of this research, we will study the group of surrounding organs classed as intraperitoneal, namely: the liver, spleen and hollow viscera (the stomach and the small and large intestines), as well as the adjacent abdominal wall and diaphragm. These organs/tissues were chosen as they had the most surface area in contact with the peritoneum (Rubin et al., 1988a). They also have a variety of fluid mechanical properties that affect fluid regulation in the peritoneal cavity, which are described below.

Liver

As mentioned previously, the liver lies underneath the diaphragm, in the upper right quadrant of the abdomen. The connection between the liver and the peritoneal cavity has already been detailed in Section 1.2.1.1 of this thesis. Under normal physiological conditions, the liver acts as a source of fluid into the peritoneal cavity, since excess interstitial fluid from the space of Disse leaks into the peritoneal cavity through the Glissonian–peritoneal membrane. Any increase in blood portal pressure is likely to result in an increase in fluid loss via the surface of the liver, and hence into the peritoneal cavity, as shown in the studies by Siggers et al. (2014).

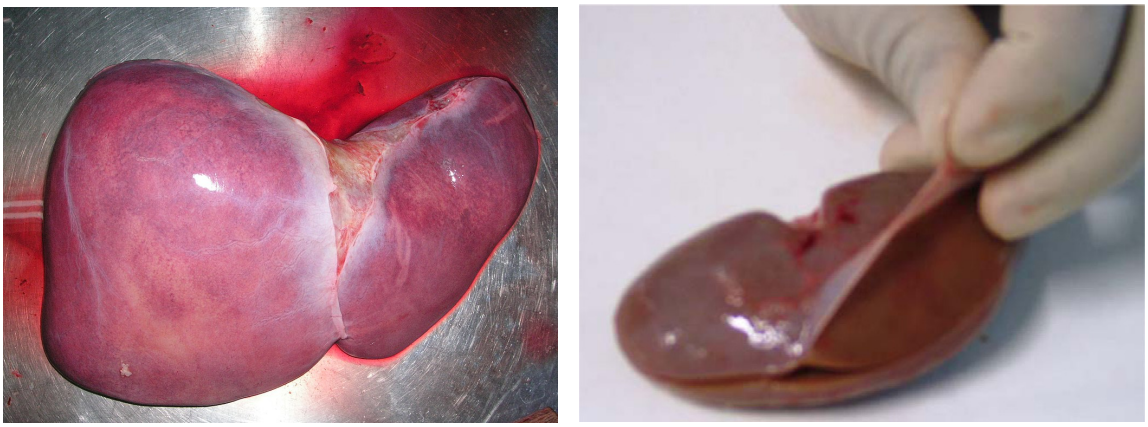
Spleen

The spleen also lies underneath the diaphragm, but in the upper left quadrant of the abdomen. Like the liver, it has a brownish tissue enclosed in a fibrous membrane (see Figure 1.9[ij]), which is covered by the peritoneal membrane, and its blood supply is via the splenic artery, which bifurcates in repeated generations until the terminal sinusoidal vessels, in which the blood

[i]Photo of liver taken by Suseno from Autopsy, Public Domain, `https://commons.wikimedia.org/w/index.php?curid=5118838`

[j]Figure of spleen taken from Umale et al. (2013).

plasma is filtered. As with most organs, the spleen has lymphatic vessels that drain interstitial fluid from its parenchyma. Since the liver and spleen both have permeable sinusoidal vessels and a fibrous capsular enclosure, we will assume that interstitial fluid can be lost from the spleen via pressure-driven flow through its surface, although no experimental data have been found to quantify its value. On the other hand, the spleen membrane could have a two–way permeability. In which case excess fluid can also flow from the peritoneal cavity and into the spleen in order to obtain an equilibrium pressure within the cavity.



(a) Liver Tissue (b) Spleen Tissue

Figure 1.9: Comparison of human liver tissue vs spleen tissue.

Diaphragm

The diaphragm is a thin sheet of skeletal muscle separating the thoracic cavity from the abdominal cavity. It lies directly above the liver, spleen and peritoneal cavity. In addition to its respiratory function, the diaphragm also acts as a drain for interstitial fluid from the adjacent pleural and peritoneal cavities.

Histological images of the diaphragm tissue reveal that both the upper and lower surfaces are covered with stomata, which are circular openings between its superficial mesothelial cells (see Figure 1.10[k]). These openings collect fluid from the surrounding cavities, which then enters a rich plexus of terminal lymphatics within the submesothelial layer called the lacunae. The fluid then enters the transverse lymphatic vessels, which transport it through the skeletal muscle fibres and into the central lymphatic collectors, from where it is drained out of the diaphragm (Moriondo et al., 2010; Negrini and Moriondo, 2011). Morphological studies of the diaphragm have also shown that the distribution of stomata and lacunae on the surfaces and within the diaphragm is non-uniform (Negrini et al., 1991, 1992), with higher densities in the central tendinous region of the diaphragm than in the muscular outer region. Furthermore, they

[k] All 3 images obtained from Moriondo et al. (2010).

are four times as numerous on the peritoneal side of the diaphragm than on the pleural side, suggesting there is a much higher rate of drainage and fluid turnover on that side (Negrini et al., 1992). There are several factors that could affect the rate of uptake of fluid by the diaphragmatic lymphatics. These include, but are not limited to, contraction and relaxation of the diaphragm during normal breathing, changes in respiratory pattern, changes in posture, and changes in intraperitoneal pressure (Abu-Hijleh et al., 1995). For the purpose of this research, we will only consider the effect of intraperitoneal pressure changes on the diaphragmatic lymphatic drainage.

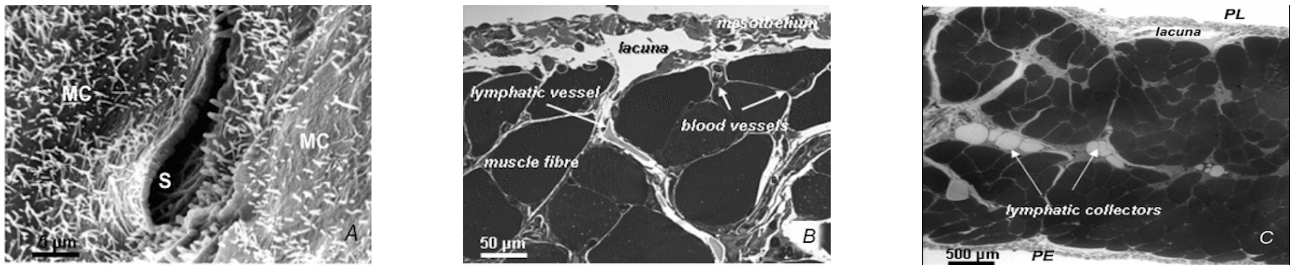


Figure 1.10: A: Electronic micrograph image of a rat diaphragm showing a stoma (S) nestled between mesothelial cells (MC). B: Partial cross–section of a rat diaphragm showing the mesothelial and muscle layers. Within them, the lacuna, muscle fibres, blood and lymphatic vessels. C: Full cross–section of a rat diaphragm showing both the pleural (PL) and peritoneal (PE) sides. Lymphatic vessels carry fluid from the lacuna, through the muscle fibres, and into the lymphatic collectors.

Abdominal Wall

The abdominal wall, covered by the peritoneal membrane, encloses the abdominal cavity and consists of three layers of tissue: muscle, subcutaneous fat and skin, the latter of which is further divided into the dermal and epidermal sublayers (Drake et al., 2014). Under normal physiological conditions, the abdominal wall acts as a drain of fluid from the peritoneal cavity. Fluid from the peritoneal cavity is absorbed into the abdominal wall tissue, from where it is taken up by the underlying network of blood and lymphatic vessels in the muscle, subcutaneous and dermal sublayer of the skin, each of which has a different composite structure (Negrini and Moriondo, 2011). The epidermis is the outermost sublayer of the skin and has no blood vessels. It acts as a barrier between the inner skin layers and the external environment.

Hollow Viscera

The hollow viscera consist of the stomach, small and large intestines, and each has four layers – mucosa, submucosa, muscle, serosa – of varying thickness. The lymphatic vessels of the hollow

viscera lie predominantly within the mucosal and submucosal sublayers and empty into various nodes around the organs. Blood capillaries, in addition to lymphatic vessels, also serve to regulate interstitial fluid volume when there is a change in plasma protein concentration. Most of the excess interstitial fluid, e.g in the case of oedema, is drained out into the lumen of the hollow viscera (Kvietys and Granger, 2010). While parts of the hollow viscera lie adjacent to the peritoneal cavity, we did not find any experimental data on the role they play (if any) on the normal regulation of fluid volume in the peritoneal cavity (Rubin et al., 1988b), and hence, we neglect them in this thesis.

1.3 Literature Review

1.3.1 Mathematical Models of Physiological Fluid Flow in the Liver

Studies on hepatic blood flow occupy a small section within the field of liver modelling, compared to say liver metabolism (Jerby et al., 2010). Only a few approaches have been made towards developing mathematical models of blood and interstitial fluid flow in the liver. These are summarised in this section of the thesis.

1.3.1.1 Electrical Analogue Models

The first electrical analogue model of the liver was developed by Van Der Plaats et al. (2004) to describe the haemodynamics in the network of blood vessels of a dog liver. The model was based on an analogy of the Navier–Stokes equations (for fluid flow through a cylindrical tube) and the electrical equations (for current flow through an electrical circuit). This was achieved by relating the serial resistance R_s, parallel resistance R_p and parallel conductance C of a circuit with the vascular resistance, viscoelasticity and elasticity of the blood vessels, respectively, and the serial inductance L with the inertia of the blood, thus forming the 4 components of an electrical π-filter. There were two blood inlet branches via the hepatic artery (HA) and the portal vein (PV) and outlet branch via the hepatic vein (HV), which further branch into several generations of smaller blood vessels. Each generation of blood vessels in the hepatic vascular tree was represented by one π-filter, and the total hepatic circulation was modelled as a series connection of π-filters (see Figure 1.11[l]). This system of equations was used to obtain the pressure drop and flow along successive generations (branches) of the vessels.

Debbaut et al. (2011) adapted the model by Van Der Plaats et al. (2004) to simulate blood flow in the human liver. As very little information was available on the parameters needed for the human liver model, they made use of a combination of vascular corrosion casting, micro-CT scanning and image processing to obtain detailed anatomical data and a 3D geometric replica of the liver vasculature (see Figure 1.12[m]). This included all three vascular trees: the hepatic arterial (HA), portal venous (PV) and hepatic venous (HV) trees. Data obtained showed an exponential decrease in vessel radii across each successive generation. Mean pressures and flows in the vessels, as well as pulsatile pressure and flow profiles against time, were obtained for the whole liver.

The results obtained by Van Der Plaats et al. (2004) had a significant discrepancy with respect to normal physiological data. This error was attributed to inaccurate diameter input of the vessels. Debbaut et al. (2011) provided a more accurate method of measuring vascular diameters. However, the experimental data obtained was from only one human liver, meaning

[l]Figure obtained from Debbaut et al. (2011).
[m]Figure obtained from Debbaut et al. (2011).

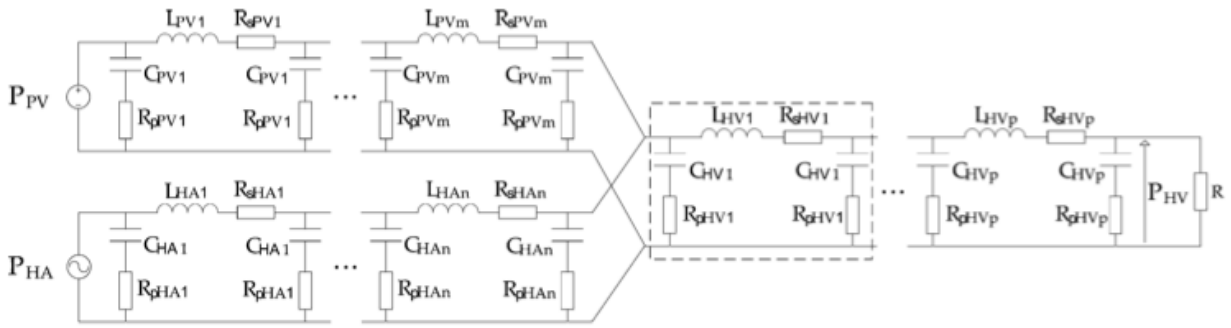


Figure 1.11: Schematic diagram of the electrical analog model of the liver showing the two inlets of the portal vein and hepatic artery, P_{PV} and P_{HA}, respectively, and the outlet via the hepatic vein P_{HV}. Each generation of blood vessels is represented by one π-filter with blood inertia L, vascular resistance R_s, vessel wall viscoelasticity R_p and vessel compliance C. The generations of the portal vein, hepatic artery and hepatic vein are numbered from $1, \cdots, m$, $1, \cdots, n$ and $1, \cdots, p$, respectively.

that the results presented could be patient specific. Also, data was only collected for the first few generations of vessels, and extrapolated to get the results for higher generations. The difficulty lies in measuring the resolution of a few micrometers, and hence, the computational limitation. However, since this model gives a good representation of physiological data, more experimental data would enable a generic model of the liver vasculature. The most recent attempt at obtaining these, using more refined and optimised measurement techniques, is by Peeters et al. (2017). Note however, that measurements carried out in the latter were that of a rat liver and not human.

Examples of other applications of the electrical analogue model include modelling of the hepatic arterial buffer response (HABR) by Ho et al. (2013a) and hemodynamic analysis of transjugular intrahepatic portosystemic shunt (TIPS) by Ho et al. (2013b). HABR is the homeostatic response of the liver to maintaining a constant portal venous flow through the variation of hepatic arterial flow (Lautt, 1985), while TIPS is a form of treatment strategy for portal hypertension (Ochs, 2005), the studies of which are both important in the understanding of physiological blood flow in the liver and improving current treatment procedures. The results obtained by Ho et al. (2013a) showed that although hepatic arterial blood flow increases immediately in response to a decrease in portal venous blood flow, only about 23.5% of lost portal venous flow was recovered through HABR. The clinical estimate of this value is within the range of 25–60% (Eipel et al., 2010). In Ho et al. (2013b), a 3D model of blood flow was used to simulate blood flow within a patient-specific TIPS system and visualise the resultant velocity streamlines and wall shear stress. The results obtained were validated against experimental data, and further used to investigate more complex flow patterns pre- and post-TIPS.

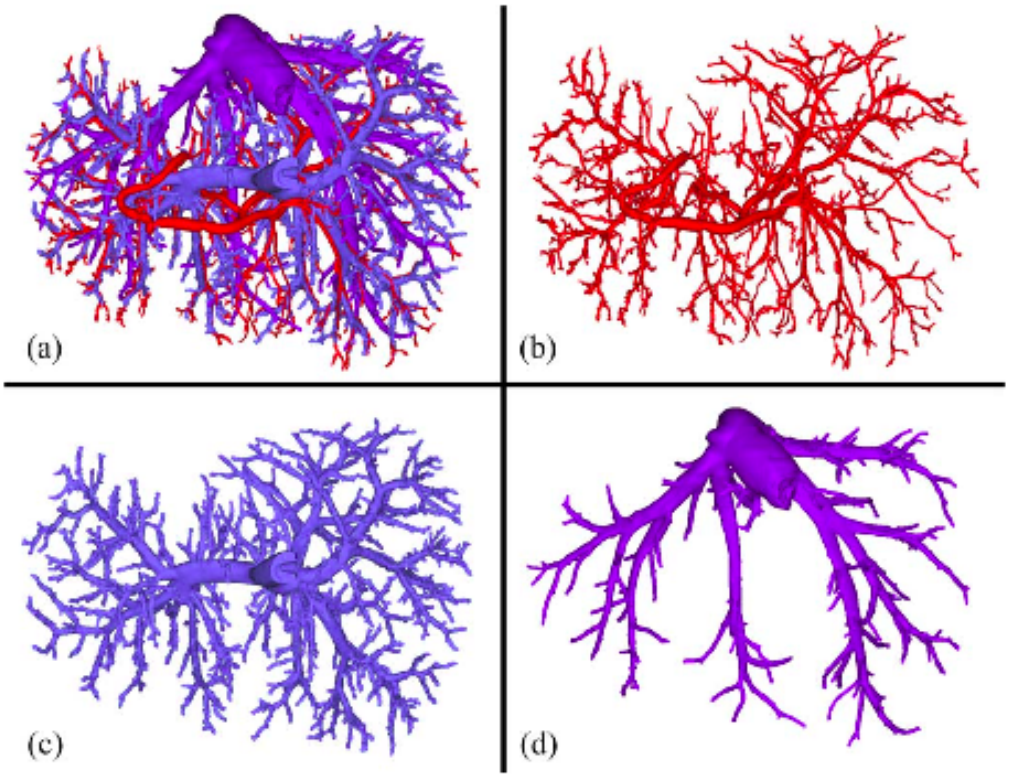


Figure 1.12: 3D replica of the vasculature of a human liver showing: (a) all 3 networks of blood vessels (b) the hepatic artery network with 6 generations (c) the portal vein network with 6 generations (d) the hepatic venous network with 5 generations.

1.3.1.2 3D CFD Models

A three-dimensional model of blood flow in the liver was presented by Rani et al. (2006). Blood flow was defined using the incompressible Navier–Stokes equations. Its shear thinning effect, i.e. ability for its viscosity to decrease under shear strain, was also taken into consideration. They had two inlet blood flows with different fluid properties. This was done in order to take into consideration the high-pressure and oxygen concentration of the arteriole, as well as the low-pressure and nutrient rich portal venule. The outlet consisted of a fenestrated sinusoidal path, and an open ended hepatic vein. A commercially available finite volume software, CFDRC by CFD Research Corporation, was used to simulate the numerical results of pressure and axial velocity in the vessels. It was found that pressure in the hepatic artery was the driving force for flow into the sinusoids, since it was much higher than that of the portal vein, thereby sweeping blood from the venule without much mixing of blood from the two inlets. The results were also compared for Newtonian and non-Newtonian blood flow. The axial velocity profile for the Newtonian fluid was found to be parabolic while that of the non-Newtonian fluid was flattened; a trait attributed to the shear thinning property of the blood. This model only considers flow in a single path, and does not take into consideration the whole lobule or liver.

After the studies on the electrical analogue model, Debbaut et al. (2012) performed micro-CT scan on the sinusoids of a liver sample in order to develop a 3D computational fluid dynamics (CFD) model of microcirculation. They investigated the possible anisotropy of the tissue and impact of the presence of vascular septa on blood perfusion by calculating the sinusoidal porosity and permeability tensor. Results obtained confirmed that the sinusoids were indeed anisotropic, with the permeability being highest in the direction parallel to the central vein. A similar result was also found in a more recent study of the cirrhotic liver by Peeters et al. (2015), where a 3D cast was also made in order to develop a 3D CFD model of fluid flow.

1.3.1.3 Biphasic Model

Ricken et al. (2010) devised a continuum mechanical model to investigate the remodelling of liver sinusoids following liver resection. The model consisted of two phases: a solid phase, representing the tissue structure, and a fluid phase, representing blood. They hypothesised that the rearrangement of the sinusoids after resection is dependent on the resulting pressure gradient. In addition to pressure changes, simulated results included the angles between the pressure gradient and the direction of the sinusoids' movement against time following an outflow obstruction (Ricken et al., 2010). This model, however, did not take into account mass transport across the two phases. More recently, it has been extended to incorporate glucose metabolism in the hepatocyte cells of the liver (Ricken et al., 2014) and simulate steatosis zonation in the liver lobule (Ricken et al., 2018). Daily variation of glucose metabolism was simulated under different glucose profiles, which confirmed the production of glucose by the liver in between meals or during fasting, and the uptake of glucose after a meal (Ricken et al., 2014). These conditions were also tested against the presence of fat deposits within the liver, which resulted in a decrease in blood perfusion and an altered glucose metabolism rate (Ricken et al., 2018).

1.3.1.4 Porous Media Models

Bonfiglio et al. (2010) presented a 2D model based on the classic hexagonal geometry of the liver lobules (see Figure 1.13[n]). Because of their tortuous nature, the sinusoids were treated as a porous medium and Darcy's law was used to describe the flow of blood through them. The model was further applied to study the possible anisotropy of sinusoids, the shear thinning of blood and deformation of the liver tissue. Results showed that the effects of anisotropy and shear thinning were negligible on the flow of blood through the lobule under small deformations. Significant differences between the original and the deformable liver model highlighted the importance of incorporating tissue compliance in modelling liver perfusion.

A number of other porous media models have been developed since the studies by Bonfiglio et al. (2010). Siggers et al. (2014) extended the model into a lobule lattice model of the whole

[n]Figure obtained from Bonfiglio et al. (2010).

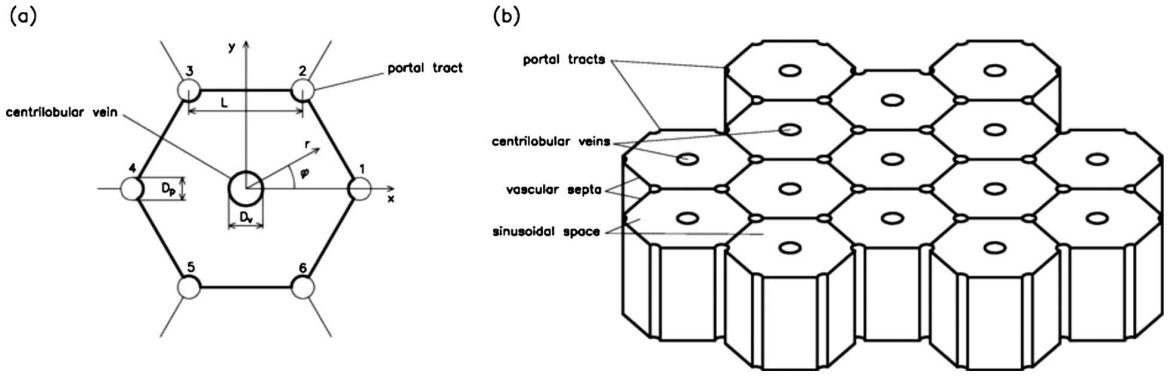


Figure 1.13: Sketch of a cross–section of the domain used by Bonfiglio et al. (2010), showing: (a) single hexagonal lobule with side length L, six portal tracts of diameter D_p and a central vein of diameter D_v (b) hypothetical lobule lattice highlighting the sinusoidal space and vascular septa.

liver and also included the flow of interstitial fluid and lymph uptake within the liver. This model is described in more detail in Section 2 of this thesis, as we will be making use of it as the basis of our poro-elastic liver model. The poro-elastic model aims to capture blood and interstitial fluid flow in a deformable (compliant) liver tissue, for both a single lobule and a lobule lattice structure representing the whole liver organ.

Subsequent studies by Debbaut et al. (2014) also resulted in a 3D porous medium model of blood flow in the liver lobule, taking into consideration anisotropy of the sinusoids in the transverse direction and the flow of blood across the vascular septa. The inclusion of anisotropy resulted in a more spatially homogeneous magnitude of blood velocity field compared with having isotropy within the lobule, while including flow across the vascular septa resulted in better blood perfusion between neighbouring portal tracts compared to simulations with no blood flow across the vascular septa. Lettmann and Hardtke–Wolenski (2014) incorporated a reaction-transport model for dissolved substances, such as oxygen and cytokines, into a 2D porous liver model, thus obtaining oxygen uptake profiles and spatial distribution of secreted cytokines within the lobule. Hu et al. (2017) analysed the flow dynamics in fibrotic liver tissue by increasing the resistance to blood flow, i.e. decreasing the tissue permeability, in a 3D porous liver model. This resulted in a subsequent decrease in average blood velocity across the lobule, agreeing with clinical observations that the presence of fibrotic tissue leads to decreased blood perfusion in the liver.

1.3.2 Mathematical Models of Physiological Fluid Flow Across the Peritoneal Membrane

Only a few previous studies have modelled the transport of fluid across the peritoneal cavity, one of the first of which was by Flessner et al. (1984), who developed a distributed mathematical model of fluid and small solute flow across a layer of capillary-rich peritoneal tissue (see Figure 1.14[o]). Flow across the tissue was governed by diffusion and convection, while uptake was through capillary membranes. The model was then coupled with lymphatic drainage through the diaphragm and transport of fluid through the rest of the body to form a compartmental model. Some of the results simulated include the concentration of sucrose across the width of the peritoneal tissue and over time, for different starting values of sucrose concentrations in the peritoneal cavity. Their theoretical model was also later validated experimentally in studies by Flessner et al. (1985a,b).

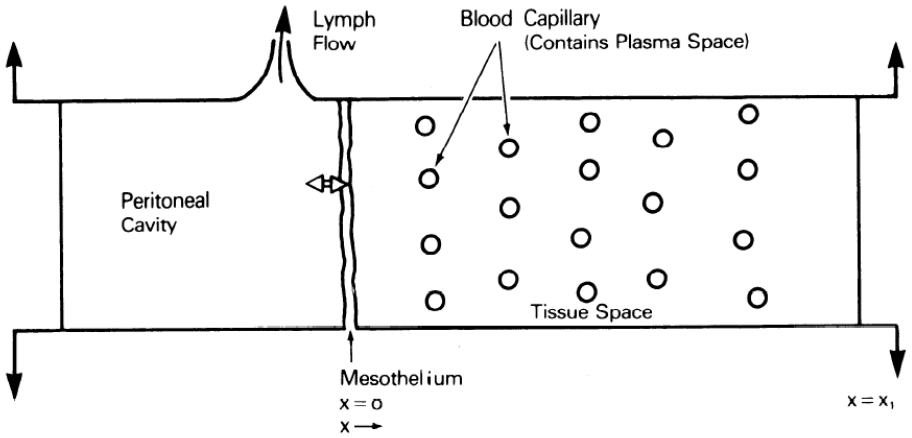


Figure 1.14: Illustration of fluid transport across a peritoneal tissue space of thickness x_1 by Flessner et al. (1984). The tissue is assumed to be evenly distributed with blood capillaries. Fluid drainage is through blood capillaries in the tissue and lymphatic uptake from the peritoneal cavity.

A series of more recent studies treats the parietal peritoneum (which lines the abdominal wall) and the visceral peritoneum (which lines the visceral organs), with the respective abdominal wall and visceral organ walls, as layers of rigid porous media whose void volume fraction is dependent on the interstitial pressure (Stachowska-Pietka and Waniewski, 2011; Stachowska-Pietka et al., 2004, 2006). This was done in order to model the transport of dialysis fluid across the peritoneal tissue, which had a different protein content to that of normal plasma/interstitial fluid. Flow across the tissue layers was governed by Darcy's law, while again, interstitial fluid uptake was through capillary membranes and lymphatic vessels. The abdominal wall was modelled as a double layer of thick muscle and thin skin, with an impermeable outer boundary.

[o]Figure obtained from Flessner et al. (1984).

The visceral organs were modelled as a lumped tissue layer with a permeable outer boundary. Results obtained included pressure and flow profiles across the different layers, as well as the timescale to equilibrium volume flux values, for both hydrostatic and osmotic pressure driven flows. Intra-peritoneal pressure was found to be the driving force for fluid flow across the tissue. The higher the pressure, the more fluid is absorbed from the peritoneal cavity into the surrounding tissue. Once within the tissue, interstitial fluid pressure decreases exponential towards the edge of the abdominal wall/lumen of the hollow viscera.

None of the models mentioned above consider the role played by the liver in peritoneal fluid accumulation. That is why in Chapter 5 of this thesis, we develop a compartmental model of fluid exchange in the peritoneal cavity that takes account of the fluid transport across the liver surface and the walls of some of the organs/tissue adjacent to the peritoneal cavity, which are the spleen, abdominal wall and diaphragm. We use appropriate models of fluid transport for each organ. For the liver organ, we make use of the poro-elastic liver model to be developed in this thesis (Chapters 2–3). For the spleen and diaphragm, we make use of membrane transport equations and finally, for the abdominal wall, we make use of a modified version of the porous medium model by Stachowska-Pietka et al. (2004, 2006).

1.4 Mathematical Background: Introduction to Poroelasticity

The theory of poroelasticity, also known as Biot theory of poromechanics, is a branch of engineering used to study the flow of fluids in deformable porous materials. It was originally formulated in the field of geomechanics to study the flow of fluids in soil, and oil and gas in rocks. More recently, it has also been used in the study of biological systems such as cerebrospinal fluid transport in the brain (Chou et al., 2014; Tully and Ventikos, 2009, 2011), gas exchange in the lungs (Berger et al., 2014, 2016), cardiac perfusion (Chapelle et al., 2010; Yang et al., 1994) and fluid dynamics in the eye (Aletti, 2017; Causin et al., 2014; Repetto et al., 2011). We will be making use of the theory in this thesis to model the microcirculation of blood and interstitial fluid in the liver.

In this section, we introduce the governing equations for fluid flow in a poroelastic material. We begin by presenting the system of equations governing the flow of fluid in a rigid porous medium, then the mechanics of elastic solids and finally, the Biot equation for poroelasticity.

1.4.1 Fluid Flow in Porous Media

A porous material is any solid that is permeated with pores or capillary networks, which are filled with gas and/or fluid. In addition to soil and rocks, other examples include sponge, wood, cement and some biological tissues such as bone. Fluid flow in a porous medium is governed by Darcy's law, which can be derived from the Navier–Stokes equation (Bear, 2013). It works on the assumption that the fluid is viscous and incompressible, and that its velocity can be approximated to a volume averaged flux through the material. This theory holds if we work in terms of material volume scales that are large compared to that of an individual pore. The equation for Darcy's law is summarised below (Bear, 2013; Tweedy, 2017).

1.4.1.1 Darcy's Law

Darcy's law states that the average volume flux per unit area, $\mathbf{v}$, of a viscous fluid in a porous medium is given by:

$$\mathbf{v} = \frac{\kappa}{\mu}(\mathbf{f} - \boldsymbol{\nabla} p_f), \tag{1.1}$$

where p_f is the fluid pressure, $\mathbf{f}$ is the total body force per unit volume acting on the fluid (e.g. gravity), μ is the shear viscosity of the fluid and κ is the permeability of the medium.

A typical average fluid velocity within the pores is given by $\mathbf{v}/\varphi$, where φ is the porosity – a measure of the amount of pores in the solid. The fluid velocity and pressure can be obtained using mass conservation. For an incompressible fluid, mass conservation results in the continuity

equation, which is given by

$$\boldsymbol{\nabla} \cdot \mathbf{v} = \mathcal{Q}, \tag{1.2}$$

where $\boldsymbol{\nabla}$ is the gradient tensor and $\mathcal{Q}$ is the net volume of fluid produced per unit volume per unit time in the medium. Combining Equations (1.1) and (1.2) gives

$$\boldsymbol{\nabla} \cdot (\kappa \mathbf{f}) - \boldsymbol{\nabla} \cdot (\kappa \boldsymbol{\nabla} p_f) = \mu \mathcal{Q}. \tag{1.3}$$

If we assume that there are no body forces acting on the medium, or that their effects are negligible, i.e. $\mathbf{f} = 0$, then Equation (1.3) simplifies to

$$\boldsymbol{\nabla} \cdot (\kappa \boldsymbol{\nabla} p_f) = -\mu \mathcal{Q}, \tag{1.4}$$

and if we further have that the net change in volume flux in the medium is zero, i.e. $\mathcal{Q} = 0$, then we have

$$\boldsymbol{\nabla} \cdot (\kappa \boldsymbol{\nabla} p_f) = 0. \tag{1.5}$$

The equation of Darcy's law presented above will be used to obtain pressure and flow profiles of blood in the sinusoids and interstitial fluid in the interstitial space in Chapters 2–3 of this thesis.

Permeability of the Medium κ

The permeability of the medium κ is a measure of how much 'resistance' the solid medium provides to the flow of fluid through it. It depends on both the porosity of the medium and the geometry of the pores themselves, and in particular, the tortuosity of the pores and the degree to which they are interconnected (Tweedy, 2017). In general, κ is a 2-tensor (i.e. 3×3 matrix) but this depends on the dimensions of the problem being considered. For an isotropic solid, i.e. one whose material properties are the same in all three principal directions, κ is a constant in space. However, κ would vary in anisotropic (non-isotropic) materials (Tweedy, 2017).

One of the most common formulas used to determine κ is the Carmen–Kozeny equation, which was developed for flow through a packed bed of sand. It states that

$$\kappa = \frac{d^2}{4c} \frac{\varphi^3}{(1-\varphi^2)}, \tag{1.6}$$

where d is the average diameter of the sand grains, c is the Kozeny constant and φ is the porosity of the bed (Bear, 2013). Since we will be modelling the flow of blood in a bed of capillaries, not sand grains, we will make use of a modified version of the Carmen–Kozeny equation which is derived in the section below.

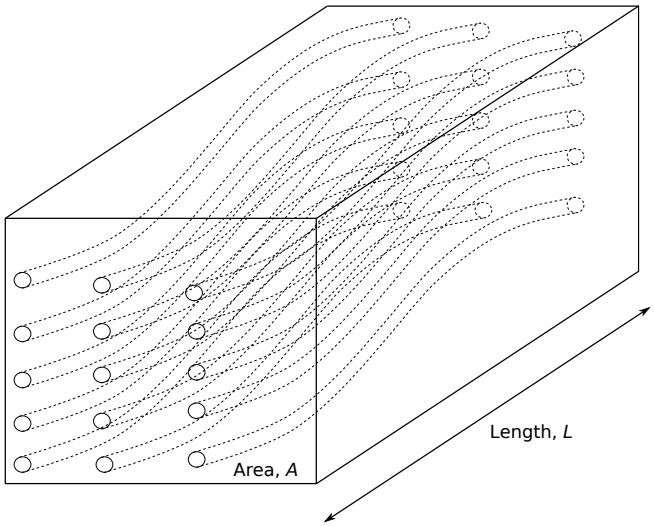


Figure 1.15: Hypothetical block of porous medium of volume $\mathcal{V}$, end area A, and length L in the third direction, containing N idealised cylindrical capillaries.

1.4.1.2 Modified Carmen–Kozeny Equation

Consider a block of volume $\mathcal{V}$, cross-sectional area A and length L in the third direction, so that $\mathcal{V} = AL$ (see Figure 1.15). We shall assume that the block has N idealised cylindrical capillaries of length l (where $l >> L$) and radius r. We will also assume that Poiseuille's law holds in each of the capillaries, such that the volumetric flux Q in each capillary is given by

$$Q = \frac{\pi r^4}{8\mu}\frac{\Delta p}{l}, \tag{1.7}$$

where μ is the viscosity of the fluid and Δp is the pressure drop across the capillary. Therefore, the total volumetric flux through the block is given by

$$Q_{\text{TOT}} = NQ = \frac{N\pi r^4}{8\mu}\frac{\Delta p}{l}. \tag{1.8}$$

Recall, also, that by Darcy's law (1.1),

$$Q_{\text{TOT}} = A\mathbf{v} = A\frac{\kappa}{\mu}\boldsymbol{\nabla} p = A\frac{\kappa}{\mu}\frac{\Delta p}{L}. \tag{1.9}$$

Therefore,

$$\kappa = \left(\frac{Q_{\text{TOT}}}{A}\right)\frac{\mu L}{\Delta p} = \left(\frac{N\pi r^4}{8\mu A}\frac{\Delta p}{l}\right)\frac{\mu L}{\Delta p} = \frac{N\pi r^4}{8A}\frac{L}{l}. \tag{1.10}$$

Next, we define other useful parameters as follows:

- **Tortuosity:**

$$\tau = \frac{\text{Length of a capillary}}{\text{Length of block}} = \frac{l}{L}.$$

- **Porosity:**

$$\varphi = \frac{\text{Total capillary volume}}{\text{Total block volume}} = \frac{\mathcal{V}_{\text{pore}}}{\mathcal{V}} = \frac{N\pi r^2 l}{AL} = \frac{N\pi r^2}{A}\tau.$$

- **Specific Surface Area:**

$$\mathcal{S} = \frac{\text{Total capillary wall area}}{\text{Total block volume}} = \frac{\mathcal{W}_{\text{pore}}}{\mathcal{V}} = \frac{N2\pi rl}{AL} = \frac{2N\pi r}{A}\tau = \frac{2\varphi}{r}.$$

Hence, Equation (1.10) becomes

$$\kappa = \frac{1}{8}\left(\frac{N\pi r^2}{A}\right)\frac{r^2 L}{l} = \frac{1}{8}\left(\frac{\varphi}{\tau}\right)\left(\frac{2\varphi}{\mathcal{S}}\right)^2\frac{1}{\tau} = \frac{\varphi^3}{2\tau^2\mathcal{S}^2}. \tag{1.11}$$

Therefore, for any capillary pore network, the permeability κ can be obtained using

$$\kappa = \frac{\varphi^3}{2\tau^2\mathcal{S}^2}, \tag{1.12}$$

which we refer to as the modified Carmen–Kozeny Equation.

During deformation, there are a number of assumptions that could be made about the changing properties of the porous block. We will choose to assume that the length of the capillaries l remains constant during deformation, then from Equation (1.10),

$$\kappa = \frac{N\pi r^4}{8A}\frac{L}{l} = \frac{N\pi r^4}{8A}\frac{L}{l}\frac{\mathcal{V}_{\text{pore}}^2}{(N\pi r^2 l)^2} = \frac{\mathcal{V}_{\text{pore}}^2}{8NA\pi}\frac{L}{l^3} = \frac{\mathcal{V}_{\text{pore}}^2}{8N\pi\mathcal{V}}\frac{L^2}{l^3} = \frac{L^2\mathcal{V}_{\text{pore}}^2}{n\mathcal{V}}. \tag{1.13}$$

That is to say

$$\kappa = \frac{L^2\mathcal{V}_{\text{pore}}^2}{n\mathcal{V}}, \tag{1.14}$$

where $n = 8\pi N l^3$ is a constant. We make use of Equation (1.14) in Section 2.5 of this thesis to derive the hydraulic conductivities of the sinusoids and interstitial space, respectively, as functions of tissue deformation.

The assumption of a constant capillary length l was made in order to obtain a version of the modified Carmen–Kozeny Equation that was not dependent on pore tortuosity τ, since no physiological value of τ could be found for the liver sinusoids and interstitial space or how its value changes with deformation. Having a constant l is synonymous to the capillary vessels unfolding as the block of tissue expands. This also ensures that we do not have to be concerned about capillary breakage within our model, since $l >> L$.

1.4.2 Mechanics of Elastic Solid Deformation

In this section, we summarise the mechanics of solid material deformation. We also consider two different types of materials: linearly elastic, which make use of small deformation theory, and hyperelastic materials, which make use of large deformation theory.

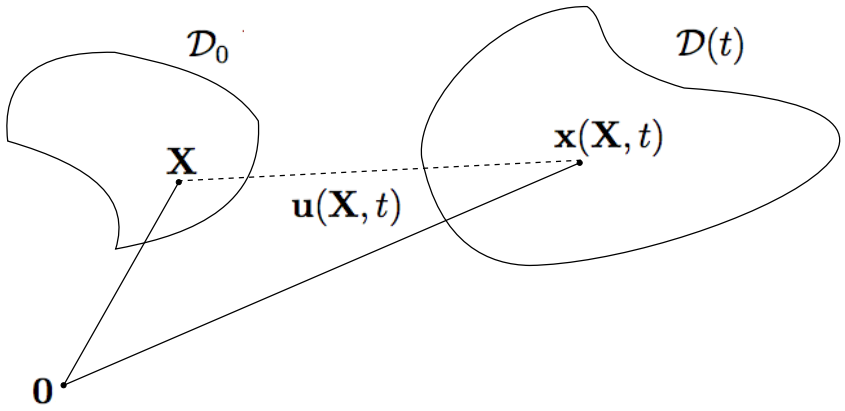


Figure 1.16: Movement of material particle from reference configuration $\mathcal{D}_0$ to current configuration $\mathcal{D}$ during deformation.

1.4.2.1 Introduction

The deformation of solid materials can be modelled as the movement of material particles in space from an initial point in time. Let the volume $\mathcal{D}_0$ be the undeformed (Lagrangian) reference configuration and let $\mathbf{X}$ indicate the position of a particle in $\mathcal{D}_0$ at $t = 0$. The position of a particle in the deformed configuration $\mathcal{D}(t)$ at time $t > 0$ is given by $\mathbf{x}(\mathbf{X}, t)$ (see Figure 1.16). The displacement field of the particle is thus given by

$$\mathbf{u}(\mathbf{X}, t) = \mathbf{x}(\mathbf{X}, t) - \mathbf{X}. \tag{1.15}$$

The deformation gradient tensor is defined as

$$\mathbf{F}(\mathbf{X}, t) = \frac{\partial \mathbf{x}}{\partial \mathbf{X}}, \tag{1.16}$$

and the Jacobian of the deformation gradient is defined as

$$J = \det(\mathbf{F}), \tag{1.17}$$

which represents the change in an infinitesimal control volume from the reference configuration $\mathcal{D}_0$ to the current configuration $\mathcal{D}$. Note that since

$$\frac{\partial \mathbf{u}}{\partial \mathbf{X}} = \frac{\partial \mathbf{x}}{\partial \mathbf{X}} - \frac{\partial \mathbf{X}}{\partial \mathbf{X}} = \mathbf{F} - \mathbf{I}, \tag{1.18}$$

where $\mathbf{I}$ is the identity matrix,

$$J = \det(\mathbf{F}) = \det\left(\mathbf{I} + \frac{\partial \mathbf{u}}{\partial \mathbf{X}}\right) = \det\left(\mathbf{I} + \boldsymbol{\nabla}\mathbf{u}\right). \tag{1.19}$$

The displacement field $\mathbf{u}$ can be obtained by balancing the stress forces $\boldsymbol{\sigma}(\mathbf{u})$ on the solid

material. At equilibrium,

$$\boldsymbol{\nabla} \cdot \boldsymbol{\sigma} = -\mathcal{F}, \tag{1.20}$$

where $\mathcal{F}$ is the net surface force per unit volume acting on the material, e.g due to contact load. The equation of $\boldsymbol{\sigma}(\mathbf{u})$ depends on material properties of the solid, e.g. isotropic or anisotropic, linear or hyperelastic. For the purpose of this thesis, we will only work with isotropic solids, i.e. materials that deform uniformly in all three principal directions. Materials in which the displacement increases linearly with stress applied are known as linearly elastic materials. For linearly elastic materials, the small deformation theory (Section 1.4.2.2) can be used to obtain the equation of the stress tensor (Section 1.4.2.3), proof of which can be found, for example, in Holzapfel (2000). Other materials which have a non-linear relationship between stress and displacement are known as hyperelastic materials. The non-linear stress–strain behaviour is captured by what is referred to as a strain energy function. Details of this is covered in Sections 1.4.2.4–1.4.2.5 of this thesis.

1.4.2.2 Small Deformation Theory

Small deformation theory, also known as infinitesimal strain theory, assumes that the displacement of the particles in the solid material is very small, or infinitesimally small, compared to the size of the material itself. Mathematically, this means that we can neglect higher order multiples of the gradient of the displacement $\boldsymbol{\nabla}\mathbf{u}$ when they appear, since they will be much smaller than the displacement gradient itself (Lai et al., 2009). For example, consider the Jacobian of the deformation gradient defined in Equation (1.19) and for simplicity, assume deformation occurs in 2D such that $\mathbf{F}$ is a 1-tensor (i.e. 2×2 matrix), $\mathbf{u} = (u_1, u_2)$ and $\mathbf{X} = (X_1, X_2)$. Then,

$$\begin{aligned} J = \det(\mathbf{F}) =& \det\left(\mathbf{I} + \frac{\partial \mathbf{u}}{\partial \mathbf{X}}\right) \\ =& \left(1 + \frac{\partial u_1}{\partial X_1} + \frac{\partial u_2}{\partial X_2} + \frac{\partial u_1}{\partial X_1}\frac{\partial u_2}{\partial X_2} - \frac{\partial u_1}{\partial X_2}\frac{\partial u_2}{\partial X_1}\right). \end{aligned} \tag{1.21}$$

According to small deformation theory, the last two terms of Equation (1.21) can be neglected since

$$\frac{\partial u_1}{\partial X_1}\frac{\partial u_2}{\partial X_2} \ll \frac{\partial u_1}{\partial X_1}, \frac{\partial u_2}{\partial X_2} \quad \text{and} \quad \frac{\partial u_1}{\partial X_2}\frac{\partial u_2}{\partial X_1} \ll \frac{\partial u_1}{\partial X_1}, \frac{\partial u_2}{\partial X_2}. \tag{1.22}$$

Therefore,

$$J = \det\left(\mathbf{I} + \boldsymbol{\nabla}\mathbf{u}\right) = \det\left(\mathbf{I} + \frac{\partial \mathbf{u}}{\partial \mathbf{X}}\right) \approx \left(1 + \frac{\partial u_1}{\partial X_1} + \frac{\partial u_2}{\partial X_2}\right) = \left(1 + \boldsymbol{\nabla} \cdot \mathbf{u}\right). \tag{1.23}$$

The small strain theory results in the linearisation, and thus simplification, of the equations of solid deformation. This includes the equation of the Cauchy stress tensor, which is presented

in the next section.

1.4.2.3 Cauchy Stress Tensor for Linear Elastic Materials

For isotropic and homogenous linear elastic materials, the Cauchy stress tensor $\boldsymbol{\sigma}$ is derived from Hooke's law (see e.g. Lai et al., 2009) and defined as

$$\boldsymbol{\sigma} = \frac{E\nu}{(1-\nu)(1-2\nu)}(\boldsymbol{\nabla}\cdot\mathbf{u})\mathbf{I} + \frac{E}{(1+\nu)}\boldsymbol{\varepsilon}, \tag{1.24}$$

where E and ν are the Young's modulus and Poisson's ratio of the materials, respectively, and $\boldsymbol{\varepsilon}$ is the strain tensor given by

$$\boldsymbol{\varepsilon} = \frac{1}{2}(\boldsymbol{\nabla}\mathbf{u} + \boldsymbol{\nabla}\mathbf{u}^{\mathrm{T}}). \tag{1.25}$$

1.4.2.4 Large Deformation Theory

Large deformation theory, or finite strain theory, holds for larger displacements where the small deformation theory no longer holds. In this case, there is a clear difference between the undeformed (reference) configuration and the deformed (current) configuration and material properties must be defined in each case. First, we define some of the terminologies used in large deformation theory as we change from the reference to the current configurations.

Terminology/Definitions

Volume Change: Changes in volume with deformation is given by

$$\mathrm{d}V = J\ \mathrm{d}V_0, \tag{1.26}$$

where V and V_0 are the volumes in the deformed/current and undeformed/reference configurations, respectively. Note that $J > 0$.

Surface Area Change: Changes in surface area is given by

$$\mathbf{n}\ \mathrm{d}A = J\mathbf{F}^{-\mathrm{T}}\mathbf{n}_0\ \mathrm{d}A_0, \tag{1.27}$$

where A and A_0 are the areas and $\mathbf{n}$ and $\mathbf{n}_0$ are the unit normal vectors in the deformed/current and undeformed/reference configurations, respectively. This equation is also known as Nanson's formula (Holzapfel, 2000).

Cauchy–Green Tensors: The symmetric right and left Cauchy–Green deformation tensors are defined as $\mathbf{C} = \mathbf{F}^{\mathrm{T}}\mathbf{F}$ and $\mathbf{B} = \mathbf{F}\mathbf{F}^{\mathrm{T}}$, respectively.

Strain Invariants: The first, second and third invariants of the right (and left) Cauchy–Green

deformation tensors, respectively, are given by

$$I_1 = \text{tr}(\mathbf{C}), \quad I_2 = \frac{1}{2}[(\text{tr}(\mathbf{C}))^2 - \text{tr}(\mathbf{C}^2)] \quad \text{and} \quad I_3 = \det(\mathbf{C}) = J^2. \tag{1.28}$$

The invariants do not change with rotation of the coordinate system.

Hyperelastic Material: An idealised material whose stress–strain relationship can be derived from a strain energy density/function $W(\mathbf{C}) = \tilde{W}(\mathbf{F}) = \hat{W}(I_1, I_2, I_3) = \check{W}(I_1, I_2, J)$.

Strain Energy Function: A strain energy function is any function that captures the non-linear stress–strain behaviour of an elastic solid. There are many different types of strain energy functions, including polynomial and logarithmic, which can be found empirically for each different type of solid material (Wex et al., 2015). The strain energy function of the material can also be decomposed into two components:

$$W = W_{\text{vol}} + W_{\text{iso}}. \tag{1.29}$$

W_{vol} relates to the volumetric response of the material while W_{iso} accounts for the shear behaviour of the material. For an isotropic (nearly) incompressible material, $W_{\text{vol}} = W_{\text{vol}}(J)$ and $W_{\text{iso}} = W_{\text{iso}}(I_1, I_2)$.

1.4.2.5 Cauchy Stress Tensor for Hyperelastic Materials

The Cauchy stress tensor for a hyperelastic material $\boldsymbol{\sigma}_e$ is given by

$$\boldsymbol{\sigma}_e = \frac{1}{J}\frac{\partial W}{\partial \mathbf{F}}\mathbf{F}^{\text{T}}. \tag{1.30}$$

The equation above holds for both isotropic and anisotropic materials, since the variation between the two occurs in the strain energy function W (Holzapfel, 2000).

Equation (1.30) can also be written in terms of the right and left Cauchy–Green tensors, respectively, as

$$\boldsymbol{\sigma}_e = \frac{2}{J}\mathbf{F}\frac{\partial W}{\partial \mathbf{C}}\mathbf{F}^{\text{T}} \quad \text{and} \quad \boldsymbol{\sigma}_e = \frac{2}{J}\mathbf{B}\frac{\partial W}{\partial \mathbf{B}}, \tag{1.31}$$

Given that $W = W_{\text{vol}}(J) + W_{\text{iso}}(I_1, I_2)$, Equation (1.30) can be further differentiated and simplified to obtain

$$\boldsymbol{\sigma}_e = \frac{2}{J}\left\{\left(\frac{\partial W_{\text{iso}}}{\partial I_1} + I_1\frac{\partial W_{\text{iso}}}{\partial I_2}\right)\mathbf{B} - \frac{\partial W_{\text{iso}}}{\partial I_2}\mathbf{B}^2\right\} + \frac{\partial W_{\text{vol}}}{\partial J}\mathbf{I}, \tag{1.32}$$

the derivation of which is shown below.

Proof: Differentiation of Cauchy Stress Equation for an Isotropic Hyperelastic Material

The Cauchy stress tensor for a hyperelastic material can be written in terms of the right Cauchy–Green tensor as $(1.31)_a$:

$$\boldsymbol{\sigma}_e = \frac{2}{J}\mathbf{F}\frac{\partial W}{\partial \mathbf{C}}\mathbf{F}^{\mathrm{T}}. \tag{1.33}$$

By differentiation,

$$\frac{\partial W}{\partial \mathbf{C}} = \frac{\partial \hat{W}}{\partial I_1}\frac{\partial I_1}{\partial \mathbf{C}} + \frac{\partial \hat{W}}{\partial I_2}\frac{\partial I_2}{\partial \mathbf{C}} + \frac{\partial \hat{W}}{\partial I_3}\frac{\partial I_3}{\partial \mathbf{C}}. \tag{1.34}$$

Note also that

$$\frac{\partial I_1}{\partial \mathbf{C}} = \frac{\partial(\mathrm{tr}(\mathbf{C}))}{\partial \mathbf{C}} = \mathrm{tr}\left(\frac{\partial \mathbf{C}}{\partial \mathbf{C}}\right) = \mathbf{I}, \tag{1.35}$$

$$\frac{\partial I_2}{\partial \mathbf{C}} = \frac{\partial}{\partial \mathbf{C}}\left(\frac{1}{2}[(\mathrm{tr}(\mathbf{C}))^2 - \mathrm{tr}(\mathbf{C}^2)]\right) = \frac{1}{2}\left[\frac{\partial}{\partial \mathbf{C}}\left(I_1^2\right) - \frac{\partial}{\partial \mathbf{C}}\left(\mathrm{tr}(\mathbf{C}^2)\right)\right] = I_1\mathbf{I} - \mathbf{C}, \tag{1.36}$$

$$\frac{\partial I_3}{\partial \mathbf{C}} = \frac{\partial(\det(\mathbf{C}))}{\partial \mathbf{C}} = \det(\mathbf{C})\mathbf{C}^{-1}. \tag{1.37}$$

Therefore, Equation (1.34) becomes

$$\begin{aligned}\frac{\partial W}{\partial \mathbf{C}} &= \frac{\partial \hat{W}}{\partial I_1}\cdot\mathbf{I} + \frac{\partial \hat{W}}{\partial I_2}\cdot(I_1\mathbf{I} - \mathbf{C}) + \frac{\partial \hat{W}}{\partial I_3}\cdot(\det(\mathbf{C})\mathbf{C}^{-1}) \\ &= \frac{\partial \hat{W}}{\partial I_1}\mathbf{I} + \frac{\partial \hat{W}}{\partial I_2}\cdot(I_1\mathbf{I} - \mathbf{F}^{\mathrm{T}}\mathbf{F}) + \frac{\partial \hat{W}}{\partial I_3}\cdot(I_3\mathbf{F}^{-1}\mathbf{F}^{-\mathrm{T}}).\end{aligned} \tag{1.38}$$

Plugging this into the Cauchy Stress Equation (1.33),

$$\begin{aligned}\boldsymbol{\sigma}_e &= \frac{2}{J}\mathbf{F}\left(\frac{\partial \hat{W}}{\partial I_1}\mathbf{I} + \frac{\partial \hat{W}}{\partial I_2}\cdot(I_1\mathbf{I} - \mathbf{F}^{\mathrm{T}}\mathbf{F}) + \frac{\partial \hat{W}}{\partial I_3}\cdot(I_3\mathbf{F}^{-1}\mathbf{F}^{-\mathrm{T}})\right)\mathbf{F}^{\mathrm{T}} \\ &= \frac{2}{J}\left(\frac{\partial \hat{W}}{\partial I_1}\mathbf{F}\mathbf{F}^{\mathrm{T}} + \frac{\partial \hat{W}}{\partial I_2}\cdot(I_1\mathbf{F}\mathbf{F}^{\mathrm{T}} - \mathbf{F}\mathbf{F}^{\mathrm{T}}\mathbf{F}\mathbf{F}^{\mathrm{T}}) + \frac{\partial \hat{W}}{\partial I_3}\cdot I_3\mathbf{I}\right).\end{aligned} \tag{1.39}$$

Recall that $\mathbf{B} = \mathbf{F}\mathbf{F}^{\mathrm{T}}$ and $I_3 = \det(\mathbf{C}) = J^2$. Hence,

$$\boldsymbol{\sigma}_e = \frac{2}{J}\left(\frac{\partial \hat{W}}{\partial I_1}\mathbf{B} + \frac{\partial \hat{W}}{\partial I_2}\cdot(I_1\mathbf{B} - \mathbf{B}^2) + J^2\frac{\partial \hat{W}}{\partial I_3}\mathbf{I}\right). \tag{1.40}$$

Since $W = \hat{W} = W_{\text{vol}}(J) + W_{\text{iso}}(I_1, I_2)$,

$$\begin{aligned}
\boldsymbol{\sigma}_e &= \frac{2}{J}\left(\frac{\partial W_{\text{iso}}}{\partial I_1}\mathbf{B} + \frac{\partial W_{\text{iso}}}{\partial I_2}\cdot(I_1\mathbf{B} - \mathbf{B}^2) + J^2\frac{\partial W_{\text{vol}}}{\partial I_3}\mathbf{I}\right) \\
&= \frac{2}{J}\left\{\left(\frac{\partial W_{\text{iso}}}{\partial I_1} + \frac{\partial W_{\text{iso}}}{\partial I_2}\cdot I_1\right)\mathbf{B} - \frac{\partial W_{\text{iso}}}{\partial I_2}\mathbf{B}^2 + J^2\frac{\partial W_{\text{vol}}}{\partial I_3}\mathbf{I}\right\} \\
&= \frac{2}{J}\left\{\left(\frac{\partial W_{\text{iso}}}{\partial I_1} + I_1\frac{\partial W_{\text{iso}}}{\partial I_2}\right)\mathbf{B} - \frac{\partial W_{\text{iso}}}{\partial I_2}\mathbf{B}^2\right\} + 2J\frac{\partial W_{\text{vol}}}{\partial I_3}\mathbf{I}. \qquad (1.41)
\end{aligned}$$

Finally, note that

$$\frac{\partial W_{\text{vol}}}{\partial I_3} = \frac{\partial W_{\text{vol}}}{\partial J}\frac{\partial J}{\partial I_3} = \frac{\partial W_{\text{vol}}}{\partial J}\frac{1}{2J}. \qquad (1.42)$$

Therefore,

$$\boldsymbol{\sigma}_e = \frac{2}{J}\left\{\left(\frac{\partial W_{\text{iso}}}{\partial I_1} + I_1\frac{\partial W_{\text{iso}}}{\partial I_2}\right)\mathbf{B} - \frac{\partial W_{\text{iso}}}{\partial I_2}\mathbf{B}^2\right\} + 2J\frac{\partial W_{\text{vol}}}{\partial I_3}\mathbf{I} \qquad (1.43)$$

$$= \frac{2}{J}\left\{\left(\frac{\partial W_{\text{iso}}}{\partial I_1} + I_1\frac{\partial W_{\text{iso}}}{\partial I_2}\right)\mathbf{B} - \frac{\partial W_{\text{iso}}}{\partial I_2}\mathbf{B}^2\right\} + \frac{\partial W_{\text{vol}}}{\partial J}\mathbf{I}. \qquad (1.44)$$

1.4.2.6 Material Vs Geometric Nonlinearities

Material nonlinearities refer to the nonlinearities in solutions that occur as a result of a nonlinear constitutive equation for the stress–strain behaviour of the solid, while geometric nonlinearities refer to nonlinearities from kinematic quantities such as strain–displacement relationships (Sönnerlind, 2015). Geometric nonlinearities can occur due to large displacements, strains or rotations (Sönnerlind, 2013). The net nonlinearities observed in numerical solutions is a combination of both material and geometric nonlinearities.

In Chapter 2, we assume a linear stress–strain behaviour for the liver tissue and, hence, have material linearity. In Chapter 3, we model the liver tissue as a hyperelastic material with a nonlinear stress–strain behaviour and, hence, expect material nonlinearities. Note that solids that have material linearity can also exhibit geometric nonlinearities, for example, under large strains.

Geometric linearity is often implied under small strains. In this case, the equations of equilibrium are formulated in the undeformed state and are not updated with the deformation. This is because the deformations are assumed to be so small compared to the original geometry, that any resultant numerical error is negligible (Sönnerlind, 2015). In Chapter 2, we shall assume geometric linearities for the liver tissue since we will be studying small strain deformations. In Chapter 3, we will be considering large deformations of the liver tissue and hence, must take into consideration geometric nonlinearities. According to (Sönnerlind, 2013), this is when we

start to consider that area elements actually change, that there is a distinction between an original length and a deformed length, and that directions may change during the deformation, as defined in Section 1.4.2.4. Further details on how this is done is given in Chapter 3.

1.4.3 Fluid Flow in Poroelastic Media

The Biot equation for poroelasticity works on the theory that the net Cauchy stress $\tilde{\boldsymbol{\sigma}}$ in the poroelastic medium consists of the elastic solid stress component, $\boldsymbol{\sigma}$ for a linear elastic material and $\boldsymbol{\sigma}_e$ for a hyperelastic material, and the fluid stress component $\boldsymbol{p}_f$. Therefore, any increase in fluid volume, and hence pressure, in the pore networks is likely to increase the net stress on the elastic solid and therefore result in an expansion of the material, i.e.

$$\tilde{\boldsymbol{\sigma}} = \begin{cases} \boldsymbol{\sigma} - p_f \mathbf{I}, & \text{for a linear elastic material, and} \\ \boldsymbol{\sigma}_e - p_f \mathbf{I}, & \text{for a hyperelastic material,} \end{cases} \tag{1.45}$$

where $\boldsymbol{\sigma}$ and $\boldsymbol{\sigma}_e$ are defined in Equations (1.24) and (1.30), respectively. For the remainder of this thesis, $\tilde{\boldsymbol{\sigma}}$ will be referred to as the modified Cauchy stress tensor. Neglecting any external load, the constitutive equation for poroelastic deformation is then given by

$$\boldsymbol{\nabla} \cdot \tilde{\boldsymbol{\sigma}} = 0. \tag{1.46}$$

Note that for the liver microcirculation model, we will have a double pore/capillary network of blood and interstitial fluid and hence, p_f in Equation (1.45) above will be the sum of two different fluid pressures.

Part II

Microcirculation in a Poroelastic Model of the Liver

Chapter 2

Linear Elastic Deformation Model

2.1 Introduction

One of the aims of this research is to develop a mathematical model of the liver tissue capable of accommodating changes in arterial and porto venous vasodilation. This can be achieved by coupling the equations of physiological fluid flow with the mechanics of elastic solid deformation. In this chapter, we develop a mathematical model of microcirculation of blood and interstitial fluid in a linearly elastic model of the liver tissue, which is later used to study the effect of liver fibrosis on flow dynamics and filtration capability of the organ.

We begin by detailing the set-up of our model, which includes our modelling assumptions and governing equations. Using prescribed boundary conditions, we solve the system of governing equations using the COMSOL Multiphysics software, the results of which are presented and analysed at the end of this chapter.

2.2 Modelling Assumptions

For the purposes of this study, we make use of the following assumptions on the fluid and solid components of our system, as well as the geometry of the liver tissue. These assumptions hold throughout the thesis, unless otherwise stated.

2.2.1 Physiological Fluids

Blood Rheology: Blood is composed of about 54% plasma fluid and 46% red blood cells (Ethier and Simmons, 2007). Plasma is an incompressible fluid, whose viscosity is slightly higher than that of water. Red blood cells are quite deformable and their suspension within plasma fluid results in the shear thinning behaviour of blood, hence, its classification as a non-Newtonian fluid (Ethier and Simmons, 2007). However, it has been

suggested by Bonfiglio et al. (2010) that taking into account the shear thinning effect of blood in the microcirculation of the liver lobule has a negligible effect on the pressure and flow values obtained, and so we neglect it in this study and treat blood in the sinusoids as an incompressible Newtonian fluid with a constant dynamic viscosity μ_s. This assumption can be revisited in future studies of the liver.

Interstitial Fluid Rheology: Interstitial fluid has the same water content as plasma fluid, but with slightly different solute concentration (Ethier and Simmons, 2007). In this study, it is also treated as an incompressible Newtonian fluid with dynamic viscosity μ_i.

2.2.2 Liver Tissue

Homogenous Porous Media: Following Siggers et al. (2014), the liver lobule is modelled as double-porous network of sinusoids, containing blood, and interstitial space, containing interstitial fluid, which are connected through the exchange of plasma fluid. The pore space containing interstitial fluid, φ_i, is assumed to be smaller than that of blood, φ_s, since the fenestrations between endothelial cells ($\sim 1\,\mu$m) is a lot smaller than the average diameter of a sinusoid ($\sim 10\,\mu$m). The sinusoidal and interstitial spaces are also assumed to be homogeneously distributed within the lobule.

Incompressibility: The volume of tissue $\mathcal{V}_{\text{tissue}}$ within the liver is assumed to remain constant during deformation. This is motivated by the fact that over 70% of the liver tissue is water and $< 1\%$ of it becomes ash (Mitchell et al., 1945). Since ash is a measure of the solid content within a material, it means that less than 1% of the liver tissue is compressible, and thus, expected tissue volume changes are much less than 1%. So we can assume that, as a whole, the tissue is incompressible since water is also assumed to be incompressible.

Homogenous Elastic Tissue: The liver tissue is treated as a homogenous elastic porous material. This implies that we assume the same material properties for the sinusoids and interstitial space.

Linear Elasticity: For deformations up to 10%, we treat the tissue as a linearly elastic solid and make use of the small deformation theory detailed in Section 1.4.2.2. This is covered in this chapter of the thesis.

Hyperelasticity: In order to capture deformations up to the maximum of 40%, the liver tissue is treated as a hyperelastic solid (defined in Section 1.4.2.4). This is necessary in order to capture the non-linear behaviour of the tissue at large strains and is covered in Chapter 3 of this thesis.

Pressurised System: Since the liver organ is pressurised even in the healthy case, we work in terms of pressures referenced against their values in the normal physiological case, the latter of which is termed as the *undeformed* state of the liver. Any deviation in the blood

portal pressure above the undeformed state will result in the expansion of the sinusoidal and interstitial pore networks and, hence, expansion of the liver tissue as a whole.

2.2.3 Geometry

As in the studies by Siggers et al. (2014), the liver tissue is modelled as a 3D lattice of identical lobules (see Figure 2.1). Lobules located within the liver, which we call interior lobules, are chosen to have the regular hexagonal prism shape with side length l_{lob}, thickness $t_{\text{lob}} = \sqrt{3}l_{\text{lob}}$ and height h_{lob} (Figure 2.2). Each interior lobule also has circular portal tracts of diameter d_{pt} at each of its six corners and a circular central vein of diameter d_{cv} at its centre (see Figure 2.2a). The assumption here is that each circular portal tract consists of a combination of blood from terminal endings of the hepatic artery and the portal vein, while the circular central vein acts as a single drainage site for blood filtered by all sinusoidal vessels. Lobules located next to the outer surface of the liver are pentagonal, rather than hexagonal, and are called the exterior lobules. The shape of the exterior lobules was chosen in order to capture the flatness and smoothness of the outer surface of the liver. Although each exterior lobule has five portal tracts surrounding a central vein, they have the same area and volume as the interior lobules (see Figure 2.2b).

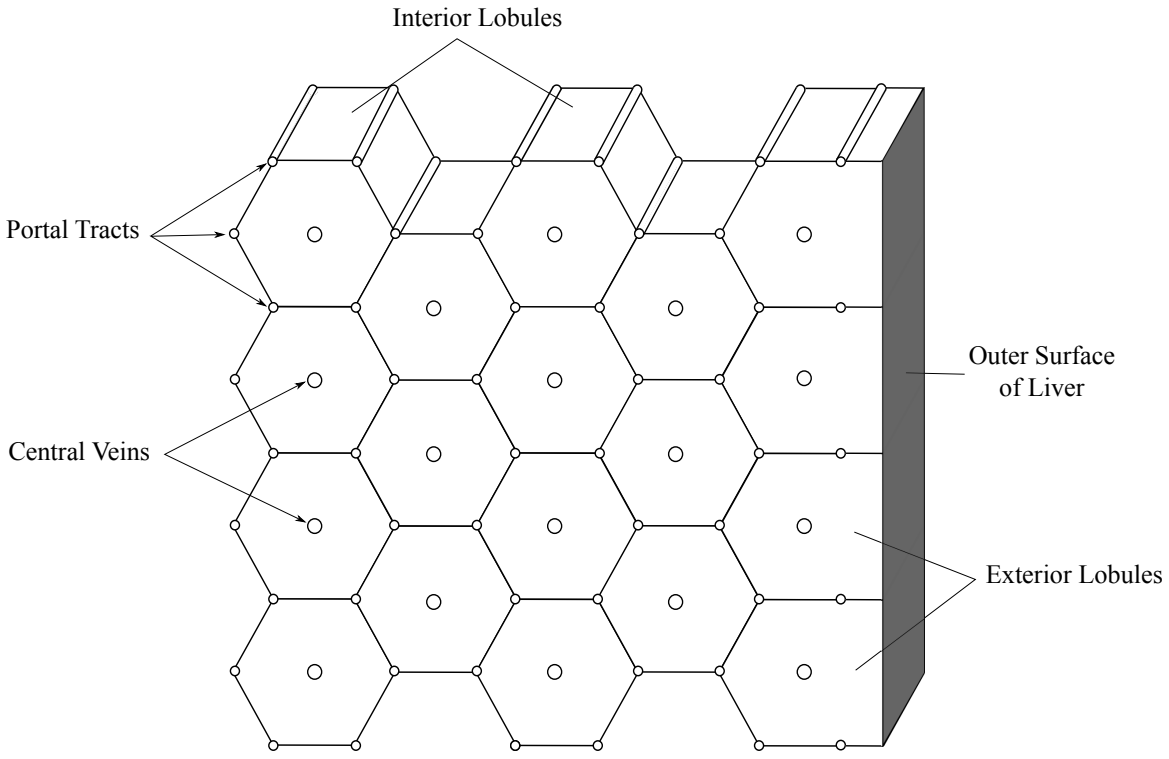


Figure 2.1: Illustration of the lattice arrangement of the liver lobules used to model the liver. The diagram shows both the interior lobules, located within the tissue, and the exterior lobules located next to the outer surface of the liver. Each lobule has one central vein surrounded by five or six portal tracts.

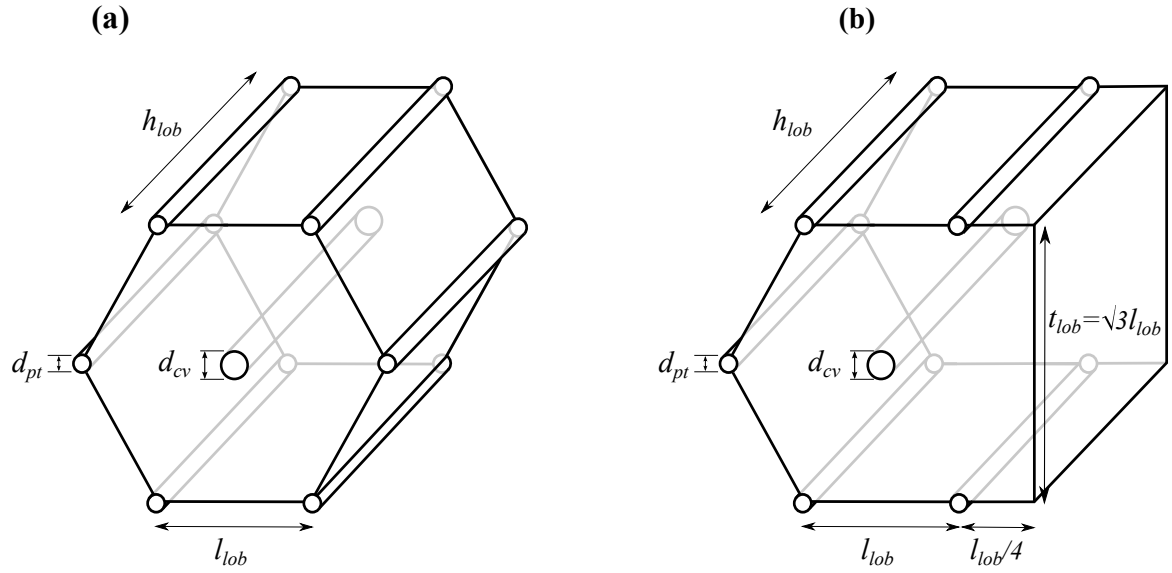


Figure 2.2: Illustration of (a) Interior lobule and (b) Exterior lobule. Interior lobules are located within the liver tissue and have six portal tracts surrounding a central vein. Exterior lobules are located next to the outer surface of the liver and have five portal tracts surrounding a central vein.

2D Approximation

In this chapter, we only consider flow in the cross-sectional plane, thereby neglecting the third direction. We will also assume that there is no deformation in the third direction and cross-sectional deformation is isotropic. These assumptions are relaxed in Chapter 3, where we consider 3D flow and deformation.

2.3 Equations Governing Fluid Flow

In this section, we present the equations governing the flow of blood in the sinusoids and interstitial fluid in the interstitial space of the liver lobule. These are covered in two subsections. In the first subsection, we reproduce the equations of flow in the rigid model developed by Siggers et al. (2014). This is done solely to obtain blood and interstitial fluid pressure distributions to be used as reference cases for deformation. In the second subsection, we develop the equations of flow in a deformable liver, which take into consideration expansion of the pore network to accommodate increase in blood and/or interstitial fluid pressures referenced against the rigid case.

2.3.1 Undeformed Liver Lobule

The undeformed liver is defined as the normal physiological state of the liver with no expansion of the tissue (i.e. rigid state as in Siggers et al., 2014), and this will be used as the reference

state for any subsequent tissue deformation. Note that the liver tissue is in a condition of non-zero stress in this state, and indeed all body tissues are typically never in an unpressurised state before death. The following set of equations have been reproduced from the study by Siggers et al. (2014).

Both the sinusoidal and interstitial space networks are modelled as homogenous porous media. This motivates the use of Darcy's law to define the flow of blood and interstitial fluid in the undeformed lobule, respectively, as

$$\mathbf{v}_{s,\mathrm{ref}} = -\frac{\boldsymbol{\kappa}_{s,\mathrm{ref}}}{\mu_s}\boldsymbol{\nabla} p_{s,\mathrm{ref}} \quad \text{and} \quad \mathbf{v}_{i,\mathrm{ref}} = -\frac{\boldsymbol{\kappa}_{i,\mathrm{ref}}}{\mu_i}\boldsymbol{\nabla} p_{i,\mathrm{ref}}, \tag{2.1}$$

where $\mathbf{v}_{s,\mathrm{ref}}$ and $\mathbf{v}_{i,\mathrm{ref}}$ are the volume-averaged flux per unit area (also known as Darcy velocity) in the sinusoids and interstitial space, respectively; $\boldsymbol{\kappa}_{s,\mathrm{ref}}$ and $\boldsymbol{\kappa}_{i,\mathrm{ref}}$ are permeabilities of the undeformed sinusoids and interstitial space, respectively; μ_s and μ_i are the effective viscosities of blood and interstitial fluid, respectively; and $p_{s,\mathrm{ref}}$ and $p_{i,\mathrm{ref}}$ are blood pressure in the sinusoids and interstitial fluid pressure in the interstitial space; respectively, in the undeformed lobule.

By the law of mass conservation, the fluid volume flux in each pore compartment must be conserved. Recall that as blood flows across the sinusoids, plasma fluid is filtered from the blood and into the surrounding interstitial space. According to Starling's hypothesis (see e.g. Ethier and Simmons, 2007), fluid flux across a capillary wall is driven by both mechanical and oncotic pressure differences. However, it has been shown in experimental studies by Laine et al. (1979) that there is a lack of sieving of plasma proteins across the sinusoidal capillaries of dog livers during portal venous hypertension. As a result, they argued that the plasma protein sieving coefficient must be close to zero at the sinusoidal wall. This is probably due to wall membrane structure of the sinusoids highlighted in the introductory Section 1.2.1.1. Secondly, they observed that the protein content of the lymph fluid was 95% that of the plasma value in the liver. Hence, they concluded that the typical oncotic pressure differences in the liver are negligible compared to the mechanical pressure difference (Laine et al., 1979). Therefore, we also neglect oncotic pressure differences in the liver and so define the plasma flux per unit volume into the interstitial space as

$$q_{\mathrm{plasma}} = C_f(p_{s,\mathrm{ref}} - p_{i,\mathrm{ref}}). \tag{2.2}$$

where C_f is the hepatic filtration coefficient.

Note that according to Equation (2.2), if the pressure difference between the sinusoidal capillary and the surrounding interstitial space is positive, plasma flow direction while be from blood to the interstitial space. However, a reversal of flow is possible, i.e. from the interstitial space into the sinusoids, if the pressure difference becomes negative.

Excess plasma fluid can also be drained from the interstitial space by initial lymphatic vessels embedded within the tissue. We assume that fluid uptake by the lymphatic vessels in

the lobule is a linear function of mechanical interstitial fluid pressure (Elk et al., 1988), and given by the equation

$$q_{\text{lymph}} = C_l \max\left(p_{i,\text{ref}} - p_0, 0\right), \tag{2.3}$$

where C_l is the conductance of the lymphatic vessels and p_0 is the average pressure within the flowing lymphatic vessels. Note that lymph uptake is always positive as lymphatic vessels have valves to prevent the backward flow of fluid.

Applying mass conservation to both the sinusoidal and interstitial spaces gives us the governing equations for flow

$$\boldsymbol{\nabla} \cdot \mathbf{v}_{s,\text{ref}} + q_{\text{plasma}} = 0, \tag{2.4}$$

$$\boldsymbol{\nabla} \cdot \mathbf{v}_{i,\text{ref}} - q_{\text{plasma}} + q_{\text{lymph}} = 0. \tag{2.5}$$

Combining the above equations with Equations (2.2)–(2.3) gives

$$\boldsymbol{\nabla} \cdot \mathbf{v}_{s,\text{ref}} + C_f(p_{s,\text{ref}} - p_{i,\text{ref}}) = 0, \tag{2.6}$$

$$\boldsymbol{\nabla} \cdot \mathbf{v}_{i,\text{ref}} - C_f(p_{s,\text{ref}} - p_{i,\text{ref}}) + C_l \max(p_{i,\text{ref}} - p_0, 0) = 0, \tag{2.7}$$

and incorporating Equations $(2.1)_\text{a}$–$(2.1)_\text{b}$ gives

$$\boldsymbol{\nabla} \cdot \left(-\frac{\boldsymbol{\kappa}_{s,\text{ref}}}{\mu_s} \boldsymbol{\nabla} p_{s,\text{ref}}\right) + C_f(p_{s,\text{ref}} - p_{i,\text{ref}}) = 0, \tag{2.8}$$

$$\boldsymbol{\nabla} \cdot \left(-\frac{\boldsymbol{\kappa}_{i,\text{ref}}}{\mu_i} \boldsymbol{\nabla} p_{i,\text{ref}}\right) - C_f(p_{s,\text{ref}} - p_{i,\text{ref}}) + C_l \max(p_{i,\text{ref}} - p_0, 0) = 0, \tag{2.9}$$

which can be used to find the pressure distributions of blood and interstitial fluid across the lobule in the undeformed case.

The permeabilities of the sinusoidal and interstitial space, $\boldsymbol{\kappa}_{s,\text{ref}}$ and $\boldsymbol{\kappa}_{i,\text{ref}}$, respectively, are assumed to be isotropic in the first instance, unless otherwise stated. That is to say that $\boldsymbol{\kappa}_{s,\text{ref}} = \kappa_{s,\text{ref}}\mathbf{I}$ and $\boldsymbol{\kappa}_{i,\text{ref}} = \kappa_{i,\text{ref}}\mathbf{I}$, where $\mathbf{I}$ is the identity matrix. For the undeformed case of the liver lobule, we choose $\kappa_{s,\text{ref}}$ and $\kappa_{i,\text{ref}}$ to be constants and have the same values as used by Siggers et al. (2014).

2.3.2 Deformed Liver Lobule

The same assumption of a homogenous double porous network holds in the case of the deformed liver lobule. We denote blood pressure in the sinusoids and interstitial fluid pressure in the interstitial space of the deformed liver as p_s and p_i, respectively. Using Darcy's law and mass conservation as in Section 2.3.1, and again neglecting oncotic pressure differences, we obtain the following coupled equations for fluid flow in the deformable liver lobule:

$$\boldsymbol{\nabla} \cdot \left(-\frac{\boldsymbol{\kappa}_s}{\mu_s} \boldsymbol{\nabla} p_s \right) + C_f (p_s - p_i) = 0, \tag{2.10}$$

$$\boldsymbol{\nabla} \cdot \left(-\frac{\boldsymbol{\kappa}_i}{\mu_i} \boldsymbol{\nabla} p_i \right) - C_f (p_s - p_i) + C_l \max(p_i - p_0, 0) = 0, \tag{2.11}$$

where $\boldsymbol{\kappa}_s$ and $\boldsymbol{\kappa}_i$ are permeabilities of the deformed sinusoids and interstitial space, respectively, while μ_s, μ_i, C_f, C_l and p_0 remain unchanged as in Section 2.3.1 above.

The equations above can be rewritten in the form

$$\boldsymbol{\nabla} \cdot \mathbf{v}_s + C_f (p_s - p_i) = 0, \tag{2.12}$$

$$\boldsymbol{\nabla} \cdot \mathbf{v}_i - C_f (p_s - p_i) + C_l \max(p_i - p_0, 0) = 0, \tag{2.13}$$

where

$$\mathbf{v}_s = -\frac{\boldsymbol{\kappa}_s}{\mu_s} \boldsymbol{\nabla} p_s \quad \text{and} \quad \mathbf{v}_i = -\frac{\boldsymbol{\kappa}_i}{\mu_i} \boldsymbol{\nabla} p_i, \tag{2.14}$$

are the averaged Darcy velocities of blood and interstitial space, respectively, in the deformed case.

The permeabilities of the sinusoidal and interstitial space, $\boldsymbol{\kappa}_s$ and $\boldsymbol{\kappa}_i$, respectively, in the deformed lobule are no longer constants as they were in the rigid case (Section 2.3.1). Instead, they are chosen to be variables dependent on the expansion of the pores, following an increase in the referenced fluid pressures. In Section 2.5, we formulate equations for $\boldsymbol{\kappa}_s$ and $\boldsymbol{\kappa}_i$, which will be dependent on the tissue deformation $\mathbf{u}$. But first, we introduce the constitutive equation for tissue stress that determines the deformation $\mathbf{u}$ in Section 2.4 below.

2.4 Equations Governing Tissue Deformation

In this section, we present the equations governing the deformation of the liver lobule. Deformation of the lobule occurs as a result of expansion of the blood and interstitial fluid pore networks to accommodate changes in blood and/or interstitial fluid mechanical pressures. Since the liver organ is pressurised even in the normal physiological case, we work in terms of fluid pressures referenced against their values in the normal physiological case (i.e. the undeformed liver).

2.4.1 Stress–Strain Relationship

The constitutive equation for stress within the liver tissue can be derived using the theory of poroelasticity (Section 1.4). We make use of the modified Cauchy stress tensor $\tilde{\boldsymbol{\sigma}}$, which was introduced in Section 1.4.3:

$$\tilde{\boldsymbol{\sigma}} = \boldsymbol{\sigma} - p_f \mathbf{I}, \tag{2.15}$$

where $\boldsymbol{\sigma}$ is the Hookean Cauchy stress tensor (see Section 1.4.2.3), p_f is the net fluid pressure and $\mathbf{I}$ is the identity matrix. Recall that we have chosen to work in terms of fluid pressures referenced against their normal physiological values (see Section 2.2.2) and so can define p_f as

$$p_f = (p_s - p_{s,\text{ref}}) + (p_i - p_{i,\text{ref}}), \tag{2.16}$$

where p_s and $p_{s,\text{ref}}$ are sinusoidal blood pressures in the deformed and undeformed (reference) cases, respectively, and p_i and $p_{i,\text{ref}}$ are interstitial fluid pressures in the deformed and undeformed (reference) cases, respectively. Therefore, the modified Cauchy stress tensor becomes

$$\tilde{\boldsymbol{\sigma}} = \boldsymbol{\sigma} - [(p_s - p_{s,\text{ref}}) + (p_i - p_{i,\text{ref}})]\mathbf{I}, \tag{2.17}$$

For the linearly elastic liver tissue, the Hookean Cauchy stress tensor $\boldsymbol{\sigma}$ is defined in Section 1.4.2.3 as

$$\boldsymbol{\sigma} = \frac{E_L \nu_L}{(1-\nu_L)(1-2\nu_L)} (\boldsymbol{\nabla} \cdot \mathbf{u}) \mathbf{I} + \frac{E_L}{(1+\nu_L)} \boldsymbol{\varepsilon}, \tag{2.18}$$

where E_L and ν_L are the elastic constant and Poisson ratio of liver tissue, respectively, $\mathbf{u}$ is the total tissue displacement and $\boldsymbol{\varepsilon}$ is the strain tensor defined by

$$\boldsymbol{\varepsilon} = \frac{1}{2} \left[(\boldsymbol{\nabla}\mathbf{u}) + (\boldsymbol{\nabla}\mathbf{u})^{\mathrm{T}} \right]. \tag{2.19}$$

The divergence of the stress tensor is the force per unit volume acting in the solid, and, neglecting inertia of the tissue, we have the equation governing tissue deformation as

$$\boldsymbol{\nabla} \cdot \tilde{\boldsymbol{\sigma}} = 0. \tag{2.20}$$

2.5 Hydraulic Conductivity of Pore Networks

In this section, we make use of the modified Carmen–Kozeny equation presented in Section 1.4.1.2 to obtain the equation of hydraulic conductivities of the sinusoidal and interstitial spaces of the liver lobule. We first begin by defining the porosity of the individual pore spaces.

2.5.1 Tissue Porosity

Porosity is a measure of the quantity of pores in any porous medium. It can be estimated by dividing the volume of fluid within the pores by the total volume of the medium.

Consider a small control volume section $\mathcal{V}$ of the liver that is large compared to the distance between neighbouring sinusoidal vessels but small compared to the size of the lobule. We shall assume that such a volume is composed of tissue, blood in the sinusoids and interstitial fluid in

the interstitial space, which have volumes $\mathcal{V}_{\text{tissue}}$, $\mathcal{V}_{\text{blood}}$ and $\mathcal{V}_{\text{ifluid}}$, respectively. That is to say

$$\mathcal{V} = \mathcal{V}_{\text{tissue}} + \mathcal{V}_{\text{blood}} + \mathcal{V}_{\text{ifluid}}. \tag{2.21}$$

The volume $\mathcal{V}$ is also related to the undeformed volume $\mathcal{V}_{\text{ref}}$ by

$$\mathcal{V} = J\mathcal{V}_{\text{ref}} = \det(\mathbf{F})\mathcal{V}_{\text{ref}} = \det(\mathbf{I} + \boldsymbol{\nabla}\mathbf{u})\mathcal{V}_{\text{ref}} \approx (1 + \boldsymbol{\nabla} \cdot \mathbf{u})\mathcal{V}_{\text{ref}}, \tag{2.22}$$

where $\mathbf{F}$ is the deformation gradient tensor. The approximation in Equation (2.22) was deduced using small deformation theory (Section 1.4.2.2).

We assume that the volume of fluid in each individual pore network in $\mathcal{V}$ is given by the pore volume in the undeformed case, $\mathcal{V}_{\text{ref}}$, plus any increased fluid volume due to the expansion of the individual pore network. Hence, the volume of blood and interstitial fluid in $\mathcal{V}$, respectively, are given by

$$\mathcal{V}_{\text{blood}} = \mathcal{V}_{\text{blood,ref}} + \beta_s(\mathcal{V} - \mathcal{V}_{\text{ref}}) \quad \text{and} \quad \mathcal{V}_{\text{ifluid}} = \mathcal{V}_{\text{ifluid,ref}} + \beta_i(\mathcal{V} - \mathcal{V}_{\text{ref}}), \tag{2.23}$$

where $\mathcal{V}_{\text{blood,ref}}$ and $\mathcal{V}_{\text{ifluid,ref}}$ are blood and interstitial fluid volumes, respectively, in the undeformed liver, and β_s and β_i are coefficients defined by

$$\beta_s = \frac{(p_s - p_{s,\text{ref}})}{(p_s - p_{s,\text{ref}}) + (p_i - p_{i,\text{ref}})} \quad \text{and} \quad \beta_i = \frac{(p_i - p_{i,\text{ref}})}{(p_s - p_{s,\text{ref}}) + (p_i - p_{i,\text{ref}})} \tag{2.24}$$

for the sinusoidal and interstitial space, respectively. Using the small deformation theory, we have that

$$\begin{aligned} \mathcal{V}_{\text{blood}} = \mathcal{V}_{\text{blood,ref}} + \beta_s(\mathcal{V} - \mathcal{V}_{\text{ref}}) &= \mathcal{V}_{\text{blood,ref}} + \beta_s((1 + \boldsymbol{\nabla} \cdot \mathbf{u})\mathcal{V}_{\text{ref}} - \mathcal{V}_{\text{ref}}) \\ &= \mathcal{V}_{\text{blood,ref}} + \beta_s(\boldsymbol{\nabla} \cdot \mathbf{u})\mathcal{V}_{\text{ref}} \end{aligned} \tag{2.25}$$

and

$$\begin{aligned} \mathcal{V}_{\text{ifluid}} = \mathcal{V}_{\text{ifluid,ref}} + \beta_i(\mathcal{V} - \mathcal{V}_{\text{ref}}) &= \mathcal{V}_{\text{ifluid,ref}} + \beta_i((1 + \boldsymbol{\nabla} \cdot \mathbf{u})\mathcal{V}_{\text{ref}} - \mathcal{V}_{\text{ref}}) \\ &= \mathcal{V}_{\text{ifluid,ref}} + \beta_i(\boldsymbol{\nabla} \cdot \mathbf{u})\mathcal{V}_{\text{ref}}. \end{aligned} \tag{2.26}$$

The total volume of fluid in the pores of the liver lobule is given by the sum of blood and interstitial fluid volumes, which according to Equations (2.21) & (2.22), is

$$\mathcal{V}_{\text{blood}} + \mathcal{V}_{\text{ifluid}} = \mathcal{V} - \mathcal{V}_{\text{tissue}} = (1 + \boldsymbol{\nabla} \cdot \mathbf{u})\mathcal{V}_{\text{ref}} - \mathcal{V}_{\text{tissue}}. \tag{2.27}$$

The total porosity of the liver φ_L can then be defined as

$$\begin{aligned}\varphi_L &= \frac{\mathcal{V}_{\text{blood}} + \mathcal{V}_{\text{ifluid}}}{\mathcal{V}} \\ &= \frac{\mathcal{V} - \mathcal{V}_{\text{tissue}}}{\mathcal{V}} \\ &= \frac{(1 + \boldsymbol{\nabla} \cdot \mathbf{u})\mathcal{V}_{\text{ref}} - \mathcal{V}_{\text{tissue}}}{(1 + \boldsymbol{\nabla} \cdot \mathbf{u})\mathcal{V}_{\text{ref}}} \\ &= \frac{(1 + \boldsymbol{\nabla} \cdot \mathbf{u}) - \frac{\mathcal{V}_{\text{tissue}}}{\mathcal{V}_{\text{ref}}}}{(1 + \boldsymbol{\nabla} \cdot \mathbf{u})} \\ &= \frac{(1 + \boldsymbol{\nabla} \cdot \mathbf{u}) - (1 - \varphi_{L,\text{ref}})}{(1 + \boldsymbol{\nabla} \cdot \mathbf{u})} \\ &= \frac{\boldsymbol{\nabla} \cdot \mathbf{u} + \varphi_{L,\text{ref}}}{(1 + \boldsymbol{\nabla} \cdot \mathbf{u})},\end{aligned} \tag{2.28}$$

where $\varphi_{L,\text{ref}}$ is the porosity of the liver in the undeformed case. Note that the total porosity of the liver can also be defined as the sum of the individual porosities due to the sinusoidal and interstitial space networks, φ_s and φ_i respectively, i.e. $\varphi_L = \varphi_s + \varphi_i$. The same is true for the undeformed case in which $\varphi_{L,\text{ref}} = \varphi_{s,\text{ref}} + \varphi_{i,\text{ref}}$, where $\varphi_{s,\text{ref}}$ and $\varphi_{s,\text{ref}}$ are the porosities due to the blood sinusoidal and interstitial fluid networks, respectively. In Equation (2.28), we have made use of the assumption that the volume of the tissue remains constant with deformation, and so it can be defined as the total volume minus the fluid volume within the pores in the undeformed case, i.e. $\mathcal{V}_{\text{tissue}} = \mathcal{V}_{\text{ref}} - \varphi_{L,\text{ref}}\mathcal{V}_{\text{ref}} = (1 - \varphi_{L,\text{ref}})\mathcal{V}_{\text{ref}}$.

Finally, by definition, the porosities of the sinusoidal and interstitial networks, respectively, in the deformed case are given by

$$\varphi_s = \frac{\mathcal{V}_{\text{blood}}}{\mathcal{V}} = \frac{\mathcal{V}_{\text{blood,ref}} + \beta_s(\boldsymbol{\nabla} \cdot \mathbf{u})\mathcal{V}_{\text{ref}}}{(1 + \boldsymbol{\nabla} \cdot \mathbf{u})\mathcal{V}_{\text{ref}}} = \frac{\varphi_{s,\text{ref}} + \beta_s(\boldsymbol{\nabla} \cdot \mathbf{u})}{(1 + \boldsymbol{\nabla} \cdot \mathbf{u})} \tag{2.29}$$

and

$$\varphi_i = \frac{\mathcal{V}_{\text{ifluild}}}{\mathcal{V}} = \frac{\mathcal{V}_{\text{ifluid,ref}} + \beta_i(\boldsymbol{\nabla} \cdot \mathbf{u})\mathcal{V}_{\text{ref}}}{(1 + \boldsymbol{\nabla} \cdot \mathbf{u})\mathcal{V}_{\text{ref}}} = \frac{\varphi_{i,\text{ref}} + \beta_i(\boldsymbol{\nabla} \cdot \mathbf{u})}{(1 + \boldsymbol{\nabla} \cdot \mathbf{u})}. \tag{2.30}$$

2.5.2 Tissue Permeability

For consistency, we make use of the same block of the liver parenchyma of volume $\mathcal{V}$, area A and length L in the third direction discussed in Section 1.4.1.2. From our analysis, the permeability of a cylindrical pore network within $\mathcal{V}$ can be obtained using Equation 1.14. When applied to the blood pore network of volume block $\mathcal{V}_{\text{blood}}$, the permeabilities of the sinusoidal space in the deformed and undeformed liver lobule, respectively, are defined by

$$\kappa_s = \frac{\mathcal{L}^2\mathcal{V}_{\text{blood}}^2}{n_s\mathcal{V}} \qquad \text{and} \qquad \kappa_{s,\text{ref}} = \frac{\mathcal{L}_{\text{ref}}^2\mathcal{V}_{\text{blood,ref}}^2}{n_s\mathcal{V}_{\text{ref}}}, \tag{2.31}$$

where $\mathcal{L}$ and $\mathcal{L}_{\text{ref}}$ are the lengths of $\mathcal{V}$ in the third direction in the deformed and undeformed cases, respectively. n_s is a constant and assumed to remain so during deformation. If we take the ratio of κ_s and $\kappa_{s,\text{ref}}$, we have

$$\begin{aligned}\frac{\kappa_s}{\kappa_{s,\text{ref}}} = \frac{\mathcal{L}^2\mathcal{V}_{\text{blood}}^2}{n_s\mathcal{V}} \cdot \frac{n_s\mathcal{V}_{\text{ref}}}{\mathcal{L}_{\text{ref}}^2\mathcal{V}_{\text{blood,ref}}^2} &= \left(\frac{\mathcal{L}}{\mathcal{L}_{\text{ref}}}\right)^2 \left(\frac{\mathcal{V}_{\text{blood}}}{\mathcal{V}_{\text{blood,ref}}}\right)^2 \left(\frac{\mathcal{V}_{\text{ref}}}{\mathcal{V}}\right) \\ &= \left(\frac{\lambda\mathcal{L}_{\text{ref}}}{\mathcal{L}_{\text{ref}}}\right)^2 \left(\frac{\mathcal{V}_{\text{blood}}}{\mathcal{V}_{\text{blood,ref}}}\right)^2 \left(\frac{\mathcal{V}_{\text{ref}}}{(1+\boldsymbol{\nabla}\cdot\mathbf{u})\,\mathcal{V}_{\text{ref}}}\right) \\ &= \frac{\lambda^2}{(1+\boldsymbol{\nabla}\cdot\mathbf{u})} \left(\frac{\mathcal{V}_{\text{blood}}}{\mathcal{V}_{\text{blood,ref}}}\right)^2, \end{aligned} \tag{2.32}$$

where we have made use of the fact that $\mathcal{L} = \lambda\mathcal{L}_{\text{ref}}$, $\lambda = |\mathbf{F}\mathbf{a}_0|$ is the stretch of the domain, with $\mathbf{a}_0$ being the orientation of the block. Using Equation (2.25),

$$\begin{aligned}\frac{\kappa_s}{\kappa_{s,\text{ref}}} = \frac{\lambda^2}{(1+\boldsymbol{\nabla}\cdot\mathbf{u})} \left(\frac{\mathcal{V}_{\text{blood}}}{\mathcal{V}_{\text{blood,ref}}}\right)^2 &= \frac{\lambda^2}{(1+\boldsymbol{\nabla}\cdot\mathbf{u})} \left(\frac{(\varphi_{s,\text{ref}} + \beta_s(\boldsymbol{\nabla}\cdot\mathbf{u}))\mathcal{V}_{\text{ref}}}{\varphi_{s,\text{ref}}\mathcal{V}_{\text{ref}}}\right)^2 \\ &= \frac{\lambda^2}{(1+\boldsymbol{\nabla}\cdot\mathbf{u})} \left(1 + \frac{\beta_s\boldsymbol{\nabla}\cdot\mathbf{u}}{\varphi_{s,\text{ref}}}\right)^2. \end{aligned} \tag{2.33}$$

Finally, for the 2D case, we assume that there is no deformation in the third direction and that the block deforms uniformly in the cross sectional plane, i.e. $J \approx (1+\boldsymbol{\nabla}\cdot\mathbf{u}) = \lambda^2$. Therefore,

$$\frac{\kappa_s}{\kappa_{s,\text{ref}}} = \frac{\lambda^2}{(1+\boldsymbol{\nabla}\cdot\mathbf{u})} \left(1 + \frac{\beta_s\boldsymbol{\nabla}\cdot\mathbf{u}}{\varphi_{s,\text{ref}}}\right)^2 = \left(1 + \frac{\beta_s\boldsymbol{\nabla}\cdot\mathbf{u}}{\varphi_{s,\text{ref}}}\right)^2. \tag{2.34}$$

By making a similar analysis for the interstitial space, we have

$$\frac{\kappa_i}{\kappa_{i,\text{ref}}} = \left(1 + \frac{\beta_i\boldsymbol{\nabla}\cdot\mathbf{u}}{\varphi_{i,\text{ref}}}\right)^2. \tag{2.35}$$

Using the same isotropy assumption for flow in the liver tissue, we have the permeabilities of the sinusoidal and interstitial spaces in the deformed case, respectively, as

$$\boldsymbol{\kappa}_s = \kappa_s\mathbf{I} \quad \& \quad \boldsymbol{\kappa}_i = \kappa_i\mathbf{I}, \tag{2.36}$$

and we can define the respective hydraulic conductivities as

$$\mathbf{K}_s = \frac{\boldsymbol{\kappa}_s}{\mu_s} \quad \& \quad \mathbf{K}_i = \frac{\boldsymbol{\kappa}_i}{\mu_i}. \tag{2.37}$$

For the undeformed lobule, we have the hydraulic conductivities of the sinusoidal and interstitial spaces, respectively, as

$$\mathbf{K}_{s,\text{ref}} = \frac{\boldsymbol{\kappa}_{s,\text{ref}}}{\mu_s} \quad \& \quad \mathbf{K}_{i,\text{ref}} = \frac{\boldsymbol{\kappa}_{i,\text{ref}}}{\mu_i}. \tag{2.38}$$

2.6 Summary of Governing Equations

Here, we summarise the governing equations of our system. These are

$$\boldsymbol{\nabla} \cdot \tilde{\boldsymbol{\sigma}} = \mathbf{0}, \tag{2.39}$$

$$\boldsymbol{\nabla} \cdot (-\mathbf{K}_s \boldsymbol{\nabla} p_s) + C_f(p_s - p_i) = 0, \tag{2.40}$$

$$\boldsymbol{\nabla} \cdot (-\mathbf{K}_i \boldsymbol{\nabla} p_i) - C_f(p_s - p_i) + C_l \max(p_i - p_0, 0) = 0, \tag{2.41}$$

$$\boldsymbol{\nabla} \cdot (-\mathbf{K}_{s,\text{ref}} \boldsymbol{\nabla} p_{s,\text{ref}}) + C_f(p_{s,\text{ref}} - p_{i,\text{ref}}) = 0, \tag{2.42}$$

$$\boldsymbol{\nabla} \cdot (-\mathbf{K}_{i,\text{ref}} \boldsymbol{\nabla} p_{i,\text{ref}}) - C_f(p_{s,\text{ref}} - p_{i,\text{ref}}) + C_l \max(p_{i,\text{ref}} - p_0, 0) = 0, \tag{2.43}$$

where $\tilde{\boldsymbol{\sigma}}$ is defined by Equation (2.17), $\mathbf{K}_s$ & $\mathbf{K}_i$ are defined in Equation (2.37) and $\mathbf{K}_{s,\text{ref}}$ & $\mathbf{K}_{i,\text{ref}}$ are defined in Equation (2.38).

In the case of the deformed liver lobule, the constitutive equations for stress (2.39) and fluid flow (2.40)–(2.41) are solved on the deformed domain $\mathcal{D}$ with boundary $\partial\mathcal{D}$ (Section 1.4.2.1). For the undeformed liver lobule, the constitutive equations for fluid flow (2.42)–(2.43) are solved on the reference domain $\mathcal{D}_0$ with boundary $\partial\mathcal{D}_0$ (Section 1.4.2.1). Note that the reference stress in the undeformed case is assumed to be zero.

The system of coupled PDEs above are solved numerically using the *Weak Form PDE* interface on COMSOL Multiphysics. In order to achieve this, we first needed to derive the weak formulation of the equations, which is shown in the next subsection.

2.6.1 Weak Formulation of Governing Equations

Let $\mathbf{w}$ be any regular test function of $\tilde{\boldsymbol{\sigma}}$. In order to construct the weak form of the constitutive equation for linear elasticity, we multiply Equation (2.39) by $\mathbf{w}$ and integrate over the domain $\mathcal{D}$:

$$\int_{\mathcal{D}} (\boldsymbol{\nabla} \cdot \tilde{\boldsymbol{\sigma}}) \cdot \mathbf{w} \, \mathrm{d}V = 0. \tag{2.44}$$

Applying the divergence theorem to the LHS of Equation (2.44), we obtain

$$\int_{\mathcal{D}} \tilde{\boldsymbol{\sigma}} : \boldsymbol{\nabla}\mathbf{w} \, \mathrm{d}V - \int_{\partial\mathcal{D}} (\tilde{\boldsymbol{\sigma}}\mathbf{n}) \cdot \mathbf{w} \, \mathrm{d}A = 0, \tag{2.45}$$

which holds for all $\mathbf{w} \in \mathbb{W}$, where $\mathbb{W}$ is defined as the space of all tensor functions whose derivatives are square integrable and that vanish on $\partial\mathcal{D}$. Here, $\mathrm{d}V$ and $\mathrm{d}A$ are the infinitesimal volume and area of the deformed lobule, respectively.

The same can be done for the governing equations of fluid flow in the deformed lobule, Equations (2.40)–(2.41), to obtain:

$$\int_{\mathcal{D}} (\mathbf{K}_s \boldsymbol{\nabla} p_s) \cdot \boldsymbol{\nabla} \check{p}_s \, \mathrm{d}V - \int_{\partial\mathcal{D}} \check{p}_s \, (\mathbf{K}_s \boldsymbol{\nabla} p_s) \cdot \mathbf{n} \, \mathrm{d}A = - \int_{\mathcal{D}} C_f(p_s - p_i) \check{p}_s \, \mathrm{d}V \tag{2.46}$$

and

$$\int_{\mathcal{D}} (\mathbf{K}_i \boldsymbol{\nabla} p_i) \cdot \boldsymbol{\nabla} \check{p}_i \, \mathrm{d}V - \int_{\partial \mathcal{D}} \check{p}_i \, (\mathbf{K}_i \boldsymbol{\nabla} p_i) \cdot \mathbf{n} \, \mathrm{d}A = \int_{\mathcal{D}} C_f (p_s - p_i) \check{p}_i \, \mathrm{d}V - \int_{\mathcal{D}} C_l \max(p_i - p_0, 0) \check{p}_i \, \mathrm{d}V, \quad (2.47)$$

with $\check{p}_s$ and $\check{p}_i$ as test functions of p_s and p_i, respectively, and for the governing equations of fluid flow in the undeformed lobule, Equations (2.42)–(2.43), to obtain:

$$\int_{\mathcal{D}_0} \left(\mathbf{K}_{s,\mathrm{ref}} \overline{\boldsymbol{\nabla}} p_{s,\mathrm{ref}}\right) \cdot \overline{\boldsymbol{\nabla}} \check{p}_{s,\mathrm{ref}} \, \mathrm{d}V_0 - \int_{\partial \mathcal{D}_0} \check{p}_{s,\mathrm{ref}} \left(\mathbf{K}_{s,\mathrm{ref}} \overline{\boldsymbol{\nabla}} p_{s,\mathrm{ref}}\right) \cdot \mathbf{n}_0 \, \mathrm{d}A_0 = - \int_{\mathcal{D}_0} C_f (p_{s,\mathrm{ref}} - p_{i,\mathrm{ref}}) \check{p}_{s,\mathrm{ref}} \, \mathrm{d}V_0 \quad (2.48)$$

and

$$\int_{\mathcal{D}_0} \left(\mathbf{K}_{i,\mathrm{ref}} \overline{\boldsymbol{\nabla}} p_{i,\mathrm{ref}}\right) \cdot \overline{\boldsymbol{\nabla}} \check{p}_{i,\mathrm{ref}} \, \mathrm{d}V_0 - \int_{\partial \mathcal{D}_0} \check{p}_{i,\mathrm{ref}} \left(\mathbf{K}_{i,\mathrm{ref}} \overline{\boldsymbol{\nabla}} p_{i,\mathrm{ref}}\right) \cdot \mathbf{n}_0 \, \mathrm{d}A_0 = \int_{\mathcal{D}_0} C_f (p_{s,\mathrm{ref}} - p_{i,\mathrm{ref}}) \check{p}_{i,\mathrm{ref}} \, \mathrm{d}V_0 - \int_{\mathcal{D}_0} C_l \max(p_{i,\mathrm{ref}} - p_0, 0) \check{p}_{i,\mathrm{ref}} \, \mathrm{d}V_0, \quad (2.49)$$

with $\check{p}_{s,\mathrm{ref}}$ and $\check{p}_{i,\mathrm{ref}}$ as test functions of $p_{s,\mathrm{ref}}$ and $p_{i,\mathrm{ref}}$, respectively, and where $\mathrm{d}V_0$ and $\mathrm{d}A_0$ are the infinitesimal volume and area of the undeformed lobule, respectively, and $\boldsymbol{\nabla}$ and $\overline{\boldsymbol{\nabla}}$ are the gradient tensors in $\mathcal{D}$ and $\mathcal{D}_0$, respectively.

2.7 Boundary Conditions

In order to obtain numerical solutions for our system of equations summarised in Section 2.6, we impose the following conditions on the boundaries of our domain.

2.7.1 Fluid Flow Boundary Conditions

For the fluid flow, we have:

1. At the portal tracts of the lobule, blood sinusoidal pressure is prescribed for both the undeformed and the deformed cases, i.e. $p_{s,\mathrm{ref}} = p_{s,\mathrm{ref}}^{pt}$ and $p_s = p_s^{pt}$, respectively, where $p_{s,\mathrm{ref}}^{pt}$ and p_s^{pt} are constants and $p_s^{pt} > p_{s,\mathrm{ref}}^{pt}$.

2. Similarly, at the central vein of the lobule, blood sinusoidal pressure is also prescribed for the undeformed and the deformed cases, i.e. $p_{s,\mathrm{ref}} = p_{s,\mathrm{ref}}^{cv}$ and $p_s = p_s^{cv}$, respectively. Again, $p_{s,\mathrm{ref}}^{cv}$ and p_s^{cv} are constants, but in this case we choose $p_s^{cv} = p_{s,\mathrm{ref}}^{cv}$. This is so we can estimate the pressure drop across the deformed lobule, referenced against the undeformed case.

3. No blood flow across the edges of the lobule due to the presence of the vascular septa, for both the undeformed and deformed cases, i.e. $\mathbf{v}_{s,\text{ref}} \cdot \mathbf{n}_0 = \mathbf{v}_s \cdot \mathbf{n} = 0$.

4. No interstitial fluid flow into the portal tracts and central vein for both the undeformed and deformed cases, i.e. $\mathbf{v}_{i,\text{ref}} \cdot \mathbf{n}_0 = \mathbf{v}_i \cdot \mathbf{n} = 0$.

5. **Single Lobule:** In the case of a single lobule, we also impose zero interstitial fluid flow across the sides of the lobule for both the undeformed and deformed cases, i.e. $\mathbf{v}_{i,\text{ref}} \cdot \mathbf{n} = \mathbf{v}_i \cdot \mathbf{n} = 0$. This condition is modified in the case of a multiple lobule lattice.

6. **Lobule Lattice:** For a multiple lobule lattice, we allow interstitial fluid flow continuity across the sides of the lobules. The exception is at the surface of the liver.

7. **Liver Surface:** At the boundary of the outer surface of the liver, we impose

   (a) No blood flow across the surface for both the undeformed and deformed cases, i.e. $\mathbf{v}_{s,\text{ref}} \cdot \mathbf{n}_0 = \mathbf{v}_s \cdot \mathbf{n} = 0$.

   (b) Interstitial fluid flow across the surface of the undeformed and deformed liver.

      i. For flows across the Glissonian–peritoneal surface, flux equations for the undeformed and deformed liver, respectively, are given by

$$\mathbf{v}_{i,\text{ref}} \cdot \mathbf{n}_0 = M_{GP}(p_{i,\text{ref}} - P_{PC}) \quad \text{and} \quad \mathbf{v}_i \cdot \mathbf{n} = M_{GP}(p_i - P_{PC}), \tag{2.50}$$

      where M_{GP} is the hydraulic conductivity per unit area of the Glissonian–peritoneal membrane and P_{PC} is the pressure within the peritoneal cavity.

      ii. For flows across the bare area surface of the liver, flux equations for the undeformed and deformed cases, respectively, are given by

$$\mathbf{v}_{i,\text{ref}} \cdot \mathbf{n}_0 = M_{BA}(p_{i,\text{ref}} - P_{BA}) \quad \text{and} \quad \mathbf{v}_i \cdot \mathbf{n} = M_{BA}(p_i - P_{BA}), \tag{2.51}$$

      where M_{BA} is the hydraulic conductivity of the bare area per unit area and P_{BA} is the pressure adjacent to the outer surface of the bare area.

2.7.2 Tissue Deformation Boundary Conditions

For tissue deformation:

1. At the portal tracts, we impose that the normal stresses are due to sinusoidal blood pressure increase, i.e. $\mathbf{n} \cdot (\tilde{\boldsymbol{\sigma}} \mathbf{n}) = -\left(p_s^{pt} - p_{s,\text{ref}}^{pt}\right)$. The assumption here is that deformation in the portal tract is due to the referenced sinusoidal blood pressure change, and so any change in pressure translates to a change in shape in a direction normal to the circumference of the portal tract.

2. At the central vein, we also prescribe normal stresses due to referenced sinusoidal blood pressure change, i.e. $\mathbf{n} \cdot (\tilde{\boldsymbol{\sigma}}\mathbf{n}) = -\left(p_s^{cv} - p_{s,\text{ref}}^{cv}\right)$. Note that since $p_s^{cv} = p_{s,\text{ref}}^{cv}$, the normal stresses are actually zero.

3. For the case of a single lobule, we impose a zero stress condition along the sides of the lobule. This means that there is no restriction on the deformation of the vascular septa. For a lobule lattice, the zero stress condition is imposed along the outer boundaries of the domain, while the inner vascular septa sides have a stress continuity condition.

4. We assume that there are no tangential stresses along all boundaries, i.e. $\mathbf{m} \cdot (\tilde{\boldsymbol{\sigma}}\mathbf{n}) = 0$, where $\mathbf{m}$ is the unit tangent vector.

5. We also need a reference point so we fix the centre of the lobule, i.e. $\mathbf{u} = 0$.

2.8 Derived Values

Using our system of equations summarised in Section 2.6, together with the boundary conditions in Section 2.7, we can solve for the pressure and flow profiles in the undeformed and deformed lobules as well as the deformation magnitude given a prescribed increase in blood sinusoidal portal pressure. We can also find estimates for other important values, such as the total volumetric flux of blood into the liver, the lymphatic uptake rate and total fluid loss via the surface of the liver.

2.8.1 Total Blood Flux

All the blood that enters the liver must go through the portal tracts to be filtered by the sinusoids. We can estimate the total volume flux of blood into the liver by integrating the volumetric flux through the portal tracts of a single lobule, and then multiplying the resultant value by the average number of lobules within the liver N_{lob}. In the 3D case, N_{lob} can be estimated by dividing the total volume of the liver, V_{liv}, by the volume of a single lobule, V_{lob},:

$$N_{\text{lob}} = \frac{V_{\text{liv}}}{V_{\text{lob}}} = \frac{V_{\text{liv}}}{A_{\text{lob}} h_{\text{lob}}} = \frac{V_{\text{liv}}}{(3\sqrt{3}l_{\text{lob}}^2/2)h_{\text{lob}}}, \tag{2.52}$$

where $A_{\text{lob}} = (3\sqrt{3}l_{\text{lob}}^2/2)$ is the area of the lobule, and l_{lob} and h_{lob} are the side length and height of the lobule, respectively, as described in Section 2.2.3.

In the 2D approximation of the lobule, we work in terms of the number of lobules times the height of a lobule $\mathcal{N}_{\text{lob}}$, which is given by

$$\mathcal{N}_{\text{lob}} = N_{\text{lob}} * h_{\text{lob}} = \frac{V_{Liv}}{(3\sqrt{3}l_{\text{lob}}^2/2)}. \tag{2.53}$$

Note that both N_{lob} and $\mathcal{N}_{\text{lob}}$ would remain constant with deformation since the tissue is isotropic and the volume of the liver is assumed to expand in the same ratio as the volume of the lobule. The total volumetric flux of blood in the undeformed liver can then be estimated by taking a line integral along the portal tract boundary of the lobule:

$$Q_{\text{blood,ref}} = -\mathcal{N}_{\text{lob}} \int_{\text{Portal tracts}} \mathbf{v}_{s,\text{ref}} \cdot \mathbf{n}_0 \, \mathrm{d}l_0, \tag{2.54}$$

while that of the deformed liver is given by

$$Q_{\text{blood}} = -\mathcal{N}_{\text{lob}} \int_{\text{Portal tracts}} \mathbf{v}_s \cdot \mathbf{n} \, \mathrm{d}l, \tag{2.55}$$

where $\mathbf{n}$ and $\mathbf{n}_0$ are the outward pointing unit normal in the deformed and undeformed domains, respectively.

2.8.2 Total Lymphatic Uptake

The rate of fluid uptake by the lymphatic vessels within the liver tissue can be estimated by integrating q_{lymph} over the surface area of a single lobule, and then multiplying the resultant value by the average number of lobules across the liver. The total uptake rate of fluid by lymphatic vessels in the undeformed and deformed liver, respectively, is given by

$$\begin{aligned} Q_{\text{lymph,ref}} &= \mathcal{N}_{\text{lob}} \int_{\text{Cross-sectional area}} q_{\text{lymph}} \, \mathrm{d}A_0 \\ &= \mathcal{N}_{\text{lob}} \int_{\text{Cross-sectional area}} C_l \max(p_{i,\text{ref}} - p_0, 0) \, \mathrm{d}A_0, \end{aligned} \tag{2.56}$$

and

$$\begin{aligned} Q_{\text{lymph}} &= \mathcal{N}_{\text{lob}} \int_{\text{Cross-sectional area}} q_{\text{lymph}} \, \mathrm{d}A \\ &= \mathcal{N}_{\text{lob}} \int_{\text{Cross-sectional area}} C_l \max(p_i - p_0, 0) \, \mathrm{d}A. \end{aligned} \tag{2.57}$$

2.8.3 Fluid Loss via Liver Surface

Interstitial fluid loss through the outer surface of the liver is a combination of fluid loss via the bare area and fluid loss via the Glissonian–peritoneal membrane. Since we are only considering a small section of the liver surface in our model, we can estimate the total fluid loss across the whole liver by multiplying the interstitial fluid loss per unit edge considered in our model by the total surface area of the liver covered by the bare area and Glissonian–peritoneal membrane.

In the undeformed liver, fluid loss via the bare area and the Glissonian–peritoneal surface,

respectively, are given by

$$Q_{\mathrm{L_{ref},BA}} = \frac{A_{\mathrm{L,BA}}}{L_{\mathrm{ref,edge}}} \int_{\mathrm{edge}} \mathbf{v}_{i,\mathrm{ref}} \cdot \mathbf{n}_0 \, \mathrm{d}l_0 \quad \text{and} \quad Q_{\mathrm{L_{ref},PC}} = \frac{A_{\mathrm{L,GP}}}{L_{\mathrm{ref,edge}}} \int_{\mathrm{edge}} \mathbf{v}_{i,\mathrm{ref}} \cdot \mathbf{n}_0 \, \mathrm{d}l_0, \quad (2.58)$$

where $A_{\mathrm{L,BA}}$ is the surface area of the liver not covered by the peritoneal membrane, i.e. the bare area, $A_{\mathrm{L,GP}}$ is the area of the Glissonian–peritoneal membrane and $L_{\mathrm{ref,edge}}$ is the length of the edge of the liver over which the integral is taken over, in the undeformed case.

For the linearly elastic model, we shall assume that the surface area of the Glissonian membrane remains fairly constant within small strains. This is synonymous to the membrane straightening out any "kinks" as the lobules within expand in volume. Hence, for the deformed liver, we estimate the fluid loss via the bare area and Glissonian–peritoneal surface, respectively, as

$$Q_{\mathrm{L,BA}} = \frac{A_{\mathrm{L,BA}}}{L_{\mathrm{edge}}} \int_{\mathrm{edge}} \mathbf{v}_i \cdot \mathbf{n} \, \mathrm{d}l \quad \text{and} \quad Q_{\mathrm{L,PC}} = \frac{A_{\mathrm{L,GP}}}{L_{\mathrm{edge}}} \int_{\mathrm{edge}} \mathbf{v}_i \cdot \mathbf{n} \, \mathrm{d}l, \quad (2.59)$$

where L_{edge} is the length of the deformed edge of the liver over which the integral is taken over.

2.9 Physiological Parameter Values

Since this chapter is an extension of the work by Bonfiglio et al. (2010) and Siggers et al. (2014), most of the parameter values used in the numerical solution of the model were obtained from their studies, with the rest obtained from readily available literature. These parameters and their values are are listed in Tables 2.1–2.3, together with references, except where otherwise stated.

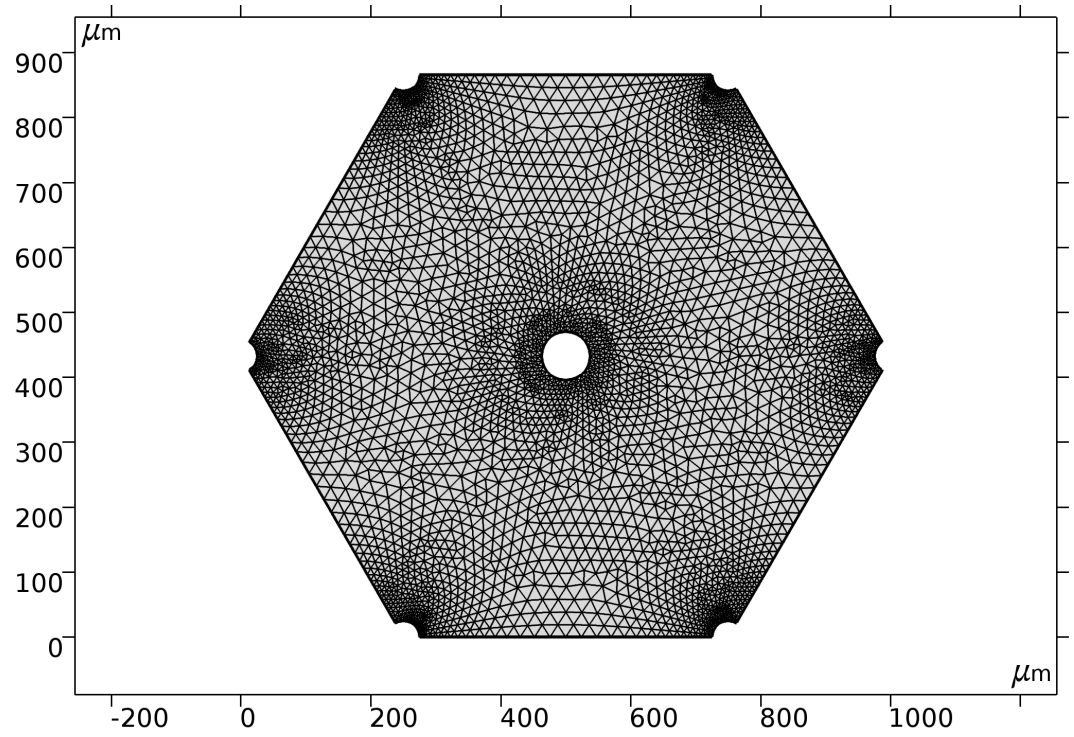
2.10 Results and Discussion

In this section, we present the results of the linear poroelasticity model in the case of the healthy liver tissue, i.e. with parameter values chosen to be within the normal physiological range. We also compare the results of the undeformed liver and the deformed liver following a 10% increase in blood portal pressure, both in a single lobule and in a lattice arrangement of multiple lobules close to the liver surface.

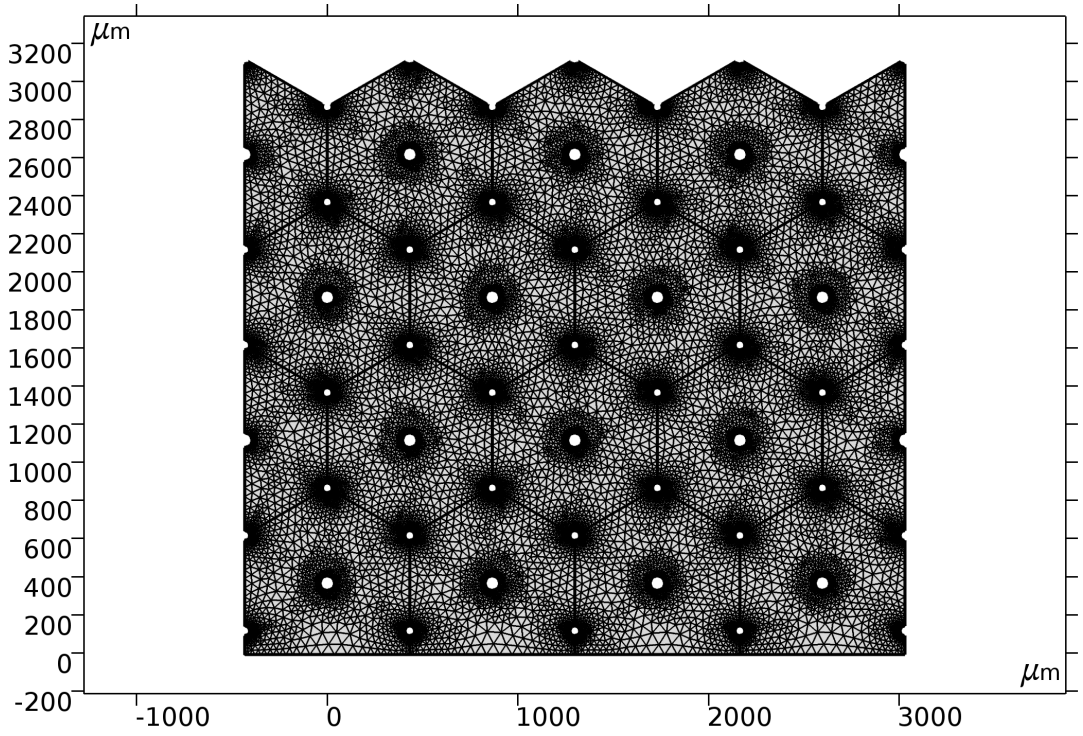
2.10.1 Domain Mesh

The domain mesh used for numerical computations was chosen based on a balance between accuracy and computational efficiency. In the case of the 2D lobule, the predefined COMSOL Multiphysics mesh for fluid dynamics was used for both the single and the lattice cases (Figures 2.3a and 2.3b, respectively).

Within COMSOL Multiphysics, the degree of triangular mesh sizing exists in 9 levels, going from: extremely coarse, extra coarse, coarser, coarse, normal, fine, finer, extra fine to extremely fine. Numerical simulations for the 2D linearly elastic model were run using different mesh sizes, starting from normal, until one was attained which gave the same numerical value for the average volume change ratio J to 3 decimal places, thereby reducing the mesh refining absolute error to less than 0.001, and in the shortest amount of time. For the 2D single lobule, the "finer" mesh size was used, which had a maximum and minimum mesh element size of $24\,\mu$m and $0.346\,\mu$m, respectively, and computational time of 25 s. Whereas for the lobule lattice, the "coarse" mesh size was used, with a maximum mesh element size of $209\,\mu$m, a minimum mesh element size of $9.34\,\mu$m, and computational time of 1 min 35 s.



(a) Single Lobule



(b) Lobule Lattice

Figure 2.3: COMSOL Multiphysics mesh distribution used in the 2D linear elastic liver model to obtain numerical solutions.

2.10.2 Single Lobule

For a single lobule, the results of the blood and interstitial fluid pressure and velocity profiles are presented below, as well as the deformation of the tissue following a 10% increase in sinusoidal blood portal pressure.

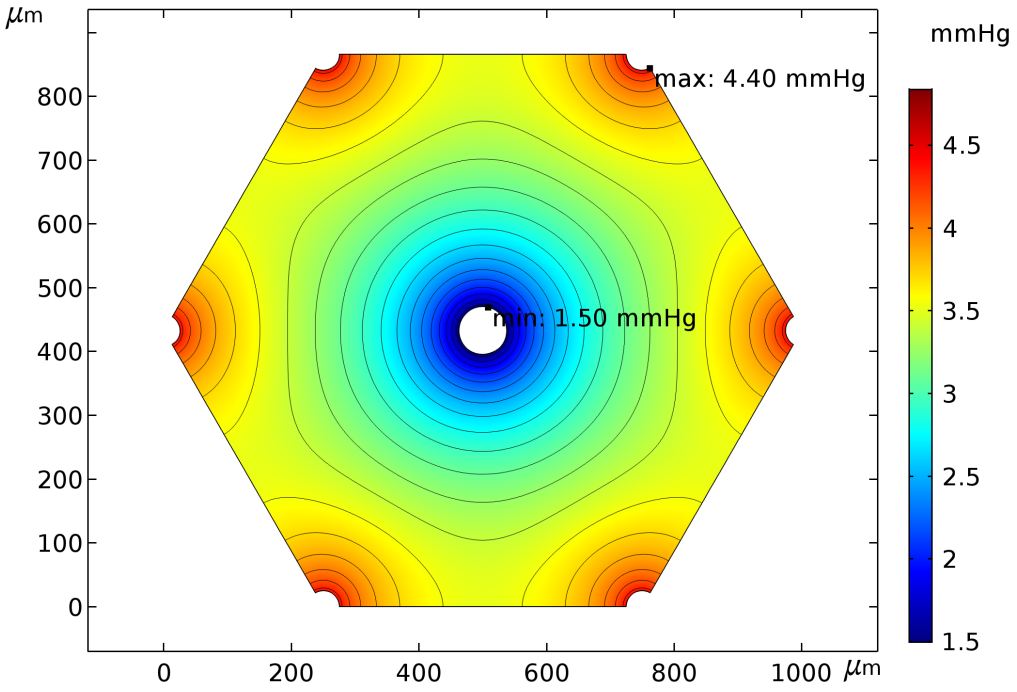
2.10.2.1 Blood Pressure and Velocity

Blood pressure distribution within the sinusoids, for both the undeformed and deformed lobules, is shown in Figure 2.4. For the undeformed lobule, a sinusoidal blood pressure of 4.4 mmHg is imposed at the portal tracts and 1.5 mmHg at the central vein, resulting in a pressure drop of 2.9 mmHg (see Figure 2.4a). This pressure drop is what drives the flow of blood across the lobule. In order to simulate expansion of the tissue, sinusoidal blood pressure at the portal tracts is increased by 10% with respect to the value in the undeformed case (i.e. 4.84 mmHg) while keeping the central vein pressure fixed, thus, resulting in a 15% increase in pressure drop (3.34 mmHg) across the surface of the deformed lobule.

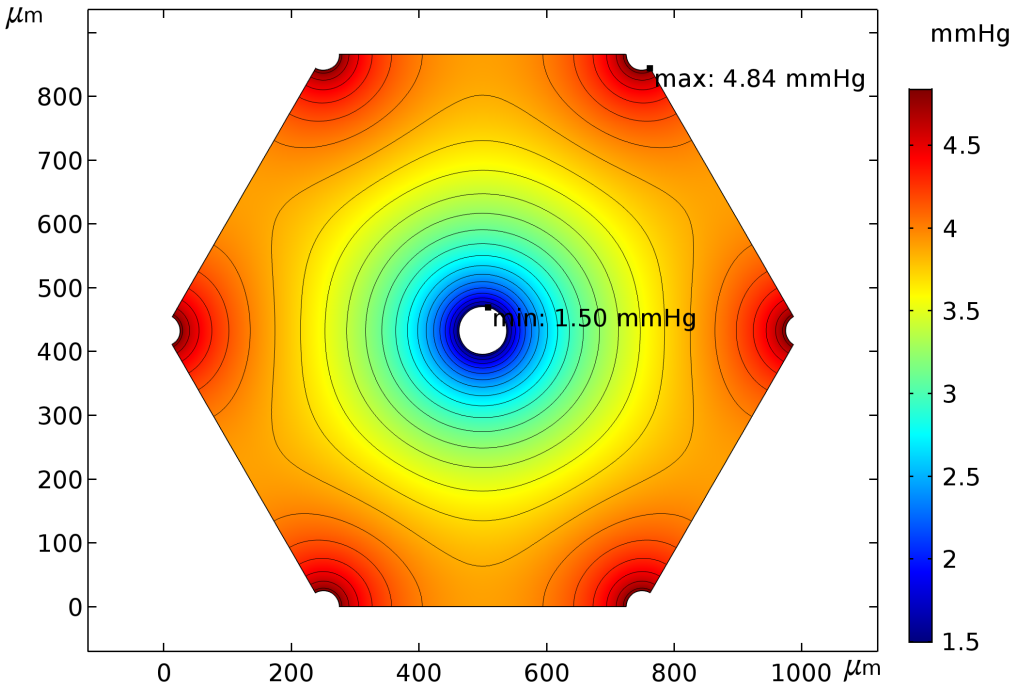
Blood drainage at the central vein has a higher velocity magnitude than blood inflow at the portal tracts, as seen in the Darcy velocity profiles of both the undeformed and deformed lobules in Figure 2.5. In the case of the undeformed lobule, inflow Darcy velocity is approximately 0.0015 cm/s while outflow Darcy velocity is approximately 0.0021 cm/s (see Figure 2.5a). Whereas for the deformed lobule, inflow and outflow Darcy velocities are approximately 0.0021 cm/s and 0.0029 cm/s, respectively, following a 10% increase in sinusoidal blood portal pressure (see Figure 2.5b). This means that on average, a 10% rise in sinusoidal blood portal pressure can lead to a 40% increase in sinusoidal blood velocity in the healthy liver tissue. In both the undeformed and deformed cases, blood Darcy velocity is minimum along the middle of the edge of the lobule, possibly due to the no flux condition imposed along the vascular septa, and maximum close to the central vein (see Figure 2.5).

The Darcy velocity of a fluid can be divided by the porosity of the medium within which it flows to obtain the average fluid velocity within the pores. For blood flow within the sinusoids, the blood Darcy velocity obtained from our model is divided by the liver porosity due to the sinusoids to obtain the average blood velocity within the sinusoid vessels (see Figure 2.6). For the undeformed lobule, this corresponds to an average blood velocity range of 0.012 cm/s to 0.018 cm/s between the portal tracts and central vein, respectively (see Figure 2.6a). Following a 10% increase in blood sinusoidal portal pressure, these values increase to 0.016 cm/s and 0.025 cm/s, respectively (see Figure 2.6b). All the values above lie within the range of expected hepatic sinusoidal blood velocities ($0.017 - 0.281$ cm/s) obtained in an experimental study by Puhl et al. (2003). Note also that the maximum blood velocity values obtained are within the physiological range estimated by Caro et al. (1974), i.e. $0.02 - 0.17$cm/s, for peak blood velocity in capillary-like vessels. Again, in both undeformed and deformed cases, average blood velocity

within the sinusoids is minimum along the middle of the edge of the lobule and maximum close to the central vein.

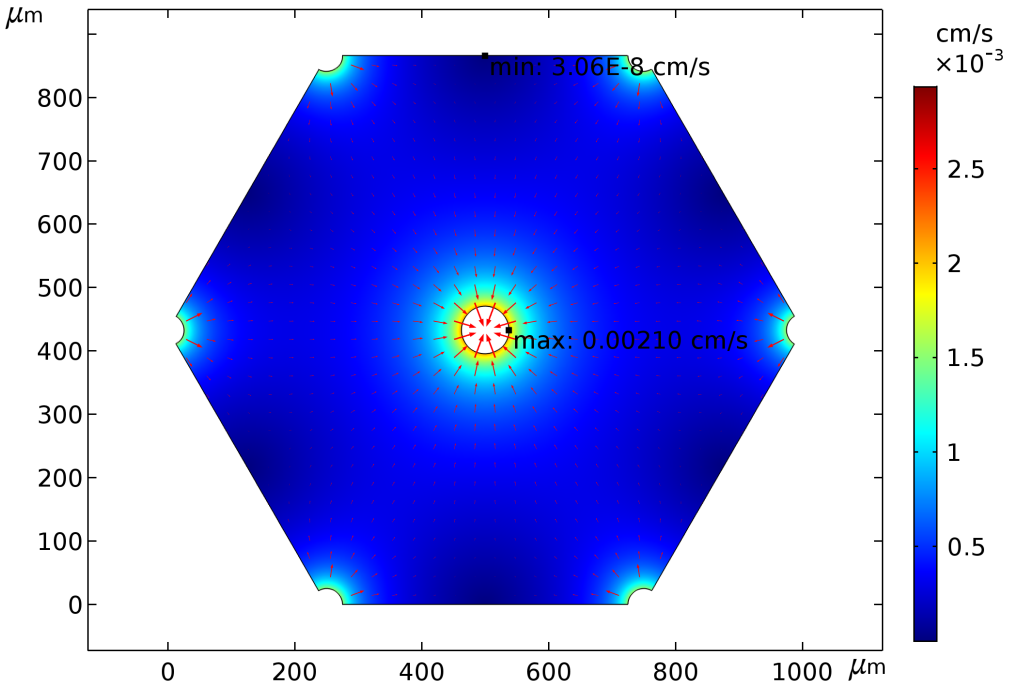


(a) $p_{s,\mathrm{ref}}$

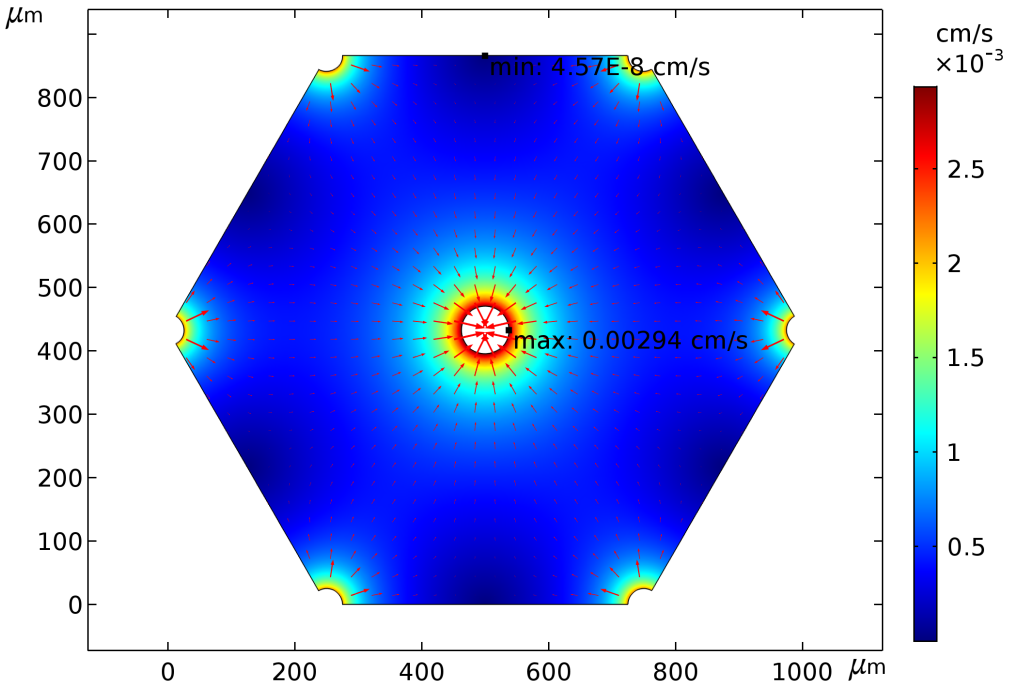


(b) p_s

Figure 2.4: Blood pressure distribution in 2D: (a) undeformed liver lobule and (b) deformed linearly elastic liver lobule following a 10% increase in sinusoidal blood portal pressure. Colour bars show pressure magnitude and have the same range in both subfigures. Pressure contours at intervals of 0.15 mmHg are also plotted in both subfigures.

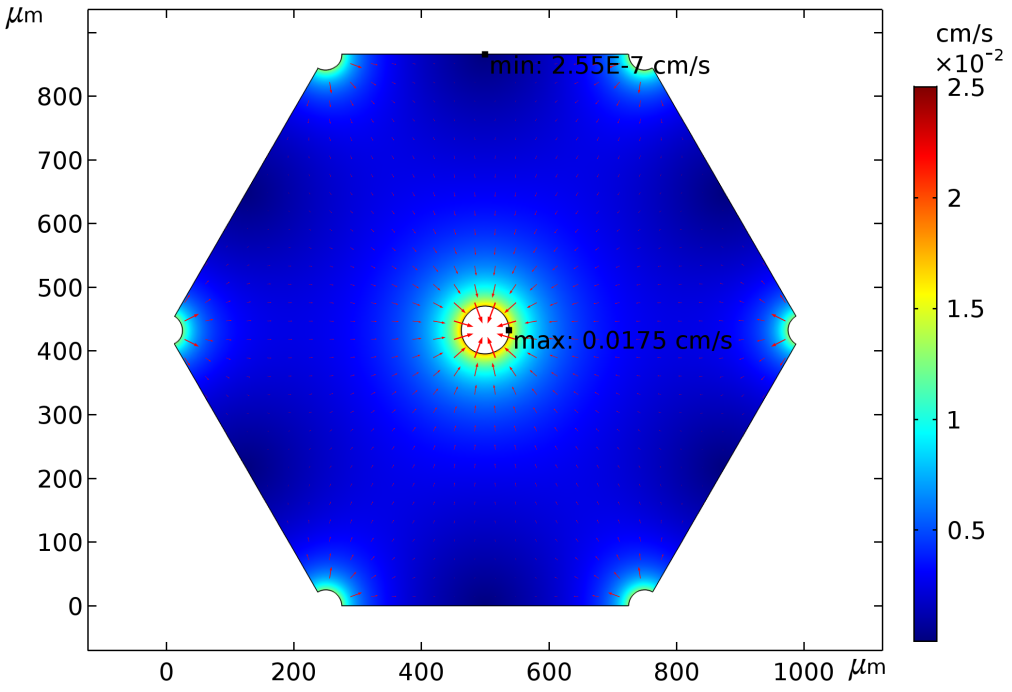


(a) $\mathbf{v}_{s,\text{ref}}$

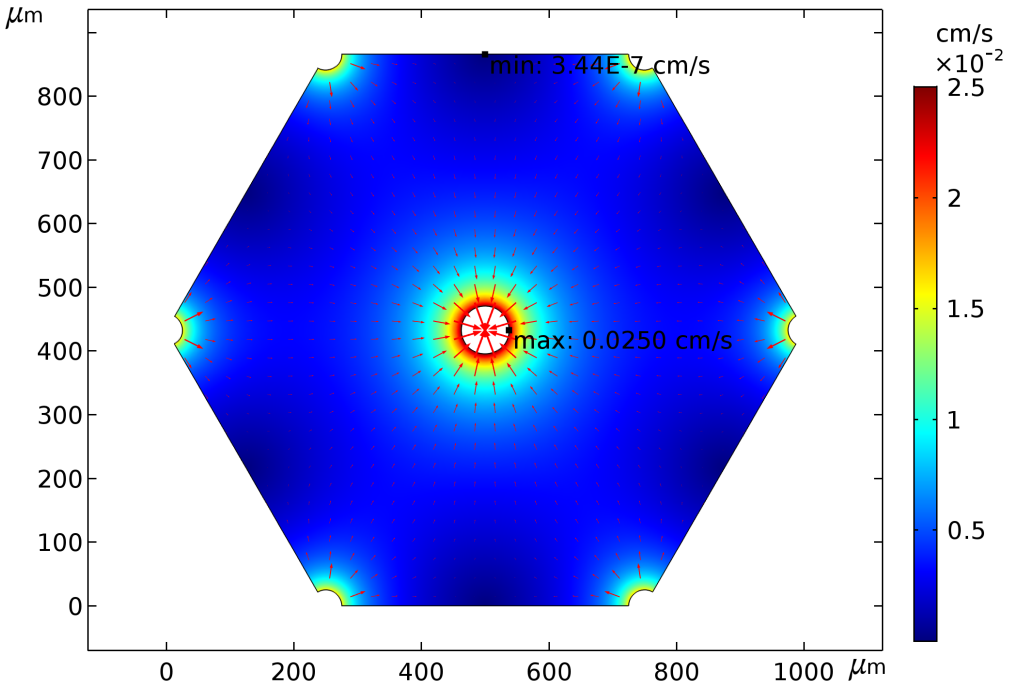


(b) $\mathbf{v}_s$

Figure 2.5: Blood Darcy velocity in 2D: (a) undeformed liver lobule and (b) deformed linearly elastic liver lobule following a 10% increase in sinusoidal blood portal pressure. In both subfigures, arrows show the direction of flow and are proportional to the magnitude of flow velocity. Colour bars show velocity magnitude and are of the same range for both subfigures.



(a) $\mathbf{v}_{s,\mathrm{ref}}/\varphi_{s,\mathrm{ref}}$



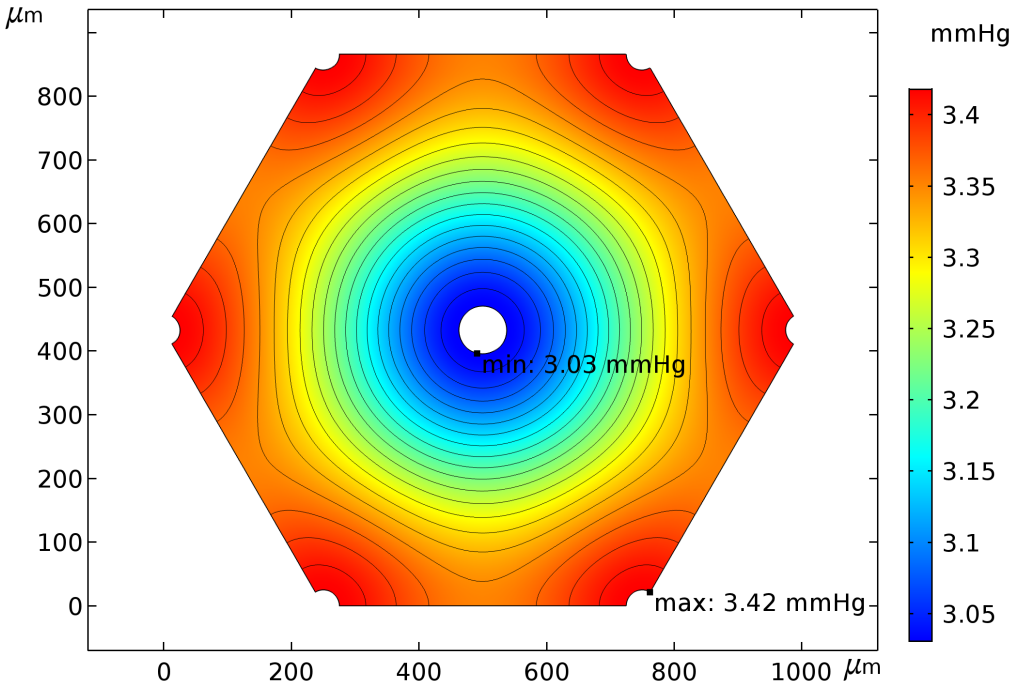
(b) $\mathbf{v}_s/\varphi_s$

Figure 2.6: Average blood pore velocity in 2D: (a) undeformed liver lobule and (b) deformed linearly elastic liver lobule following a 10% increase in sinusoidal blood portal pressure. In both subfigures, arrows show the direction of flow and are proportional to the magnitude of flow velocity. Colour bars show velocity magnitude and are of the same range for both subfigures.

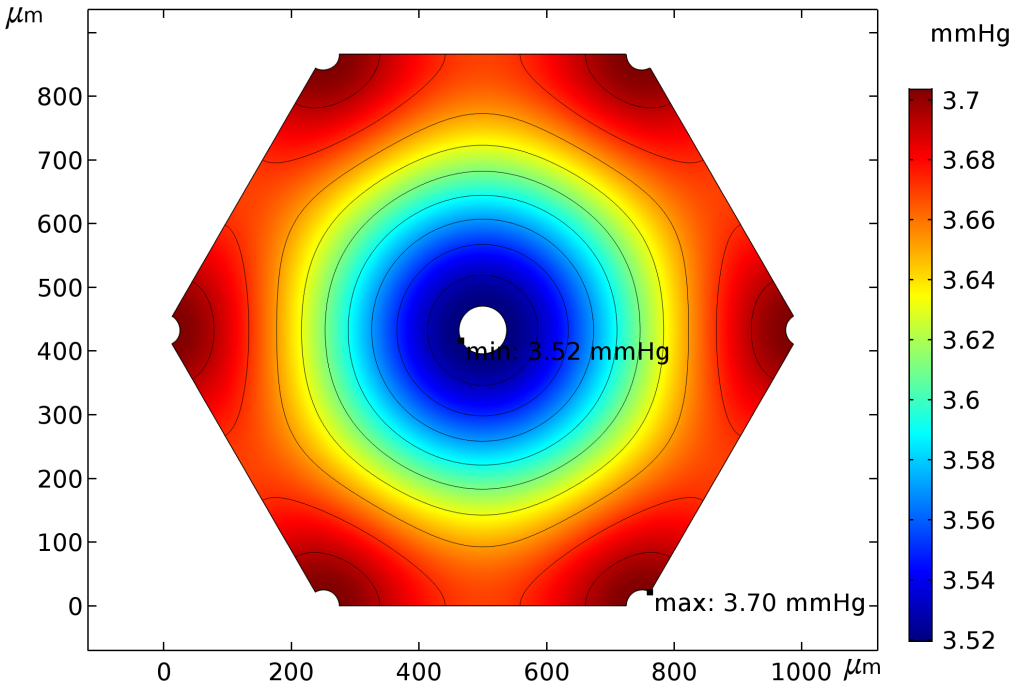
2.10.2.2 Interstitial Fluid Pressure and Velocity

Interstitial fluid pressure distribution, in both the undeformed and deformed lobules, is shown in Figure 2.7. Recall that no interstitial fluid pressure conditions were imposed on any of the lobule boundaries in our model. Nonetheless, the interstitial fluid pressure distribution follows a similar profile to that of blood pressure in the lobule, with a maximum value at the portal tracts and a minimum value at the central vein. This is because plasma fluid filtration is dependent on sinusoidal blood pressure, and since blood pressure is maximum at the portal tracts and minimum at the central vein, plasma fluid being filtered at these locations also has corresponding maximal and minimal pressure value, respectively. In the undeformed lobule, an interstitial fluid pressure of 3.42 mmHg is observed at the portal tracts and 3.03 mmHg at the central vein, resulting in a pressure drop of 0.39 mmHg across the lobule (see Figure 2.7a). Following a 10% increase in sinusoidal blood portal pressure, interstitial fluid pressure increases to 3.70 mmHg and 3.52 mmHg at the portal tracts and central vein, respectively (see Figure 2.7b). This means that on average, a 10% increase in sinusoidal blood portal pressure can lead to $8\% - 16\%$ increase in interstitial fluid pressure between the portal tracts and central vein. However, the interstitial fluid pressure drop across the lobule actually drops by about 54%, to a value of 0.18 mmHg, following a 10% increase in sinusoidal blood portal pressure.

The magnitudes of both the Darcy velocity and pore velocity of the interstitial fluid, in the undeformed and deformed lobules, are minimal along the portal tracts, the central vein and the middle of the vascular septa due to the no flux condition imposed along those boundaries and maximum at halfway points between the portal tracts and the central vein (see Figures 2.8–2.9). In the undeformed lobule (Figures 2.8a and 2.9a), the surface averaged Darcy and pore velocities of the interstitial fluid are estimated to be 1.85×10^{-7} cm/s and 7.35×10^{-6} cm/s, respectively. Following a 10% increase in sinusoidal blood portal pressure, the surface averaged Darcy velocity of the interstitial fluid increases to 2.41×10^{-7} cm/s, which is an approximate increase of 30% from the referenced undeformed value (see Figure 2.8b). On the other hand, the surface averaged pore velocity of interstitial fluid decreases by about 18% (6.05×10^{-6} cm/s), following the 10% increase in sinusoidal blood portal pressure (Figure 2.9b).

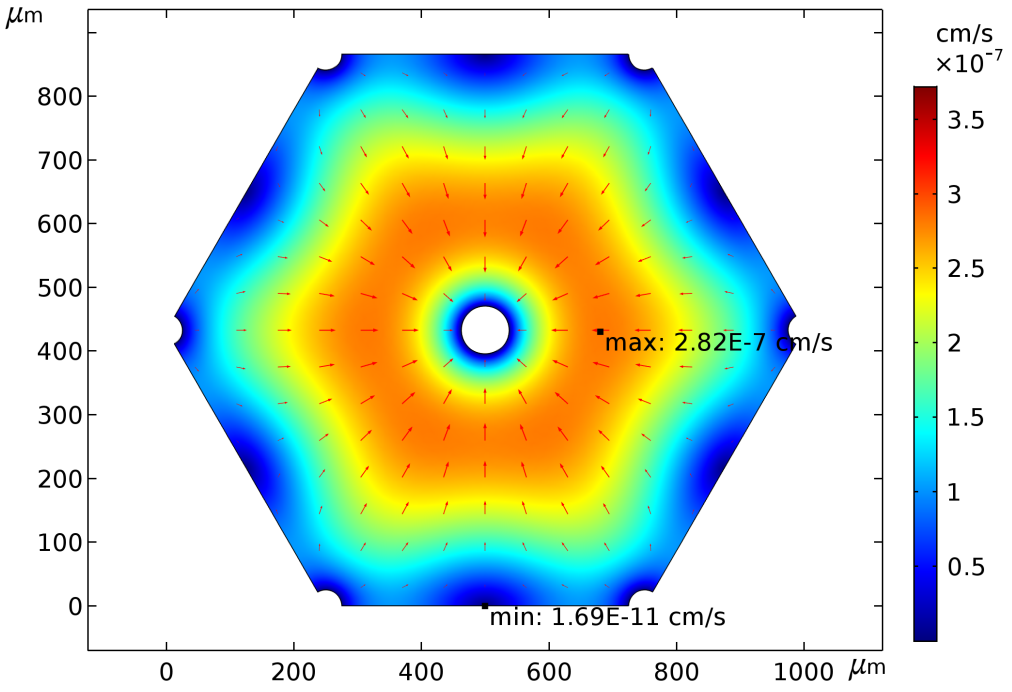


(a) $p_{i,\mathrm{ref}}$

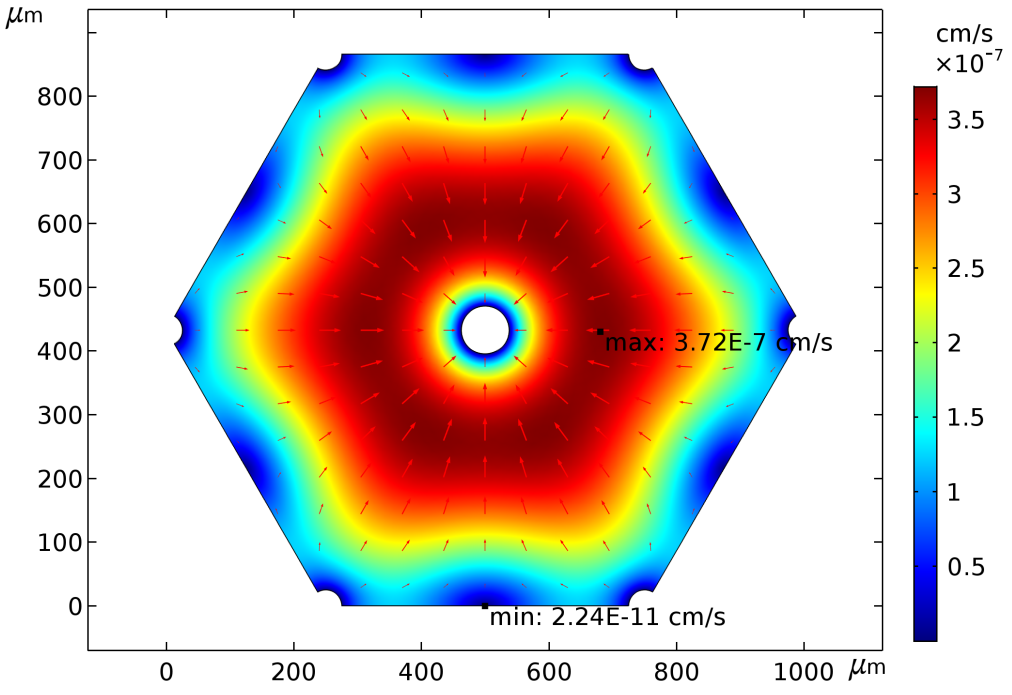


(b) p_i

Figure 2.7: Interstitial fluid pressure distribution in 2D: (a) undeformed liver lobule and (b) deformed linearly elastic liver lobule following a 10% increase in sinusoidal blood portal pressure. Colour bars show pressure magnitude and have different ranges in each subfigure. Pressure contours are at intervals of 0.02 mmHg in both subfigures.

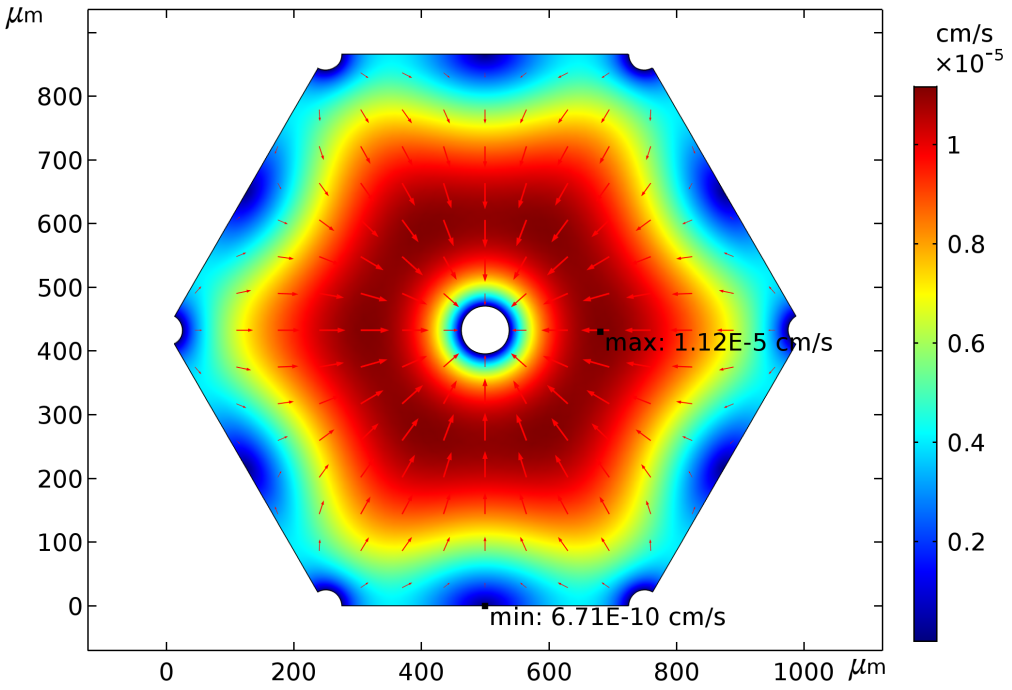


(a) $\mathbf{v}_{i,\text{ref}}$

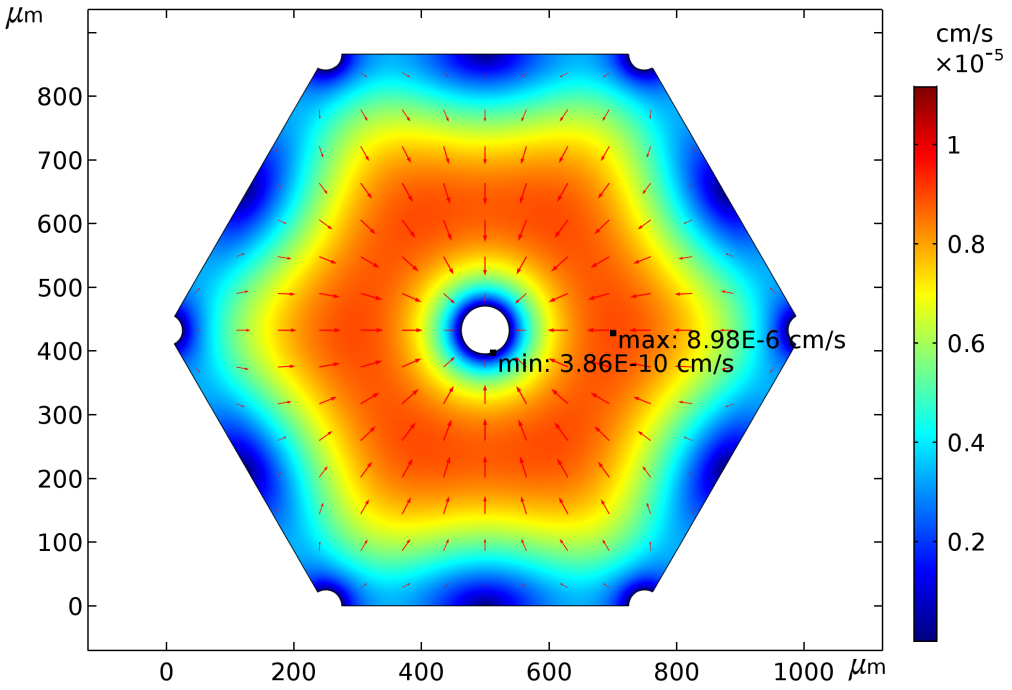


(b) $\mathbf{v}_i$

Figure 2.8: Interstitial fluid Darcy velocity in 2D: (a) undeformed liver lobule and (b) deformed linearly elastic liver lobule following a 10% increase in sinusoidal blood portal pressure. In both subfigures, arrows show the direction of flow and are proportional to the magnitude of flow velocity. Colour bars show velocity magnitude and are of the same range for both subfigures.



(a) $\mathbf{v}_{i,\mathrm{ref}}/\varphi_{i,\mathrm{ref}}$

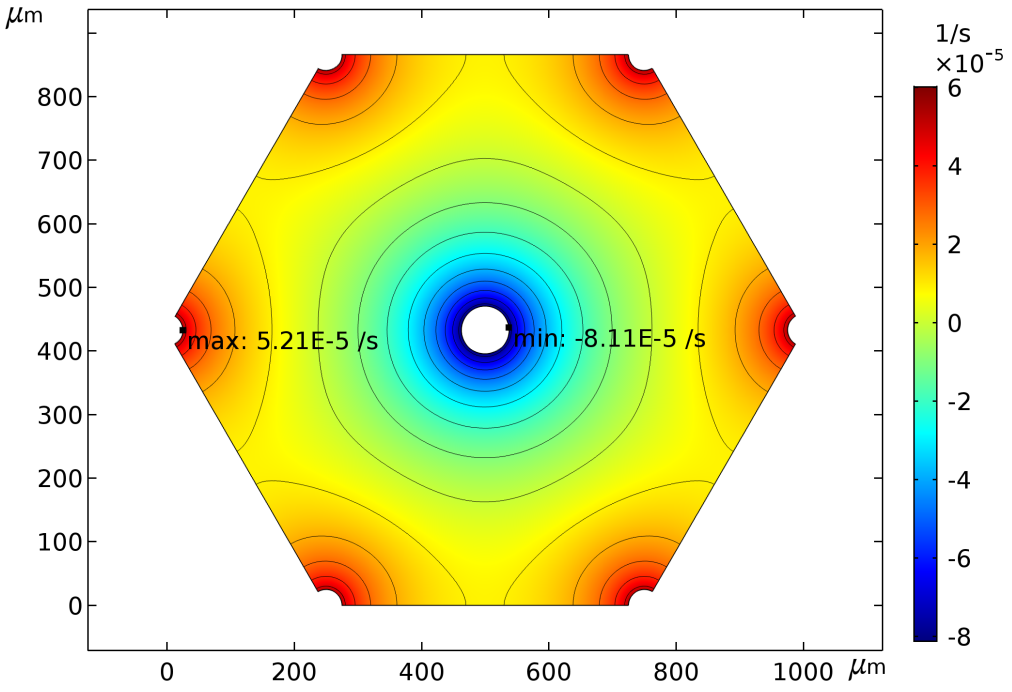


(b) $\mathbf{v}_i/\varphi_i$

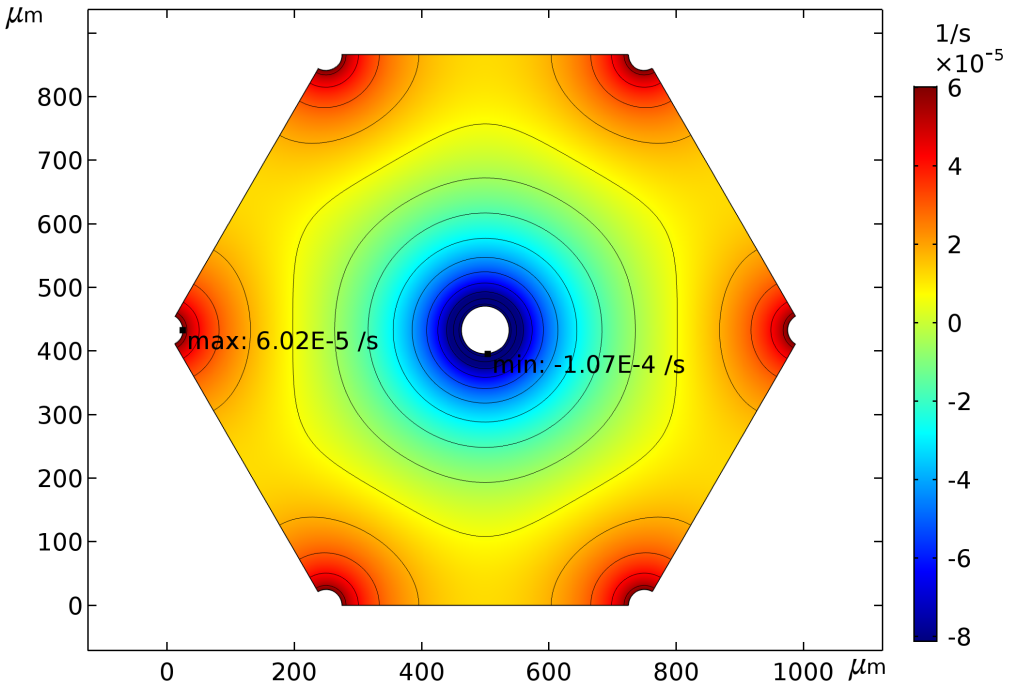
Figure 2.9: Average interstitial fluid pore velocity in 2D: (a) undeformed liver lobule and (b) deformed linearly elastic liver lobule following a 10% increase in sinusoidal blood portal pressure. Arrows show the direction of flow and are proportional to the magnitude of flow velocity. Colour bars show velocity magnitude and are of the same range for both subfigures.

2.10.2.3 Fluid Exchange Across Sinusoidal Vessels

Plasma fluid flux q_{plasma} from the sinusoidal walls into the interstitial space is maximum close to the portal tracts. This is where fluid pressure difference is maximum between blood in the sinusoids and interstitial fluid in the interstitial space. Plasma flux becomes zero in the middle of the lobule, after which flow reversal occurs from the interstitial space to the sinusoids. Maximum plasma drainage from the interstitial space into the sinusoids occurs close to the central vein. This is the case in both the undeformed liver lobule (Figure 2.10a) and the deformed liver lobule following a 10% increase in sinusoidal blood portal pressure (Figure 2.10b). Surface averaged plasma flux per unit volume increases from $1.9 \times 10^{-6}\,\text{s}^{-1}$ in the undeformed liver to $2.1 \times 10^{-6}\,\text{s}^{-1}$ in the deformed liver following a 10% increase in sinusoidal blood portal pressure, suggesting that the average filtration rate within the liver increases with increase in blood portal pressure.



(a)



(b)

Figure 2.10: Plasma flux per unit volume into the interstitial space q_{plasma} in 2D: (a) undeformed liver lobule and (b) deformed linearly elastic liver lobule following a 10% increase in sinusoidal blood portal pressure. Colour bars show the magnitude of plasma exchange and are of the same range for both subfigures. Contours are of intervals of $1\,\text{s}^{-1}$ in both subfigures.

2.10.2.4 Deformation Profile

The deformation of the liver lobule following a 10% increase in blood portal pressure is shown in Figure 2.11. The magnitude of displacement is maximum at the vascular septa and minimum at the central vein, which was kept fixed in the model. Tissue displacement is also symmetrical about the central vein due to isotropy. This can be further observed through the displacement magnitude contours plotted in Figure 2.12.

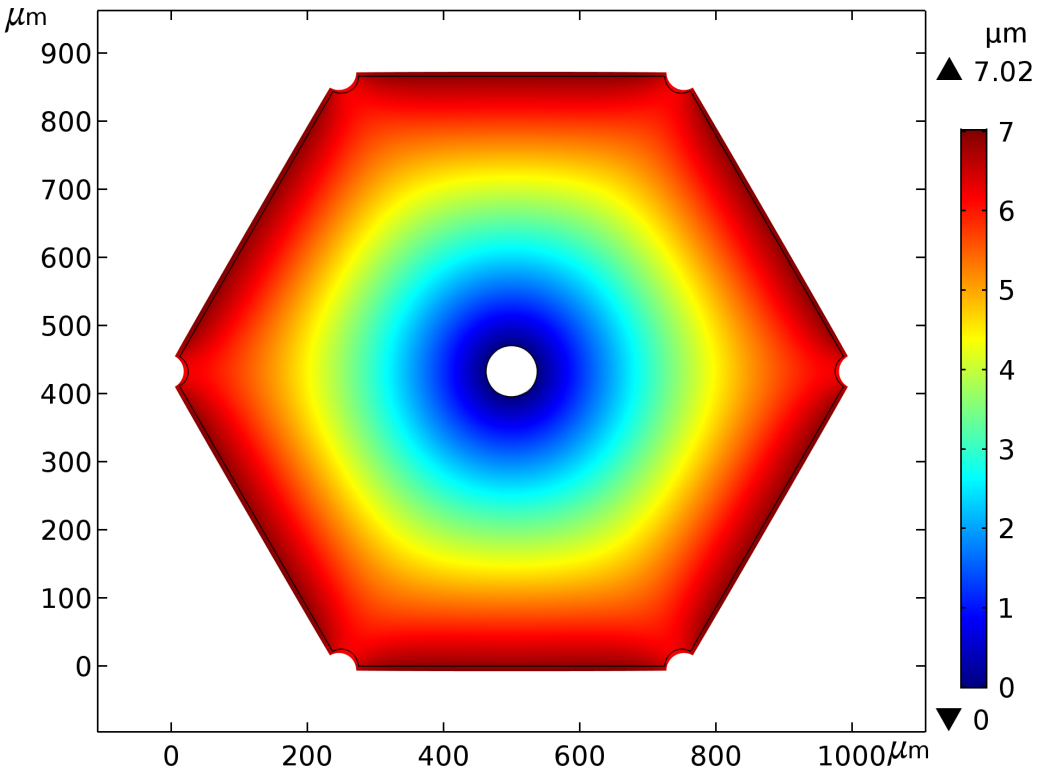


Figure 2.11: Displacement of a 2D linear elastic lobule following a 10% increase in blood sinusoidal portal pressure, referenced against the undeformed lobule (black line). Colour bar shows displacement magnitude $|\mathbf{u}|$.

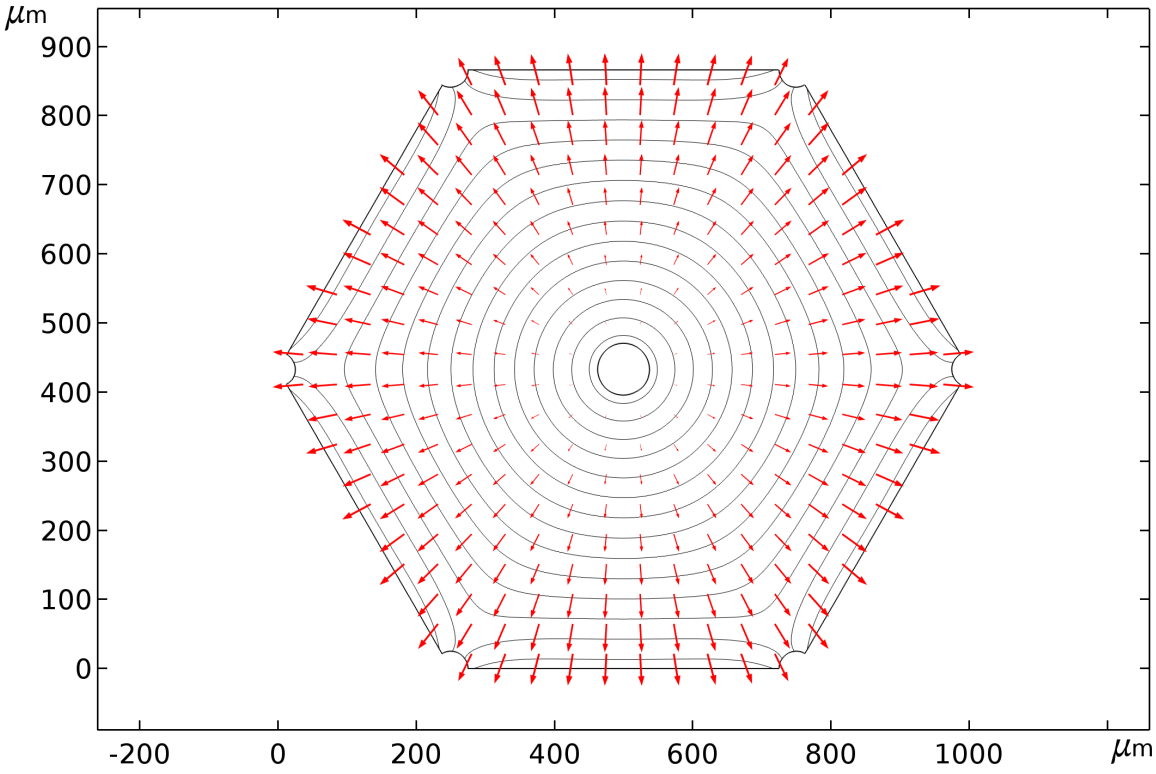


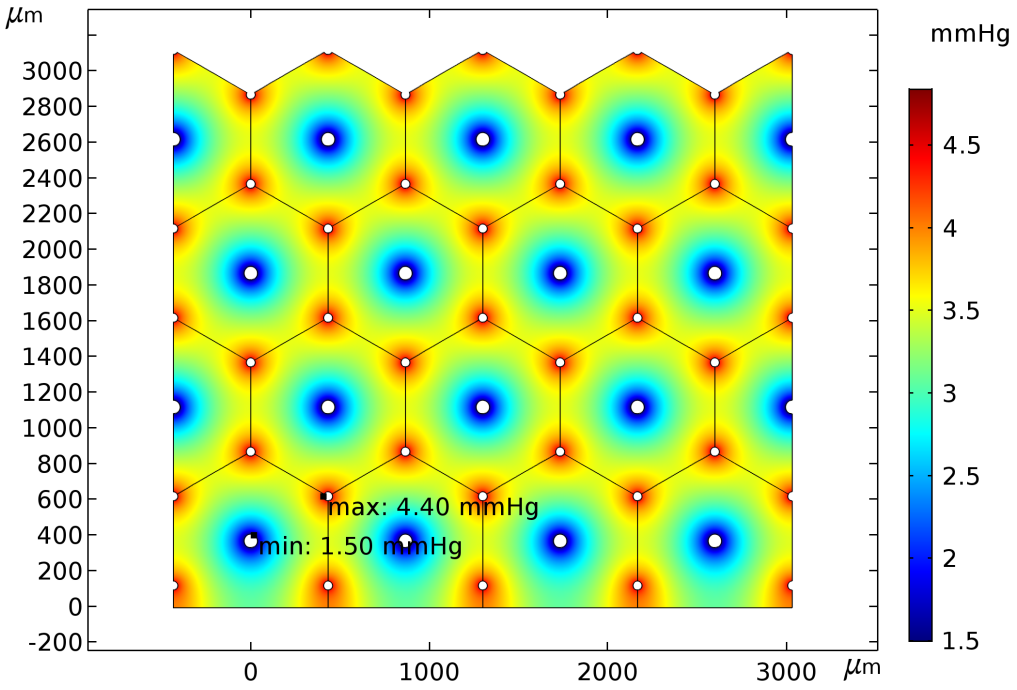
Figure 2.12: Displacement contours of a 2D linearly elastic lobule following a 10% increase in blood sinusoidal portal pressure, referenced against the undeformed lobule. The contours are at intervals of 0.5 μm. Arrows show the direction of displacement and are proportional to the magnitude of displacement.

In the next section, we study the results of the flow and deformation profiles in a lattice arrangement of multiple lobules close to the liver surface, as described in Section 2.2.3.

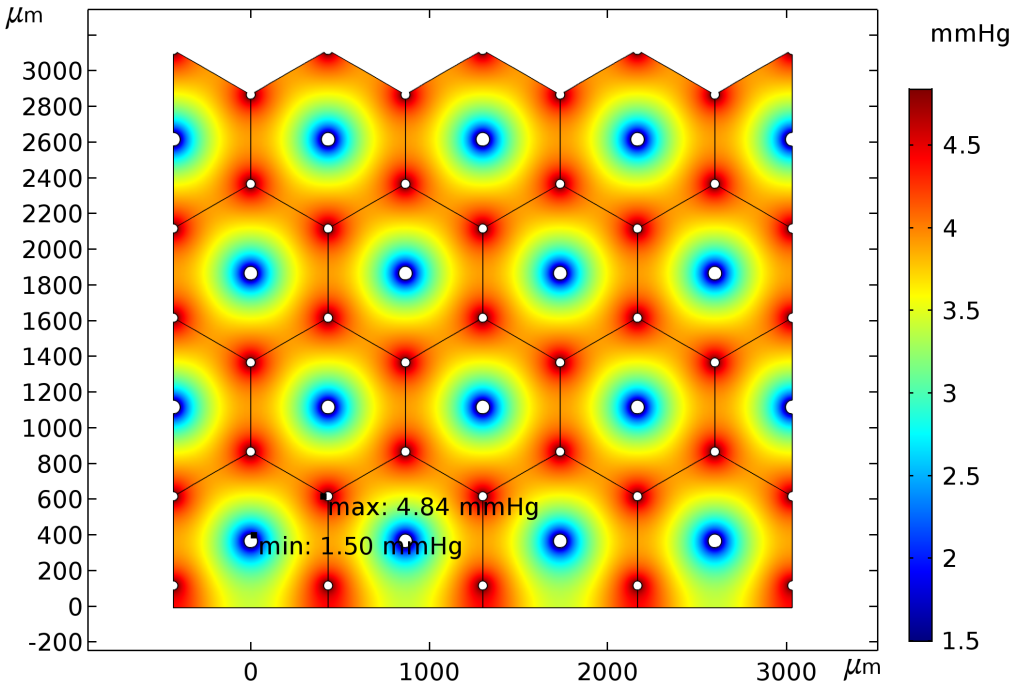
2.10.3 Multiple Lobules

2.10.3.1 Blood Pressure and Velocity

Sinusoidal blood pressure, Darcy velocity and pore velocity profiles, for both the undeformed and deformed lobule lattice, are shown in Figures 2.13–2.15. For all three parameters, both the interior lobules and the exterior lobules have the same profile as that of the single lobule presented in Section 2.10.2.1. This is due to the no blood flux condition imposed along the vascular septa of each lobule, which prevents the flow of blood across neighbouring vessels. It also means that each lobule has the same amount of blood supply and drainage, provided that the blood pressures at the portal tracts and central vein are the same for all lobules, which we assume to be so in our model.

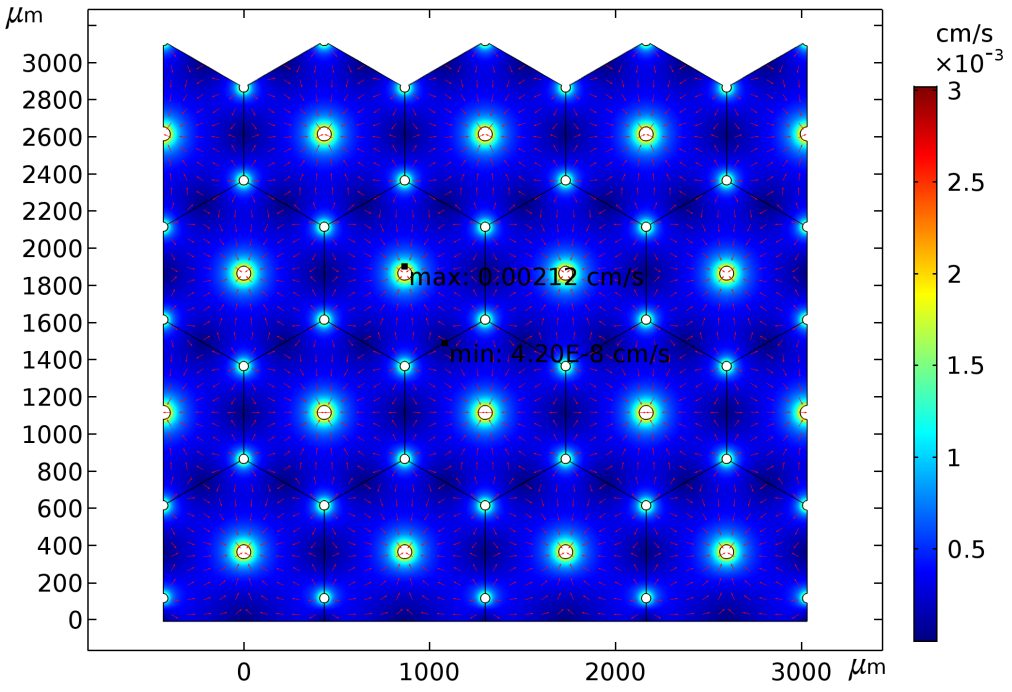


(a) $p_{s,\mathrm{ref}}$

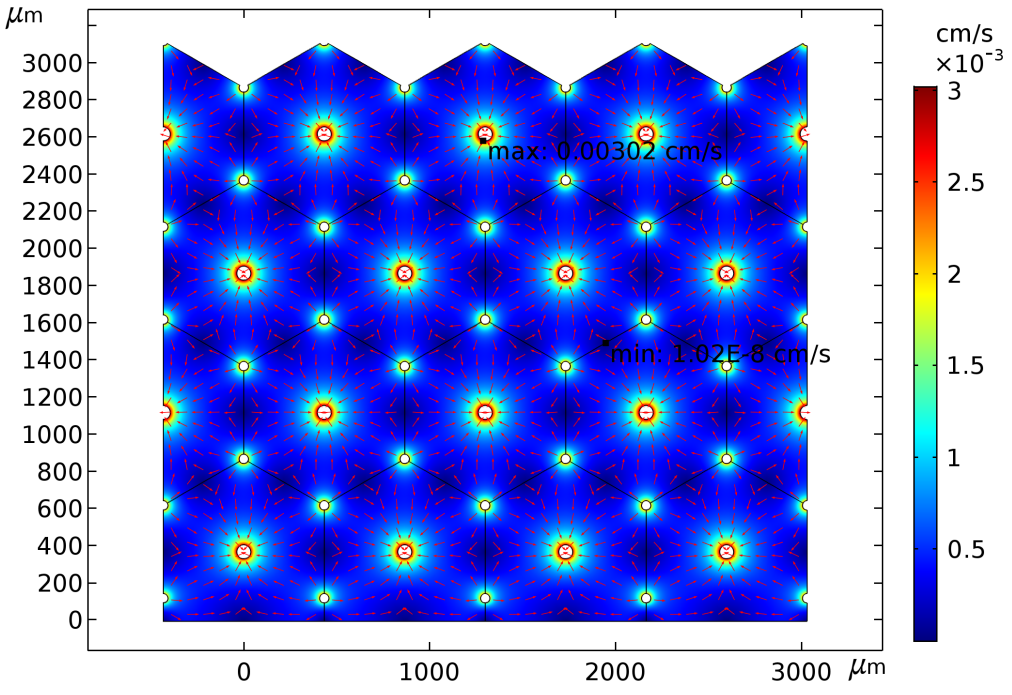


(b) p_s

Figure 2.13: Blood pressure distribution in 2D: (a) undeformed liver lobule lattice and (b) deformed linearly elastic liver lobule lattice following a 10% increase in sinusoidal blood portal pressure. Colour bars show pressure magnitude and have the same range in both subfigures.

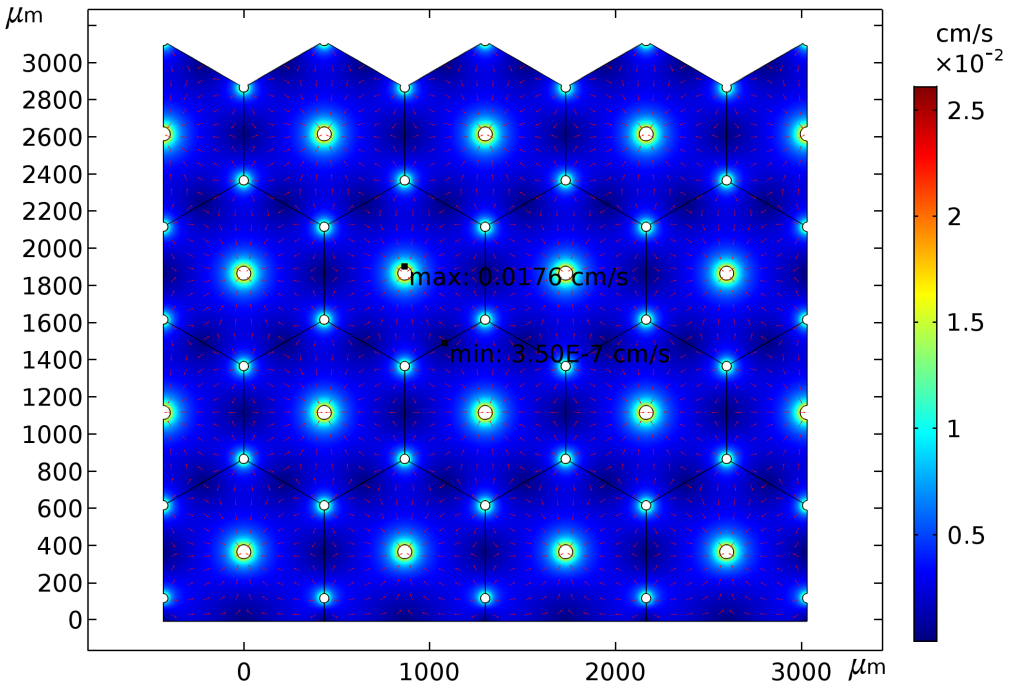


(a) $\mathbf{v}_{s,\mathrm{ref}}$

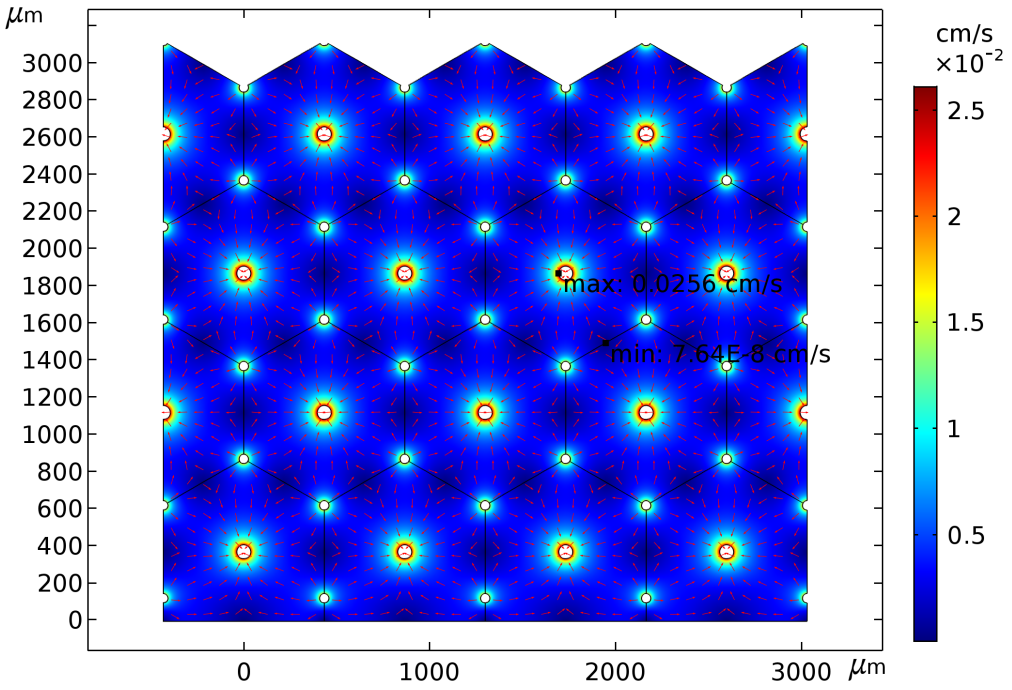


(b) $\mathbf{v}_s$

Figure 2.14: Blood Darcy velocity in 2D: (a) undeformed liver lobule lattice and (b) deformed linearly elastic liver lobule lattice following a 10% increase in sinusoidal blood portal pressure. In both subfigures, arrows show the direction of flow and are normalised to the magnitude of flow velocity. Colour bars show velocity magnitude and are of the same range for both subfigures.



(a) $\mathbf{v}_{s,\mathrm{ref}}/\varphi_{s,\mathrm{ref}}$



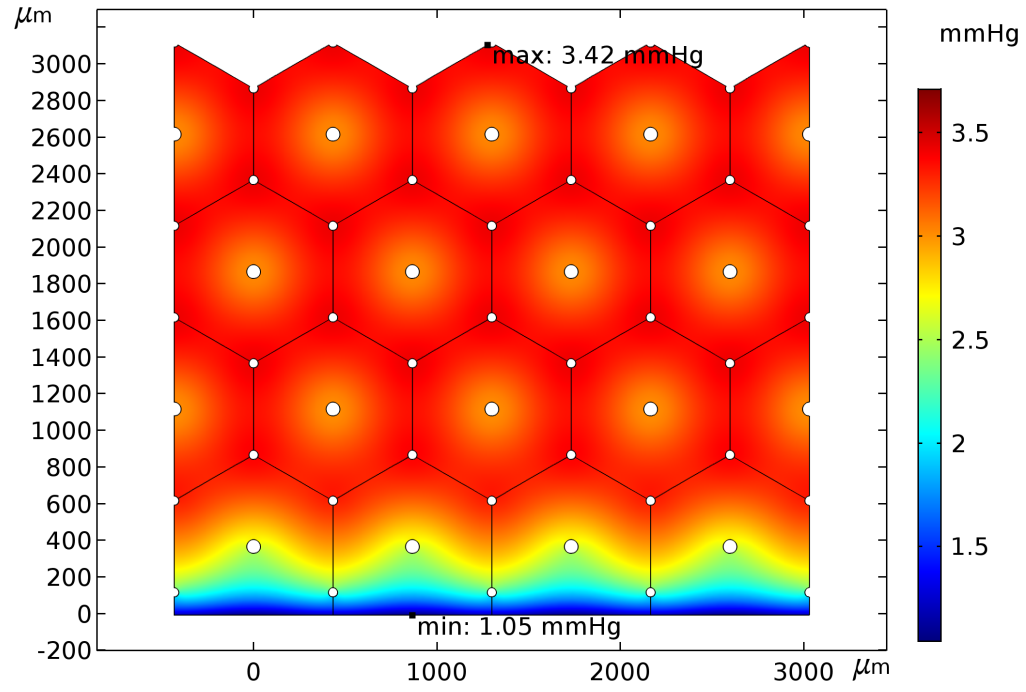
(b) $\mathbf{v}_s/\varphi_s$

Figure 2.15: Average blood pore velocity in 2D: (a) undeformed liver lobule lattice and (b) deformed linearly elastic liver lobule lattice following a 10% increase in sinusoidal blood portal pressure. In both subfigures, arrows show the direction of flow and are normalised to the magnitude of flow velocity. Colour bars show velocity magnitude and are of the same range for both subfigures.

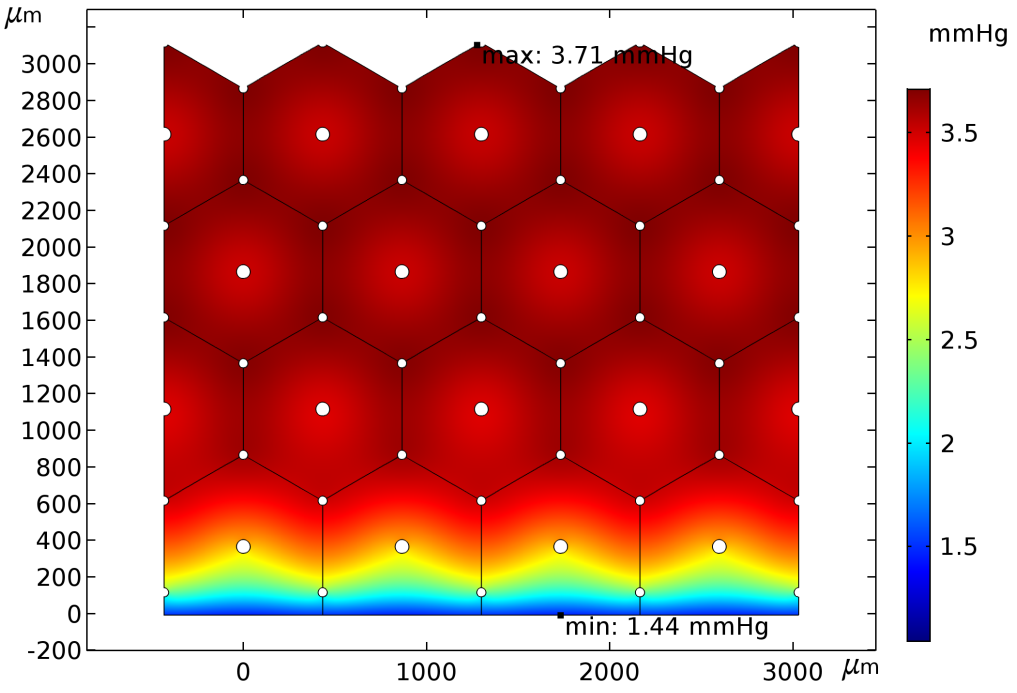
2.10.3.2 Interstitial Fluid Pressure and Velocity

Interstitial fluid pressure distribution, in both the undeformed and deformed lobule lattice, is shown in Figure 2.16. Recall that unlike blood, we have a free flow of interstitial fluid across neighbouring lobules, as well as a fluid flux across the outer surface of the liver.

The interior lobules have a similar pressure distribution to that of the single lobule shown in Section 2.10.2.2. The exterior lobules, however, have a different pressure profile. Interstitial fluid pressure is maximum towards the interior portal tracts of the exterior lobule, while the pressure is minimum close to the outer edge of the liver. The result is a larger pressure drop towards the outer surface of the liver, which drives flow across the Glisson's capsule. This also explains why the magnitude of interstitial fluid Darcy and pore velocities, in both the undeformed and deformed lobule lattice (Figures 2.17–2.18), are largest within the exterior lobules where the fluid leaks out of the liver. Other than that, interstitial fluid flow is fairly uniform within the interior lobules and has the same profile as that of the single lobule described in Section 2.10.2.2.

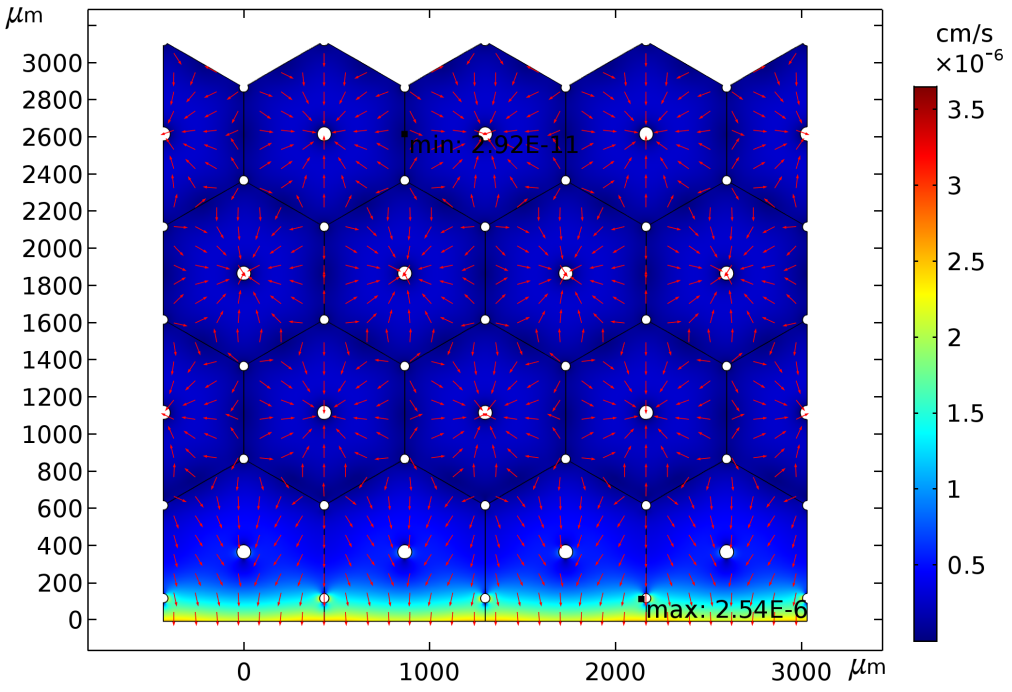


(a) $p_{i,\mathrm{ref}}$

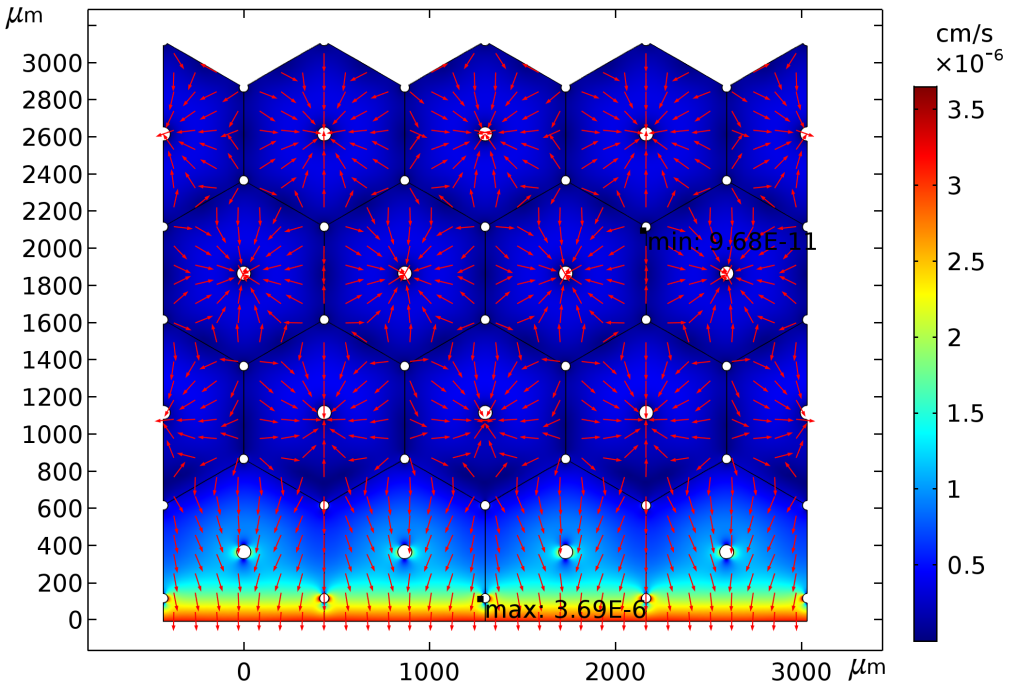


(b) p_i

Figure 2.16: Interstitial fluid pressure distribution in 2D: (a) undeformed liver lobule lattice and (b) deformed linearly elastic liver lobule following a 10% increase in sinusoidal blood portal pressure. Colour bars show pressure magnitude and have the same range in each subfigure.

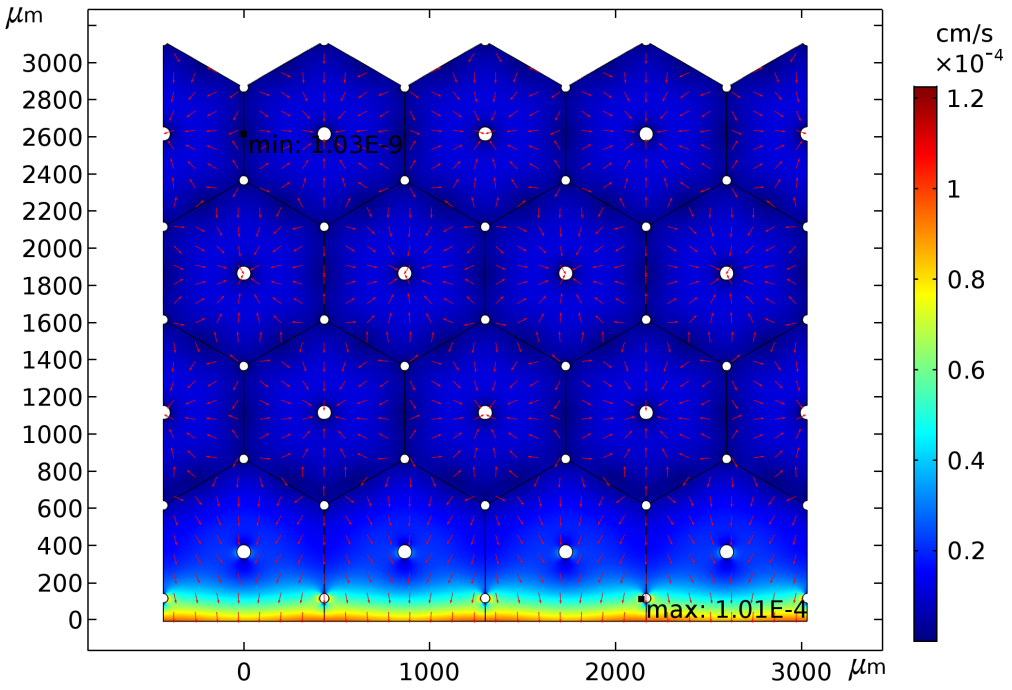


(a) $\mathbf{v}_{i,\text{ref}}$

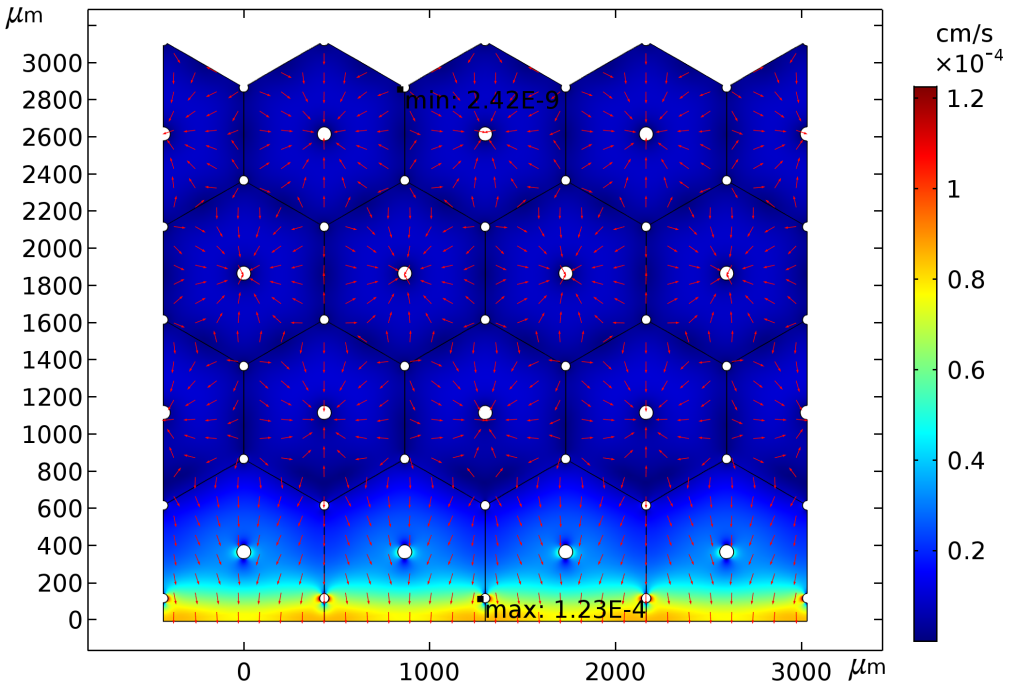


(b) $\mathbf{v}_i$

Figure 2.17: Interstitial fluid Darcy velocity in 2D: (a) undeformed liver lobule lattice and (b) deformed linearly elastic liver lobule lattice following a 10% increase in sinusoidal blood portal pressure. In both subfigures, arrows show the direction of flow and are normalised to the magnitude of flow velocity. Colour bars show velocity magnitude and are of the same range for both subfigures.



(a) $\mathbf{v}_{i,\mathrm{ref}}/\varphi_{i,\mathrm{ref}}$

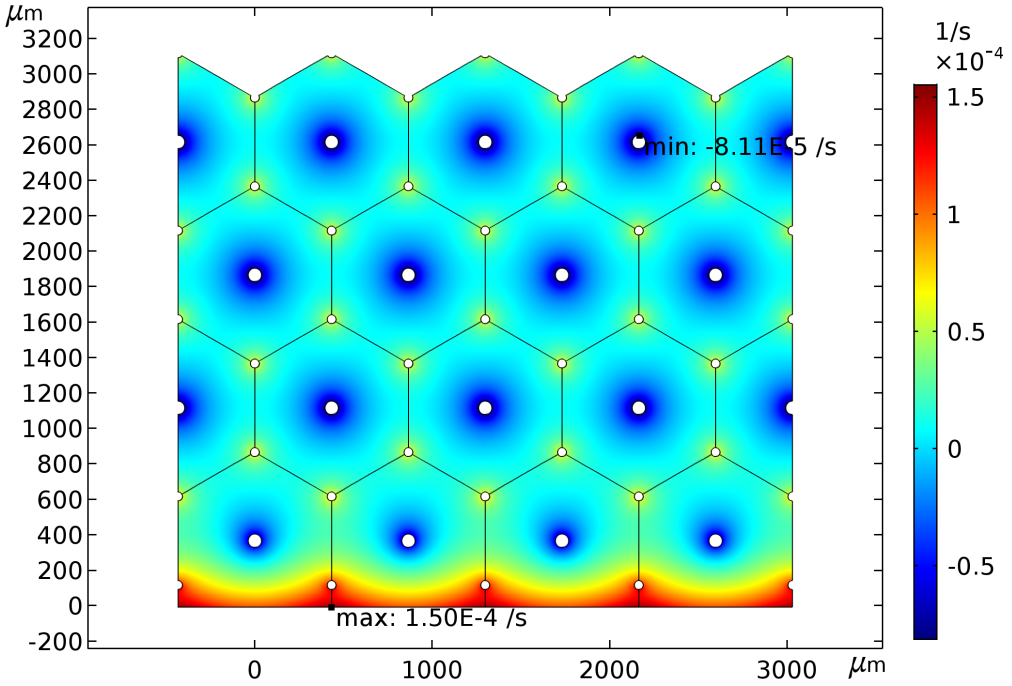


(b) $\mathbf{v}_i/\varphi_i$

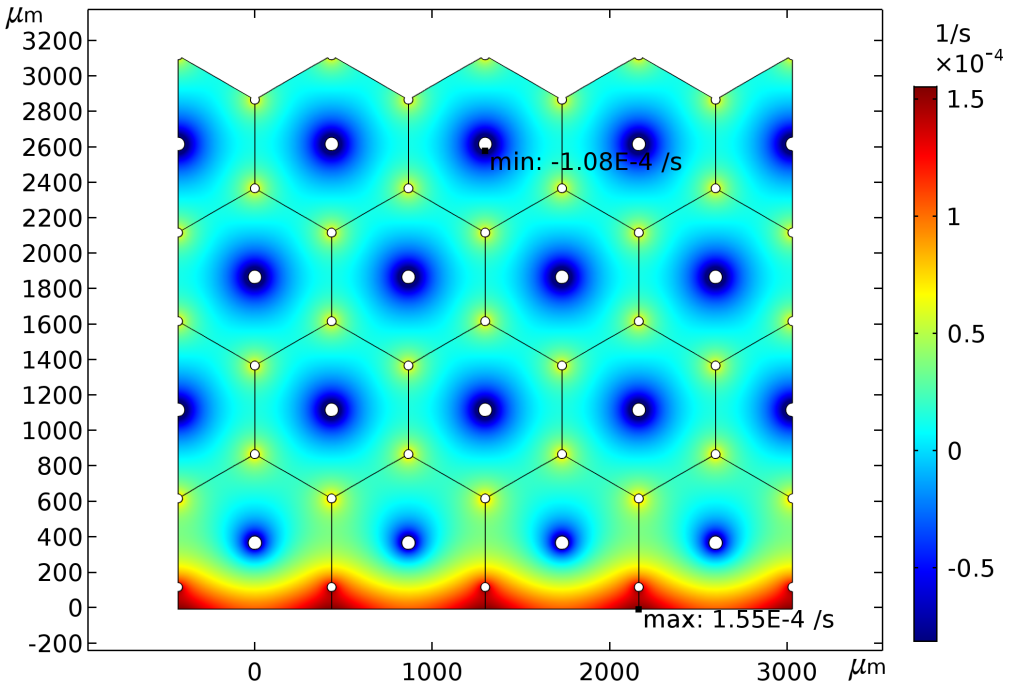
Figure 2.18: Average interstitial fluid pore velocity in 2D: (a) undeformed liver lobule lattice and (b) deformed linearly elastic liver lobule lattice following a 10% increase in sinusoidal blood portal pressure. Arrows show the direction of flow and are normalised to the magnitude of flow velocity. Colour bars show velocity magnitude and are of the same range for both subfigures.

2.10.3.3 Fluid Exchange Across Sinusoidal Vessels

Estimated plasma flux exchange across the sinusoidal vessels of the lobule lattice, for both the undeformed and deformed liver, is shown in Figures 2.19a–2.19b. The interior lobules have a similar plasma flux exchange profile as that of the single lobule shown in Section 2.10.2.3, with plasma flow going from the sinusoidal walls to the interstitial space between the portal tracts and the middle of the lobule, where a reversal of flow then occurs before reaching the central vein. Across the lattice, plasma exchange is maximum towards the outer surface of the lobule, which explains why interstitial fluid velocity magnitude is also maximum at this point (see Figures 2.17a–2.17b).



(a)



(b)

Figure 2.19: Plasma flux per unit volume into the interstitial space q_{plasma} in 2D: (a) undeformed liver lobule lattice and (b) deformed linearly elastic liver lobule lattice following a 10% increase in sinusoidal blood portal pressure. Colour bars show the magnitude of plasma exchange and are of the same range for both subfigures.

2.10.3.4 Deformation Profile

The displacement profile of the lobule lattice following a 10% increase in sinusoidal portal pressure is shown in Figure 2.20. In this simulation, we have fixed the uppermost, middle central vein at coordinates $(x, y) = (1300\,\mu\text{m}, 1000\,\mu\text{m})$. This is why tissue displacement is symmetric about said central vein, as the tissue expands radially outwards to accommodate the expansion of the sinusoidal and interstitial pore networks (see contour plots in Figure 2.21). Changing the location of the fixed point changes the displacement profile of the lattice, as expected, however, it has a negligible effect of on the average volume change ratio of the lattice.

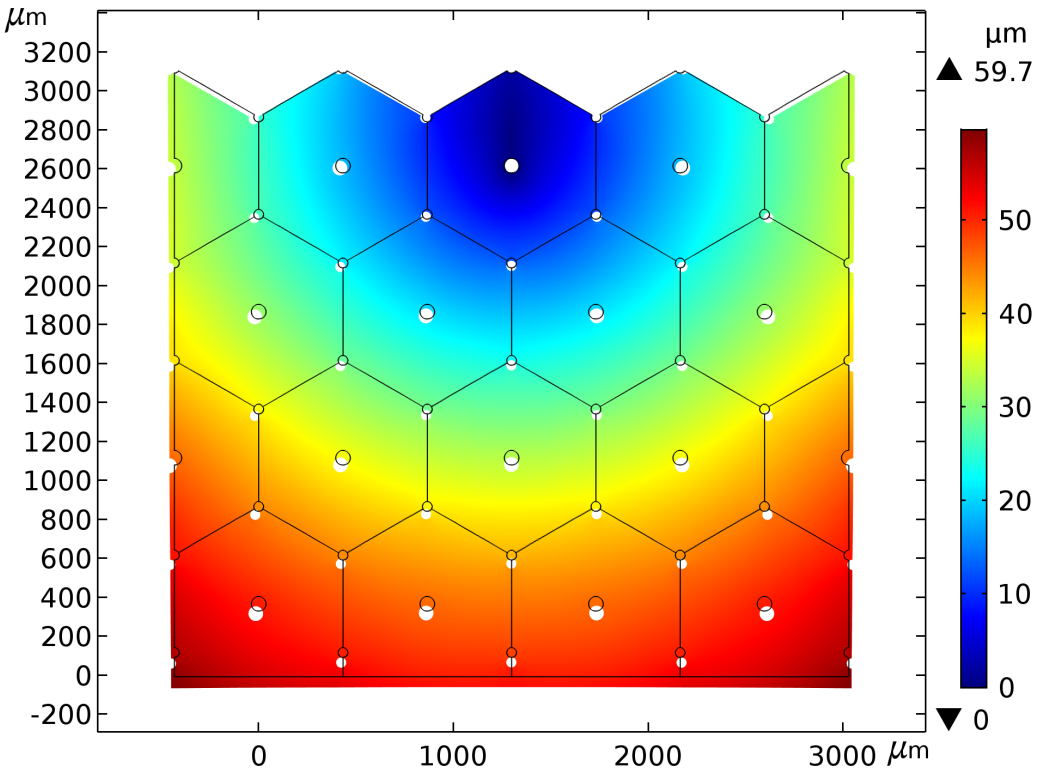


Figure 2.20: Displacement magnitude of a 2D linearly elastic lobule lattice following a 10% increase in blood sinusoidal portal pressure, referenced against the undeformed lobule.

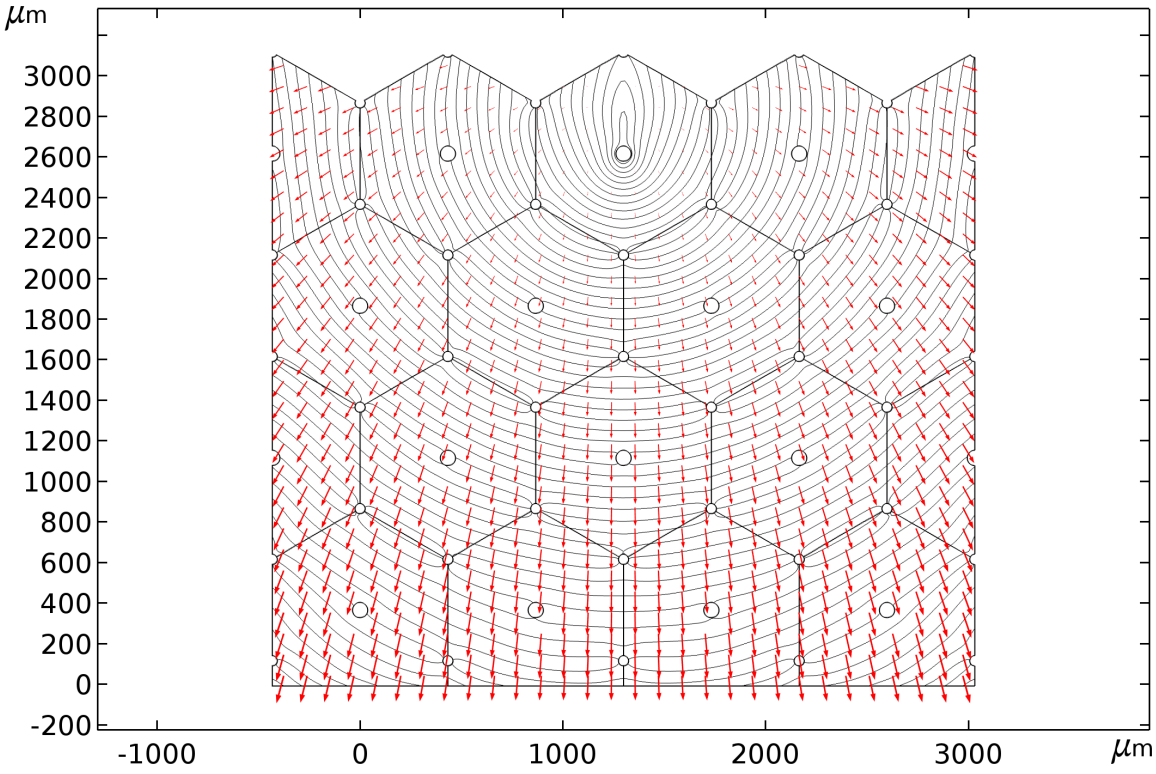


Figure 2.21: Displacement contours of a 2D linearly elastic lobule lattice following a 10% increase in blood sinusoidal portal pressure, referenced against the undeformed lobule. The contours are at intervals of 1 μm. Arrows show the direction of displacement and are proportional to the magnitude of displacement.

2.10.4 Effect of Portal Pressure Variation on Tissue Expansion

The numerical results presented in the previous subsections only highlight the deformation of the liver lobule following a 10% increase in blood portal tract pressure. In this section, we look at the effect of blood portal tract pressure increase on deformation parameters, such as volume change ratio, cross-sectional stretch and porosity. Other parameters such as fluid velocity and hydraulic conductivity are not shown here, since they are both dependent on the volume change ratio mentioned above.

The surface averaged volume change ratio $\mathcal{V}/\mathcal{V}_{\text{ref}} = J \approx (1 + \boldsymbol{\nabla} \cdot \mathbf{u})$ and cross-sectional stretch of the tissue $\lambda \approx (1 + \boldsymbol{\nabla} \cdot \mathbf{u})^{1/2}$ for varying percentages of blood portal pressure increase, up to 50%, are shown in Figure 2.22. The volume change ratio increases linearly as blood pressure at the portal tracts increases, while the cross-sectional stretch is slightly non-linear for sinusoidal portal pressure increases up to 50%. This result is expected, since the deformation equations used are that of a linearly elastic material. Liver porosity, as shown in Figure 2.23, also has an slight non-linear behaviour with increase in blood portal pressure up to 50%.

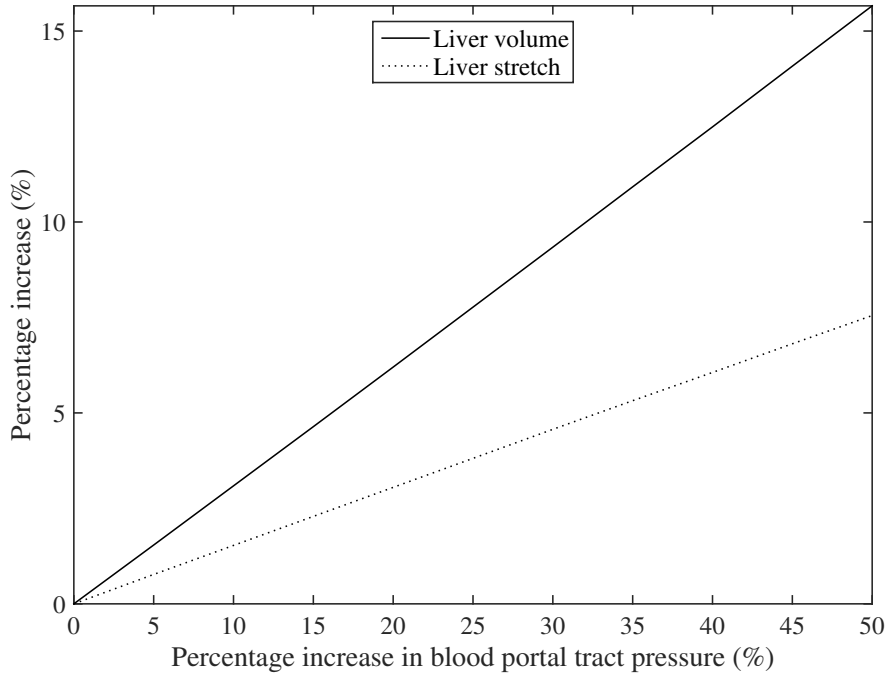


Figure 2.22: Surface averaged increase in liver volume $\mathcal{V}/\mathcal{V}_{\text{ref}}$ and cross–sectional stretch λ against increase in sinusoidal blood pressure at the portal tracts, using the 2D linear elastic liver model.

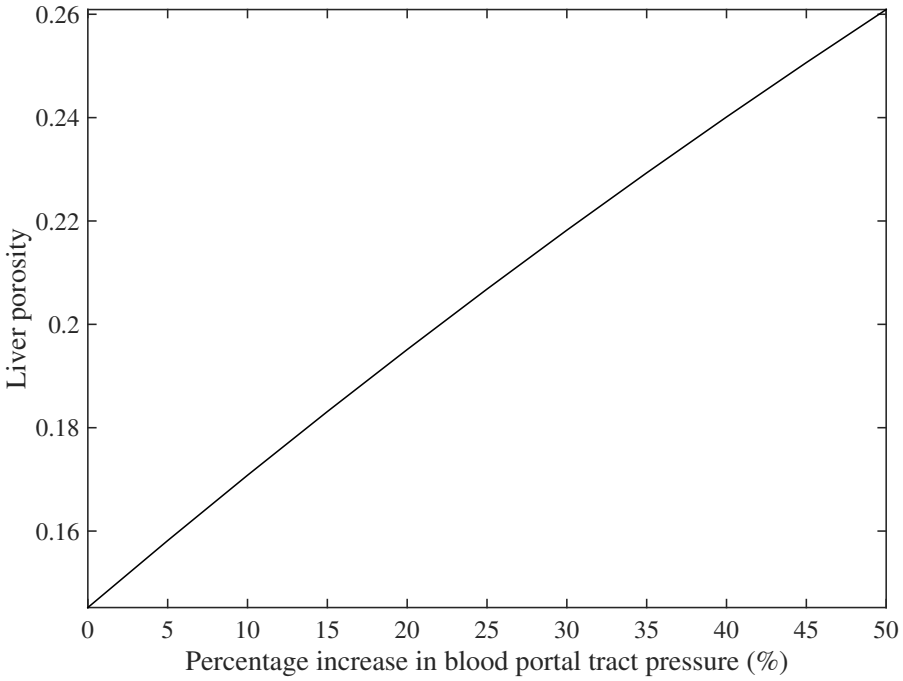


Figure 2.23: Surface averaged liver porosity against increase in sinusoidal blood pressure at the portal tracts, using the 2D linear elastic liver model.

2.10.5 Derived Values

In this section, we present the estimates of total volume flux of blood through the liver, lymphatic uptake rate within the liver and fluid loss via the surface membrane of the liver. We compare the values obtained in both the undeformed (rigid) liver model and the deformable linear elastic model following an increase in blood sinusoidal portal pressure.

2.10.5.1 Total Blood Flux

The total volume flux of blood being filtered by the liver in the physiological undeformed case is estimated to be approximately 0.66 L/min, using Equation (2.54), same as in Siggers et al. (2014). Following a 10% increase in sinusoidal blood portal pressure this value was found to increase by about 39% (≈ 0.92 L/min) in the linearly elastic model, using Equation (2.55), as opposed to the 15% increase (≈ 0.77 L/min) predicted by the rigid model in Siggers et al. (2014). This means that, for example, the rigid model underestimates the filtration capacity of the liver by up to 24%, following a 10% increase in sinusoidal blood portal pressure.

Figure 2.24 highlights the difference between the blood flux values obtained in the rigid model by Siggers et al. (2014) and the linear elastic model developed in this chapter. As the blood sinusoidal portal pressure is increased, the linearly elastic model predicts a much higher volume flux of blood into the liver than the rigid model. This is expected since the liver tissue is now capable of expanding to accommodate increase in blood flow. Also, increase in blood flux is approximately linear with increase in blood sinusoidal portal pressure in the rigid model, while it is non-linear in the linearly elastic liver model model.

2.10.5.2 Lymphatic Uptake Rate

Similarly, lymphatic uptake rate within the liver is estimated to be approximately 0.17 mL/min, using Equation (2.56), in the undeformed case. Following a 10% increase in sinusoidal blood portal pressure, the lymphatic uptake rate increases to approximately 0.19 mL/min, using Equation (2.57), in the linearly elastic model compared to 0.18 mL/min predicted by the rigid model of Siggers et al. (2014). The difference between the values estimated by the two models is less than 2.5% for a 10% increase in blood sinusoidal portal pressure.

Increase in total lymphatic uptake against increase in blood sinusoidal portal pressure, for both the rigid liver model and the linearly elastic model, is shown in Figure 2.25. In both models, lymphatic uptake increases linearly as sinusoidal blood portal pressure increases, albeit with a higher gradient in the linearly elastic liver model.

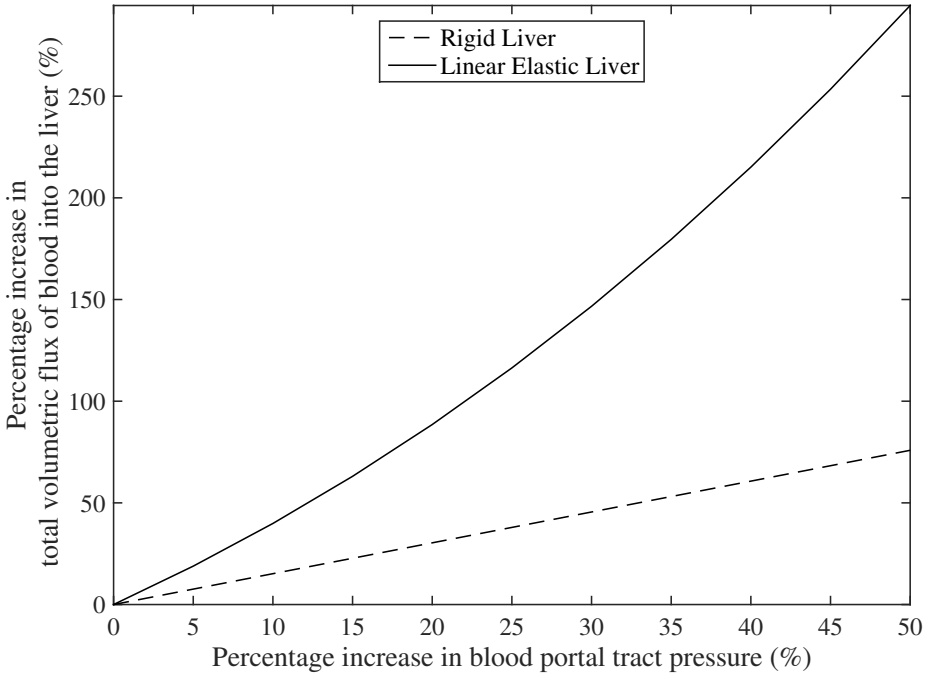


Figure 2.24: Total volume flux of blood in the linearly elastic liver model versus the rigid liver model by Siggers et al. (2014), for different percentage increase in blood sinusoidal portal pressure.

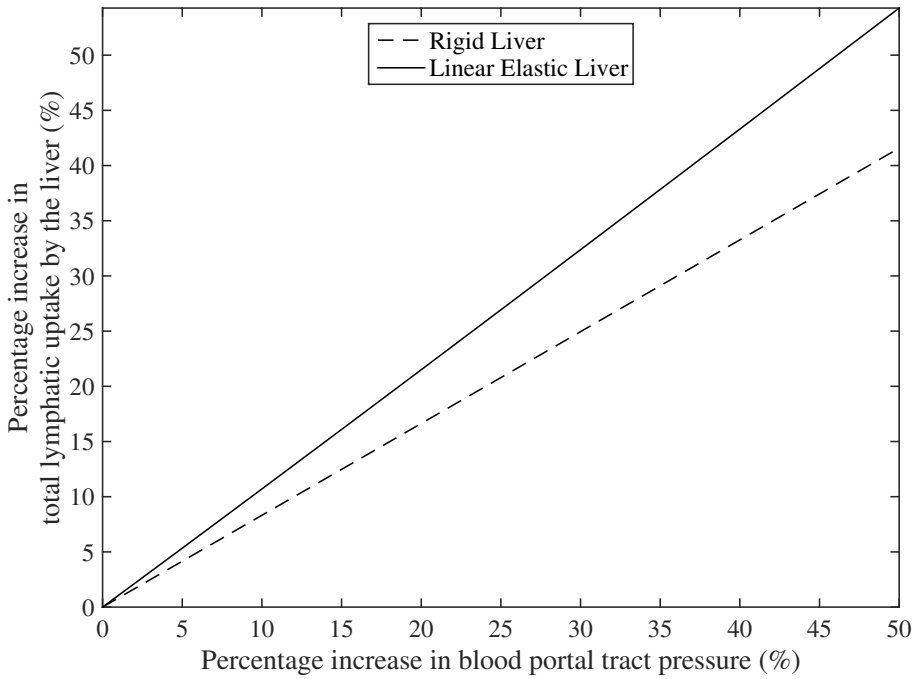


Figure 2.25: Total lymphatic uptake within the linearly elastic liver model versus the rigid liver model by Siggers et al. (2014), for different percentage increase in blood sinusoidal portal pressure.

2.10.5.3 Fluid Loss into the Peritoneal Cavity

The total fluid loss via the Glisson's capsule of the liver in the undeformed case was found to be approximately 0.183 mL/min, 0.146 mL/min of which is lost via the Glissonian–peritoneal membrane and the remaining 0.027 mL/min through the bare area. Since we are primarily interested in fluid accumulation in the peritoneal cavity, we will only study the result of fluid lost through the Glissonian–peritoneal surface in this section and for the remainder of the thesis.

Following a 10% increase in blood sinusoidal portal pressure, the rigid model of the liver by Siggers et al. (2014) predicts a fluid loss increase of 0.158 mL/min into the peritoneal cavity. In our linearly elastic liver model, increased fluid loss was found to be 0.193 mL/min, using Equation $(2.59)_b$, with a 10% increase in sinusoidal blood portal pressure, resulting in a difference of 0.035 mL/min due to the expansion of the interstitial fluid pore network. Increase in fluid loss into the peritoneal cavity is approximately linear with increase in blood sinusoidal portal pressure (see Figure 2.26). Again, the gradient of fluid loss is a lot higher in the linearly elastic model compared to the rigid model by Siggers et al. (2014).

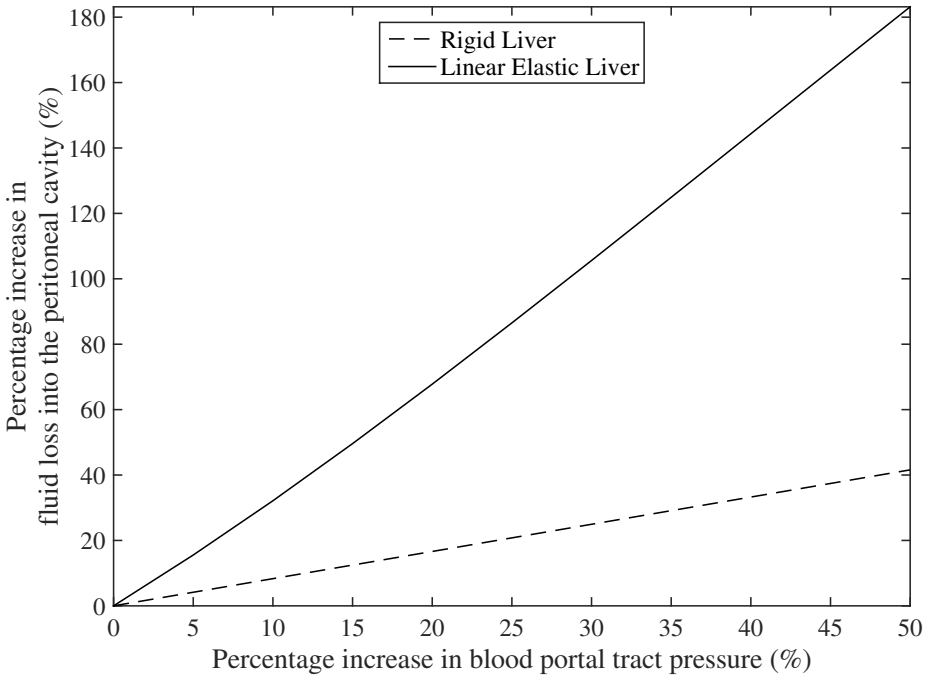


Figure 2.26: Fluid loss into the peritoneal cavity using the linearly elastic liver model versus the rigid liver model by Siggers et al. (2014), for different percentage increase in blood sinusoidal portal pressure.

2.11 Summary and Conclusion

The focus of this chapter was on developing a deformable mathematical model of the liver capable of accommodating changes in portal blood pressure and the resulting increase in plasma fluid filtration into the interstitial space. As a first approximation, we considered a 2D model of the liver, structured as a lattice of lobules with identical cross sectional area, and assumed a linear elastic behaviour for the tissue. Flow of blood in the sinusoids and interstitial fluid in the interstitial space were modelled as that of fluids in a porous media. Using mass conservation and a coupling between pore expansion and the hydraulic conductivity of the tissue, we solved the governing system of equations using the COMSOL Multiphysics software to obtain pressure, velocity and deformation profiles of the tissue following an increase in blood portal pressure, which was referenced against the normal undeformed case. We were also able to obtain estimates of other important parameter values, such as the total volume blood flux into the liver, lymphatic uptake rate and fluid loss via the surface of the liver. The key result of the chapter is the comparison between the linear poroelastic model developed and the current rigid porous model of the liver by Siggers et al. (2014), which shows a significant underestimate of said estimated parameter values by the rigid model following large increases in portal pressure.

Note, however, the linear elasticity approximation is only valid for liver tissue strains up to 10% (Chui et al., 2004). In our model, this corresponds to a sinusoidal blood pressure magnitude of 7.31 mmHg at the portal tracts and blood pressure drop of 5.81 mmHg across the lobule. In the next chapter, we will extend the 2D linear elastic model into a 3D hyperelastic model in order to capture the material non-linear behaviour of the liver tissue at higher pressures. Also, since such large increases in blood pressure rarely occur without damage to the liver tissue, we will look at the effect of both high blood portal pressure, also known as portal hypertension, and increased tissue stiffness, which is a structural consequence of tissue damage, on the flow and deformation profiles of the liver in Chapter 4.

Table 2.1: List of parameter values used for the lobule geometry in the 2D linear elasticity model, together with references.

Symbol	Description	Default Value	Reference
l_{lob}	Length of the side of a lobule	$500\,\mu$m	Bonfiglio et al. (2010)
d_{cv}	Diameter of central vein	$75\,\mu$m	Bonfiglio et al. (2010)
d_{pt}	Diameter of portal tract	$50\,\mu$m	Bonfiglio et al. (2010)

Table 2.2: List of parameter values used for fluid flow in the 2D linear elasticity model, together with references.

Symbol	Description	Default Value	Reference
$\kappa_{s,\text{ref}}$	Permeability of sinusoids in undeformed case	$1.56 \times 10^{-14}\,\text{m}^2$	Debbaut et al. (2012)
$\kappa_{i,\text{ref}}$	Permeability of interstitial space in undeformed case	$3.12 \times 10^{-17}\,\text{m}^2$	Siggers et al. (2014)
μ_s	Effective dynamic viscosity of blood	$0.0024\,\text{Pa}\cdot\text{s}$	Siggers et al. (2014)
μ_i	Effective dynamic viscosity of interstitial fluid	$0.0018\,\text{Pa}\cdot\text{s}$	Wells and Merrill (1961)
C_f	Hepatic filtration coefficient	$5.3 \times 10^{-5}\,\text{s}^{-1}\text{mmHg}^{-1}$	Siggers et al. (2014)
C_l	Conductance of lymphatic vessels	$5.9 \times 10^{-7}\,\text{s}^{-1}\text{mmHg}^{-1}$	Siggers et al. (2014)
p_0	Average pressure in the flowing lymphatic vessels	$0\,\text{mmHg}$	Assumed
V_{Liv}	Volume of liver	$1,474\,\text{cm}^3$	Wynne et al. (1989)
$A_{L,GP}$	Surface area of the liver covered by the peritoneal membrane	$1,018\,\text{cm}^2$	Rubin et al. (1988a)
$A_{L,BA}$	Surface area of the liver not covered by the peritoneal membrane	$0.25A_{L,GP}$	Estimated as 20% of total liver surface (Siggers et al., 2014)
M_{GP}	Hydraulic conductivity of the Glisson's capsule	$2.15\times10^{-8}\,\text{m}\cdot\text{s}^{-1}\text{mmHg}^{-1}$	Siggers et al. (2014)
P_{PC}	Pressure in the peritoneal cavity	$0\,\text{mmHg}$	Assumed
P_{BA}	Pressure adjacent to the bare area	$0\,\text{mmHg}$	Assumed
$p^{pt}_{s,\text{ref}}$	Blood sinusoidal pressure at the portal tract in the undeformed case	$4.4\,\text{mmHg}$	Siggers et al. (2014)
$p^{cv}_{s,\text{ref}}$	Blood sinusoidal pressure at the central vein in the undeformed case	$1.5\,\text{mmHg}$	Siggers et al. (2014)
p^{pt}_s	Blood sinusoidal pressure at the portal tract in the deformed case	$1.1p^{pt}_{s,\text{ref}}$	Assumed
p^{cv}_s	Blood sinusoidal pressure at the central vein in the undeformed case	$p^{cv}_{s,\text{ref}}$	Assumed

Table 2.3: List of parameter values used for tissue deformation in the linear elasticity model, together with references.

Symbol	**Description**	**Default Value**	**Reference**
ν_L	Poisson ratio of liver lobule	0.43	Chui et al. (2004)
E_L	Elastic constant of liver lobule	1185 Pa	Chui et al. (2004)
$\varphi_{s,\mathrm{ref}}$	Porosity of sinusoids in the undeformed case	0.12	Bonfiglio et al. (2010)
$\varphi_{i,\mathrm{ref}}$	Porosity of interstitial space in the undeformed case	$0.21\varphi_{s,\mathrm{ref}}$	Siggers et al. (2014)

Chapter 3

Hyperelastic Deformation Model

3.1 Introduction

In this chapter, we present the development of a 3D hyper-poroelastic model of the liver tissue, which aims to give a more accurate representation of the deformation profile of the liver lobules under high blood and interstitial fluid pressures. The work carried out here is an extension of the 2D linear poroelastic model of the liver presented in Chapter 2. As such, there are a lot of similarities between the two models, particularly in terms of modelling assumptions for fluid flow, and where this is the case, a reference is made to the relevant section in Chapter 2.

As in Chapter 2, we begin by highlighting the modelling assumptions and equations governing fluid flow and tissue deformation in our system. We then solve the resultant system of governing equations, together with prescribed boundary conditions, using COMSOL Multiphysics software. The numerical solutions obtained are then presented and analysed at the end of the chapter, including a comparison between the results obtained from this hyperelastic model and the linear elastic model presented in Chapter 2.

3.2 Modelling Assumptions

The modelling assumptions for the fluid and solid components in this chapter are similar to that of Chapter 2 (detailed in Section 2.2), except that the liver tissue is now treated as a hyperelastic material. We also consider a 3D model of flow and deformation in the liver lobule rather than the 2D approximation studied in Chapter 2.

3.3 Equations Governing Fluid Flow

Similarly, the equations governing blood and interstitial fluid flow in the sinusoids and interstitial space, respectively, are the same as those detailed in Sections 2.3.1 and 2.3.2 for the

undeformed liver lobule and the deformed liver lobule, respectively. The porosity of the liver tissue and permeabilities of the individual pore networks continue to be dependent on the tissue deformation, as in Sections 2.5.1 and 2.5.2, respectively, but without the small strain approximation theory. The resultant equations are summarised below.

3.3.1 Blood and Interstitial Fluid Volumes

Recall the small control volume section of the liver $\mathcal{V}$ consisting of tissue, blood and interstitial fluid with volumes $\mathcal{V}_{\text{tissue}}$, $\mathcal{V}_{\text{blood}}$, and $\mathcal{V}_{\text{ifluid}}$, respectively, chosen such that $\mathcal{V} = \mathcal{V}_{\text{tissue}} + \mathcal{V}_{\text{blood}} + \mathcal{V}_{\text{ifluid}}$ (2.21). The control volume $\mathcal{V}$ is also related to the undeformed control volume $\mathcal{V}_{\text{ref}}$ by $\mathcal{V} = J\mathcal{V}_{\text{ref}}$ (2.22), where J is the determinant of the deformation gradient tensor $\mathbf{F}$. The volumes of blood and interstitial fluid in $\mathcal{V}$, respectively, have been defined in Equation (2.23), and can be written in terms of J as:

$$\mathcal{V}_{\text{blood}} = \mathcal{V}_{\text{blood,ref}} + \beta_s(\mathcal{V} - \mathcal{V}_{\text{ref}}) = \mathcal{V}_{\text{blood,ref}} + \beta_s(J\mathcal{V}_{\text{ref}} - \mathcal{V}_{\text{ref}}) = \mathcal{V}_{\text{blood,ref}} + \beta_s(J-1)\mathcal{V}_{\text{ref}} \quad (3.1)$$

and

$$\mathcal{V}_{\text{ifluid}} = \mathcal{V}_{\text{ifluid,ref}} + \beta_i(\mathcal{V} - \mathcal{V}_{\text{ref}}) = \mathcal{V}_{\text{ifluid,ref}} + \beta_i(J\mathcal{V}_{\text{ref}} - \mathcal{V}_{\text{ref}}) = \mathcal{V}_{\text{ifluid,ref}} + \beta_i(J-1)\mathcal{V}_{\text{ref}}, \quad (3.2)$$

where β_s and β_i are coefficients of the sinusoidal and interstitial spaces, respectively, defined in Equation (2.24).

3.3.2 Tissue Porosity

Following Section 2.5.1, the total porosity of the liver φ_L is defined as the total pore volume divided by the total volume of the liver. The total pore volume is the sum of blood and interstitial fluid volumes, which according to (2.21), $\mathcal{V}_{\text{blood}} + \mathcal{V}_{\text{ifluid}} = \mathcal{V} - \mathcal{V}_{\text{tissue}}$. Hence,

$$\varphi_L = \frac{\mathcal{V} - \mathcal{V}_{\text{tissue}}}{\mathcal{V}} = \frac{J\mathcal{V}_{\text{ref}} - \mathcal{V}_{\text{tissue}}}{J\mathcal{V}_{\text{ref}}} = \frac{J - \frac{\mathcal{V}_{\text{tissue}}}{\mathcal{V}_{\text{ref}}}}{J} = \frac{J - (1 - \varphi_{L,\text{ref}})}{J} = \frac{(J-1) + \varphi_{L,\text{ref}}}{J}, \quad (3.3)$$

where $\varphi_{L,\text{ref}}$ is the porosity of the liver in the undeformed case, and we have made use of the assumption that the volume of the tissue remains constant with deformation.

The individual porosities of the sinusoidal and interstitial spaces, respectively, are given by

$$\varphi_s = \frac{\mathcal{V}_{\text{blood}}}{\mathcal{V}} = \frac{\mathcal{V}_{\text{blood,ref}} + \beta_s(J-1)\mathcal{V}_{\text{ref}}}{J\mathcal{V}_{\text{ref}}} = \frac{\varphi_{s,\text{ref}} + \beta_s(J-1)}{J} \quad (3.4)$$

and

$$\varphi_i = \frac{\mathcal{V}_{\text{ifluid}}}{\mathcal{V}} = \frac{\mathcal{V}_{\text{ifluid,ref}} + \beta_i(J-1)\mathcal{V}_{\text{ref}}}{J\mathcal{V}_{\text{ref}}} = \frac{\varphi_{i,\text{ref}} + \beta_i(J-1)}{J}, \quad (3.5)$$

using Equations (3.1) and (3.2), where $\varphi_{s,\text{ref}}$ and $\varphi_{i,\text{ref}}$ are the porosities of the sinusoids and interstitial space in the undeformed case, respectively.

3.3.3 Tissue Hydraulic Conductivity

To obtain the hydraulic conductivities of the individual pore networks, we follow a similar derivation to that of Section 2.5.2. For the sinusoids, we begin with Equation (2.32), in which we defined the ratio of the permeabilities of the deformed sinusoidal space, κ_s, to the undeformed sinusoidal space, $\kappa_{s,\text{ref}}$, as

$$\frac{\kappa_s}{\kappa_{s,\text{ref}}} = \frac{\lambda^2}{J}\left(\frac{\mathcal{V}_{\text{blood}}}{\mathcal{V}_{\text{blood,ref}}}\right)^2, \tag{3.6}$$

where λ is the stretch of the domain defined in Section 2.5.2. Using Equations (3.1) and (3.4),

$$\frac{\kappa_s}{\kappa_{s,\text{ref}}} = \frac{\lambda^2}{J}\left(\frac{\mathcal{V}_{\text{blood}}}{\mathcal{V}_{\text{blood,ref}}}\right)^2 = \frac{\lambda^2}{J}\left(\frac{(\varphi_{s,\text{ref}} + \beta_s(J-1))\mathcal{V}_{\text{ref}}}{\varphi_{s,\text{ref}}\mathcal{V}_{\text{ref}}}\right)^2 = \frac{\lambda^2}{J}\left(1 + \frac{\beta_s(J-1)}{\varphi_{s,\text{ref}}}\right)^2. \tag{3.7}$$

Next, and only for the 3D hyperelastic model, we will assume that the liver tissue is isotropic and so deforms uniformly in the three principal directions, i.e. $J = \lambda^3$. Therefore,

$$\frac{\kappa_s}{\kappa_{s,\text{ref}}} = \frac{1}{J^{1/3}}\left(1 + \frac{\beta_s(J-1)}{\varphi_{s,\text{ref}}}\right)^2. \tag{3.8}$$

A similar derivation for the interstitial space gives us

$$\frac{\kappa_i}{\kappa_{i,\text{ref}}} = \frac{1}{J^{1/3}}\left(1 + \frac{\beta_i(J-1)}{\varphi_{i,\text{ref}}}\right)^2, \tag{3.9}$$

where κ_i and $\kappa_{i,\text{ref}}$ are the permeabilities of the deformed interstitial space and the undeformed interstitial space, respectively.

Using the same isotropy assumption for fluid flow in the liver tissue, we have the net permeabilities of the sinusoidal and interstitial spaces, respectively, in the deformed liver as

$$\boldsymbol{\kappa}_s = \kappa_s \mathbf{I} \quad \& \quad \boldsymbol{\kappa}_i = \kappa_i \mathbf{I}, \tag{3.10}$$

where $\mathbf{I}$ is the identity matrix, and we can define the individual hydraulic conductivities as

$$\mathbf{K}_s = \frac{\boldsymbol{\kappa}_s}{\mu_s} \quad \& \quad \mathbf{K}_i = \frac{\boldsymbol{\kappa}_i}{\mu_i}, \tag{3.11}$$

respectively, where μ_s and μ_i are the effective dynamic viscosities of blood and interstitial fluid, respectively.

This assumption also holds in the undeformed liver, where the permeabilities of the sinu-

soidal and interstitial spaces, respectively, are given by

$$\boldsymbol{\kappa}_{s,\mathrm{ref}} = \kappa_{s,\mathrm{ref}}\mathbf{I} \quad \& \quad \boldsymbol{\kappa}_{i,\mathrm{ref}} = \kappa_{i,\mathrm{ref}}\mathbf{I} \tag{3.12}$$

and the hydraulic conductivities, respectively, given by

$$\mathbf{K}_{s,\mathrm{ref}} = \frac{\boldsymbol{\kappa}_{s,\mathrm{ref}}}{\mu_s} \quad \& \quad \mathbf{K}_{i,\mathrm{ref}} = \frac{\boldsymbol{\kappa}_{i,\mathrm{ref}}}{\mu_i}, \tag{3.13}$$

where $\kappa_{s,\mathrm{ref}}$ and $\kappa_{i,\mathrm{ref}}$ are constants.

3.4 Equations Governing Tissue Deformation

In this section, we present the equations governing tissue deformation for the hyperelastic liver lobule. As in the linear poroelastic model, we assume that deformation of the liver lobule occurs to accommodate changes in fluid volume as a result of blood and interstitial fluid mechanical pressure increase. Also, we continue to work in terms of fluid pressures referenced against their values in the normal physiological case (i.e. the undeformed liver).

3.4.1 Stress–Strain Relationship

Following Chapter 2, we make use of a modified version of the Cauchy stress tensor $\tilde{\boldsymbol{\sigma}}$ to define the relationship between stress within the hyperelastic tissue and referenced fluid pressure change:

$$\tilde{\boldsymbol{\sigma}} = \boldsymbol{\sigma}_e - [(p_s - p_{s,\mathrm{ref}}) + (p_i - p_{i,\mathrm{ref}})]\mathbf{I}, \tag{3.14}$$

where, in this case, $\boldsymbol{\sigma}_e$ is the hyperelastic Cauchy stress tensor, which defines the non-linear stress–strain behaviour of the tissue, p_s and p_i are blood and interstitial pressures in the deformed lobule, respectively, $p_{s,\mathrm{ref}}$ and $p_{i,\mathrm{ref}}$ are blood and interstitial pressures in the reference undeformed lobule, respectively, and $\mathbf{I}$ is the identity matrix.

As shown in Section 1.4.2.5, the Cauchy stress tensor of a hyperelastic material is given by Equation (1.31):

$$\boldsymbol{\sigma}_e = \frac{2}{J}\mathbf{B}\frac{\partial W}{\partial \mathbf{B}}, \tag{3.15}$$

where $\mathbf{B} = \mathbf{F}\mathbf{F}^{\mathrm{T}}$ is the left Cauchy–Green tensor, with $\mathbf{F}$ being the deformation gradient tensor, $J = \det(\mathbf{F})$ and W is the strain energy function, which represents the elastic behaviour of the solid tissue. The strain energy function W of a compressible hyperelastic material can be decomposed into two components; the volumetric part W_{vol} and the isochoric part W_{iso}. That is to say $W = W_{\mathrm{vol}} + W_{\mathrm{iso}} = W_{\mathrm{vol}}(J) + W_{\mathrm{iso}}(I_1, I_2)$, where J is defined above, and I_1 & I_2 are the first and second invariants of $\mathbf{B}$, respectively (see Section 1.4.2.4). Equation (3.15) can be

simplified into

$$\boldsymbol{\sigma}_e = \frac{2}{J}\left\{\left(\frac{\partial W_{\text{iso}}}{\partial I_1} + I_1\frac{\partial W_{\text{iso}}}{\partial I_2}\right)\mathbf{B} - \frac{\partial W_{\text{iso}}}{\partial I_2}\mathbf{B}^2\right\} + \frac{\partial W_{\text{vol}}}{\partial J}\mathbf{I}. \tag{3.16}$$

The derivation of Equation (3.16) has been shown in Section 1.4.2.5.

Neglecting inertia of the tissue, we have the equation governing tissue deformation as the divergence of the modified Cauchy stress tensor being equal to zero:

$$\boldsymbol{\nabla} \cdot \tilde{\boldsymbol{\sigma}} = 0. \tag{3.17}$$

In the next section, we define a set of suitable functions for W_{vol} and W_{iso} to obtain the strain energy function W.

3.4.2 Choice of Strain Energy Function

3.4.2.1 Isochoric Elastic Response

The isochoric elastic response $W_{\text{iso}}(I_1, I_2)$ accounts for the shear deformation behaviour of a hyperelastic material under uniaxial stress. For the liver tissue, this can be estimated from mechanical studies of the effect of combined compression and elongation testing on the liver tissue by Chui et al. (2004). The data obtained were fitted against different strain energy functions including polynomial, exponential, logarithmic and power law stress–strain model. The best fit to the data was found to be the 9-constant Mooney–Rivlin polynomial function. However, the second best fit, which was a combined polynomial and logarithmic function, was thought to be more numerically efficient in finite element computations (Chui et al., 2004). The data obtained by Chui et al. (2004) was subsequently fitted to a 5-constant Mooney–Rivlin polynomial function by Fu and Chui (2014), as an extension of the studies by Chui et al. (2004). Hence, we chose the 5-constant Mooney–Rivlin polynomial function to represent the isochoric elastic response of the liver tissue in our model. This is given by

$$W_{\text{iso}}(I_1, I_2) = c_1(I_1 - 3) + c_2(I_2 - 3) + c_3(I_1 - 3)^2 + c_4(I_1 - 3)(I_2 - 3) + c_5(I_2 - 3)^2, \tag{3.18}$$

where c_1, c_2, c_3, c_4 and c_5 are material constants in Fu and Chui (2014).

3.4.2.2 Volumetric Elastic Response

The volumetric elastic response $W_{\text{vol}}(J)$ accounts for the elastic behaviour of the tissue under bulk stress. Unlike, the isochoric response, no experimental data could be found in the literature that captures the volumetric elastic response of the liver tissue. For this reason, and as a first approximation, we make use of a quadratic function to define $W_{\text{vol}}(J)$, which is the most

popular option used to represent hyperelastic biological materials that are nearly incompressible (Holzapfel and Ogden, 2009). This is written as

$$W_{\text{vol}}(J) = \frac{E_{\text{bulk}}}{2}(J-1)^2, \tag{3.19}$$

where E_{bulk} is the bulk modulus of the liver tissue.

3.4.2.3 Strain Energy Function

Thus, the strain energy function of our model is given by

$$\begin{aligned} W =& W_{\text{iso}}(I_1, I_2) + W_{\text{vol}}(J) \\ =& c_1(I_1-3) + c_2(I_2-3) + c_3(I_1-3)^2 + c_4(I_1-3)(I_2-3) + c_5(I_2-3)^2 \\ &+ \frac{E_{\text{bulk}}}{2}(J-1)^2. \end{aligned} \tag{3.20}$$

Using this form of strain energy function (3.20), we find that

$$\frac{\partial W}{\partial J} = \frac{\partial W_{\text{vol}}}{\partial J} = E_{\text{bulk}}(J-1) \tag{3.21}$$

$$\frac{\partial W}{\partial I_1} = \frac{\partial W_{\text{iso}}}{\partial I_1} = c_1 + 2c_3(I_1-3) + c_4(I_2-3) \tag{3.22}$$

$$\frac{\partial W}{\partial I_2} = \frac{\partial W_{\text{iso}}}{\partial I_2} = c_2 + c_4(I_1-3) + 2c_5(I_2-3). \tag{3.23}$$

Therefore, the elastic Cauchy stress tensor, defined by (3.16), becomes

$$\begin{aligned} \boldsymbol{\sigma}_e =& \frac{2}{J}\left\{ \left(\frac{\partial W_{\text{iso}}}{\partial I_1} + I_1 \frac{\partial W_{\text{iso}}}{\partial I_2} \right) \mathbf{B} - \frac{\partial W_{\text{iso}}}{\partial I_2}\mathbf{B}^2 \right\} + \frac{\partial W_{\text{vol}}}{\partial J}\mathbf{I} \\ =& \frac{2}{J}\Big\{ \left[c_1 + 2c_3(I_1-3) + c_4(I_2-3) + I_1(c_2 + c_4(I_1-3) + 2c_5(I_2-3)) \right] \mathbf{B} \\ & - \left[c_2 + c_4(I_1-3) + 2c_5(I_2-3) \right] \mathbf{B}^2 \Big\} \\ & + [E_{\text{bulk}}(J-1)]\mathbf{I}, \end{aligned} \tag{3.24}$$

while the modified Cauchy stress tensor, given by (3.14), becomes

$$\begin{aligned} \tilde{\boldsymbol{\sigma}} =& \boldsymbol{\sigma}_e - [(p_s - p_{s,\text{ref}}) + (p_i - p_{i,\text{ref}})]\mathbf{I} \\ =& \frac{2}{J}\Big\{ \left[c_1 + 2c_3(I_1-3) + c_4(I_2-3) + I_1(c_2 + c_4(I_1-3) + 2c_5(I_2-3)) \right] \mathbf{B} \\ & - \left[c_2 + c_4(I_1-3) + 2c_5(I_2-3) \right] \mathbf{B}^2 \Big\} \\ & + [E_{\text{bulk}}(J-1)]\mathbf{I} - [(p_s - p_{s,\text{ref}}) + (p_i - p_{i,\text{ref}})]\mathbf{I}. \end{aligned} \tag{3.25}$$

3.5 Summary of Governing Equations

The governing equations of the system are summarised below:

$$\boldsymbol{\nabla} \cdot \tilde{\boldsymbol{\sigma}} = \mathbf{0}, \tag{3.26}$$

$$\boldsymbol{\nabla} \cdot (-\mathbf{K}_s \boldsymbol{\nabla} p_s) + C_f(p_s - p_i) = 0, \tag{3.27}$$

$$\boldsymbol{\nabla} \cdot (-\mathbf{K}_i \boldsymbol{\nabla} p_i) - C_f(p_s - p_i) + C_l \max(p_i - p_0, 0) = 0, \tag{3.28}$$

$$\boldsymbol{\nabla} \cdot (-\mathbf{K}_{s,\text{ref}} \boldsymbol{\nabla} p_{s,\text{ref}}) + C_f(p_{s,\text{ref}} - p_{i,\text{ref}}) = 0, \tag{3.29}$$

$$\boldsymbol{\nabla} \cdot (-\mathbf{K}_{i,\text{ref}} \boldsymbol{\nabla} p_{i,\text{ref}}) - C_f(p_{s,\text{ref}} - p_{i,\text{ref}}) + C_l \max(p_{i,\text{ref}} - p_0, 0) = 0, \tag{3.30}$$

where $\tilde{\boldsymbol{\sigma}}$ is defined by Equation (3.25), $\mathbf{K}_s$ & $\mathbf{K}_i$ are defined in Equation (3.13), $\mathbf{K}_{s,\text{ref}}$ & $\mathbf{K}_{i,\text{ref}}$ are defined in Equation (3.11), and C_f, C_l and p_0 are constants defined in Section 2.3.1.

In the case of the deformed liver lobule, the constitutive equations for stress (3.26) and fluid flow (3.27)–(3.28) are solved on the deformed domain $\mathcal{D}$ with boundary $\partial\mathcal{D}$ (Section 1.4.2.1; Figure 1.16). For the undeformed liver lobule, the constitutive equations for fluid flow (3.29)–(3.30) are solved on the reference domain $\mathcal{D}_0$ with boundary $\partial\mathcal{D}_0$ (Section 1.4.2.1; Figure 1.16). We continue to assume that the undeformed case of the liver is under a zero stress reference state.

In the next section, we derive the weak formulation of the system of coupled PDE equations above. This is done in order to solve them numerically using the *Weak Form PDE* interface on COMSOL Multiphysics. Note, however, that since we will be considering large deformations of the liver tissue, we must also take into consideration geometric nonlinearities. These were neglected in Chapter 2 as we were working under the assumption of small strain theory.

In order to consider large deformations, we must make a clear distinction between the spatial coordinates and the material coordinates of the geometry, as defined in Section 1.4.2.1. In COMSOL Multiphysics, geometric nonlinearities can be incorporated into the numerical solutions by either integrating the Cauchy stress tensor over the deformed boundary, or integrating the 1st Piola–Kirchhoff stress tensor, a different stress measure, over the same boundary in the undeformed configuration (Sönnerlind, 2013). For simplicity, we chose to do the latter. For this reason, we perform a change of reference frame for the weak form of Equations (3.26)–(3.28) from $\mathcal{D}$ to $\mathcal{D}_0$, so as to solve them on the same domain as Equations (3.29)–(3.30). This is shown in Section 3.5.2.

3.5.1 Weak Formulation of Governing Equations

Let $\mathbf{w}$ be any regular test function of the modified Cauchy stress tensor $\tilde{\boldsymbol{\sigma}}$; that is, $\mathbf{w} \in \mathbb{W}$, and where $\mathbb{W}$ is defined as the space of all rank-1 tensor functions whose derivatives are square integrable and that vanish on $\partial\mathcal{D}$. In order to construct the weak form of the constitutive equation for stress, we multiply Equation (3.26) by $\mathbf{w}$ and integrate over the domain $\mathcal{D}$ to get

$$\int_{\mathcal{D}} (\boldsymbol{\nabla} \cdot \tilde{\boldsymbol{\sigma}}) \cdot \mathbf{w} \, \mathrm{d}V = 0, \tag{3.31}$$

for all $\mathbf{w} \in \mathbb{W}$. Applying the divergence theorem to the LHS of Equation (3.31), we obtain

$$\int_{\mathcal{D}} \tilde{\boldsymbol{\sigma}} : \boldsymbol{\nabla}\mathbf{w} \, \mathrm{d}V - \int_{\partial\mathcal{D}} \mathbf{t} \cdot \mathbf{w} \, \mathrm{d}A = 0, \tag{3.32}$$

where $\mathbf{t} = \tilde{\boldsymbol{\sigma}}\mathbf{n}$. Note that $\tilde{\boldsymbol{\sigma}}$ is symmetric, so the double dot product is unambiguous. Also, $\mathrm{d}V$ and $\mathrm{d}A$ are the infinitesimal volume and area of the deformed lobule, respectively, in the domain $\mathcal{D}$.

The same can be done for the governing equations of fluid flow in the deformed and undeformed lobules, Equations (3.27)–(3.30), to obtain:

$$\int_{\mathcal{D}} (\mathbf{K}_s \boldsymbol{\nabla} p_s) \cdot \boldsymbol{\nabla} \check{p}_s \, \mathrm{d}V - \int_{\partial\mathcal{D}} \check{p}_s \, (\mathbf{K}_s \boldsymbol{\nabla} p_s) \cdot \mathbf{n} \, \mathrm{d}A = -\int_{\mathcal{D}} C_f (p_s - p_i) \check{p}_s \, \mathrm{d}V, \tag{3.33}$$

$$\int_{\mathcal{D}} (\mathbf{K}_i \boldsymbol{\nabla} p_i) \cdot \boldsymbol{\nabla} \check{p}_i \, \mathrm{d}V - \int_{\partial\mathcal{D}} \check{p}_i \, (\mathbf{K}_i \boldsymbol{\nabla} p_i) \cdot \mathbf{n} \, \mathrm{d}A = \int_{\mathcal{D}} C_f (p_s - p_i) \check{p}_i \, \mathrm{d}V - \int_{\mathcal{D}} C_l \max(p_i - p_0, 0) \check{p}_i \, \mathrm{d}V, \tag{3.34}$$

$$\int_{\mathcal{D}_0} \left(\mathbf{K}_{s,\mathrm{ref}} \overline{\boldsymbol{\nabla}} p_{s,\mathrm{ref}}\right) \cdot \overline{\boldsymbol{\nabla}} \check{p}_{s,\mathrm{ref}} \, \mathrm{d}V_0 - \int_{\partial\mathcal{D}_0} \check{p}_{s,\mathrm{ref}} \left(\mathbf{K}_{s,\mathrm{ref}} \overline{\boldsymbol{\nabla}} p_{s,\mathrm{ref}}\right) \cdot \mathbf{n}_0 \, \mathrm{d}A_0 = -\int_{\mathcal{D}_0} C_f (p_{s,\mathrm{ref}} - p_{i,\mathrm{ref}}) \check{p}_{s,\mathrm{ref}} \, \mathrm{d}V_0 \tag{3.35}$$

and

$$\int_{\mathcal{D}_0} \left(\mathbf{K}_{i,\mathrm{ref}} \overline{\boldsymbol{\nabla}} p_{i,\mathrm{ref}}\right) \cdot \overline{\boldsymbol{\nabla}} \check{p}_{i,\mathrm{ref}} \, \mathrm{d}V_0 - \int_{\partial\mathcal{D}_0} \check{p}_{i,\mathrm{ref}} \left(\mathbf{K}_{i,\mathrm{ref}} \overline{\boldsymbol{\nabla}} p_{i,\mathrm{ref}}\right) \cdot \mathbf{n}_0 \, \mathrm{d}A_0 = \int_{\mathcal{D}_0} C_f (p_{s,\mathrm{ref}} - p_{i,\mathrm{ref}}) \check{p}_{i,\mathrm{ref}} \, \mathrm{d}V_0 - \int_{\mathcal{D}_0} C_l \max(p_{i,\mathrm{ref}} - p_0, 0) \check{p}_{i,\mathrm{ref}} \, \mathrm{d}V_0, \tag{3.36}$$

with $\check{p}_s$ and $\check{p}_i$ as test functions of p_s and p_i, respectively, $\check{p}_{s,\mathrm{ref}}$ and $\check{p}_{i,\mathrm{ref}}$ as test functions of $p_{s,\mathrm{ref}}$ and $p_{i,\mathrm{ref}}$, respectively, and where $\mathrm{d}V_0$ and $\mathrm{d}A_0$ are the infinitesimal volume and area of the undeformed lobule, respectively, in the domain $\mathcal{D}_0$, and $\boldsymbol{\nabla}$ and $\overline{\boldsymbol{\nabla}}$ are the gradient tensors

in $\mathcal{D}$ and $\mathcal{D}_0$, respectively. Also, $\check{p}_s$ and $\check{p}_i \in \mathbb{X}$, while $\check{p}_{s,\text{ref}}$ and $\check{p}_{i,\text{ref}} \in \mathbb{X}_0$, where $\mathbb{X}$ and $\mathbb{X}_0$ are the spaces of all scalar functions whose derivatives exist, are square integrable and that vanish on $\partial\mathcal{D}$ and $\partial\mathcal{D}_0$, respectively.

3.5.2 Change of Reference Frame: Balance Principle for a Cauchy Continuum

In the general case of an elastic solid, the force balance equation is given by

$$\boldsymbol{\nabla} \cdot \mathbf{T} + \mathbf{b} = \mathbf{0}, \tag{3.37}$$

where $\mathbf{T}$ is the Cauchy stress tensor field, $\mathbf{b}$ is the force per unit volume and $\boldsymbol{\nabla}$ is the gradient tensor, all defined in the domain $\mathcal{D}$. In order to make a change of reference frame, we make use of the balance principle for a Cauchy continuum (see e.g. Tadmor et al., 2012), which states that at any time and for any regular test velocity field $\mathbf{w}$,

$$\int_{\mathcal{D}} \mathbf{b} \cdot \mathbf{w} \, \mathrm{d}V + \int_{\partial\mathcal{D}} \mathbf{t} \cdot \mathbf{w} \, \mathrm{d}A - \int_{\mathcal{D}} \mathbf{T} : \boldsymbol{\nabla}\mathbf{w} \, \mathrm{d}V = 0 \tag{3.38}$$

where $\mathbf{t} = \mathbf{T}\mathbf{n}$ is the surface force distribution on the boundary $\partial\mathcal{D}$, with unit normal vector $\mathbf{n}$ also defined on $\partial\mathcal{D}$. The principle can be conveniently restated by pulling back all fields from the current shape $\mathcal{D}$ to a fixed reference shape $\mathcal{D}_0$, thus requiring that for any test velocity $\mathbf{w}_0$ in the reference shape $\mathcal{D}_0$,

$$\int_{\mathcal{D}_0} \mathbf{b}_0 \cdot \mathbf{w}_0 \, \mathrm{d}V_0 + \int_{\partial\mathcal{D}_0} \mathbf{s_0} \cdot \mathbf{w}_0 \, \mathrm{d}A_0 - \int_{\mathcal{D}_0} \mathbf{S}_0 : \overline{\boldsymbol{\nabla}}\mathbf{w}_0 \, \mathrm{d}V_0 = 0, \tag{3.39}$$

where $\mathbf{S}_0 = J\mathbf{T}\mathbf{F}^{-\mathrm{T}}$ denotes the 1st Piola–Kirchhoff tensor, $\mathbf{s}_0 = \mathbf{S}_0\mathbf{n}_0$, with $\mathbf{n}_0$ being the unit normal vector to $\partial\mathcal{D}_0$, $\mathbf{b}_0 = J\mathbf{b}$ and $\overline{\boldsymbol{\nabla}}$ is the gradient tensor in $\mathcal{D}_0$. The proof of the pull back operation for the principle is shown below.

Proof: Change of Reference Frame for Weak Form of Solid Deformation Equation

In order to prove the pull back operation of the balance principle for a Cauchy continuum, we look at each of the terms in Equation (3.38) individually, starting with the first term.

$$\int_{\mathcal{D}} \mathbf{b} \cdot \mathbf{w} \, \mathrm{d}V. \tag{3.40}$$

Using the fact that $\mathrm{d}V = J\mathrm{d}V_0$, where $J = \det(\mathbf{F})$, and choosing $\mathbf{w}_0$ to be a test function

in $\mathcal{D}_0$, defined by $\mathbf{w}_0(\mathbf{x}_0) = \mathbf{w}(\mathbf{x})$ where $\mathbf{x} \mapsto \mathbf{x}_0$ is the pull back operation, we have

$$\int_{\mathcal{D}} \mathbf{b} \cdot \mathbf{w} \, \mathrm{d}V = \int_{\mathcal{D}_0} \mathbf{b} \cdot \mathbf{w}_0 \, J\mathrm{d}V_0 = \int_{\mathcal{D}_0} (J\mathbf{b}) \cdot \mathbf{w}_0 \, \mathrm{d}V_0 = \int_{\mathcal{D}_0} \mathbf{b}_0 \cdot \mathbf{w}_0 \, \mathrm{d}V_0, \tag{3.41}$$

where $\mathbf{b}_0 = J\mathbf{b} = \det(\mathbf{F})\mathbf{b}$.

For the second term in (3.38), we have

$$\int_{\partial\mathcal{D}} \mathbf{t} \cdot \mathbf{w} \, \mathrm{d}A = \int_{\partial\mathcal{D}} \mathbf{w} \cdot \mathbf{t} \, \mathrm{d}A = \int_{\partial\mathcal{D}} \mathbf{w} \cdot (\mathbf{T}\mathbf{n}) \, \mathrm{d}A, \tag{3.42}$$

where $\mathbf{n}$ is the unit normal vector in $\mathcal{D}$. Using Nanson's formula, $\mathbf{n} \, \mathrm{d}A = J\mathbf{F}^{-\mathrm{T}}\mathbf{n}_0 \, \mathrm{d}A_0$,

$$\begin{aligned}
\int_{\partial\mathcal{D}} \mathbf{w} \cdot (\mathbf{T}\mathbf{n}) \, \mathrm{d}A &= \int_{\partial\mathcal{D}_0} \mathbf{w}_0 \cdot (\mathbf{T}J\mathbf{F}^{-\mathrm{T}}\mathbf{n}_0) \, \mathrm{d}A_0 \\
&= \int_{\partial\mathcal{D}_0} \mathbf{w}_0 \cdot (J\mathbf{T}\mathbf{F}^{-\mathrm{T}}\mathbf{n}_0) \, \mathrm{d}A_0 \\
&= \int_{\partial\mathcal{D}_0} \mathbf{w}_0 \cdot (\mathbf{S}_0\mathbf{n}_0) \, \mathrm{d}A_0 \\
&= \int_{\partial\mathcal{D}_0} \mathbf{w}_0 \cdot \mathbf{s}_0 \, \mathrm{d}A_0,
\end{aligned} \tag{3.43}$$

where $\mathbf{S}_0 = J\mathbf{T}\mathbf{F}^{-\mathrm{T}} = \det(\mathbf{F})\mathbf{T}\mathbf{F}^{-\mathrm{T}}$ is the 1st Piola–Kirchoff tensor and $\mathbf{s}_0 = \mathbf{S}_0\mathbf{n}_0$.

Finally, for the last term in (3.38),

$$\begin{aligned}
\int_{\mathcal{D}} \mathbf{T} : \boldsymbol{\nabla}\mathbf{w} \, \mathrm{d}V &= \int_{\mathcal{D}} \mathrm{tr}\left[\mathbf{T}(\boldsymbol{\nabla}\mathbf{w})^{\mathrm{T}}\right] \, \mathrm{d}V \\
&= \int_{\mathcal{D}_0} \mathrm{tr}\left[\mathbf{T}(\boldsymbol{\nabla}\mathbf{w}_0)^{\mathrm{T}}\right] J \, \mathrm{d}V_0 \\
&= \int_{\mathcal{D}_0} \mathrm{tr}\left[\mathbf{T}(\overline{\boldsymbol{\nabla}}\mathbf{w}_0\mathbf{F}^{-1})^{\mathrm{T}}\right] J \, \mathrm{d}V_0 \\
&= \int_{\mathcal{D}_0} \mathrm{tr}\left[\mathbf{T}(\mathbf{F}^{-\mathrm{T}}\overline{\boldsymbol{\nabla}}\mathbf{w}_0^{\mathrm{T}})\right] J \, \mathrm{d}V_0 \\
&= \int_{\mathcal{D}_0} \mathrm{tr}\left[(\mathbf{T}\mathbf{F}^{-\mathrm{T}})(\overline{\boldsymbol{\nabla}}\mathbf{w}_0)^{\mathrm{T}}\right] J \, \mathrm{d}V_0 \\
&= \int_{\mathcal{D}_0} J\mathbf{T}\mathbf{F}^{-\mathrm{T}} : \overline{\boldsymbol{\nabla}}\mathbf{w}_0 \, \mathrm{d}V_0 \\
&= \int_{\mathcal{D}_0} \mathbf{S}_0 : \overline{\boldsymbol{\nabla}}\mathbf{w}_0 \, \mathrm{d}V_0,
\end{aligned} \tag{3.44}$$

where, again, $\mathbf{S}_0 = J\mathbf{T}\mathbf{F}^{-\mathrm{T}}$ is the 1st Piola–Kirchoff tensor and $\boldsymbol{\nabla}(\cdot) = \overline{\boldsymbol{\nabla}}(\cdot)\mathbf{F}^{-1}$ is the transformation of the gradient tensor on a vector from the current shape $\mathcal{D}$ to the fixed reference shape $\mathcal{D}_0$.

In our case, we have made use of the modified Cauchy stress tensor $\tilde{\boldsymbol{\sigma}}$ in our model, instead of the usual Cauchy stress tensor $\mathbf{T}$. Recall that the force balance equation is given by $\boldsymbol{\nabla}\cdot\tilde{\boldsymbol{\sigma}} = \mathbf{0}$ (3.26). Using the definition of $\tilde{\boldsymbol{\sigma}}$ from Equation (3.14),

$$\begin{aligned}\boldsymbol{\nabla}\cdot\tilde{\boldsymbol{\sigma}} &= \boldsymbol{\nabla}\cdot(\boldsymbol{\sigma}_e - [(p_s - p_{s,\text{ref}}) + (p_i - p_{i,\text{ref}})]\mathbf{I}) \\ &= \boldsymbol{\nabla}\cdot\boldsymbol{\sigma}_e - \boldsymbol{\nabla}[(p_s - p_{s,\text{ref}}) + (p_i - p_{i,\text{ref}})] \\ &= \boldsymbol{\nabla}\cdot\boldsymbol{\sigma}_e + \mathbf{b}_f\end{aligned} \tag{3.45}$$

where $\mathbf{b}_f = -\boldsymbol{\nabla}[(p_s - p_{s,\text{ref}}) + (p_i - p_{i,\text{ref}})]$. Assuming we neglect other body forces such as gravity, we can use the Cauchy balance principle on Equation (3.45) and change the reference frame from $\mathcal{D}$ to $\mathcal{D}_0$ to obtain

$$\int_{\mathcal{D}_0} \mathbf{b}_{f,0}\cdot\mathbf{w}_{e,0}\,\mathrm{d}V_0 + \int_{\partial\mathcal{D}_0} \mathbf{s}_{\boldsymbol{e,0}}\cdot\mathbf{w}_{e,0}\,\mathrm{d}A_0 - \int_{\mathcal{D}_0} \mathbf{S}_{e,0} : \overline{\boldsymbol{\nabla}}\mathbf{w}_{e,0}\,\mathrm{d}V_0 = 0, \tag{3.46}$$

where $\mathbf{b}_{f,0} = J\mathbf{b}_f$, $\mathbf{S}_{e,0} = J\boldsymbol{\sigma}_e\mathbf{F}^{-\mathrm{T}}$, $\mathbf{s}_{\boldsymbol{e,0}} = \mathbf{S}_{e,0}\mathbf{n}_0$ and $\mathbf{w}_{e,0}$ is any test function of $\boldsymbol{\sigma}_e$ in $\mathcal{D}_0$. Alternatively, we can apply the Cauchy balance principle on Equation (3.26) to obtain a simpler equation in terms of $\tilde{\boldsymbol{\sigma}}$:

$$\int_{\partial\mathcal{D}_0} \tilde{\mathbf{s}}_{\mathbf{0}}\cdot\tilde{\mathbf{w}}_0\,\mathrm{d}A_0 - \int_{\mathcal{D}_0} \tilde{\mathbf{S}}_0 : \overline{\boldsymbol{\nabla}}\tilde{\mathbf{w}}_0\,\mathrm{d}V_0 = 0. \tag{3.47}$$

where $\tilde{\mathbf{S}}_0 = J\tilde{\boldsymbol{\sigma}}\mathbf{F}^{-\mathrm{T}}$, $\tilde{\mathbf{s}}_{\mathbf{0}} = \tilde{\mathbf{S}}_0\mathbf{n}_0$ and $\tilde{\mathbf{w}}_0$ is any test function of $\tilde{\boldsymbol{\sigma}}$ in $\mathcal{D}_0$.

Based on Equation (3.25),

$$\tilde{\mathbf{S}}_0 = J\tilde{\boldsymbol{\sigma}}\mathbf{F}^{-\mathrm{T}} \tag{3.48}$$

$$\begin{aligned}=2\Big\{ &[c_1 + 2c_3(I_1-3) + c_4(I_2-3) + I_1(c_2 + c_4(I_1-3) + 2c_5(I_2-3))]\,\mathbf{F} \\ &- [c_2 + c_4(I_1-3) + 2c_5(I_2-3)]\,\mathbf{B}\mathbf{F}\Big\} \\ &+ J[E_{\text{bulk}}(J-1)]\mathbf{F}^{-\mathrm{T}} - J[(p_s - p_{s,\text{ref}}) + (p_i - p_{i,\text{ref}})]\mathbf{F}^{-\mathrm{T}},\end{aligned} \tag{3.49}$$

since $\mathbf{B} = \mathbf{F}\mathbf{F}^{\mathrm{T}}$.

Similarly, we can pull back the weak form of the fluid flow equations, (3.33) and (3.34), in the current shape $\mathcal{D}$ to obtain equations in the reference shape $\mathcal{D}_0$, respectively:

$$\int_{\mathcal{D}_0} \left(\mathbf{K}_{s,0}\overline{\boldsymbol{\nabla}}p_s\right)\cdot\overline{\boldsymbol{\nabla}}\hat{p}_s\,\mathrm{d}V_0 - \int_{\partial\mathcal{D}_0} \hat{p}_s\left(\mathbf{K}_{s,0}\overline{\boldsymbol{\nabla}}p_s\right)\cdot\mathbf{n}_0\,\mathrm{d}A_0 = -\int_{\mathcal{D}_0} C_{f,0}(p_s - p_i)\hat{p}_s\,\mathrm{d}V_0 \tag{3.50}$$

and

$$\int_{\mathcal{D}_0} \left(\mathbf{K}_{i,0}\overline{\boldsymbol{\nabla}} p_i\right) \cdot \overline{\boldsymbol{\nabla}}\hat{p}_i \, \mathrm{d}V_0 - \int_{\partial\mathcal{D}_0} \hat{p}_i \left(\mathbf{K}_{i,0}\overline{\boldsymbol{\nabla}} p_i\right) \cdot \mathbf{n}_0 \, \mathrm{d}A_0 = \int_{\mathcal{D}_0} C_{f,0}(p_s - p_i)\hat{p}_i \, \mathrm{d}V_0 - \int_{\mathcal{D}_0} C_{l,0} \max(p_i - p_0, 0)\hat{p}_i \, \mathrm{d}V_0, \quad (3.51)$$

where $\mathbf{K}_{s,0} = J\mathbf{F}^{-1}\mathbf{K}_s\mathbf{F}^{-\mathrm{T}}$, $\mathbf{K}_{i,0} = J\mathbf{F}^{-1}\mathbf{K}_i\mathbf{F}^{-\mathrm{T}}$, $C_{f,0} = JC_f$, $C_{l,0} = JC_l$, and $\hat{p}_s \in \mathcal{D}_0$ and $\hat{p}_i \in \mathcal{D}_0$ are test functions of p_s and p_i, respectively.

Equations (3.50) and (3.51) can also be written as

$$\int_{\mathcal{D}_0} -\overline{\mathbf{v}}_s \cdot \overline{\boldsymbol{\nabla}}\hat{p}_s \, \mathrm{d}V_0 + \int_{\partial\mathcal{D}_0} \hat{p}_s(\overline{\mathbf{v}}_s \cdot \mathbf{n}_0) \, \mathrm{d}A_0 = -\int_{\mathcal{D}_0} C_{f,0}(p_s - p_i)\hat{p}_s \, \mathrm{d}V_0 \quad (3.52)$$

and

$$\int_{\mathcal{D}_0} -\overline{\mathbf{v}}_i \cdot \overline{\boldsymbol{\nabla}}\hat{p}_i \, \mathrm{d}V_0 + \int_{\partial\mathcal{D}_0} \hat{p}_i(\overline{\mathbf{v}}_i \cdot \mathbf{n}_0) \, \mathrm{d}A_0 = \int_{\mathcal{D}_0} C_{f,0}(p_s - p_i)\hat{p}_i \, \mathrm{d}V_0 - \int_{\mathcal{D}_0} C_{l,0} \max(p_i - p_0, 0)\hat{p}_i \, \mathrm{d}V_0, \quad (3.53)$$

respectively, where $\overline{\mathbf{v}}_s = -\mathbf{K}_{s,0}\overline{\boldsymbol{\nabla}} p_s$ and $\overline{\mathbf{v}}_i = -\mathbf{K}_{i,0}\overline{\boldsymbol{\nabla}} p_i$, are Darcy velocities of blood and interstitial fluid in the deformed lobule, respectively. These can now be solved, together with the force balance equation (3.47) and the fluid flow equations in the undeformed lobule (3.35)–(3.36), on the same domain. The proof of the pull back operation on the weak form of the fluid flow equations is shown below.

Proof: Change of Reference Frame for Weak Form of Fluid Flow Equations

The equation for blood flow in the current shape $\mathcal{D}$ is given by

$$\int_{\mathcal{D}} (\mathbf{K}_s \boldsymbol{\nabla} p_s) \cdot \boldsymbol{\nabla}\check{p}_s \, \mathrm{d}V - \int_{\partial\mathcal{D}} \check{p}_s \left(\mathbf{K}_s \boldsymbol{\nabla} p_s\right) \cdot \mathbf{n} \, \mathrm{d}A = -\int_{\mathcal{D}} C_f(p_s - p_i)\check{p}_s \, \mathrm{d}V, \quad (3.54)$$

with $\check{p}_s$ as the regular test function of p_s. Next, we pull back the equation into a fixed reference shape $\mathcal{D}_0$ by considering each of the terms individually and choosing the test function $\hat{p}_s : \mathcal{D}_0 \mapsto \mathbb{R}$ such that $\hat{p}_s(\mathbf{x}_0) = \check{p}_s(\mathbf{x})$. Starting with the first term,

$$\begin{aligned}\int_{\mathcal{D}} (\mathbf{K}_s \boldsymbol{\nabla} p_s) \cdot \boldsymbol{\nabla}\check{p}_s \, \mathrm{d}V &= \int_{\mathcal{D}_0} \left(\mathbf{K}_s\mathbf{F}^{-\mathrm{T}}\overline{\boldsymbol{\nabla}} p_s\right) \cdot \left(\mathbf{F}^{-\mathrm{T}}\overline{\boldsymbol{\nabla}}\hat{p}_s\right) \, J\mathrm{d}V_0 \\ &= \int_{\mathcal{D}_0} \left(J\mathbf{F}^{-1}\mathbf{K}_s\mathbf{F}^{-\mathrm{T}}\overline{\boldsymbol{\nabla}} p_s\right) \cdot \overline{\boldsymbol{\nabla}}\hat{p}_s \, \mathrm{d}V_0 \\ &= \int_{\mathcal{D}_0} \left(\mathbf{K}_{s,0}\overline{\boldsymbol{\nabla}} p_s\right) \cdot \overline{\boldsymbol{\nabla}}\hat{p}_s \, \mathrm{d}V_0, \end{aligned} \quad (3.55)$$

where $\mathbf{K}_{s,0} = J\mathbf{F}^{-1}\mathbf{K}_s\mathbf{F}^{-\mathrm{T}}$ and using $\mathrm{d}V = J\ \mathrm{d}V_0$ and $\boldsymbol{\nabla}\phi = \mathbf{F}^{-\mathrm{T}}\overline{\boldsymbol{\nabla}}\phi$, where ϕ is a scalar. Secondly,

$$\begin{aligned}\int_{\partial\mathcal{D}} \check{p}_s \left(\mathbf{K}_s\boldsymbol{\nabla}p_s\right)\cdot\mathbf{n}\ \mathrm{d}A &= \int_{\partial\mathcal{D}_0} \hat{p}_s \left(\mathbf{K}_s\mathbf{F}^{-\mathrm{T}}\overline{\boldsymbol{\nabla}}p_s\right)\cdot\left(J\mathbf{F}^{-\mathrm{T}}\mathbf{n}_0\right)\ \mathrm{d}A_0\\ &= \int_{\partial\mathcal{D}_0} \hat{p}_s \left(J\mathbf{F}^{-1}\mathbf{K}_s\mathbf{F}^{-\mathrm{T}}\overline{\boldsymbol{\nabla}}p_s\right)\cdot\mathbf{n}_0\ \mathrm{d}A_0\\ &= \int_{\partial\mathcal{D}_0} \hat{p}_s \left(\mathbf{K}_{s,0}\overline{\boldsymbol{\nabla}}p_s\right)\cdot\mathbf{n}_0\ \mathrm{d}A_0, \end{aligned} \tag{3.56}$$

where $\mathbf{K}_{s,0}$ is as above and using Nanson's formula $\mathbf{n}\ \mathrm{d}A = J\mathbf{F}^{-\mathrm{T}}\mathbf{n}_0\ \mathrm{d}A_0$.

Finally, we have

$$\begin{aligned}\int_{\mathcal{D}} C_f(p_s - p_i)\check{p}_s\ \mathrm{d}V &= \int_{\mathcal{D}_0} C_f(p_s - p_i)\hat{p}_s J\ \mathrm{d}V_0\\ &= \int_{\mathcal{D}_0} JC_f(p_s - p_i)\hat{p}_s\ \mathrm{d}V_0\\ &= \int_{\mathcal{D}_0} C_{f,0}(p_s - p_i)\hat{p}_s\ \mathrm{d}V_0, \end{aligned} \tag{3.57}$$

where $C_{f,0} = JC_f$.

To summarise, we have the weak form equation for blood flow in the deformed liver lobule as

$$\int_{\mathcal{D}_0} \left(\mathbf{K}_{s,0}\overline{\boldsymbol{\nabla}}p_s\right)\cdot\overline{\boldsymbol{\nabla}}\hat{p}_s\ \mathrm{d}V_0 - \int_{\partial\mathcal{D}_0} \hat{p}_s \left(\mathbf{K}_{s,0}\overline{\boldsymbol{\nabla}}p_s\right)\cdot\mathbf{n}_0\ \mathrm{d}A_0 = -\int_{\mathcal{D}_0} C_{f,0}(p_s - p_i)\hat{p}_s\ \mathrm{d}V_0. \tag{3.58}$$

A similar analysis for the weak form equation of interstitial fluid flow

$$\begin{aligned}\int_{\mathcal{D}} \left(\mathbf{K}_i\boldsymbol{\nabla}p_i\right)\cdot\boldsymbol{\nabla}\check{p}_i\ \mathrm{d}V - \int_{\partial\mathcal{D}} \check{p}_i \left(\mathbf{K}_i\boldsymbol{\nabla}p_i\right)\cdot\mathbf{n}\ \mathrm{d}A &= \int_{\mathcal{D}} C_f(p_s - p_i)\check{p}_i\ \mathrm{d}V\\ &\quad - \int_{\mathcal{D}} C_l \max(p_i - p_0, 0)\check{p}_i\ \mathrm{d}V, \end{aligned} \tag{3.59}$$

results in

$$\begin{aligned}\int_{\mathcal{D}_0} \left(\mathbf{K}_{i,0}\overline{\boldsymbol{\nabla}}p_i\right)\cdot\overline{\boldsymbol{\nabla}}\hat{p}_i\ \mathrm{d}V_0 - \int_{\partial\mathcal{D}_0} \hat{p}_i \left(\mathbf{K}_{i,0}\overline{\boldsymbol{\nabla}}p_i\right)\cdot\mathbf{n}_0\ \mathrm{d}A_0 &= \int_{\mathcal{D}_0} C_{f,0}(p_s - p_i)\hat{p}_i\ \mathrm{d}V_0\\ &\quad - \int_{\mathcal{D}_0} C_{l,0} \max(p_i - p_0, 0)\hat{p}_i\ \mathrm{d}V_0, \end{aligned} \tag{3.60}$$

where $\mathbf{K}_{i,0} = J\mathbf{F}^{-1}\mathbf{K}_i\mathbf{F}^{-\mathrm{T}}$, $C_{l,0} = JC_l$, $C_{f,0}$ is as above, and $\hat{p}_i : \mathcal{D}_0 \mapsto \mathbb{R}$, which satisfies $\hat{p}_i(\mathbf{x}_0) = \check{p}_i(\mathbf{x})$, is any regular test function of p_i on $\mathcal{D}_0$.

3.6 Boundary Conditions

In Section 2.7, we presented the boundary conditions used to obtain the numerical solutions for the 2D linear poroelastic model of the liver lobule. We shall assume that those boundary conditions also hold across the hyperelastic liver lobule. Furthermore, for the 3D case, we impose additional boundary conditions along the top and bottom surface of the lobule, which are detailed below. Lastly, for all boundary conditions imposed on the domain $\mathcal{D}$, we also perform a change of reference frame from $\partial\mathcal{D}$ to $\partial\mathcal{D}_0$.

3.6.1 Top and Bottom Surface of the 3D lobule

For the fluid flow equations, we impose:

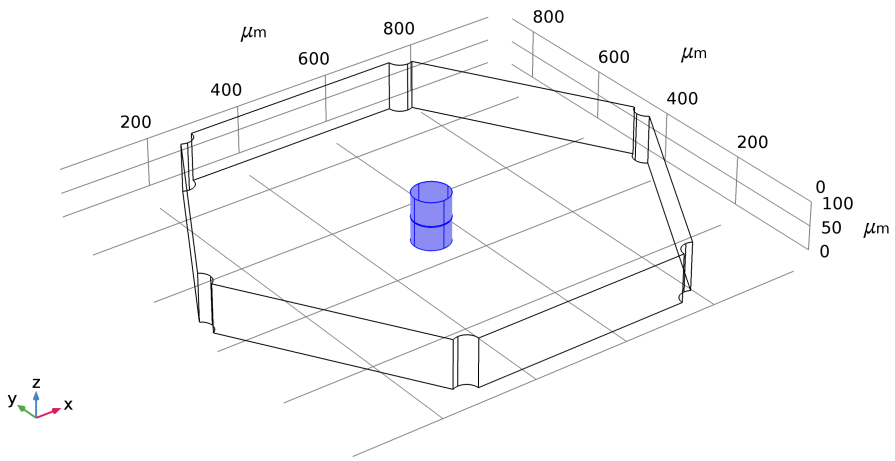
1. No blood and interstitial fluid flux across the top and bottom surface of the lobule, i.e. $\mathbf{v}_{s,\text{ref}} \cdot \mathbf{n}_0 = \mathbf{v}_s \cdot \mathbf{n} = 0$ and $\mathbf{v}_{i,\text{ref}} \cdot \mathbf{n}_0 = \mathbf{v}_i \cdot \mathbf{n} = 0$, respectively.

For tissue deformation:

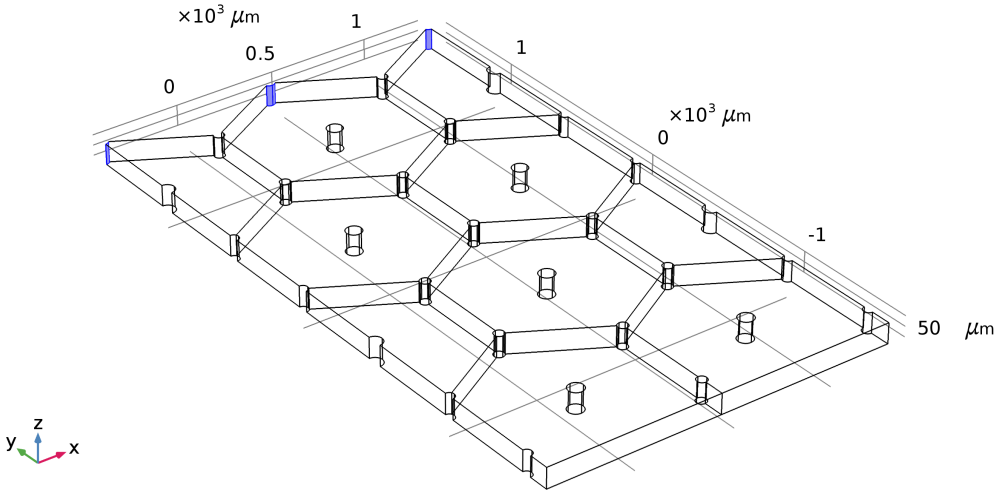
1. We assume zero normal and tangential stresses along the top surface of the lobule ($z = h_{\text{lob}}$), i.e. $\mathbf{n} \cdot (\tilde{\boldsymbol{\sigma}}\mathbf{n}) = \mathbf{m} \cdot (\tilde{\boldsymbol{\sigma}}\mathbf{n}) = 0$, where $\mathbf{n}$ and $\mathbf{m}$ are unit normal and tangent vectors, respectively.

2. At the bottom surface of the lobule ($z = 0$), we impose zero displacement in the z–plane, i.e. $u_3 = 0$. This serves as a plane of symmetry and prevents bending of the tissue under high fluid pressures.

3. In the case of a single lobule, we also constrain the central vein to restrict deformation along the $x - y$ plane, i.e. $u_1 = u_2 = 0$ (see Figure 3.1a). For the lobule lattice, lateral displacement is restricted along the innermost portal tracts of the lobule lattice (see Figure 3.1a). These fixed reference points where chosen merely to prevent rotation of the lobule/lattice.



(a) Single lobule



(b) Lobule lattice

Figure 3.1: Constrained lateral surfaces (in blue) on the 3D deformed liver lobule in: (a) single lobule case and (b) lobule lattice case.

3.6.2 Change of Reference Frame

To enable us to solve the problem of the deformed liver lobule in COMSOL, we needed to perform a change of reference frame for the weak form equations from the current configuration $\mathcal{D}$ to a fixed reference frame $\mathcal{D}_0$ (Section 3.5.2). The corresponding change of reference frame also needs to be done for the boundary conditions. Table 3.1 summarises the boundary conditions imposed on the deformed lobule in $\mathcal{D}$ and the corresponding boundary conditions in the pulled back reference frame $\mathcal{D}_0$. The boundary conditions imposed on the undeformed lobule for $p_{s,\text{ref}}$ and $p_{i,\text{ref}}$ do not need any change in reference frame since they were already prescribed on the domain $\mathcal{D}_0$.

	Current reference frame $\mathcal{D}$	Fixed reference frame $\mathcal{D}_0$
1.	Blood sinusoidal pressure is prescribed at the portal tracts and the central vein, i.e. $p_s = p_s^{pt}$ and $p_s = p_s^{cv}$, respectively, where p_s^{pt} and p_s^{cv} are constants.	Same, since pressure is a scalar.
2.	No blood flow across the edges of the lobule due to the presence of the vascular septa, i.e. $\mathbf{v}_s \cdot \mathbf{n} = 0$.	$\overline{\mathbf{v}}_s \cdot \mathbf{n}_0 = 0$.
3.	No interstitial fluid flow into the portal tracts and central vein, i.e. $\mathbf{v}_i \cdot \mathbf{n} = 0$.	$\overline{\mathbf{v}}_i \cdot \mathbf{n}_0 = 0$.
4.	No blood and interstitial fluid flux across the top and bottom surface of the lobule, i.e. $\mathbf{v}_s \cdot \mathbf{n} = \mathbf{v}_i \cdot \mathbf{n} = 0$.	$\overline{\mathbf{v}}_s \cdot \mathbf{n}_0 = \overline{\mathbf{v}}_i \cdot \mathbf{n}_0 = 0$.
5.	For a single lobule, we also impose no interstitial fluid flow across the edges of the lobule, i.e. $\mathbf{v}_i \cdot \mathbf{n} = 0$. In a lobule lattice, this condition is changed to a flow continuity, except at the outer surface of the liver where we have $\mathbf{v}_i \cdot \mathbf{n} = M_{GP}(p_i - P_{PC})$ across the Glissonian–peritoneal surface and $\mathbf{v}_i \cdot \mathbf{n} = M_{BA}(p_i - P_{BA})$ across the bare area.	$\overline{\mathbf{v}}_i \cdot \mathbf{n}_0 = 0$ across the edges for the single lobule. For the liver surface, $\overline{\mathbf{v}}_i \cdot \mathbf{n}_0 = M_{GP}(p_i - P_{PC})$ and $\overline{\mathbf{v}}_i \cdot \mathbf{n}_0 = M_{BA}(p_i - P_{BA})$ across the Glissonian–peritoneal surface and bare area, respectively.
6.	At the portal tracts, we impose that the normal stresses are due to sinusoidal blood pressure increase, i.e. $\mathbf{n} \cdot (\tilde{\boldsymbol{\sigma}}\mathbf{n}) = \mathbf{n} \cdot \mathbf{t} = -\left(p_s^{pt} - p_{s,\mathrm{ref}}^{pt}\right)$.	$(J\mathbf{F}^{-\mathrm{T}}\mathbf{n}_0) \cdot \mathbf{s}_0 = -\left(p_s^{pt} - p_{s,\mathrm{ref}}^{pt}\right)$.
7.	Normal stresses are zero along all the other boundaries, i.e. $\mathbf{n} \cdot (\tilde{\boldsymbol{\sigma}}\mathbf{n}) = \mathbf{n} \cdot \mathbf{t} = 0$.	$\mathbf{n}_0 \cdot \tilde{\mathbf{s}}_0 = 0$.
8.	Tangential stresses are zero along all boundaries, i.e. $\mathbf{m} \cdot (\tilde{\boldsymbol{\sigma}}\mathbf{n}) = \mathbf{m} \cdot \mathbf{t} = 0$.	$\mathbf{m}_0 \cdot \tilde{\mathbf{s}}_0 = 0$.
9.	On the $z = 0$ plane, $u_3 = 0$.	Same.
10.	At the fixed central (single lobule) and chosen portal tracts (lobule lattice) surface, $u_1 = u_2 = 0$.	Same.

Table 3.1: Boundary conditions used in the deformed liver lobule and the corresponding change of reference frame from the current domain $\mathcal{D}$ to the fixed domain $\mathcal{D}_0$.

3.7 Derived Values

In this section, we present the equations used to estimate the total blood flux, lymphatic uptake rate and fluid loss via the outer surface of the liver using the 3D hyper-poroelastic model. These are all based on the assumptions and definitions detailed in Section 2.8.

3.7.1 Total Blood Flux

As stated in Section 2.8.1, the total volume flux of blood into the liver, for the undeformed and deformed lobule, respectively, can be estimated by integrating the volumetric flux of blood through the portal tracts of a single lobule and multiplying it by the average number of lobules

in the liver, N_{lob}:

$$Q_{\text{blood,ref}} = -N_{\text{lob}} \int_{\text{Portal tracts}} \mathbf{v}_{s,\text{ref}} \cdot \mathbf{n}_0 \, \mathrm{d}A_0 \tag{3.61}$$

and

$$Q_{\text{blood}} = -N_{\text{lob}} \int_{\text{Portal tracts}} \mathbf{v}_s \cdot \mathbf{n} \, \mathrm{d}A = -N_{\text{lob}} \int_{\text{Portal tracts}} \overline{\mathbf{v}}_s \cdot \mathbf{n}_0 \, \mathrm{d}A_0, \tag{3.62}$$

where $\mathbf{n}$ and $\mathbf{n}_0$ are the outward-pointing unit normal vectors on the current and reference frames, respectively, and the integral is taken along the surface area of the portal tracts.

3.7.2 Total Lymphatic Uptake

Similarly, as stated in Section 2.8.2, the total rate of fluid uptake by the lymphatics, for the undeformed and deformed lobule, respectively, can be estimated using the following equations:

$$Q_{\text{lymph,ref}} = N_{\text{lob}} \int_{\mathcal{D}_0} C_l \max(p_{i,\text{ref}} - p_0, 0) \, \mathrm{d}V_0 \tag{3.63}$$

and

$$Q_{\text{lymph}} = N_{\text{lob}} \int_{\mathcal{D}} C_l \max(p_i - p_0, 0) \, \mathrm{d}V = N_{\text{lob}} \int_{\mathcal{D}_0} C_{l,0} \max(p_i - p_0, 0) \, \mathrm{d}V_0. \tag{3.64}$$

3.7.3 Total Fluid Loss into the Peritoneal Cavity

The total fluid loss from the liver into the peritoneal cavity can be estimated by multiplying the average interstitial fluid loss per unit edge surface of the lobule lattice by the total surface area of the Glissonian–peritoneal membrane (see Section 2.8.3 for the 2D case). For the 3D undeformed liver lobule, this is given by (2.58):

$$Q_{\text{L}_{\text{ref}},\text{PC}} = \frac{A_{\text{L,GP}}}{A_{\text{ref,edge}}} \int_{\text{Outer surface}} \mathbf{v}_{i,\text{ref}} \cdot \mathbf{n}_0 \, \mathrm{d}A_0 = \frac{A_{\text{L,GP}}}{A_{\text{ref,edge}}} \int_{\text{Outer surface}} M_{GP}(p_{i,\text{ref}} - P_{PC}) \, \mathrm{d}A_0, \tag{3.65}$$

where $A_{\text{L,GP}}$ is the total area of the Glissonian–peritoneal membrane and $A_{\text{ref,edge}}$ is the area of the outer surface of the lobule lattice over which the integral is taken, both in the undeformed case.

In the linear poroelastic model, we assumed that the surface area of the Glissonian–peritoneal membrane remained constant for small strains. This assumption does not hold for large strains. Instead, we will assume that the Glissonian membrane deforms at the same strain rate as the bare area of the liver (i.e. the liver lobule tissue) in the hyperelastic model, and so its surface area will also stretch in the same proportion as the liver tissue. Note that in reality, the Glissonian membrane is a lot stiffer than the liver tissue and so will deform less than the liver tissue given the same applied stress (Umale et al., 2011). This behaviour can be incorporated into the liver model in future work.

Next, note that both $A_{\mathrm{L,GP}}$ and $A_{\mathrm{ref,edge}}$ have the same dimension [L^2], where L is a length scale. The length L is also related to the undeformed length by $\mathrm{L} = \lambda \mathrm{L}_{\mathrm{ref}}$, where λ is the stretch of the tissue. Given that we have assumed the tissue is isotropic, and that the liver tissue and the Glissonian–peritoneal membrane have the same stiffness, the expression $A_{\mathrm{L,GP}}/A_{\mathrm{ref,edge}} = \tilde{A}_{\mathrm{L,GP}}$ must remain constant with deformation. Therefore, we can estimate the total fluid loss from the deformed liver as

$$Q_{\mathrm{L,PC}} = \tilde{A}_{\mathrm{L,GP}} \int_{\text{Outer surface}} \mathbf{v}_i \cdot \mathbf{n} \, \mathrm{d}A = \tilde{A}_{\mathrm{L,GP}} \int_{\text{Outer surface}} M_{GP}(p_i - P_{PC}) \, \mathrm{d}A. \tag{3.66}$$

Equation (3.66) can be pulled from the current reference domain $\mathcal{D}$ to the fixed reference domain $\mathcal{D}_0$ to give

$$Q_{\mathrm{L,PC}} = \tilde{A}_{\mathrm{L,GP}} \int_{\text{Outer surface}} M_{GP}(p_i - P_{PC}) \, \mathrm{d}A_0. \tag{3.67}$$

Note that, as in Chapter 2, we have assumed that the hydraulic conductivity of the Glissonian–peritoneal membrane M_{GP} remains constant with deformation, as a first approximation. This is because no experimental studies could be found on the effect of stretching on the permeability of the membrane. In future studies, the membrane could also be treated as a porous medium with permeability dependent on the deformation. This is discussed further in Chapter 6 of this thesis.

3.8 Physiological Parameter Values

The parameter values used to construct the geometry of the lobule, including the side length l_{lob} and diameters of the portal tracts and central vein, d_{pt} and d_{cv}, respectively, were listed in Table 2.1, within Chapter 2. In the present 3D case, the height h_{lob} is chosen such that the pressure drop is assumed to be approximately zero along the z-axis of the portal tracts and central vein. As a first approximation, h_{lob} is chosen to be $l_{\mathrm{lob}}/5 = 100\,\mu\mathrm{m}$. This value is later varied in Section 3.9.5 in order to investigate the sensitivity of the numerical solutions to the choice of h_{lob}.

The parameter values used for the numerical simulation of blood and interstitial fluid flow in the 3D hyperelastic model are the same as those used in Chapter 2 that were listed in Table 2.2, together with references.

For solid deformation, the 5-constant Mooney–Rivlin polynomial is used (see Section 3.4.2) to represent the isochoric elastic response of the tissue, the material constants of which are listed in Table 3.2. The bulk modulus E_{bulk} can be estimated from the elastic constant E_L and the Poisson ratio ν_L of the liver, where for an isotropic tissue, $E_{\mathrm{bulk}} = E_L/(3(1-2\nu_L))$ (see e.g. Srinath, 2009), and using the values of E_L and ν_L from Chapter 2 (see Table 2.3), we have that $E_{\mathrm{bulk}} \approx 2821\,\mathrm{Pa}$. Finally, $\varphi_{s,\mathrm{ref}}$ and $\varphi_{i,\mathrm{ref}}$ also have the same values as in Table 2.3.

Constant	Default Value
c_1	286.9 Pa
c_2	−96.8 Pa
c_3	1926.0 Pa
c_4	−4164.4 Pa
c_5	2649.1 Pa

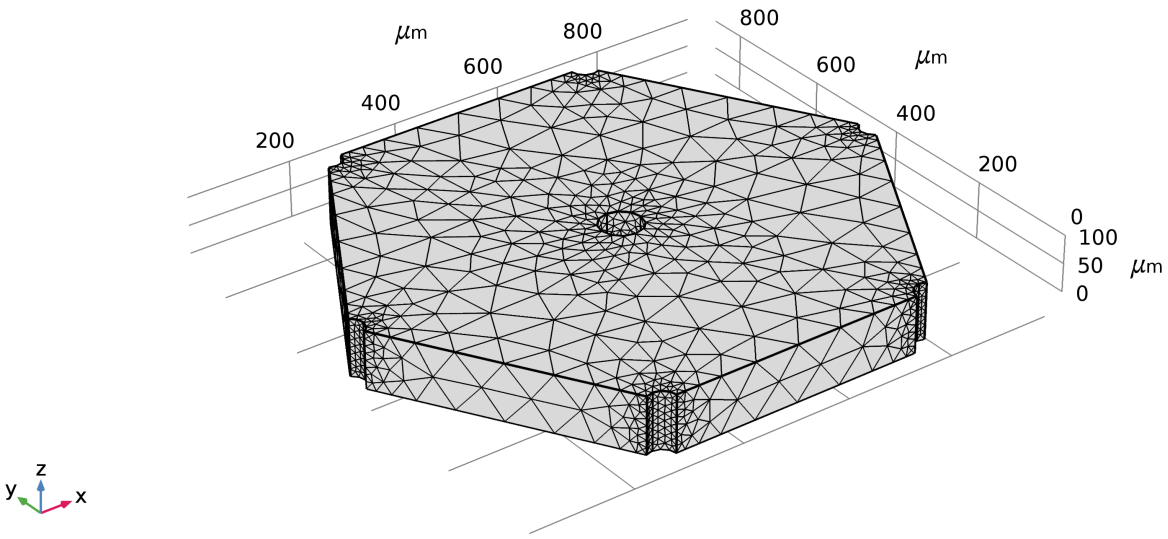
Table 3.2: Parameters of the 5-constant Mooney–Rivlin polynomial (3.18) used to describe the shear behaviour of the liver tissue obtained from the experimental studies by Fu and Chui (2014).

3.9 Results and Discussion

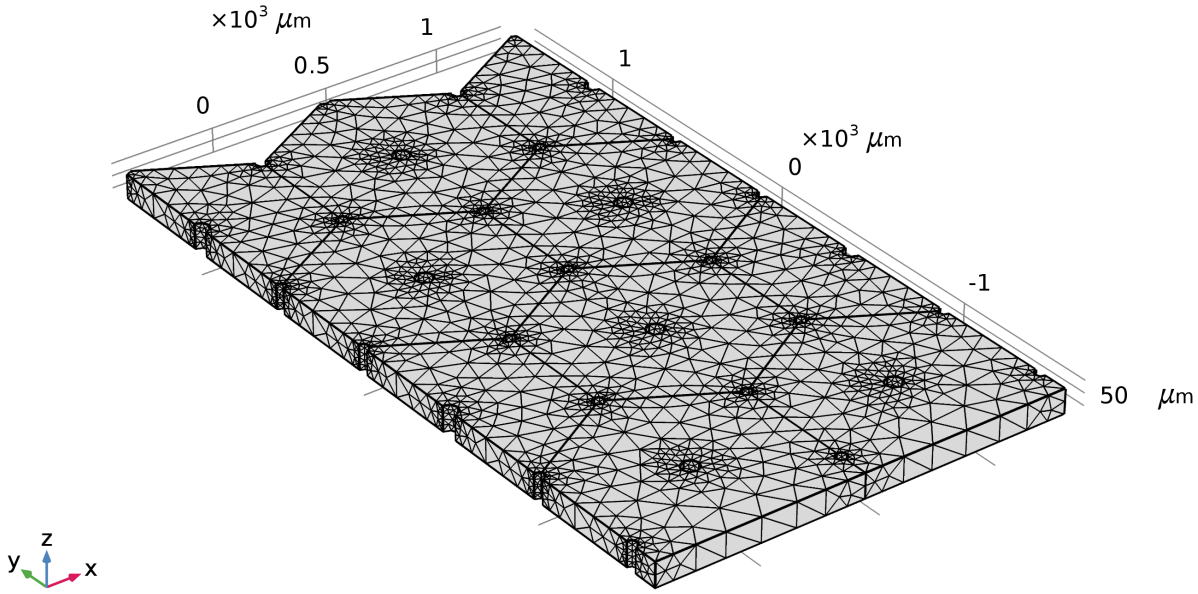
In this section, we present the results of the 3D hyperelastic liver model, for a single lobule and a lobule lattice close to the liver surface. We also make comparisons with the results of the 2D linear elastic model from Chapter 2 and other liver microcirculation models in current literature, such as the 2D linear elastic model of blood flow by Bonfiglio et al. (2010) and the 2D rigid model of blood and interstitial fluid flow by Siggers et al. (2014).

3.9.1 Domain Mesh

The domain for the 3D liver model is much larger than that of the 2D liver model, and so required more triangular mesh elements. Rather than the fluid dynamics mesh class used in the 2D liver model, another COMSOL Multiphysics predefined mesh class known as General Physics was used for the 3D liver lobule, with the same aim of minimising mesh refinement error (to less than 0.001) and optimising computational time. For both the 3D single lobule and lobule lattice, the "fine" General Physics mesh size was used (see Figures 3.2a and 3.2b, respectively). Note that the 3D single lobule had a maximum mesh element size of 78 μm, a minimum mesh element size of 9.75 μm, and took 3 min 7 s to compute. Whereas the 3D lobule lattice had a maximum mesh element size of 249 μm, a minimum mesh element size of 31.1 μm and took 4 min 25 s to compute.



(a) Single Lobule



(b) Lobule Lattice

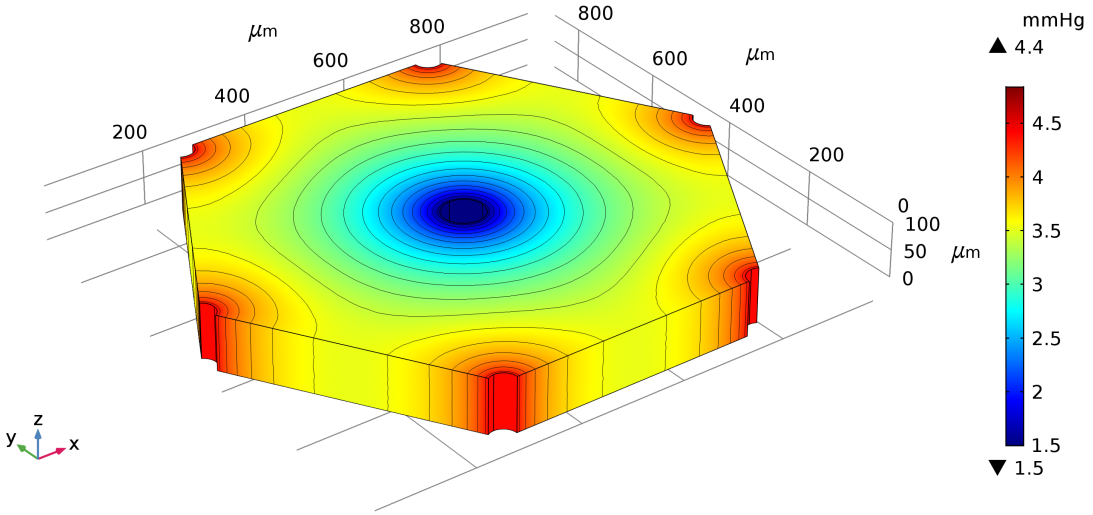
Figure 3.2: COMSOL Multiphysics mesh distribution used in the 3D hyperelastic liver model to obtain numerical solutions.

3.9.2 Single Lobule

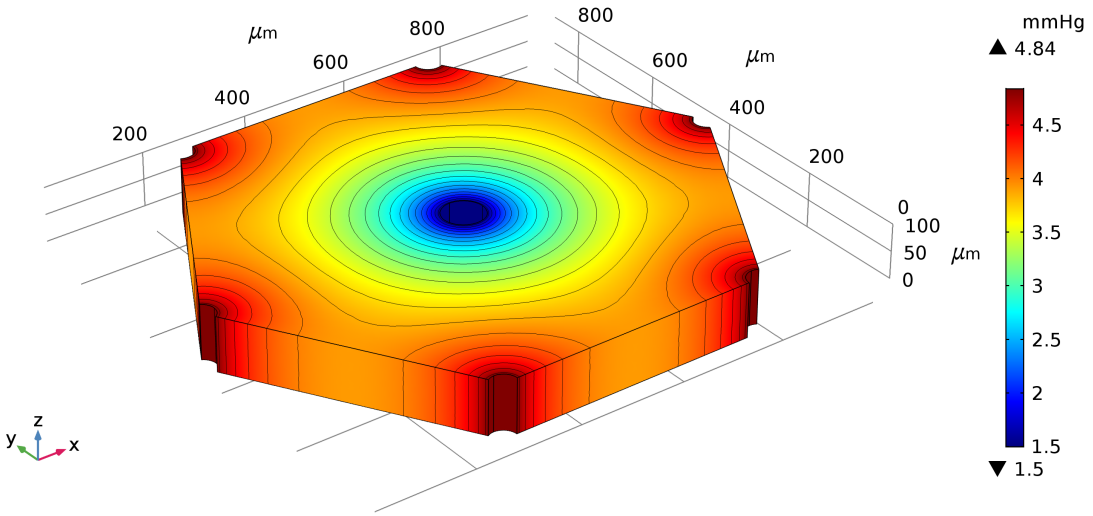
For the case of a single lobule, a 10% increase in sinusoidal blood pressure (as was done in Chapter 2) is applied, and in the following subsections we present the results of blood and interstitial fluid pressure and velocity profiles, and the deformation of the tissue.

3.9.2.1 Blood and Interstitial Fluid Pressure and Velocity Profiles

Blood sinusoidal and interstitial fluid pressure distributions and average pore velocity profiles, for both the undeformed and deformed lobules, are shown in Figures 3.3–3.6. All the results have a similar profile to those obtained in Chapter 2. This is expected since we have no pressure drop along the z–axis and the hyperelastic equations become approximately linear under small strains, which acts as a check on our calculations. The results of the 3D pressure and velocity profiles have been included here for completeness.

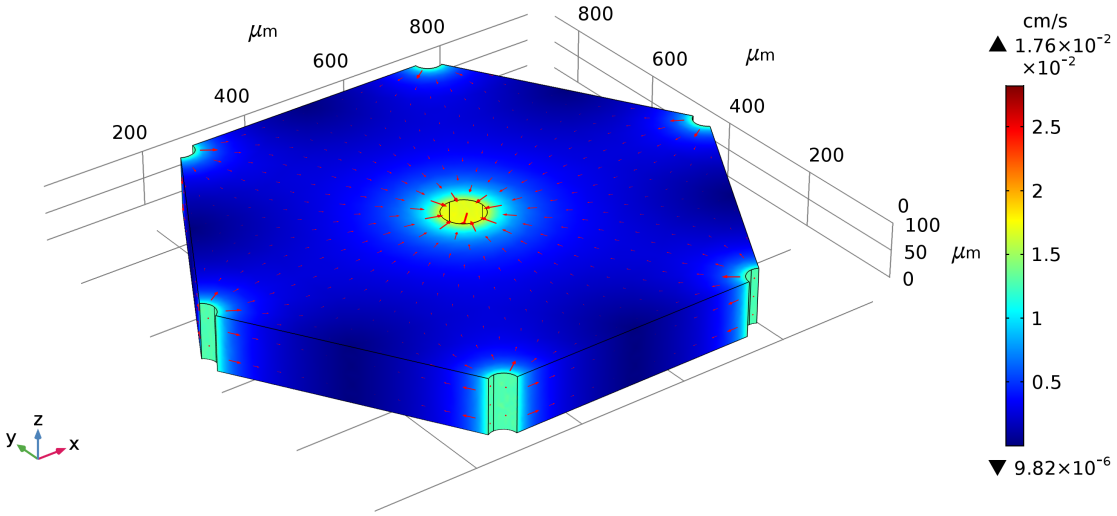


(a) $p_{s,\mathrm{ref}}$

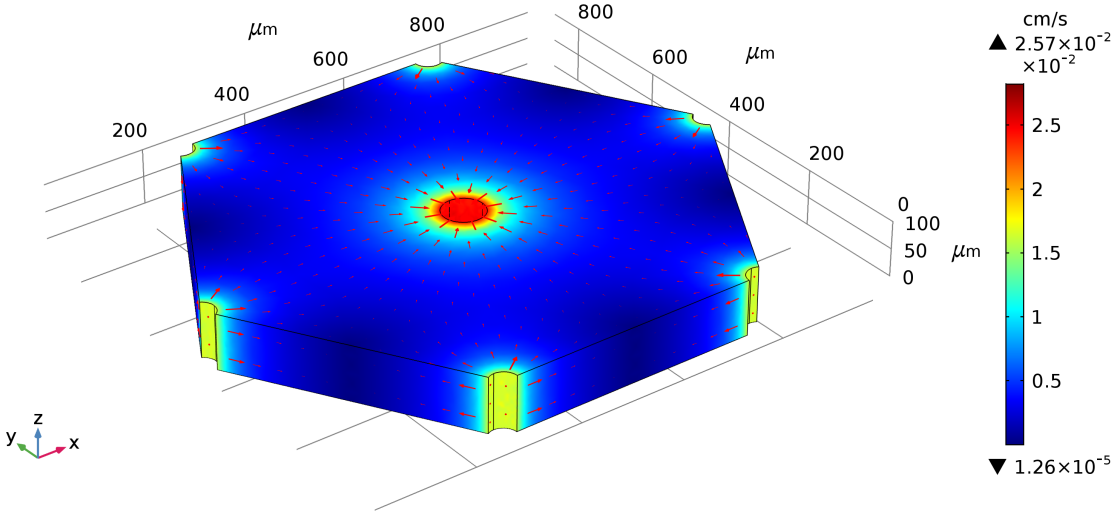


(b) p_s

Figure 3.3: Blood pressure distribution in 3D: (a) undeformed liver lobule and (b) deformed hyperelastic liver lobule following a 10% increase in sinusoidal blood portal pressure. Colour bars show pressure magnitude and have the same range in both subfigures. Pressure contours at intervals of 0.15 mmHg are also plotted in both subfigures.

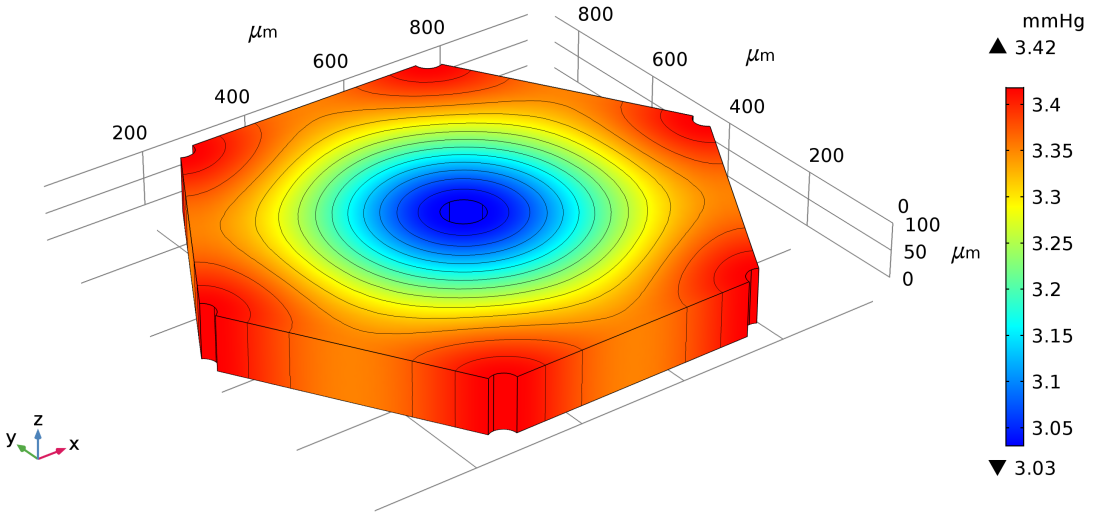


(a) $\mathbf{v}_{s,\mathrm{ref}}/\varphi_{s,\mathrm{ref}}$

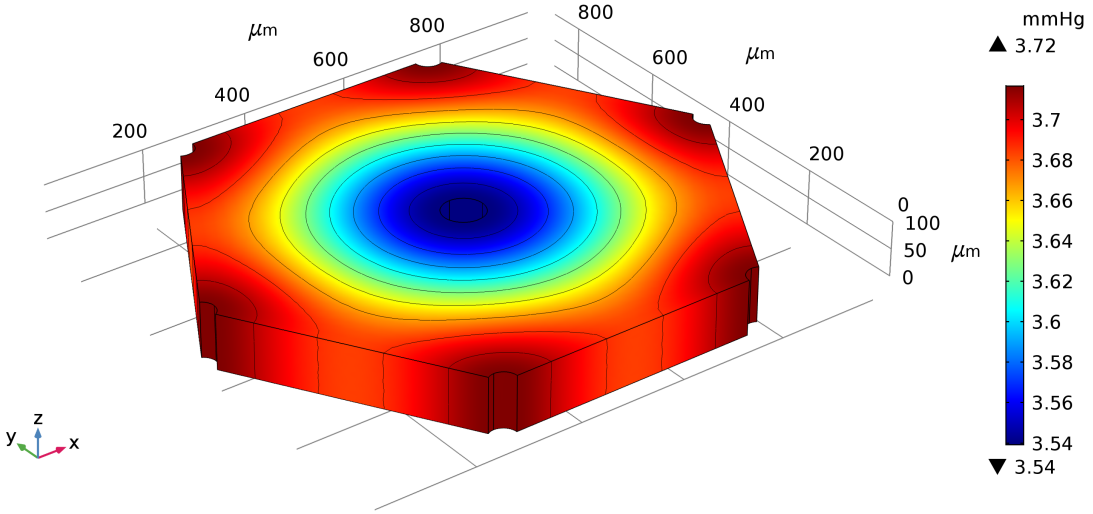


(b) $\mathbf{v}_s/\varphi_s$

Figure 3.4: Average blood pore velocity in 3D: (a) undeformed liver lobule and (b) deformed hyperelastic liver lobule following a 10% increase in sinusoidal blood portal pressure. In both subfigures, arrows show the direction of flow and are proportional to the magnitude of flow velocity. Colour bars show velocity magnitude and are of the same range for both subfigures.

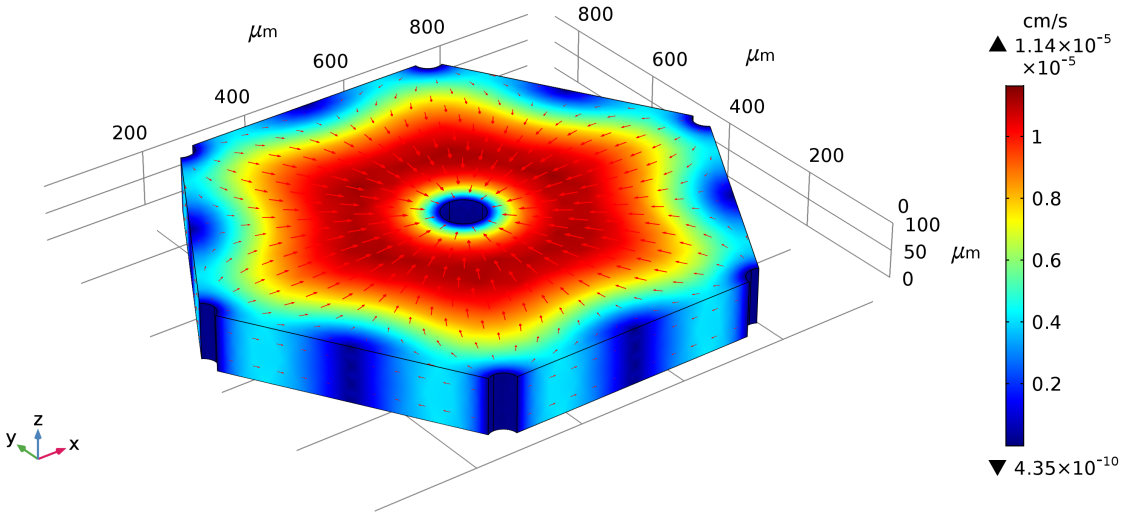


(a) $p_{i,\mathrm{ref}}$

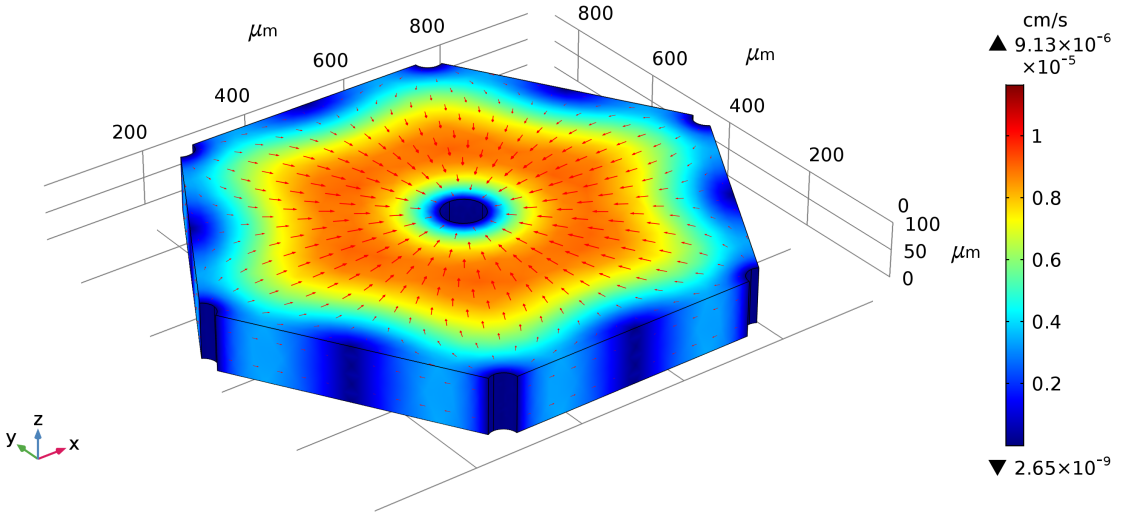


(b) p_i

Figure 3.5: Interstitial fluid pressure distribution in 3D: (a) undeformed liver lobule and (b) deformed hyperelastic liver lobule following a 10% increase in sinusoidal blood portal pressure. Colour bars show pressure magnitude and have different ranges in each subfigure. Pressure contours are at intervals of 0.02 mmHg in both subfigures.



(a) $\mathbf{v}_{i,\mathrm{ref}}/\varphi_{i,\mathrm{ref}}$

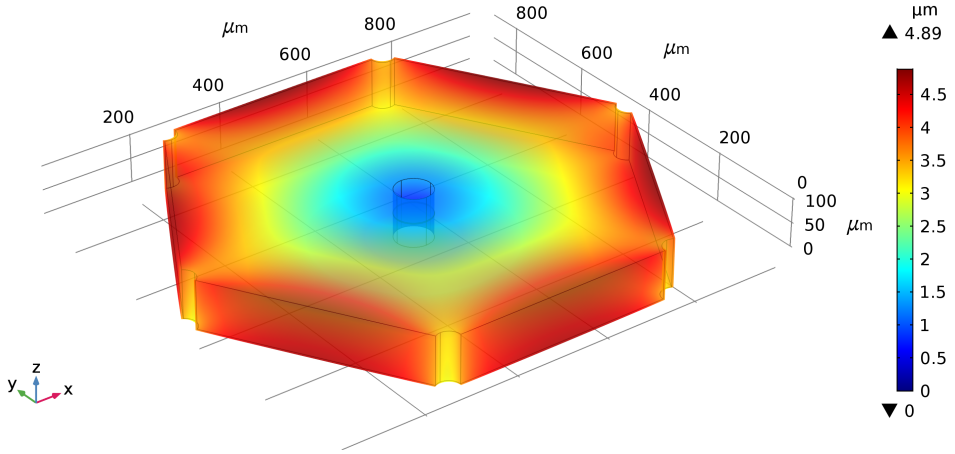


(b) $\mathbf{v}_i/\varphi_i$

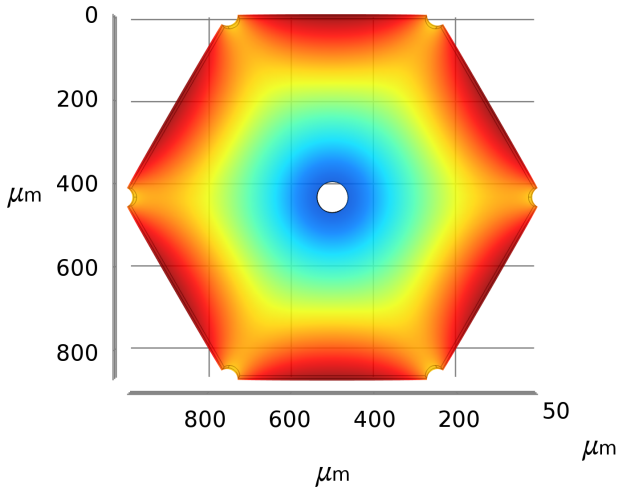
Figure 3.6: Average interstitial fluid pore velocity in 3D: (a) undeformed liver lobule and (b) deformed hyperelastic liver lobule following a 10% increase in sinusoidal blood portal pressure. Arrows show the direction of flow and are proportional to the magnitude of flow velocity. Colour bars show velocity magnitude and are of the same range for both subfigures.

3.9.2.2 Deformation Profile

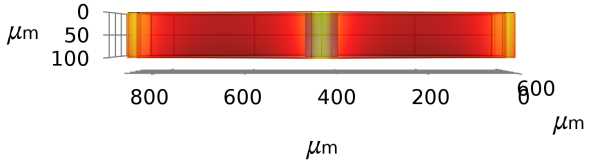
The solid deformation profile of a hyperelastic liver lobule following a 10% increase in blood portal pressure is shown in Figure 3.7. Figure 3.7a gives a 3D view of the deformed lobule, while Figures 3.7b and 3.7c give a 2D view of the x–y and y–z planes, respectively. In the x–y plane, the maximum displacement magnitude ($|\mathbf{u}| = 4.89\,\mu$m) is smaller than that of the 2D linear elastic model ($|\mathbf{u}| = 7.02\,\mu$m) presented in Figure 2.11. The result is as expected due to the added deformation of the 3D hyperelastic model in the z direction, which reduces the stretch across the x–y plane.



(a) 3D view.



(b) x–y view.



(c) y–z view.

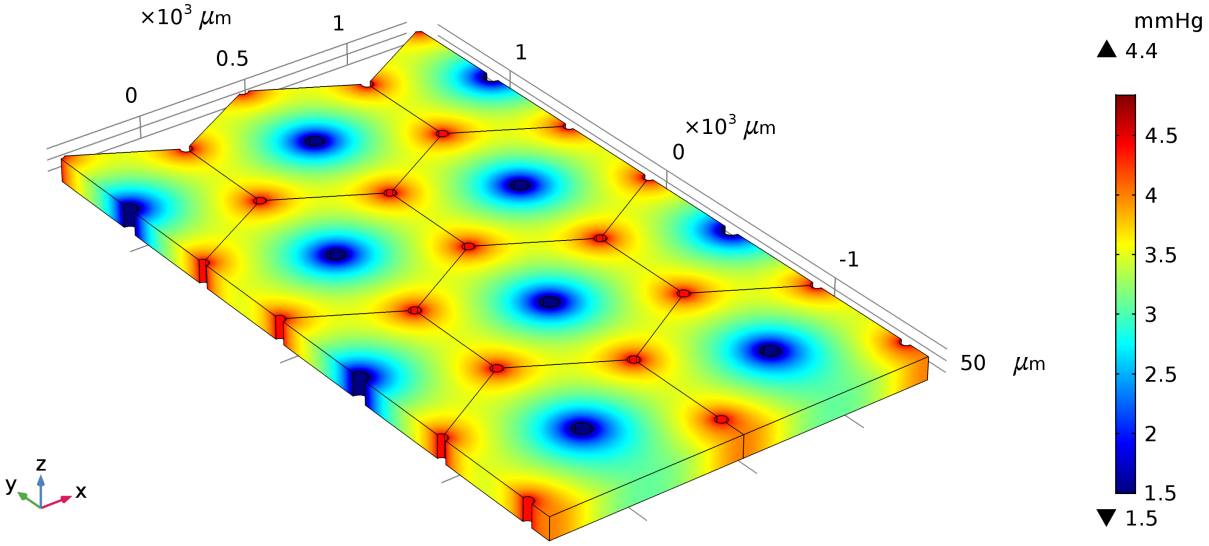
Figure 3.7: Solid deformation of a 3D hyperelastic lobule following a 10% increase in blood sinusoidal portal pressure, referenced against the undeformed lobule. Colour bar shows displacement magnitude $|\mathbf{u}|$, and is the same for all 3 subfigures.

3.9.3 Multiple Lobules

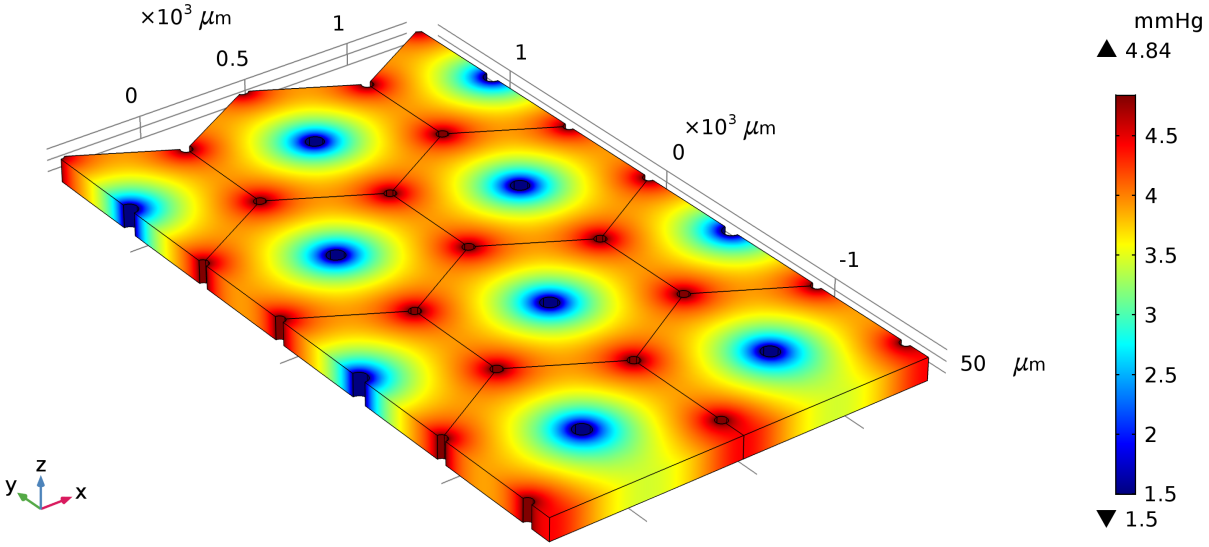
In this section, we present the results of flow and deformation profiles in a lattice arrangement of multiple lobules close to the liver surface, as described in Section 2.2.3, for the 3D hyperelastic model.

3.9.3.1 Blood and Interstitial Fluid Pressure and Velocity Profiles

As in the case of the single lobule, the results of blood and interstitial fluid pressure distributions and velocity profiles, for both the undeformed and deformed lobules, following a 10% increase in sinusoidal blood portal pressure, have similar profiles to those of the linear elastic model presented in Section 2.10.3. The results are shown here in Figures 3.8–3.11.

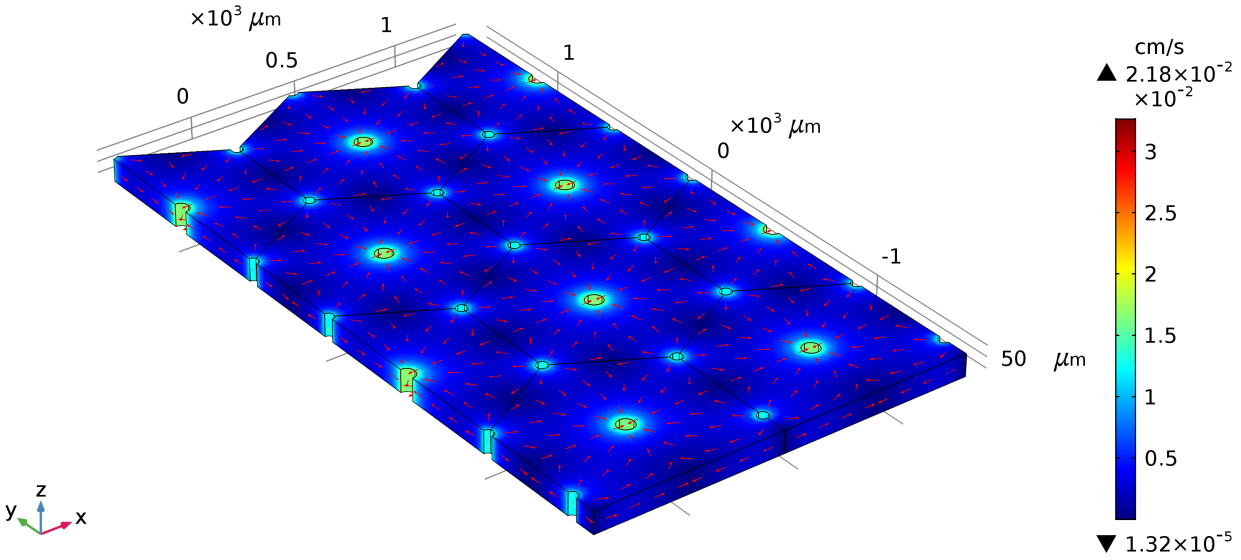


(a) $p_{s,\mathrm{ref}}$

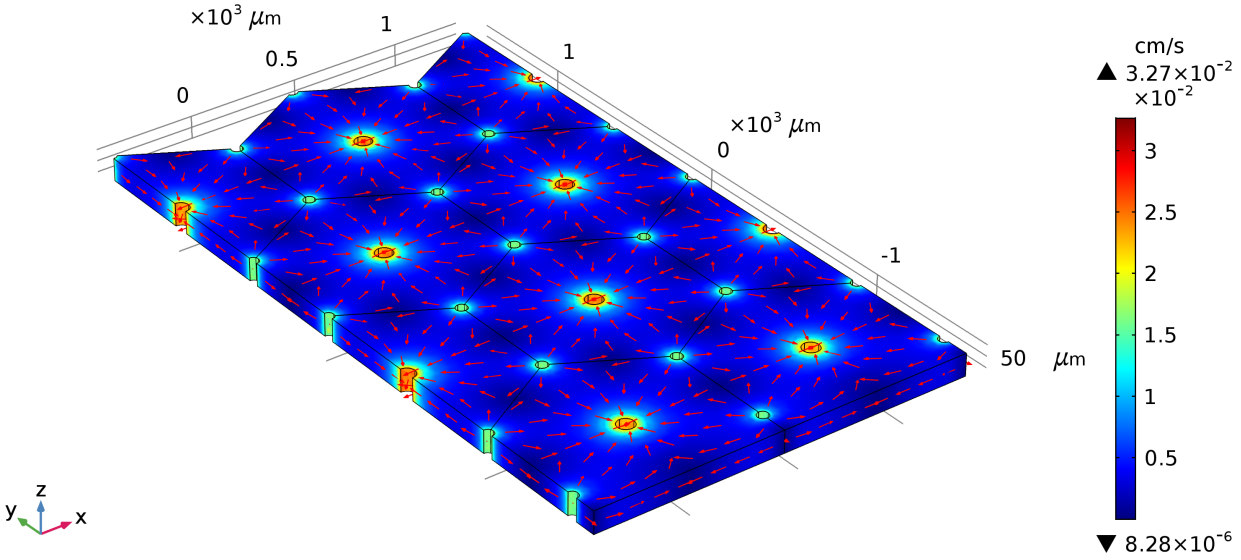


(b) p_s

Figure 3.8: Blood pressure distribution in 3D: (a) undeformed liver lobule lattice and (b) deformed hyperelastic liver lobule lattice following a 10% increase in sinusoidal blood portal pressure. Colour bars show pressure magnitude and have the same range in both subfigures.

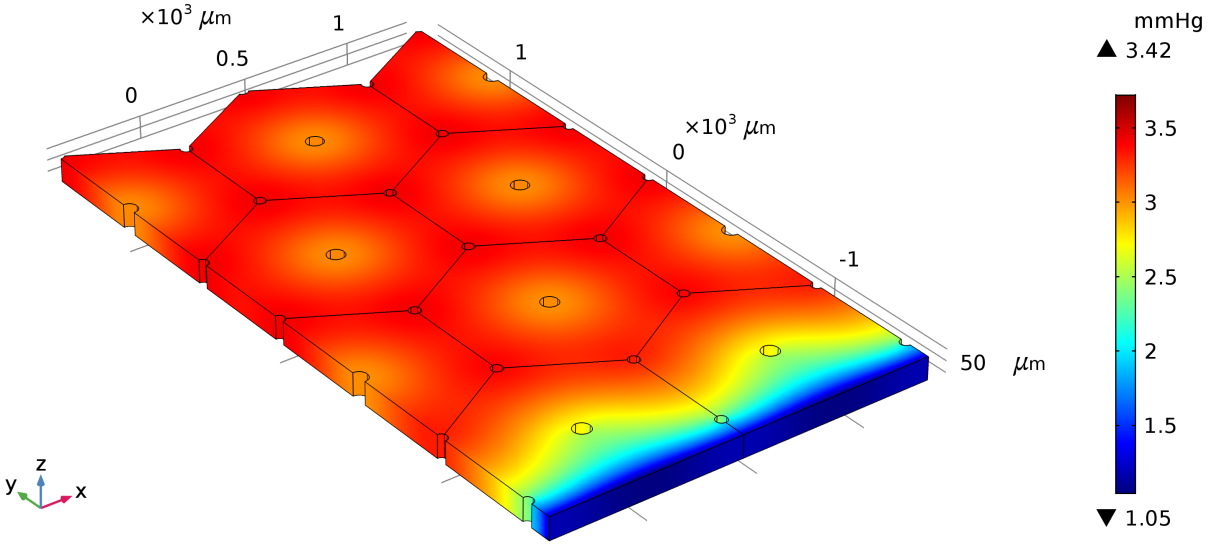


(a) $\mathbf{v}_{s,\mathrm{ref}}/\varphi_{s,\mathrm{ref}}$

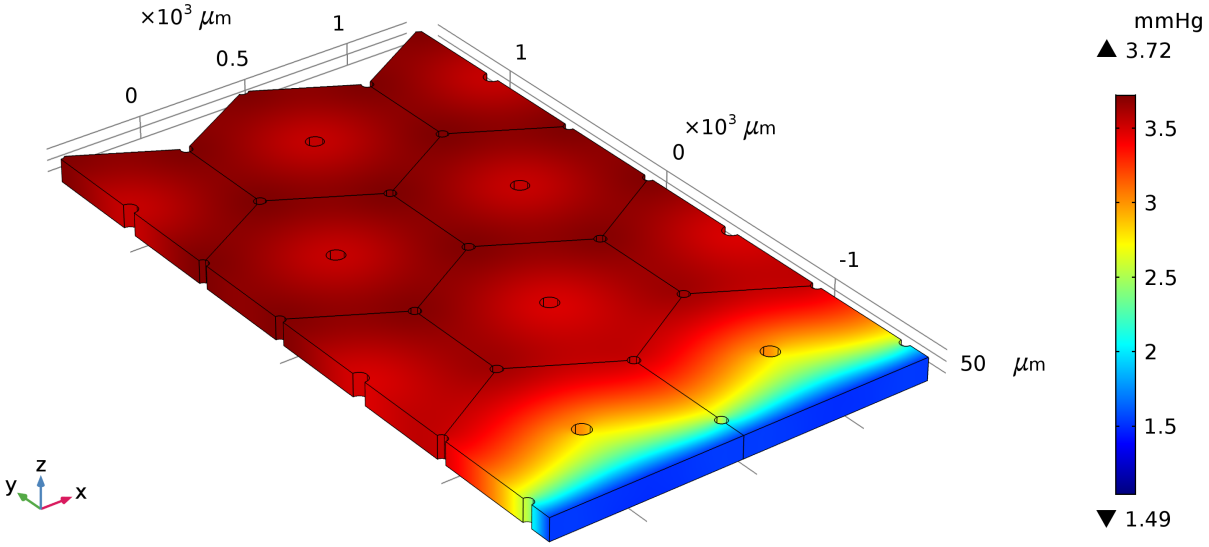


(b) $\mathbf{v}_s/\varphi_s$

Figure 3.9: Average blood pore velocity in 3D: (a) undeformed liver lobule lattice and (b) deformed hyperelastic liver lobule lattice following a 10% increase in sinusoidal blood portal pressure. In both subfigures, arrows show the direction of flow and are normalised to the magnitude of flow velocity. Colour bars show velocity magnitude and are of the same range for both subfigures.

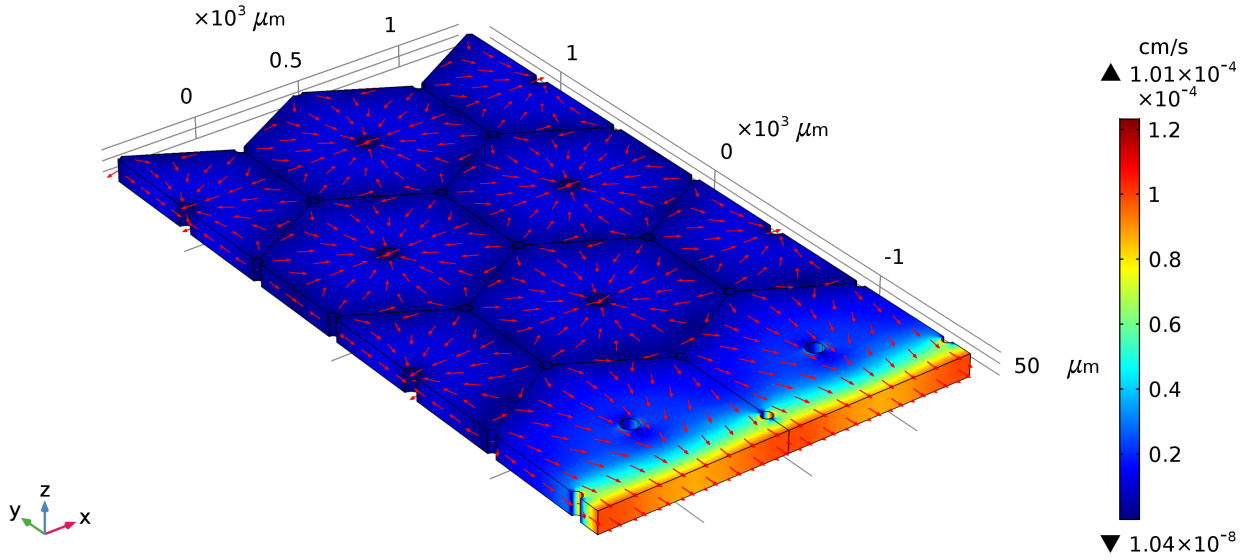


(a) $p_{i,\mathrm{ref}}$

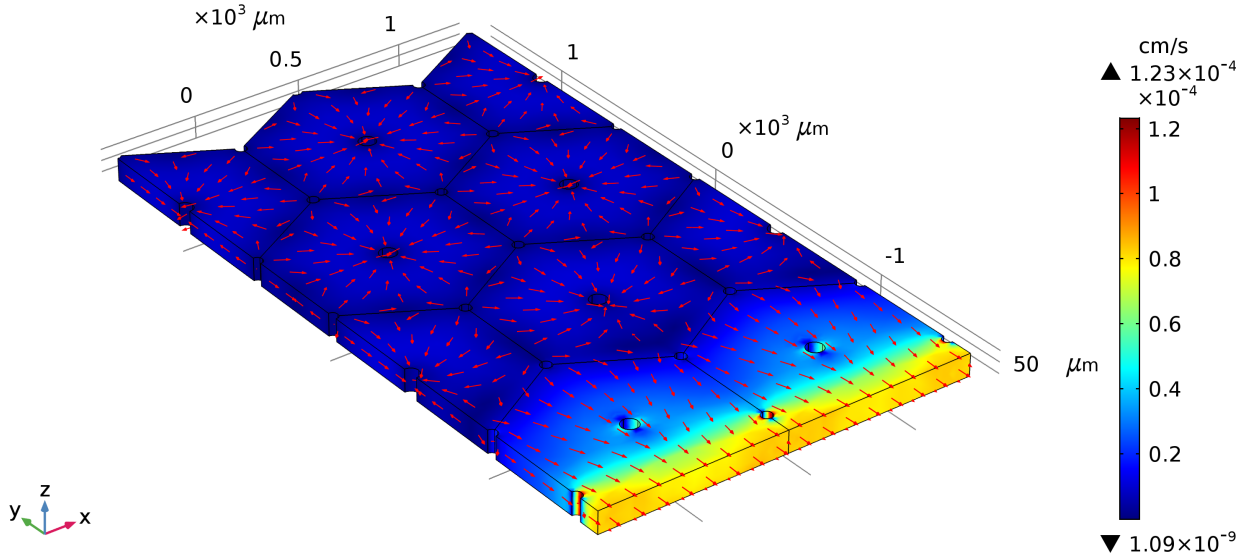


(b) p_i

Figure 3.10: Interstitial fluid pressure distribution in 3D: (a) undeformed liver lobule lattice and (b) deformed hyperelastic liver lobule following a 10% increase in sinusoidal blood portal pressure. Colour bars show pressure magnitude and have the same range in each subfigure.



(a) $\mathbf{v}_{i,\mathrm{ref}}/\varphi_{i,\mathrm{ref}}$



(b) $\mathbf{v}_i/\varphi_i$

Figure 3.11: Average interstitial fluid pore velocity in 3D: (a) undeformed liver lobule lattice and (b) deformed hyperelastic liver lobule lattice following a 10% increase in sinusoidal blood portal pressure. Arrows show the direction of flow and are proportional to the magnitude of flow velocity. Colour bars show velocity magnitude and are of the same range for both subfigures.

3.9.3.2 Deformation Profile

The displacement profile of the 3D hyperelastic liver lobule lattice following a 10% increase in blood portal pressure is shown in Figure 3.12. Tissue displacement occurs radially outwards towards the liver surface, due to the symmetry of the lattice.

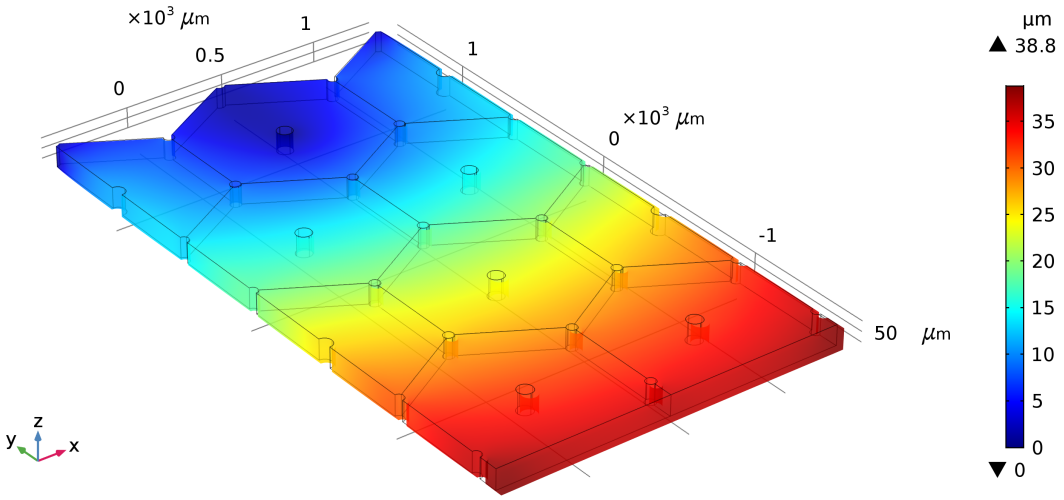


Figure 3.12: Displacement of a 3D hyperelastic lobule lattice following a 10% increase in blood sinusoidal portal pressure, referenced against the undeformed lobule. Colour bar shows displacement magnitude $|\mathbf{u}|$.

3.9.4 Comparison with Linear Elasticity Model

Here, we compare the numerical results obtained from the 3D hyperelastic liver model with the 2D linear elastic model from Chapter 2. Where applicable, we also compare the results with the 2D rigid model by Siggers et al. (2014) and the 2D linear elastic model of blood flow only by Bonfiglio et al. (2010). We will also look at estimates of tissue expansion, porosity, blood flux, lymphatic uptake and fluid loss into the peritoneal cavity as the blood portal pressure is increased.

3.9.4.1 Tissue Expansion

Figure 3.13 shows the results of volume change ratio $\mathcal{V}/\mathcal{V}_{\text{ref}} = J$ and tissue stretch λ for varying percentages of sinusoidal blood portal pressure increase, up to 300%. The volume change ratio J increases linearly with increases in sinusoidal blood portal pressure, for both the 3D hyperelastic and the 2D linear elastic liver models. It also increases at the same rate in both models for sinusoidal blood portal pressure increases up to 25%, after which the gradient of increase becomes slightly higher for the 3D hyperelastic model. The difference in J between

the two models is less than 2%. On the other hand, the stretch of the tissue, which is given by $\lambda = J^{1/3}$ for the 3D hyperelastic model and $\lambda = J^{1/2}$ for the 2D linear elastic model, increases non-linearly as sinusoidal blood portal pressure is increased. The stretch in the 2D linear elastic model is larger than that of the 3D hyper elastic model. This result is expected since displacement in the z direction is restricted and so the tissue deforms more in the $x - y$ direction to accommodate changes in fluid pressure. Note that such high increases in sinusoidal blood portal pressure, up to 300%, are unlikely to occur without damage to the liver tissue. The effect of tissue damage, as well as portal pressure increase, on deformation of the liver tissue is considered in Chapter 4. For the rest of the parameters considered in this section, we will only consider sinusoidal blood portal pressure increases up to 100% of the normal physiological value.

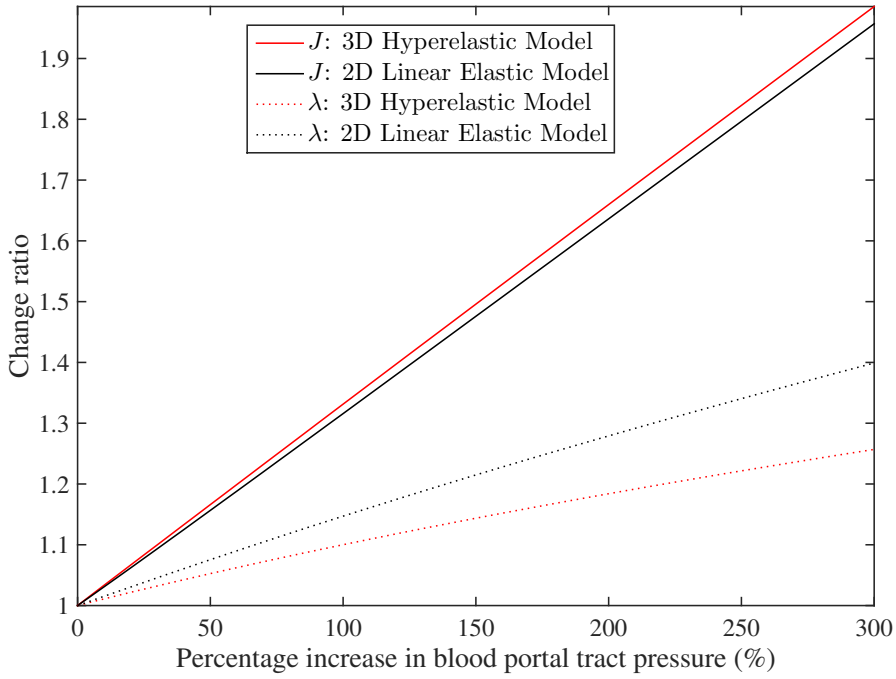


Figure 3.13: Comparison of the volume averaged increase in liver volume J (solid lines) and tissue stretch λ (dotted lines) against increase in sinusoidal blood pressure at the portal tracts between the 3D hyperelastic model (red lines) and 2D linear elastic model (black lines).

3.9.4.2 Liver Porosity

A plot of liver porosity against percentage increase in sinusoidal blood pressure, for both the 3D hyperelastic and 2D linear elastic models, is shown in Figure 3.14. In both models, liver porosity increases non-linearly as the sinusoidal blood portal pressure is increased up to double its value in the normal physiological case. Although, liver porosity increase is slightly higher in the 3D hyperelastic model than the 2D linear elastic model with change in pressure, the difference between the two models is less than 2.5%.

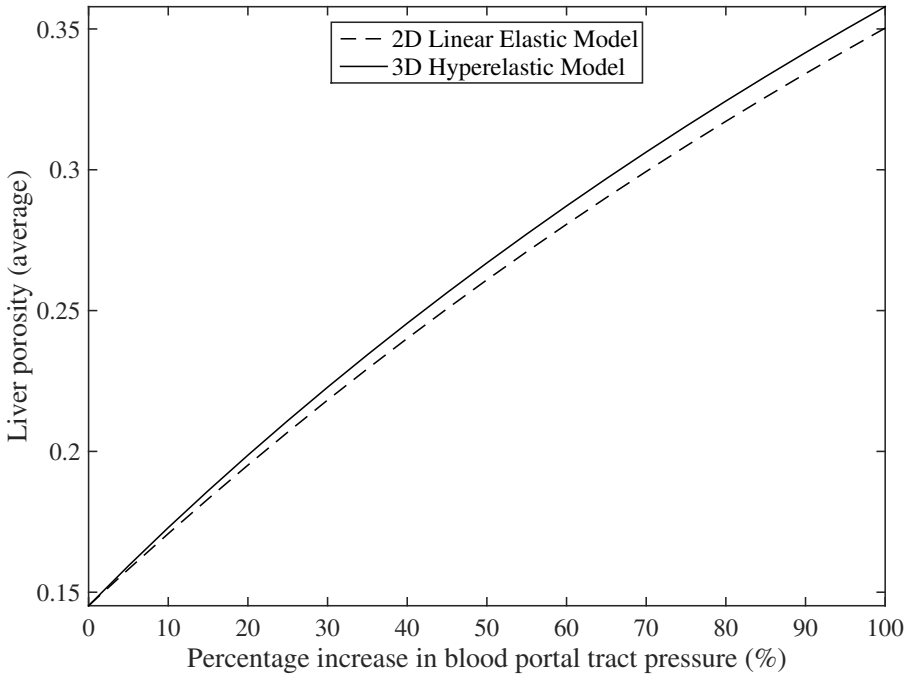


Figure 3.14: Comparison of the volume averaged liver porosity against increase in sinusoidal blood pressure at the portal tracts between the 3D hyperelastic model (solid line) and 2D linear elastic model (dashed line).

3.9.4.3 Total Blood Flux

The result of the total volume flux of blood into the 3D hyperelastic liver lobule for varying percentages of sinusoidal blood portal pressure increase, up to 100%, is shown in Figure 3.15. The same figure also has the results of the 2D linear elastic model, the 2D rigid model by Siggers et al. (2014) and the 2D linear elastic model of blood flow only by Bonfiglio et al. (2010). Note that the model by Bonfiglio et al. (2010) uses a different permeability equation (see Equation (30) of their paper) to that of our model. For the purpose of direct comparison, we make use of our permeability equation (2.34) to obtain the numerical results called Adapted Bonfiglio et al. (2010) in Figure 3.15. Also, all the results in Figure 3.15 have been scaled against the normal physiological blood flux $Q_{\text{blood,ref}} = 0.66\,\text{L/min}$.

Apart from the 2D rigid model by Siggers et al. (2014), which exhibits a linear behaviour, all three other models show a non-linear increase in blood flux as the sinusoidal blood pressure is increased. The 3D hyperelastic model shows the steepest increase with pressure, while the 2D linear elastic model and the Adapted Bonfiglio et al. (2010) show the same increase in blood flux with increased blood pressure at the portal tracts (see overlapping red and black dashed lines in Figure 3.15). The difference between the results of blood flux in the 3D hyperelastic model and the 2D linear elastic model is less than 4.5%.

Following Bonfiglio et al. (2010), we also compare our results to the experimental data by Dahmen et al. (2007), who performed stepwise tissue resection on rat livers and measured the

corresponding blood pressure and volume flux in the portal vein. With each percentage increase in resection of the tissue (0%, 30%, 70%, 90%, 95% and 97%), the portal pressure was seen to increase while the volume flux decreased, as expected. In order to obtain results of total blood volume flux against portal pressure in the liver, we scaled the experimental data from Dahmen et al. (2007), for each percentage resection, into that of a whole liver organ. Next, we assumed that an increase in blood pressure in the portal vein translates directly to increase in blood pressure in the sinusoidal portal tracts. We also neglect the results of 95% and 97% liver resection, respectively, since we believe these to be extreme cases and are unlikely to reflect the true physiological dynamics of the flow. Figure 3.16 shows the results of the scaled experimental data compared with the poroelastic models developed in this thesis and the rigid porous model by Siggers et al. (2014). The experimental data has a similar non-linear profile to the results obtained from the 3D hyperelastic and 2D linear elastic liver models. Note that the poroelastic models show total blood flow into the liver, a combination of blood volume flux from the portal vein and the hepatic artery, while the experimental data shows blood volume flux from the portal vein only.

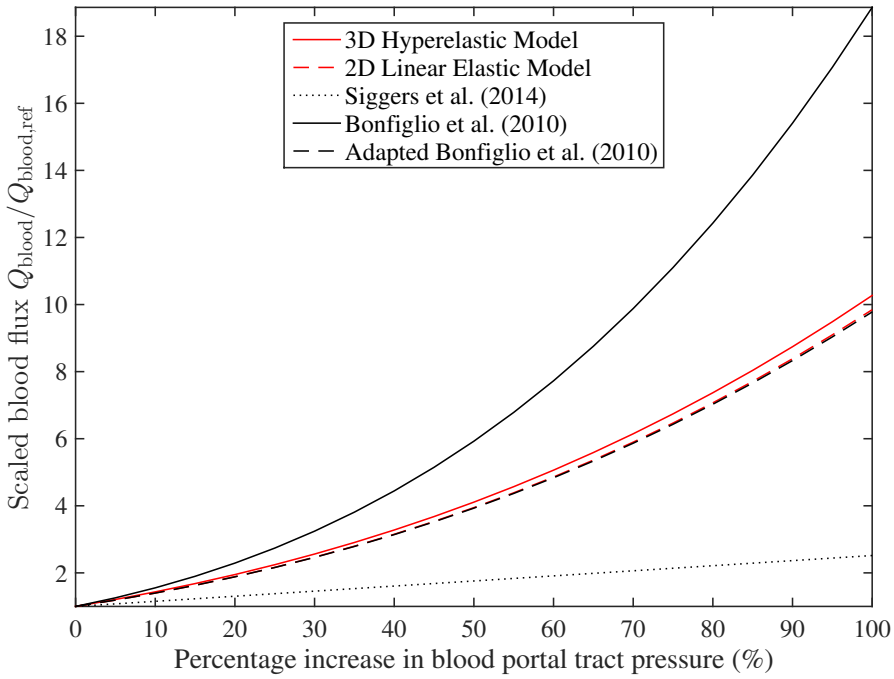


Figure 3.15: Comparison of the total volume flux of blood into the liver against blood sinusoidal portal pressure increase in the 3D hyperelastic model (red, solid line) with the 2D linear elastic model (red, dashed line) and the liver models by Siggers et al. (2014) (black, dotted line) and Bonfiglio et al. (2010) (black, solid and dashed line) .

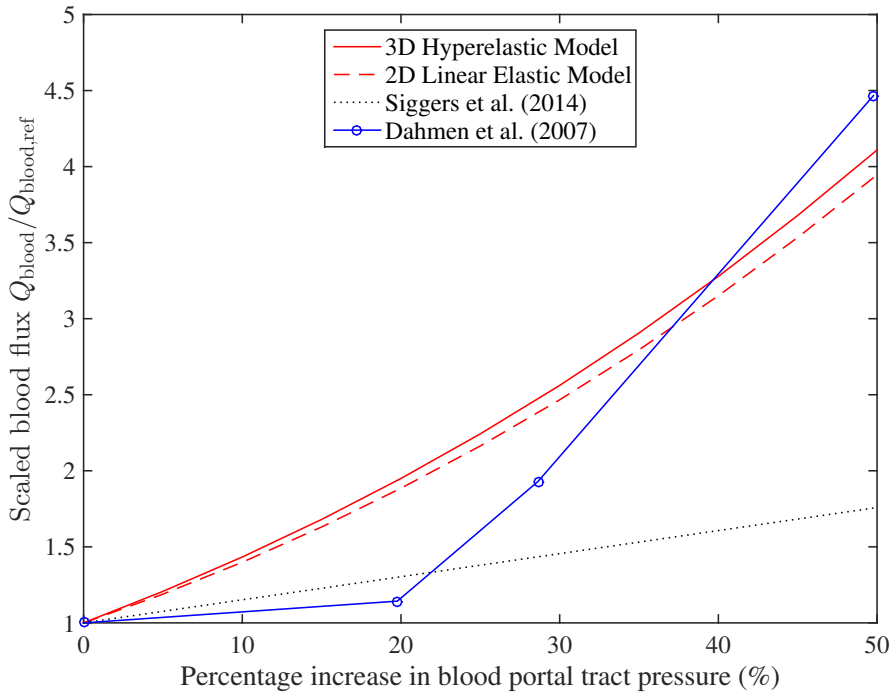


Figure 3.16: Comparison of the total volume flux of blood into the liver against blood sinusoidal portal pressure increase estimated from the 3D hyperelastic model (red, solid line), the 2D linear elastic model (red, dashed line) and the 2D rigid model by Siggers et al. (2014) (black, dotted line), with the experimental data of portal vein volume flux by Dahmen et al. (2007) (blue circles) .

3.9.4.4 Lymphatic Uptake Rate

Estimates of the lymphatic uptake rate within the 3D hyperelastic liver lobule against varying percentage increase in sinusoidal blood portal pressure, up to 100%, is shown in Figure 3.17. The results in Figure 3.17 have been scaled by the normal physiological lymphatic uptake rate $Q_{\text{lymph,ref}} = 0.17\,\text{mL/min}$. Unlike the 2D linear elastic model and the 2D rigid model by Siggers et al. (2014) (also shown in Figure 3.17), lymphatic uptake rate in the 3D hyperelastic model increases non-linearly with increase in sinusoidal blood portal tract pressure. This increase is considerably higher than both the 2D linear elastic model (up to 34% in difference) and the Siggers et al. (2014) model (up to 54% in difference).

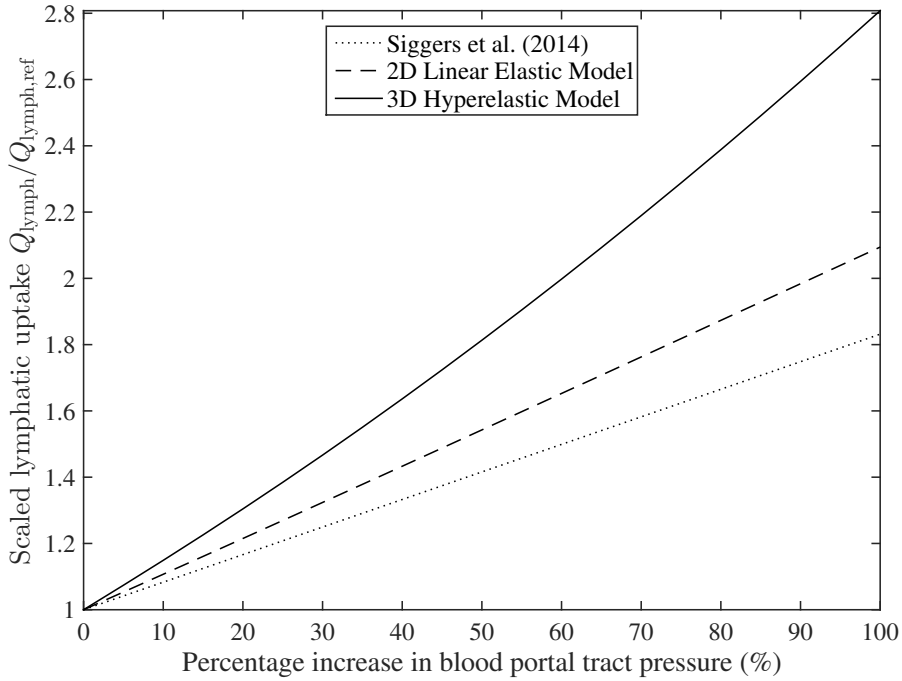


Figure 3.17: Comparison of the total lymphatic uptake within the liver against blood sinusoidal portal pressure between the 3D hyperelastic model (solid line), the 2D linear elastic model (dashed line) and the 2D rigid model by Siggers et al. (2014) (dotted line).

3.9.4.5 Fluid Loss into the Peritoneal Cavity

Fluid loss from the Glissonian–peritoneal surface of the liver into the peritoneal cavity for different percentage increase of sinusoidal blood portal pressure, up to 100%, is shown in Figure 3.18. The values obtained were scaled by the physiological value of peritoneal fluid loss $Q_{\mathrm{L_{ref},PC}} = 0.15\,\mathrm{mL/min}$, and also compared to the results of the 2D linear elastic model and the 2D rigid model by Siggers et al. (2014). As with the 2D linear elastic model, fluid loss into the peritoneal cavity using the 3D hyperelastic model increases non-linearly with sinusoidal portal pressure, for pressure increases up to 100% of the normal physiological case. The difference in fluid loss values between the two models is less than 5%.

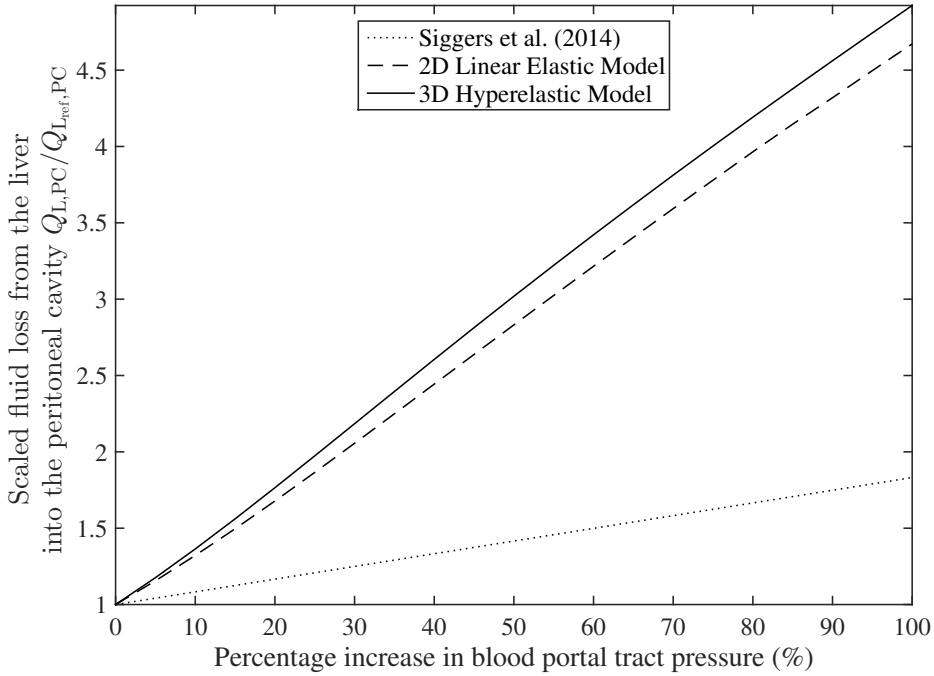


Figure 3.18: Comparison of fluid loss from the liver into the peritoneal cavity between the 3D hyperelastic model (solid line), the 2D linear elastic liver model (dashed line) and the rigid liver model by Siggers et al. (2014) (dotted line), for different percentage increases in blood sinusoidal portal pressure.

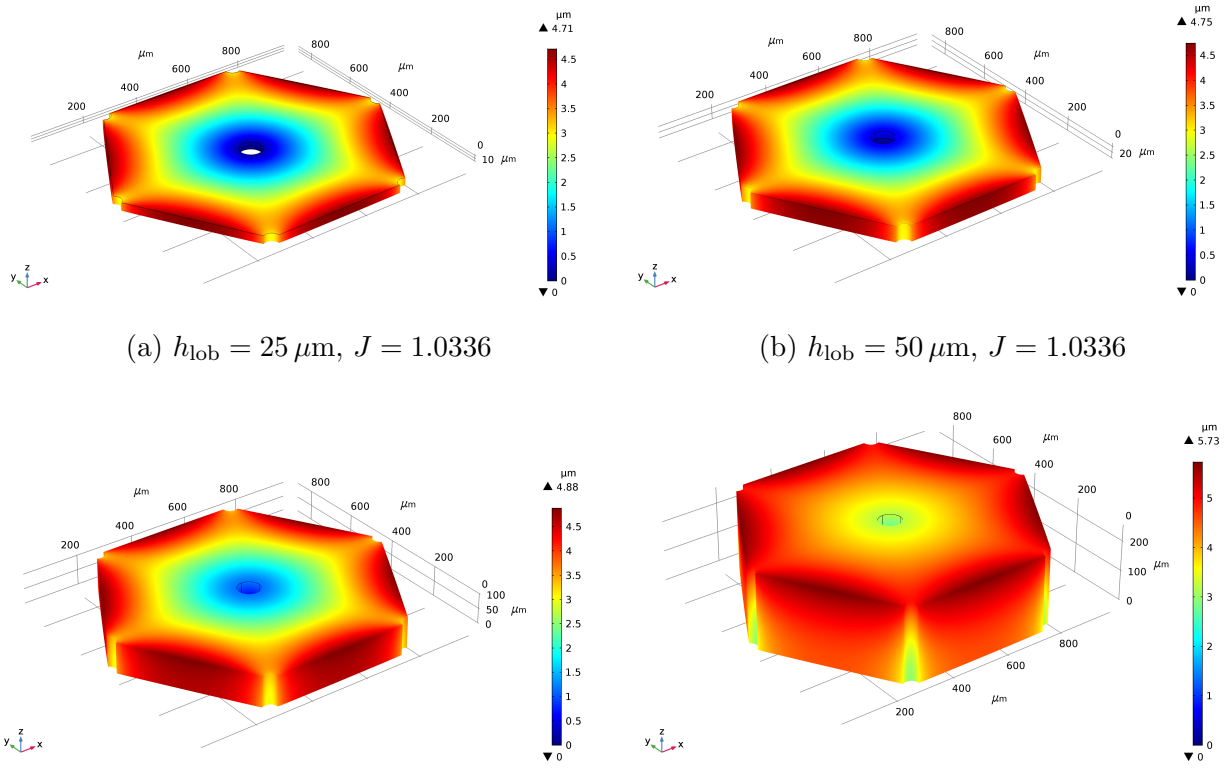
3.9.5 Variation of Boundary Conditions

The numerical results presented in Sections 3.9.2–3.9.4 were obtained using the boundary conditions detailed in Section 3.6. In this section, we consider a few variations to the boundary conditions and look at how they affect the deformation profile of the lobule. These include changes to the height of the lobule, non-uniform pressure increase across the 6 portal tracts and applying a pressure drop along the portal tracts and central vein, rather than a fixed pressure condition.

3.9.5.1 Change in Lobule Height

The lobule height, $h_{\text{lob}} = l_{\text{lob}}/5 = 100\,\mu\text{m}$, was chosen arbitrarily to represent the height of the lobule over which blood pressures in the portal tracts and central vein remain approximately constant. In this section, we consider three other variations of the lobule height, namely: $h_{\text{lob}} = l_{\text{lob}}/20, l_{\text{lob}}/10$ and $l_{\text{lob}}/2$, or $h_{\text{lob}} = 25\,\mu\text{m}, 50\,\mu\text{m}$ and $250\,\mu\text{m}$, respectively. The deformation profiles of the lobule with the different heights are shown in Figure 3.19. For each h_{lob}, we also provide the average volume change ratio J of the lobule. We see that even though the maximum displacement of the lobule increases with increase in h_{lob}, J remains fairly constant to 3 s.f.

following deformation. This tells us that as long as we keep the pressures at the portal tracts and central vein constant, the choice of h_{lob} will not affect our deformation results significantly. Note, however, that the larger we make h_{lob}, the more unrealistic having a constant pressure assumption at the portal tracts and central vein becomes, especially in terms of the fluid flow profiles. Subsequently, we consider the effect of having pressure gradients along the portal tracts and central vein in our model. This is shown later in this section.



(a) $h_{\text{lob}} = 25\,\mu\text{m}$, $J = 1.0336$

(b) $h_{\text{lob}} = 50\,\mu\text{m}$, $J = 1.0336$

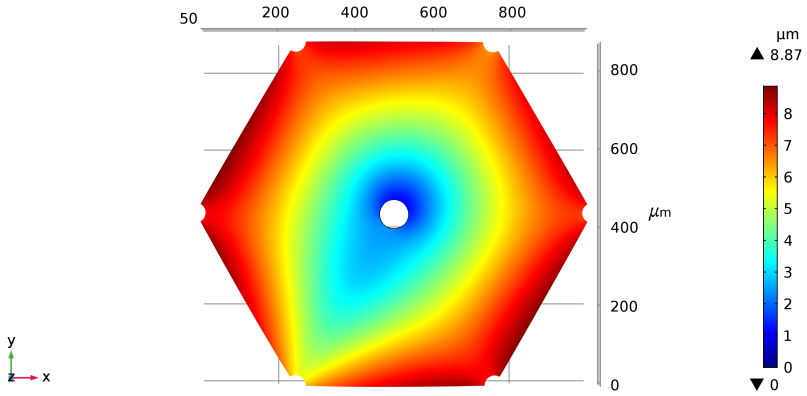
(c) $h_{\text{lob}} = 100\,\mu\text{m}$, $J = 1.0335$

(d) $h_{\text{lob}} = 250\,\mu\text{m}$, $J = 1.0334$

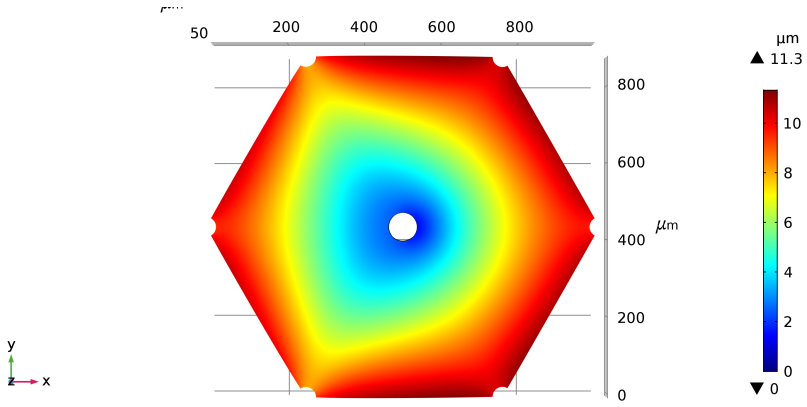
Figure 3.19: Displacement profile of the 3D hyperelastic liver lobule, with average volume change ratio J, for different heights, $h_{\text{lob}} = 25\,\mu\text{m}, 50\,\mu\text{m}$ and $250\,\mu\text{m}$, following a 10% increase in sinusoidal blood portal pressure. Colour bars show the displacement magnitude $|\mathbf{u}|$ and have different ranges in all subfigures.

3.9.5.2 Non-uniform Pressure Change Across Portal Tracts

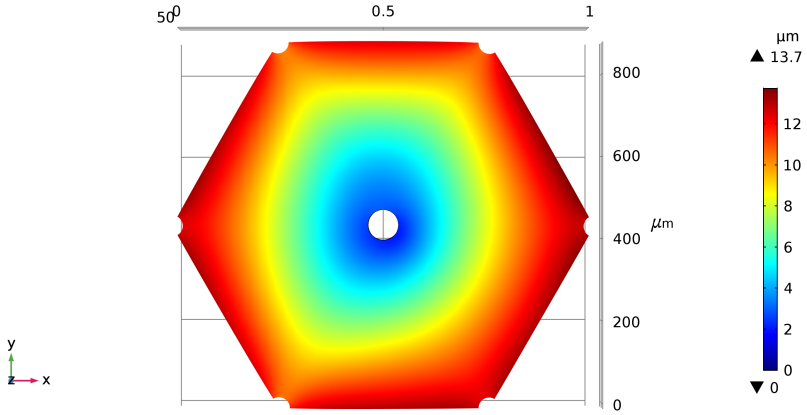
In the results presented so far, we have assumed that pressure increase occurs uniformly across all six portal tracts. This is why we obtain uniform deformation along all six lines of symmetry of the hexagonal liver lobule. This is not necessarily true in the physiological case. Pressure increase can vary in the portal tracts of a single lobule. For example, in Figure 3.20, we show the effect of non-uniform pressure increase on deformation in the tissue. In Figure 3.20a, blood pressure in the bottom, left-hand portal tract has been increased by 50%, while the other five portal tracts have a blood pressure increase of 10% only. What we observe is that tissue deformation is still symmetric, but only along 2 lines of symmetry. Figure 3.20b has both the bottom and top left-hand blood portal tract pressures increased by 50%, while Figure 3.20c has in addition the top, right-hand portal tract increased by 50%. The rest of the portal tracts in Figures 3.20b and 3.20c have a 10% increase in blood pressure only. In all 3 figures, deformation of the tissue has only 2 lines of the symmetry. The volume change ratio J increases, as expected, non-linearly from $J = 1.05$ in Figure 3.20a to $J = 1.09$ in Figure 3.20c, as it approaches the value $J = 1.15$, which is the average volume change in a lobule with uniform blood pressure increase of 40% in all six portal tracts.



(a) $J = 1.0537$



(b) $J = 1.0583$



(c) $J = 1.0894$

Figure 3.20: Displacement profile of the 3D hyperelastic liver lobule, with average volume change ratio J, for different cases of non-linear pressure increase. Sinusoidal blood portal pressure is increased by 50% in (a) one portal tract (b) two portal tracts and (c) three portal tracts, while the rest of the portal tracts have a 10% increase in pressure. Colour bars show the displacement magnitude and have different ranges in all subfigures.

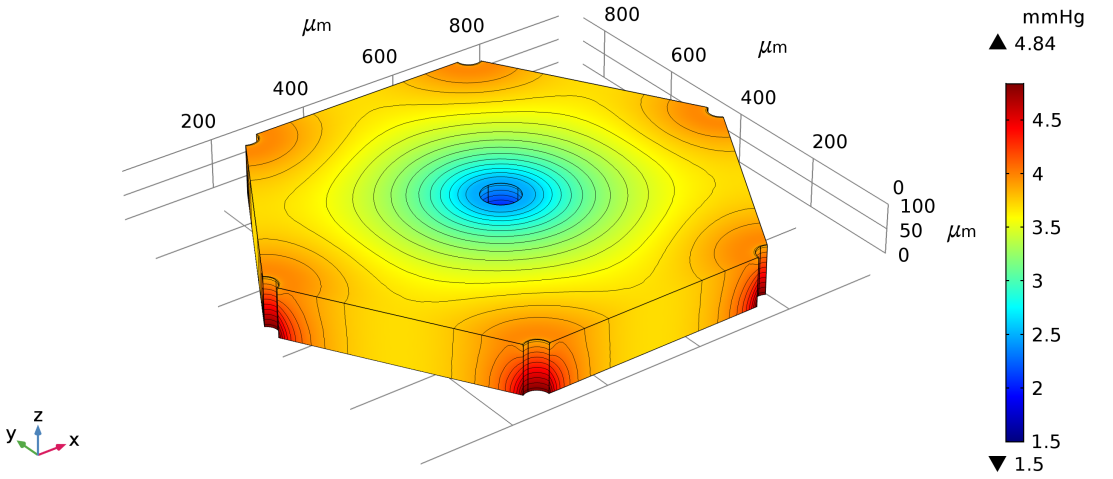
3.9.5.3 Pressure Drop Across Portal Tracts and Central Vein

Finally, we have made a generalised assumption that blood pressure along the portal tracts and central vein is constant. This assumption is valid as long as we can find the appropriate height h_{lob} of the lobule such that blood pressure is approximately constant along the z–axis. As there is very little information on the physiological height of the lobules, this height h_{lob} has to be chosen arbitrarily. In reality, there exists a pressure gradient along the longitudinal direction of the portal tracts and central vein, which drives the flow of blood along the arterioles and venule, respectively. In this section, we investigate the effect of pressure gradient on expansion of the liver tissue. Note that it is unclear what the direction of axial blood flow in the portal tracts and central vein of the liver lobule is in vivo. For this reason, we shall consider the two possible cases of counter and parallel flow directions along the portal tracts and central vein.

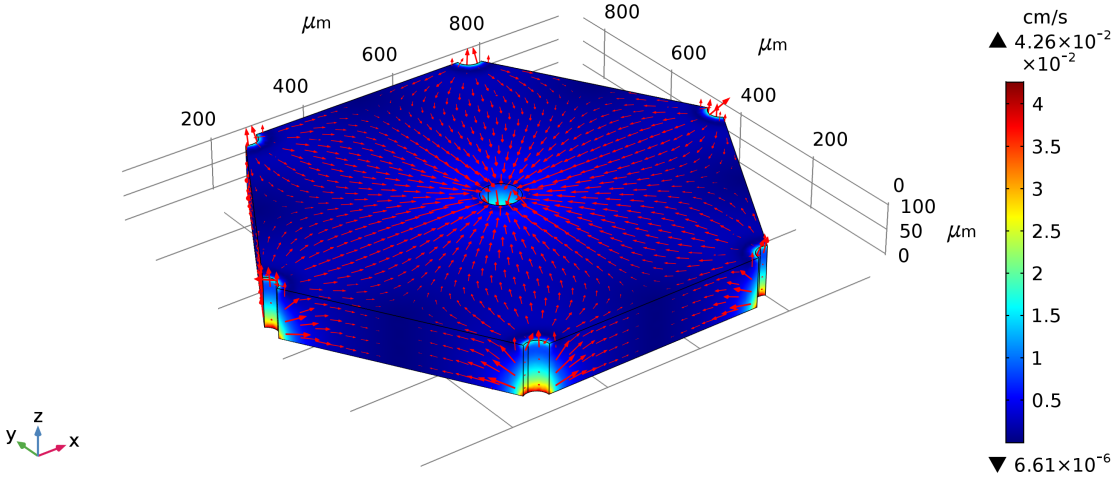
Counter Blood Flow Direction

Here, we assume that the direction of blood flow is from the bottom to the top within the portal tracts, so blood pressure is highest at the bottom and lowest at the top. On the opposite side, flow direction in the central vein is assumed to be from the top to the bottom, so blood pressure is highest at the top and lowest at the bottom. To that end, we impose the boundary conditions $p_s^{pt} = p_{s,\text{ref}}^{pt} - 1.33 \times 10^6 z$ and $p_s^{cv} = p_{s,\text{ref}}^{cv} + 1.33 \times 10^6 z$ along the portal tracts and central vein, respectively, where $p_{s,\text{ref}}^{pt}$ and $p_{s,\text{ref}}^{cv}$ are constants defined previously. This condition ensures that there is a 1 mmHg pressure drop across the height of the lobule in the portal tracts and central vein, respectively.

For example, we consider the deformation of the tissue following a 10% increase in sinusoidal blood portal pressure. Having a 1 mmHg pressure drop along the portal tracts and central vein has a negligible effect on tissue deformation. The average volume change ratio obtained is $J = 1.0313$, which is almost the same as that of the constant pressure boundary condition ($J = 1.0335$) to 3 significant figures. This result also holds for higher values of sinusoidal blood portal pressure increase. In Figure 3.21, we show the resultant blood pressure distribution and blood pore velocity of the lobule. As expected, there is now an observable pressure drop along the portal tracts and central vein of the lobule (see Figure 3.21a). As a consequence of this, we now also see a velocity gradient along the portal tracts and central vein of the lobule in Figure 3.21b, i.e. the velocity has a non-zero z–component.



(a) p_s



(b) $\mathbf{v}_s/\varphi_s$

Figure 3.21: (a) Blood pressure distribution and (b) average pore velocity in a 3D deformed hyperelastic liver lobule following a 10% increase in sinusoidal blood portal pressure with a 1 mmHg pressure gradient along the portal tracts and central vein. Blood flows in opposite directions along the portal tracts and central vein. Colour bar shows (a) pressure magnitude and (b) pore velocity magnitude. Pressure contours at intervals of 0.1 mmHg are also plotted in (a), while (b) has arrows that show the direction of flow, proportional to the magnitude of velocity.

Parallel Blood Flow Direction

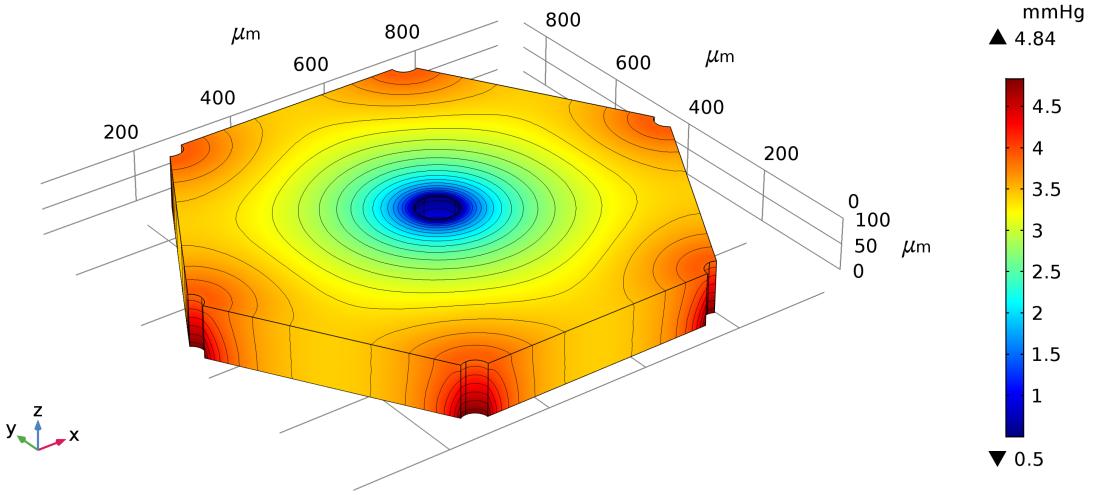
Now, we assume that blood flows in a parallel direction in the portal tracts and central veins of the liver lobules, with the pressure being highest as the bottom and lowest at the top, respectively. Again, we impose a 1 mmHg pressure drop across the portal tracts and central vein

of the lobule using the boundary conditions $p_s^{pt} = p_{s,\text{ref}}^{pt} - 1.33\times10^6 z$ and $p_s^{cv} = p_{s,\text{ref}}^{cv} - 1.33\times10^6 z$, respectively, where $p_{s,\text{ref}}^{pt}$ and $p_{s,\text{ref}}^{cv}$ are constants defined previously.

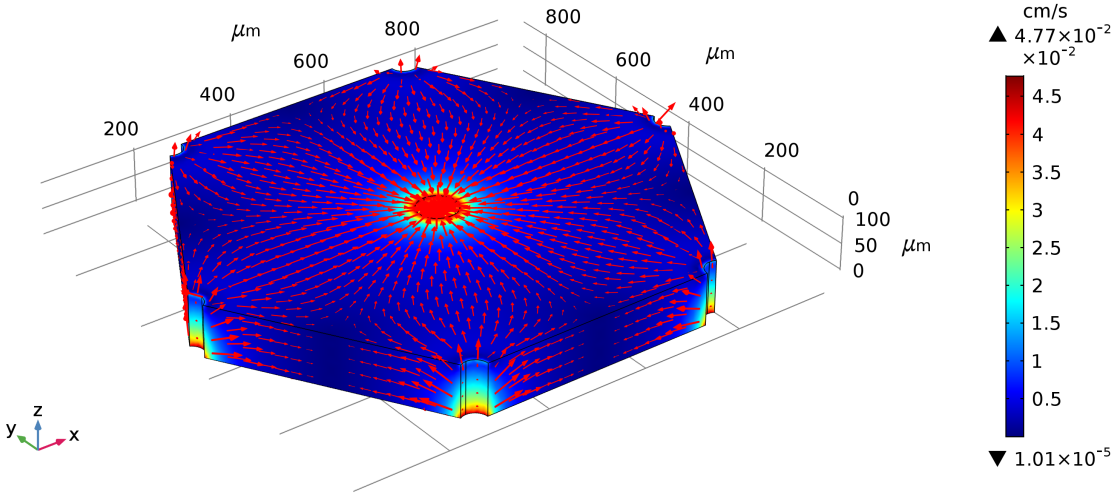
Following a 10% increase in sinusoidal blood portal pressure, and having a 1 mmHg pressure drop along the portal tracts and central vein has a negligible effect on tissue deformation, with the average volume change ratio obtained being equal to that of the constant pressure boundary condition ($J = 1.0335$). The blood pressure and pore velocity distributions are presented in Figures 3.22a and 3.22b, showing gradients along the portal tracts and central vein, respectively.

In order to compare our results of counterflow versus parallel flow in the lobule, we zoom into our solutions by considering a cut surface along the x–z plane, going from one portal tract to an opposite portal tract and across the central vein (see Figure 3.23). Figures 3.23a and 3.23b show the blood pressure distributions following a 10% increase in sinusoidal blood portal pressure. In the counterflow direction simulation (Figure 3.23a), we observe the blood pressure decreasing from the bottom of the portal tracts to the top while it decreases from the top of the central vein to the bottom. In the parallel flow direction simulation (Figure 3.23b), we observe the blood pressure decreasing from the bottom of the portal tracts and central vein to the top, respectively. Both results are expected based on the imposed boundary conditions.

Figures 3.23c and 3.23d show the blood flow patterns that will be observed based on either counterflow or parallel flow directions, respectively. In counterflow (Figure 3.23c), the direction of blood flow goes from the bottom of the portal tracts, towards the top, across the sinusoids and down into the central vein. Under parallel flow (Figure 3.23d), blood flows from the bottom of the portal tracts, towards the top, across the sinusoids and up into the central vein. Note that the maximum blood pore velocity is higher in the central vein of the parallel flow direction, compared to the counterflow direction.

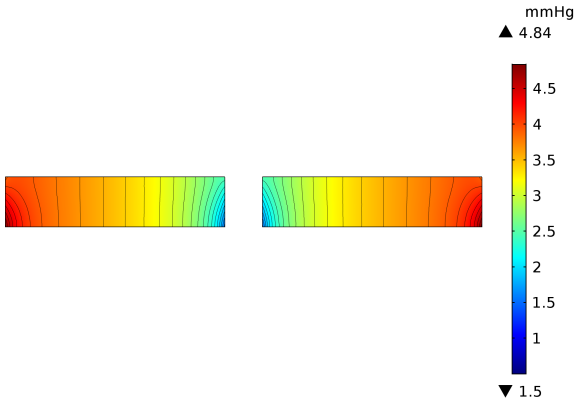


(a) p_s

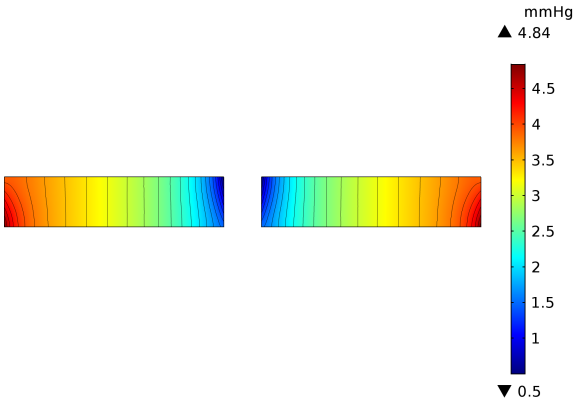


(b) $\mathbf{v}_s/\varphi_s$

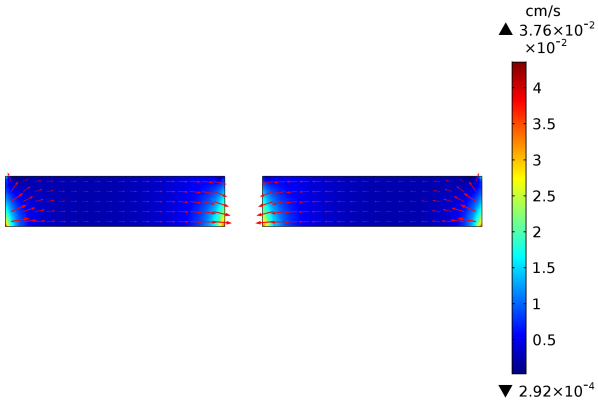
Figure 3.22: (a) Blood pressure distribution and (b) average pore velocity in a 3D deformed hyperelastic liver lobule following a 10% increase in sinusoidal blood portal pressure with a 1 mmHg pressure gradient along the portal tracts and central vein. Blood flows in a parallel direction along the portal tracts and central vein. Colour bar shows (a) pressure magnitude and (b) pore velocity magnitude. Pressure contours at intervals of 0.2 mmHg are also plotted in (a), while (b) has arrows that show the direction of flow, proportional to the magnitude of velocity.



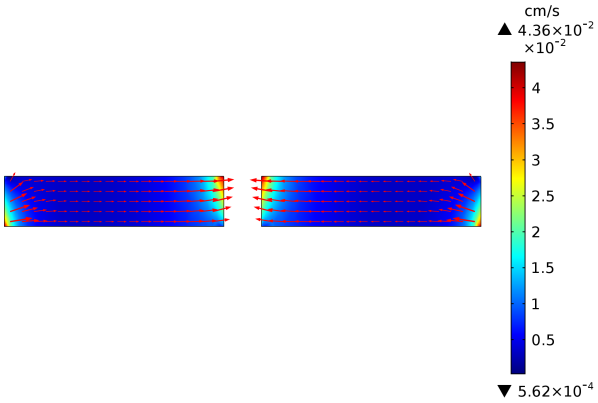
(a) p_s in counterflow direction



(b) p_s in parallel flow direction



(c) $\mathbf{v}_s/\varphi_s$ in counterflow direction



(d) $\mathbf{v}_s/\varphi_s$ in parallel flow direction

Figure 3.23: Cut surface of the 3D hyperelastic lobule along the x–y plane going from portal tract (left-hand side edge), across the central vein (space in the middle) and to another portal tract (right-hand side egde) showing the (a) blood pressure and (c) blood pore velocity distribution assuming opposite flow directions in the portal tracts and central vein and (b) blood pressure and (d) blood pore velocity distribution assuming parallel flow directions in the portal tracts and central vein. The results shown have a 1 mmHg pressure gradient along the portal tracts and central vein, following a 10% increase in sinusoidal blood portal pressure. Colour bars in (a) and (b) are the same and show pressure magnitude while those in (c) and (d) are the same and show pore velocity magnitude. Pressure contours are at intervals of 0.2 mmHg in both (a) and (b) while (c) and (d) have arrows that show the direction of flow and are proportional to the magnitude of pore velocity.

3.10 Summary and Conclusion

In this chapter, we extended the 2D linear poroelastic model of the liver developed in Chapter 2, into a 3D hyper-poroelastic model. The hyperelastic model makes use of a strain energy function, which gives a better representation of the non-linear elastic behaviour of the liver tissue under high stress. For small strains, the hyperelastic model approximates to the linear elastic model in terms of tissue deformation. The 3D representation of the liver tissue allows us to study the z–plane deformations of the tissue, unlike in the 2D case.

With the numerical results obtained, we were able to make comparisons between the 3D hyperelastic model and the 2D linear elastic model. In all the results, the 3D hyperelastic model gave higher values than that of the 2D linear elastic model, as sinusoidal blood portal pressure was increased. However, for example, the difference in values obtained for the volume change ratio J in the two models was less than 2%. Other estimated parameter values, such as average liver porosity, total blood flux volume into the liver and fluid loss across the liver surface into peritoneal cavity, all had a difference of less than 5% between the two models. The only parameter value with the most significant difference was the total lymphatic uptake by the liver lobules, which had a difference of up to 34% in values for the sinusoidal portal pressures considered, between the two models. This is probably due to the assumption that lymphatic conductance coefficient scales proportionally to J.

Overall, we can conclude that as a first approximation, the 2D linear elastic model does give a fairly good representation of tissue deformation under normal physiological pressures. However, at higher blood pressures, the 3D hyperelastic model gives us better results, which is expected. Since the main motivation of this study is to study the dynamics of flow in the diseased liver, which typically has very high portal pressures, we will make use of the 3D hyperelastic model developed in this chapter to study the effect of tissue fibrosis and portal hypertension on fluid dynamics in the liver. This is covered in Chapter 4. We also make use of the 3D hyperelastic model to develop a mathematical model of fluid exchange in the peritoneal cavity and investigate the development of ascites in Chapter 5.

Chapter 4

Liver Cirrhosis

4.1 Introduction

As mentioned previously, cirrhosis of the liver occurs as a result of long term damage to the tissue due to liver diseases. It is characterised by scarring of the healthy tissue, i.e. fibrosis, and the formation of regenerative nodules, which leads to a global increase in tissue stiffness and vascular resistance. This necessitates a higher blood portal pressure, i.e. portal hypertension, in order to filter the large volume of blood in the body. In this Chapter, we will make use of the 3D hyperelastic liver model developed in Chapter 3 to study the effects of portal hypertension and tissue fibrosis on fluid flow and deformation of the liver tissue. This entails looking at changes to the sinusoidal portal pressure, bulk tissue stiffness and permeability, and conductivity of the Glisson's capsule. We will investigate the changes in 3 progressive stages of the diseased liver: mild fibrosis, severe fibrosis and cirrhosis, and compare them against the case of a healthy liver tissue.

4.2 Portal Hypertension

Portal hypertension refers to a significant increase in blood pressure within the portal vein. Under normal physiological conditions, any slight increase in blood pressure within the portal vein, for example after a heavy meal, is mediated through auto-regulation of the blood volume in the vessels so that the blood pressure at the portal tracts remains fairly constant. In the case of a diseased liver, long term increase in blood portal pressure leads to a marked increase in blood pressure at the portal tracts of the liver. The effect of increased blood sinusoidal portal pressure alone on the flow and deformation of the liver lobule has been shown already in Section 3.9.4. However, hypertension at the portal tracts is unlikely to occur without prior damage to liver tissue. In the next Section 4.3, we study the effect of tissue fibrosis on flow and deformation in the liver, while in Section 4.4 we study the combined effect of both portal hypertension and tissue fibrosis on the liver organ.

4.3 Tissue Fibrosis

In this section, we look at two consequences of tissue fibrosis on the liver. The first is a general increase of the bulk stiffness of the tissue and the second is changes to the permeability of the tissue. Thirdly, since we are also interested in fluid loss via the outer surface of the liver, we will look at changes to the hydraulic conductivity of the Glisson's capsule due to membrane damage. We consider these effects in isolation in this section, and together in conjunction with portal hypertension in Section 4.4. The formation of regenerative nodules observed in cirrhotic liver is neglected in this thesis and has been left for future studies (Section 6.2).

4.3.1 Tissue Stiffness

Increased tissue stiffness is often indicative of the presence of fibrotic tissue within the liver. A normal healthy liver tissue can have a stiffness value up to 6 kPa (Mueller and Sandrin, 2010). Above 6 kPa, fibrosis has started setting in, and the stiffer the tissue the higher the degree of fibrosis (Mueller and Sandrin, 2010). The measurement of the amount of fibrosis in the liver is known as staging, and there are five stages of liver fibrosis widely accepted in the medical community: F0 - no scarring of tissue; F1 - minimal scarring; F2 - significant fibrosis; F3 - severe fibrosis; F4 - advanced scarring/cirrhosis. By varying the stiffness of the liver tissue, we can simulate different stages of liver diseases as categorised by Mueller and Sandrin (2010) and listed in Table 4.1.

Liver Stiffness	**Classification**
Up to 6 kPa	Normal, F0
6 kPa − 8 kPa	Mild fibrosis, F1–F2
$>$ 8 kPa	Severe fibrosis, F3
$>$ 12.5 kPa	Advanced fibrosis/Cirrhosis, F4

Table 4.1: Categorisation of liver tissue stiffness at different stages of tissue fibrosis by Mueller and Sandrin (2010).

The effect of increased bulk tissue stiffness on tissue deformation and fluid flow using the 3D hyperelastic liver, following a 10% increase in blood sinusoidal portal pressure, is shown in Figures 4.1–4.6. All the parameters considered, including volume change ratio (Figure 4.1), average blood Darcy velocity (Figure 4.2), average interstitial fluid Darcy velocity (Figure 4.3), total blood flux (Figure 4.4), lymphatic uptake rate (Figure 4.5) and fluid loss into the peritoneal cavity (Figure 4.6) decrease exponentially with increase in tissue stiffness. These results highlight the changes in flow profiles that occur in a fibrotic liver, compared to a normal healthy liver, leading to decreased blood perfusion observed in diseased patients.

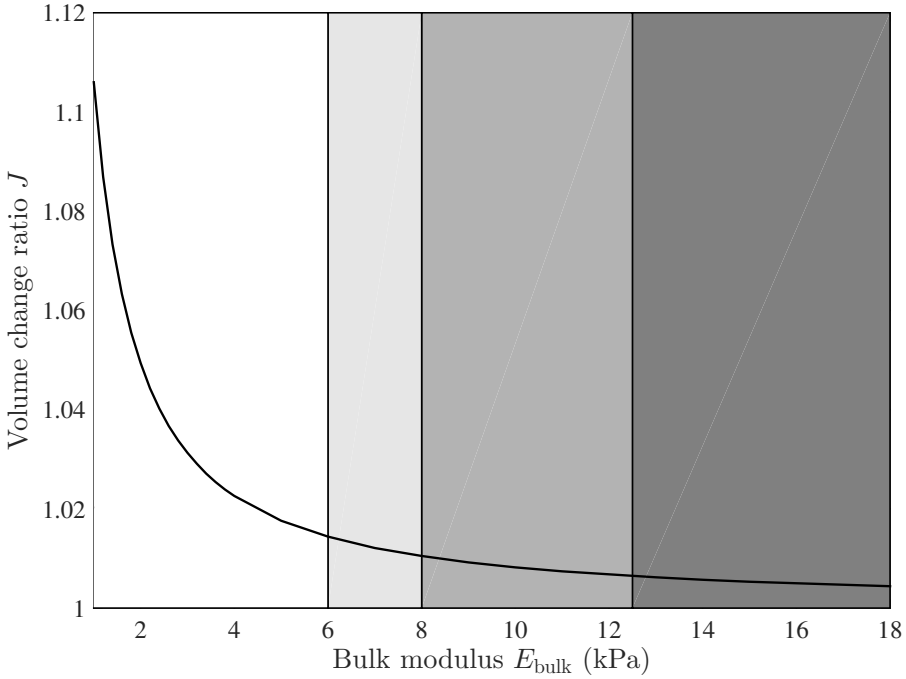


Figure 4.1: Effect of change of bulk modulus E_{bulk} on volume change ratio J in the 3D hyperelastic liver lobule, following a 10% increase in blood sinusoidal portal tract pressure. The *white* shade denotes normal tissue, *light grey* shade denotes mild fibrosis and *medium grey* shade denotes severe fibrosis and *dark grey* shade denotes advanced fibrosis/cirrhosis.

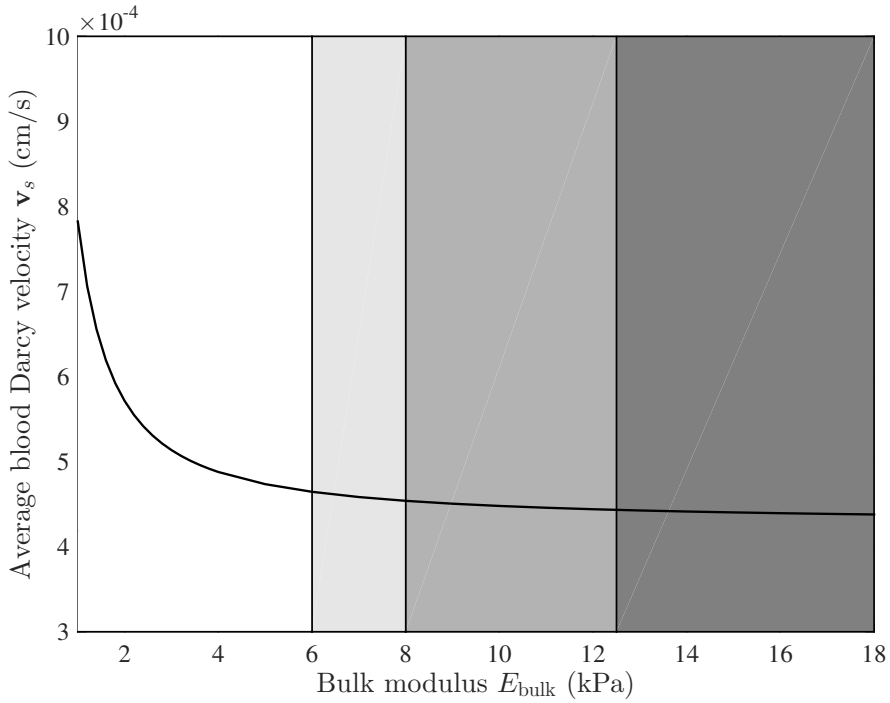


Figure 4.2: Effect of change of bulk modulus E_{bulk} on average blood Darcy velocity $\mathbf{v}_s$ in the 3D hyperelastic liver, following a 10% increase in blood sinusoidal portal tract pressure. The *white* shade denotes normal tissue, *light grey* shade denotes mild fibrosis and *medium grey* shade denotes severe fibrosis and *dark grey* shade denotes advanced fibrosis/cirrhosis.

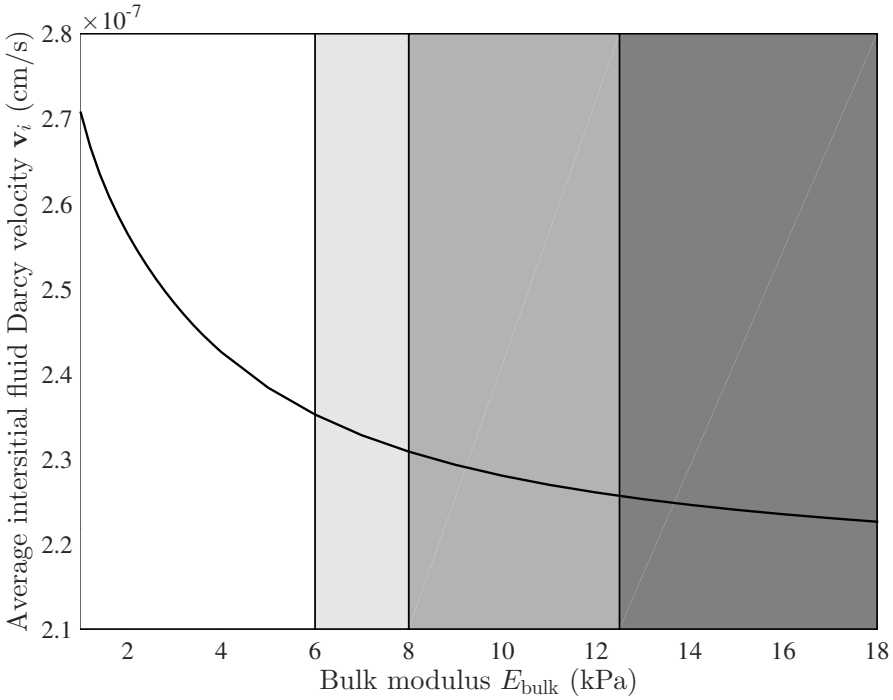


Figure 4.3: Effect of change of bulk modulus E_{bulk} on average interstitial fluid Darcy velocity $\mathbf{v}_i$ in the 3D hyperelastic liver, following a 10% increase in blood sinusoidal portal tract pressure. The *white* shade denotes normal tissue, *light grey* shade denotes mild fibrosis and *medium grey* shade denotes severe fibrosis and *dark grey* shade denotes advanced fibrosis/cirrhosis.

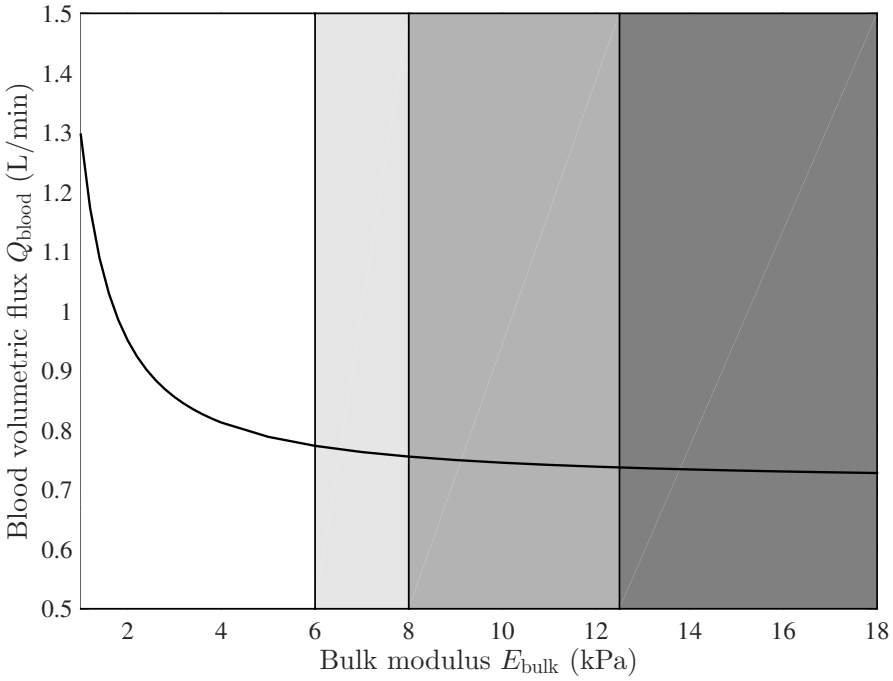


Figure 4.4: Effect of change of bulk modulus E_{bulk} on the total blood flux Q_{blood} in the 3D hyperelastic liver, following a 10% increase in blood sinusoidal portal tract pressure. The *white* shade denotes normal tissue, *light grey* shade denotes mild fibrosis and *medium grey* shade denotes severe fibrosis and *dark grey* shade denotes advanced fibrosis/cirrhosis.

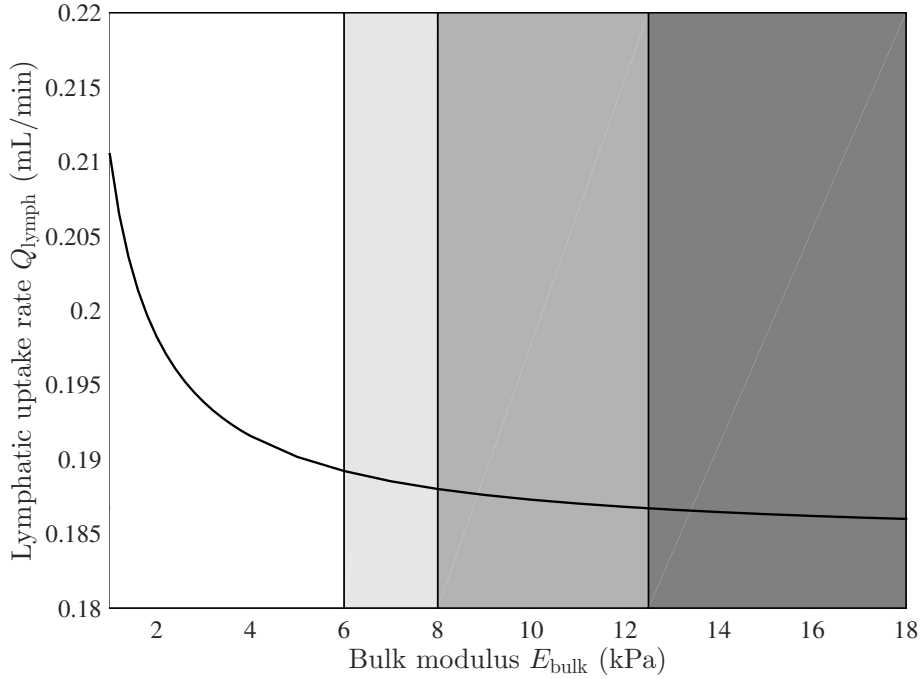


Figure 4.5: Effect of change of bulk modulus E_{bulk} on the lymphatic uptake Q_{lymph} in the 3D hyperelastic liver, following a 10% increase in blood sinusoidal portal tract pressure. The *white* shade denotes normal tissue, *light grey* shade denotes mild fibrosis and *medium grey* shade denotes severe fibrosis and *dark grey* shade denotes advanced fibrosis/cirrhosis.

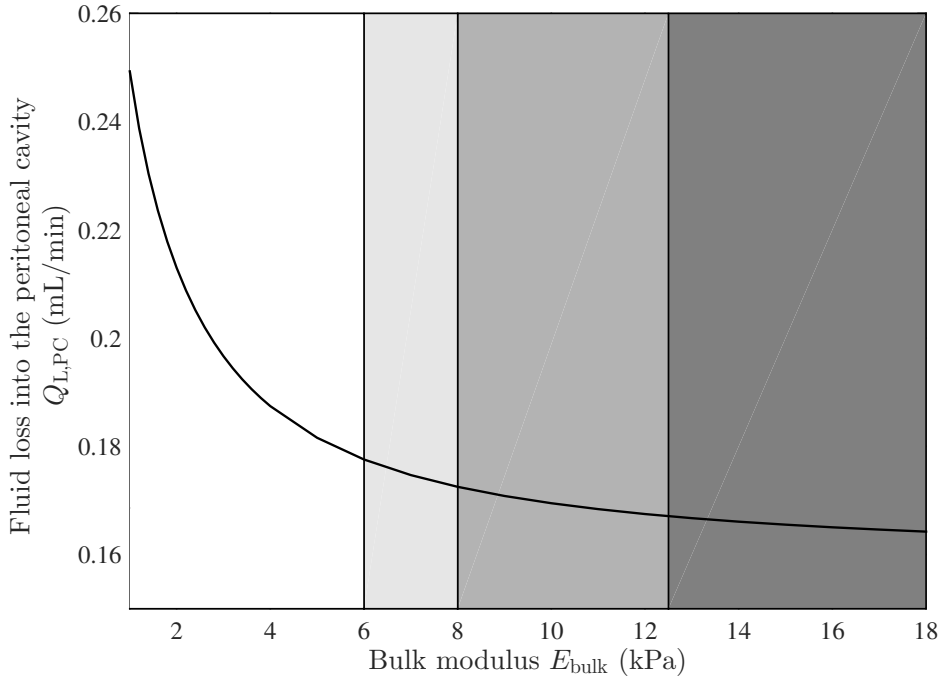


Figure 4.6: Effect of change of bulk modulus E_{bulk} on the fluid loss into the peritoneal cavity $Q_{\text{L,PC}}$ in the 3D hyperelastic liver, following a 10% increase in blood sinusoidal portal tract pressure. The *white* shade denotes normal tissue, *light grey* shade denotes mild fibrosis and *medium grey* shade denotes severe fibrosis and *dark grey* shade denotes advanced fibrosis/cirrhosis.

4.3.2 Changes in Tissue Permeability

In addition to increased tissue stiffness, the presence of fibrotic tissue also leads to the decrease in the amount of interstitial space due to the formation of scar tissue. This in turn decreases the permeability of the interstitial space of the liver. In this section, we vary the reference interstitial space permeability $\kappa_{i,\text{ref}}$ in order to study its effect on deformation and flow within the liver tissue.

Average interstitial fluid velocity decreased significantly with decrease in $\kappa_{i,\text{ref}}$ (see Figure 4.7), which is expected. Changes in $\kappa_{i,\text{ref}}$ had negligible effects on volume change ratio ($< 0.4\%$), average blood velocity ($< 0.3\%$), and total blood flux ($< 0.04\%$) in our model. In the case of a single interior lobule, changes to lymphatic uptake rate were also negligible ($< 0.07\%$). However, when we considered the case of the lobule lattice close to the liver surface, lymphatic uptake rate increased as $\kappa_{i,\text{ref}}$ was decreased (see Figure 4.8). We believe this is due to the pooling of interstitial fluid close to the liver surface, since the conductivity of the Glissonian–peritoneal membrane was kept constant in the computations. This also resulted in a decrease of fluid loss into the peritoneal cavity as $\kappa_{i,\text{ref}}$ was decreased (see Figure 4.9). In all Figures 4.7–4.9, the blood sinusoidal portal pressure was increased by 10% of its reference value and kept constant throughout.

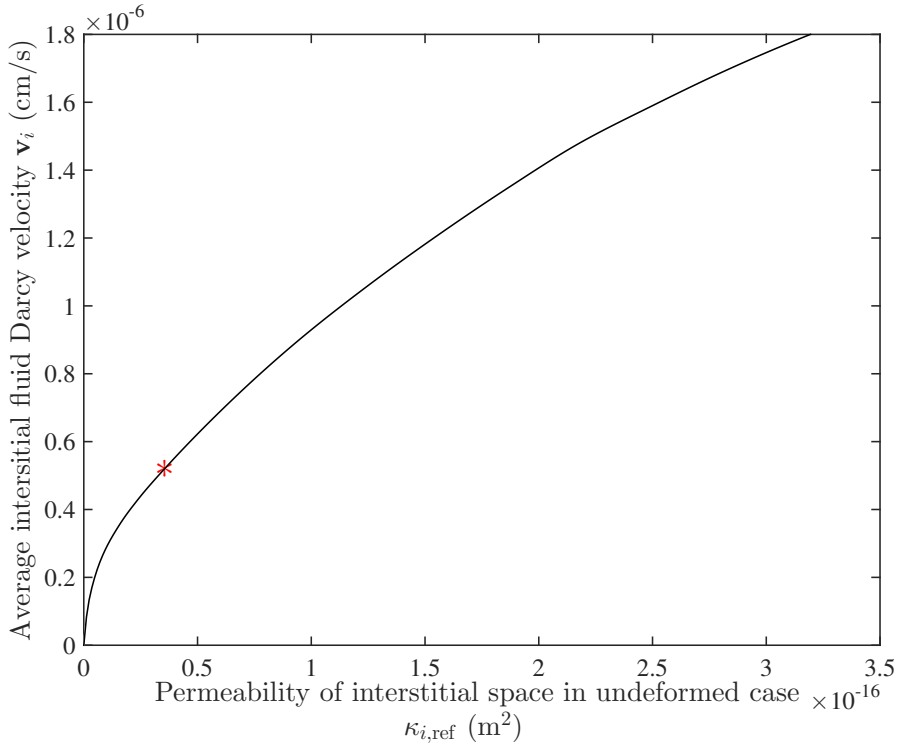


Figure 4.7: Effect of change of reference permeability of the interstitial space $\kappa_{i,\text{ref}}$ on average interstitial fluid Darcy velocity $\mathbf{v}_i$ in the 3D hyperelastic liver, following a 10% increase in blood sinusoidal portal tract pressure. The asterisk $*$ marks the physiological value.

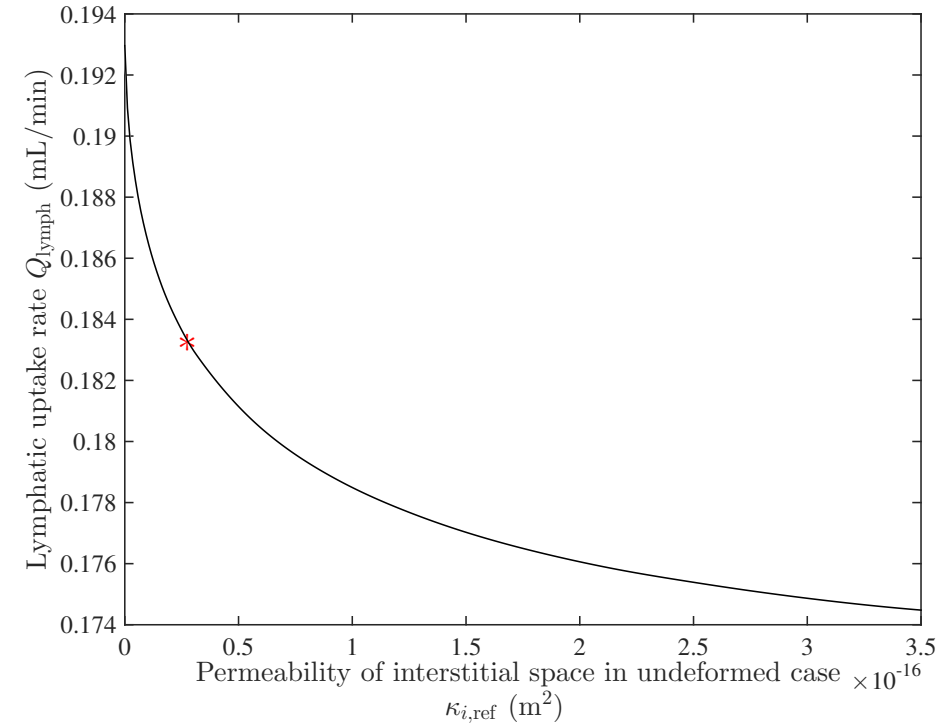


Figure 4.8: Effect of change of reference permeability of the interstitial space $\kappa_{i,\text{ref}}$ on the lymphatic uptake Q_{lymph} in the 3D hyperelastic liver, following a 10% increase in blood sinusoidal portal tract pressure. The asterisk $*$ marks the physiological value.

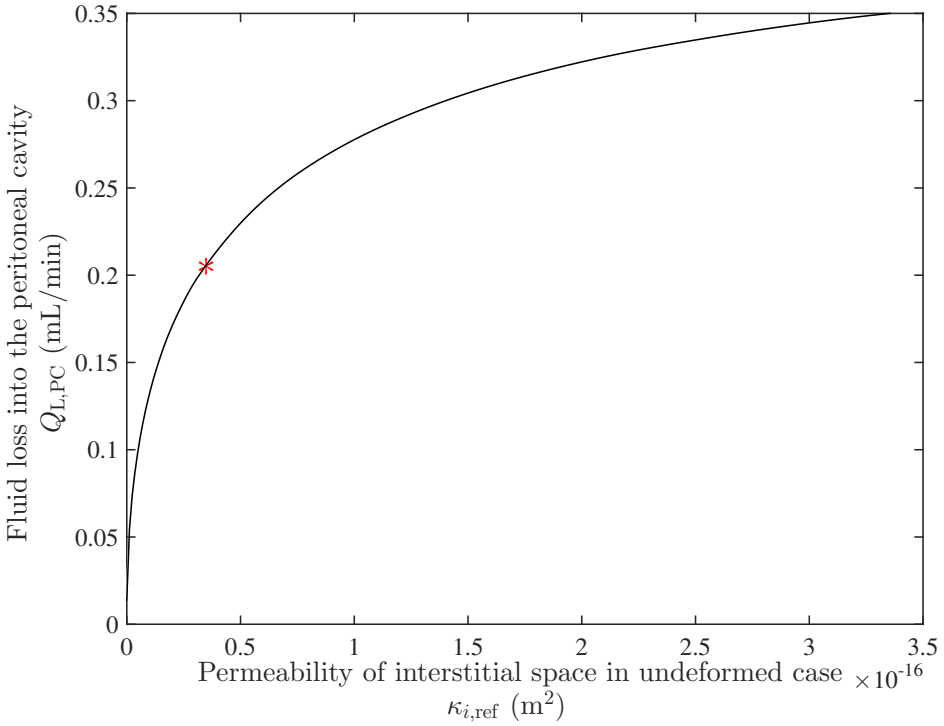


Figure 4.9: Effect of change of reference permeability of the interstitial space $\kappa_{i,\text{ref}}$ on the fluid loss into the peritoneal cavity $Q_{\text{L,PC}}$ in the 3D hyperelastic liver, following a 10% increase in blood sinusoidal portal tract pressure. The asterisk $*$ marks the physiological value.

4.3.3 Conductivity of the Glissonian–Peritoneal Membrane

Recall that the Glissonian–peritoneal membrane is a double membrane consisting of the Glisson's capsule of the liver and the peritoneum of the peritoneal cavity. Though it acts as a barrier between the liver parenchyma and the surrounding peritoneal cavity, it also allows leakage of excess interstitial fluid from one compartment to the other. In Chapter 5, we develop a mathematical model of fluid exchange between the peritoneal cavity and the organs/tissue surrounding it, including the liver, across the peritoneum. We assume that the peritoneum does not provide any limitation to the flow of transcellular fluid across it. Therefore, any limitation of interstitial fluid flow from the liver into the peritoneal cavity, and vice versa, is through the Glisson's capsule. Increase in the conductivity of the Glissonian–peritoneal membrane can occur as a result of damage to the Glisson's capsule, either mechanically or due to liver disease. In this section, we study the effect of changes of the conductivity of the Glissonian–peritoneal membrane M_{GP} on deformation and fluid flow in the liver tissue.

Changes in M_{GP} had negligible effects on the volume change ratio ($< 0.3\%$), average blood velocity ($< 0.3\%$), and total blood flux into the liver ($< 0.01\%$). Both average interstitial fluid velocity and fluid loss into the peritoneal cavity increased with increase in M_{GP} (see Figures 4.10 and 4.12, respectively), while the lymphatic uptake rate decreased (see Figure 4.11). All three parameters level off around $M_{GP} = 2.15 \times 10^6$ m/s/mmHg. Note that in all Figures 4.10–4.12, increased blood sinusoidal portal pressure was kept constant at 110% of its reference value.

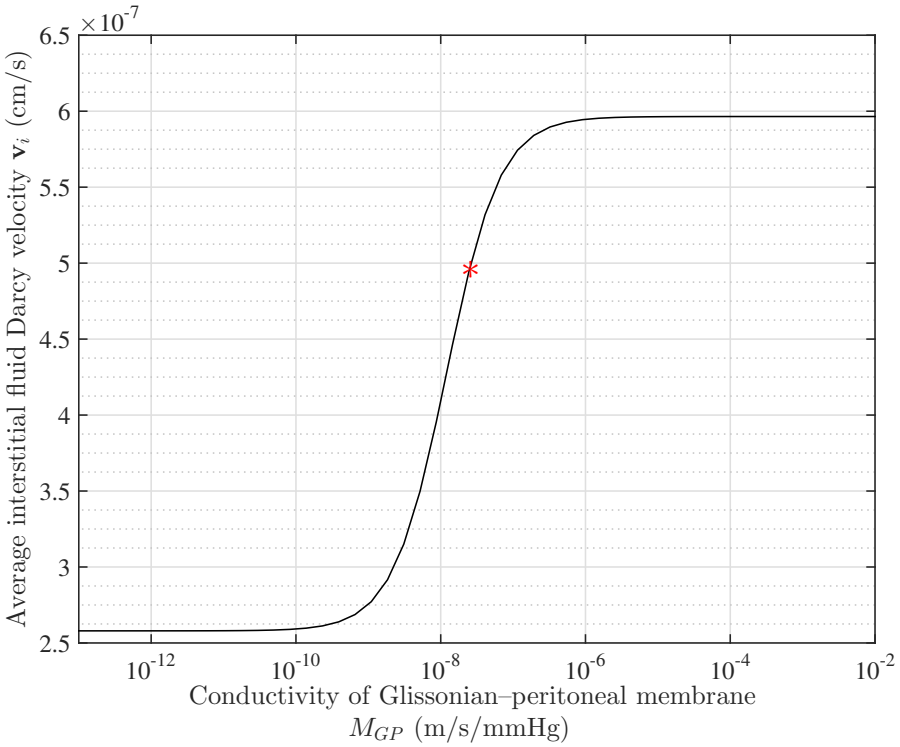


Figure 4.10: Effect of change of conductivity of the Glissonian–peritoneal membrane M_{GP} on average interstitial fluid Darcy velocity $\mathbf{v}_i$ in the 3D hyperelastic liver, following a 10% increase in blood sinusoidal portal tract pressure. The asterisk $*$ marks the physiological value.

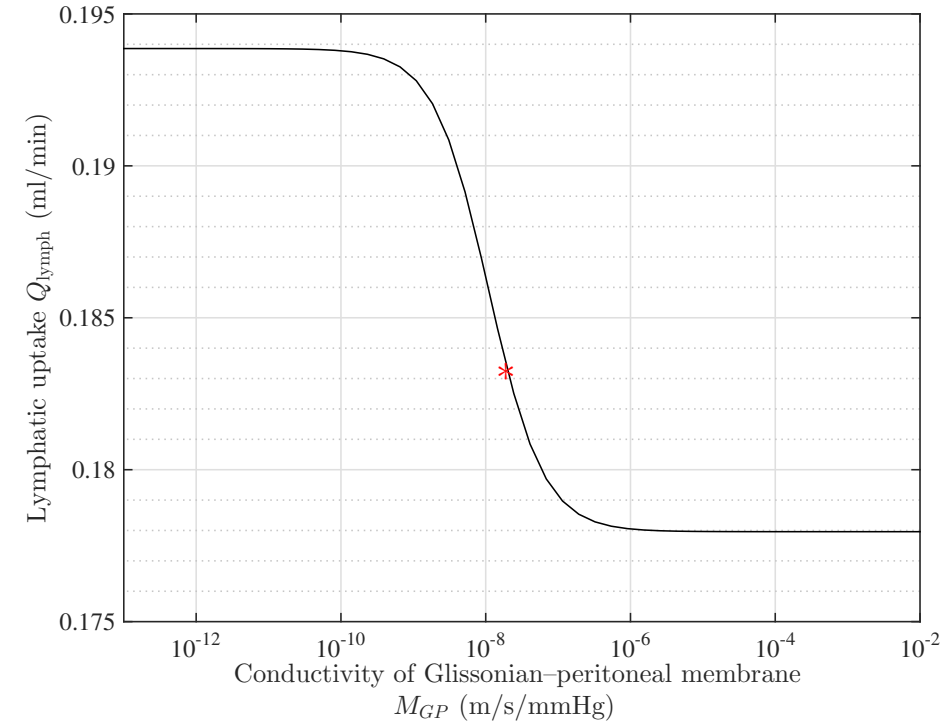


Figure 4.11: Effect of change of conductivity of the Glissonian–peritoneal membrane M_{GP} on the lymphatic uptake Q_{lymph} in the 3D hyperelastic liver, following a 10% increase in blood sinusoidal portal tract pressure. The asterisk $*$ marks the physiological value.

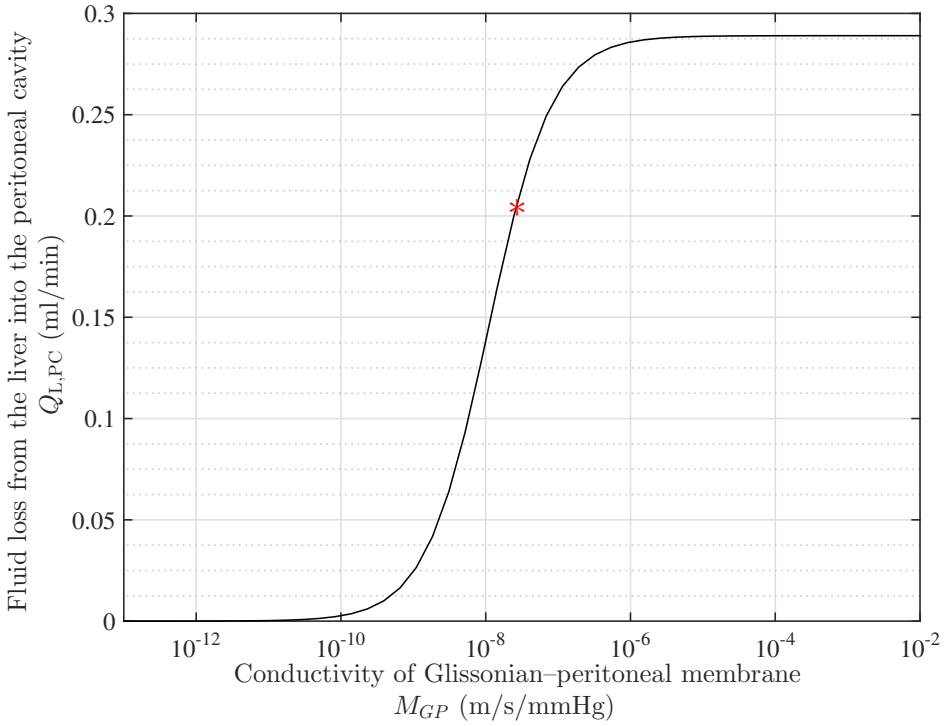


Figure 4.12: Effect of change of conductivity of the Glissonian–peritoneal membrane M_{GP} on the fluid loss into the peritoneal cavity $Q_{\text{L,PC}}$ in the 3D hyperelastic liver, following a 10% increase in blood sinusoidal portal tract pressure. The asterisk $*$ marks the physiological value.

4.4 Combined Portal Hypertension and Tissue Fibrosis

Since portal hypertension rarely occurs without prior tissue damage, we consider the effect of combined portal hypertension and tissue fibrosis in this section. As we increase the blood sinusoidal portal pressure, we will consider 4 different types of liver tissue:

1. Healthy liver tissue; with bulk tissue stiffness $E_{\text{bulk}} = E_{\text{bulk},0} = 2,821\,\text{Pa}$, interstitial space permeability $\kappa_{i,\text{ref}} = \kappa_{i,0} = 3.12 \times 10^{-17}\,\text{m}^2$ and conductivity of the Glissonian–peritoneal membrane $M_{GP} = M_{GP,0} = 2.15 \times 10^{-8}\,\text{m/s/mmHg}$. Note that $E_{\text{bulk},0}$, $\kappa_{i,0}$ and $M_{GP,0}$ are the physiological values used in previous computations for the healthy liver tissue.

2. Mild fibrotic tissue; with $E_{\text{bulk}} = 6,500\,\text{Pa}$, $\kappa_{i,\text{ref}} = 0.75\kappa_{i,0}$ and $M_{GP} = 1.25M_{GP,0}$.

3. Severe fibrotic tissue; with $E_{\text{bulk}} = 8,500\,\text{Pa}$, $\kappa_{i,\text{ref}} = 0.5\kappa_{i,0}$ and $M_{GP} = 5M_{GP,0}$.

4. Cirrhotic tissue, with $E_{\text{bulk}} = 12,500\,\text{Pa}$, $\kappa_{i,\text{ref}} = 0.1\kappa_{i,0}$ and $M_{GP} = 10M_{GP,0}$.

The parameter values listed above were chosen to represent the resultant increase in bulk tissue stiffness, decrease in the permeability of the interstitial space and increase in the conductivity of the Glissonian–peritoneal membrane, with each progressive stage of the diseased liver from a healthy tissue to mild fibrosis, severe fibrosis and finally cirrhosis. Next, we investigate the deformation and fluid flow profiles in each of the 4 tissue types above.

The results of volume change ratio J against portal hypertension for the 4 tissue types are shown in Figure 4.13. Although J increases linearly with portal hypertension, its gradient decreases with each progressive stage of liver disease, with the cirrhotic tissue having the lowest deformation per unit increase in blood portal pressure. This is due to the increased tissue stiffness at each stage of the diseased tissue. Note that the average volume change ratio of the healthy liver tissue has been capped at 1.45, since the tissue is not expected to expand more than this value (Chui et al., 2004). This will be the case for all other parameter estimates considered below, which will be capped when $J = 1.45$.

Next, we look at both sinusoidal blood velocity (Figure 4.14) and interstitial fluid velocity (Figure 4.15) in the 4 tissue types. While the average blood and interstitial fluid Darcy velocities increase with portal hypertension, both parameters decrease significantly with each increase in fibrosis stage of the liver. As expected, the cirrhotic liver tissue has the least increase in fluid flow per each increase in sinusoidal blood portal pressure. Again, highlighting the considerable decrease in blood perfusion and interstitial fluid transport in the diseased liver.

The total blood flux into the liver also decreases with each progressive fibrosis stage (see Figure 4.16), and although the lymphatic uptake rate with the liver also decreases, not much of a difference is observed between the severe fibrotic liver tissue and the cirrhotic liver tissue (see Figure 4.17). Both blood flux and lymphatic uptake increase exponentially with increase in blood portal pressure. Conversely, in order to maintain blood flow through the tissue at

any constant level, the portal pressure must increase in all 4 cases. For example, for the liver to filter 2 L/min of blood, sinusoidal blood pressure at the portal tracts must increase from 4.4 mmHg to approximately 4.93 mmHg in the healthy case, 5.26 mmHg in the mild fibrotic case, 5.34 mmHg in the severe fibrotic case and 5.46 mmHg in the cirrhotic case. The larger the amount of blood being filtered by the liver, the higher the portal pressure required at each progressive stage of fibrosis.

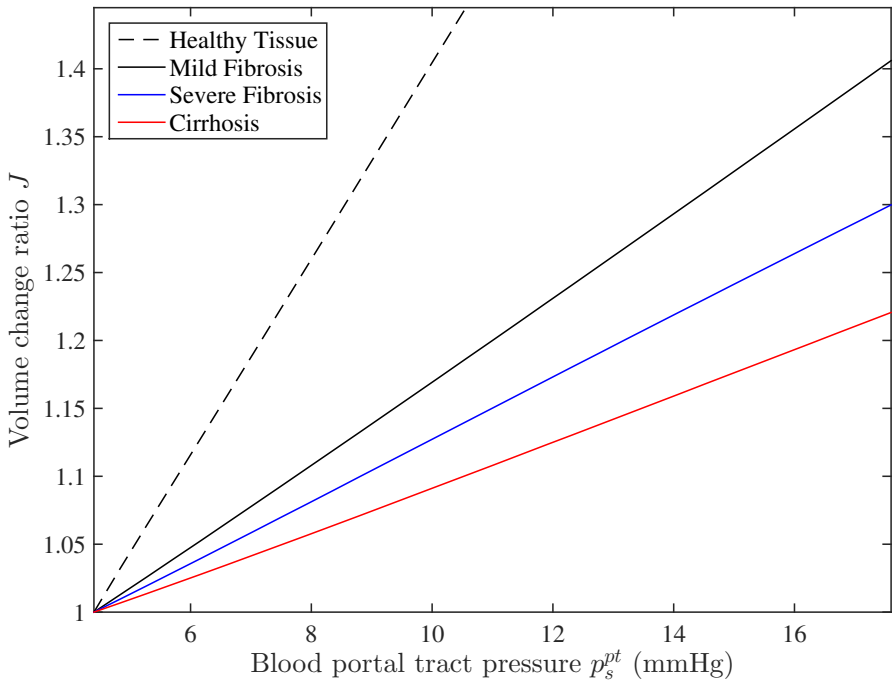


Figure 4.13: Effect of increased blood portal tract pressure p_s^{pt} (portal hypertension) on the average volume change ratio J in a healthy liver, mild fibrotic liver, severe fibrotic liver and cirrhotic liver.

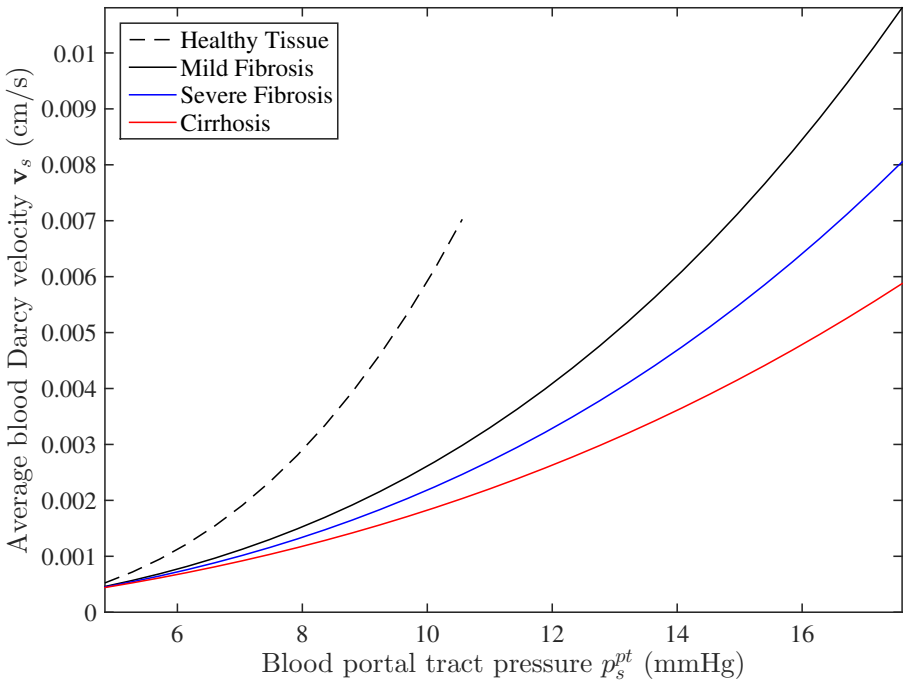


Figure 4.14: Effect of increased blood portal tract pressure p_s^{pt} (portal hypertension) on the average sinusoidal blood Darcy velocity $\mathbf{v}_s$ in a healthy liver, mild fibrotic liver, severe fibrotic liver and cirrhotic liver.

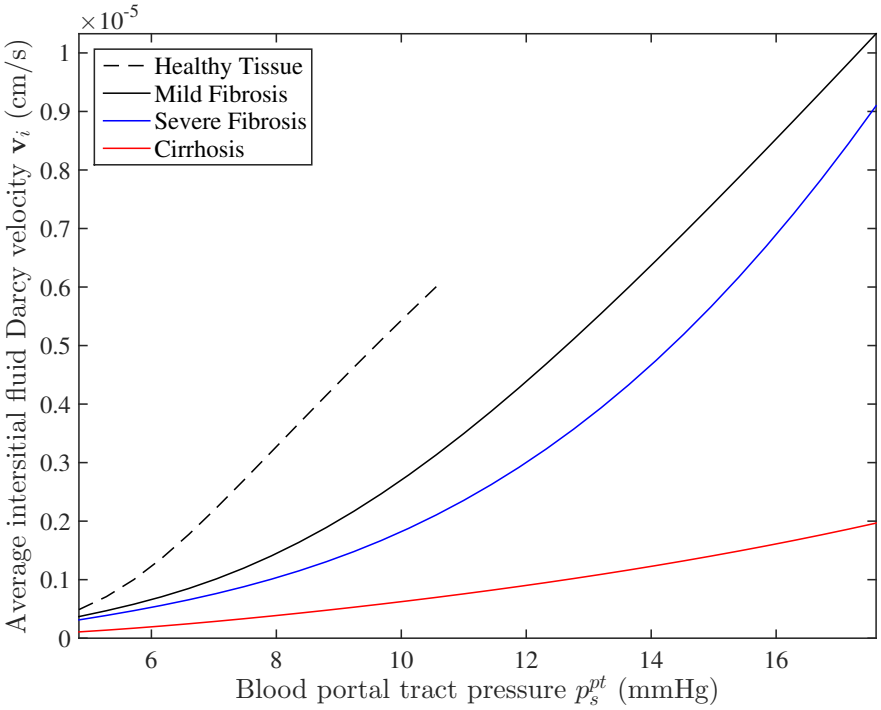


Figure 4.15: Effect of increased blood portal tract pressure p_s^{pt} (portal hypertension) on the average interstitial fluid Darcy velocity $\mathbf{v}_i$ in a healthy liver, mild fibrotic liver, severe fibrotic liver and cirrhotic liver.

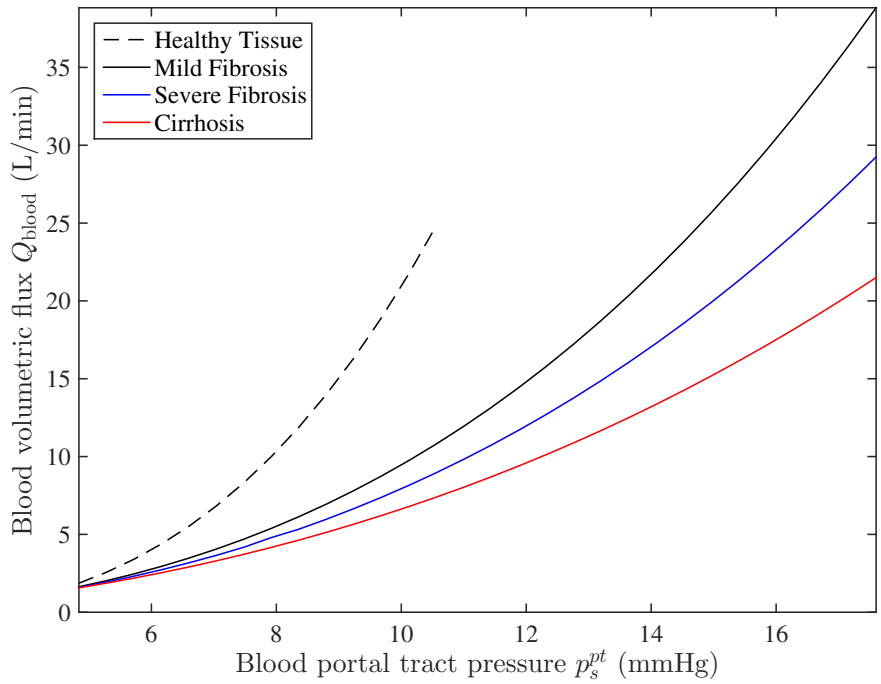


Figure 4.16: Effect of increased blood portal tract pressure p_s^{pt} (portal hypertension) on the total blood flux Q_{blood} in a healthy liver, mild fibrotic liver, severe fibrotic liver and cirrhotic liver.

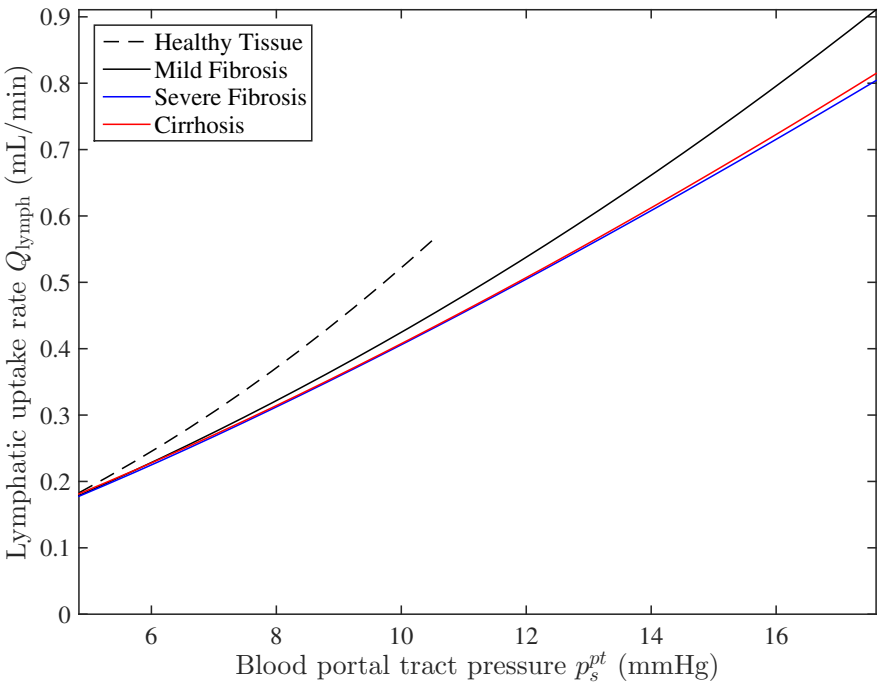


Figure 4.17: Effect of increased blood portal tract pressure p_s^{pt} (portal hypertension) on the lymphatic uptake rate Q_{lymph} in a healthy liver, mild fibrotic liver, severe fibrotic liver and cirrhotic liver.

The results of fluid loss from the liver into the peritoneal cavity $Q_{\mathrm{L,PC}}$ against portal hypertension for the 4 tissue types are shown in Figure 4.18. As will all other parameter values considered, $Q_{\mathrm{L,PC}}$ increases significantly with portal hypertension. The onset of fibrosis leads to a decrease in $Q_{\mathrm{L,PC}}$ due to the decrease in interstitial fluid permeability. However, this decrease can be offset by an increase in the conductivity of the Glissonian–peritoneal membrane M_{GP}. In Figure 4.18, we see that the severe fibrotic liver (with $M_{GP} = 5M_{GP,0}$ and $\kappa_{i,\mathrm{ref}} = 0.5\kappa_{i,0}$) had a higher $Q_{\mathrm{L,PC}}$ than the cirrhotic liver (with $M_{GP} = 10M_{GP,0}$ and $\kappa_{i,\mathrm{ref}} = 0.1\kappa_{i,0}$) for all blood portal tract pressures considered. It also had a higher $Q_{\mathrm{L,PC}}$ than the mild fibrotic liver (with $M_{GP} = 1.25M_{GP,0}$ and $\kappa_{i,\mathrm{ref}} = 0.75\kappa_{i,0}$) for blood portal tract pressures higher than 12 mmHg. This tells us that given a small interstitial permeability decrease, a higher conductivity of the Glissonian–peritoneal membrane takes precedence and leads to a larger loss of fluid from the liver into the peritoneal cavity. Only when the interstitial space permeability is greatly decreased, e.g. in the cirrhotic, do we observe a general decrease in $Q_{\mathrm{L,PC}}$ even at high Glissonian–peritoneal membrane conductivity. If, for example, we assign a smaller increase in M_{GP} in the severe fibrotic liver that is still higher than that of the mild fibrotic liver, say $M_{GP} = 1.5M_{GP,0}$ instead of $M_{GP} = 5M_{GP,0}$, then the values of $Q_{\mathrm{L,PC}}$ will lie between that of the mild fibrotic liver and the cirrhotic liver (see blue dashed line in Figure 4.19). In reality, we expect the value of $Q_{\mathrm{L,PC}}$ to lie between the two ends of the healthy tissue and the cirrhotic tissue. Note that in our model, we have considered both $\kappa_{i,\mathrm{ref}}$ and M_{GP} to be independent of the bulk tissue stiffness E_{bulk}, which is why we chose arbitrary decreasing and increasing values, respectively, for the progressive stages of fibrosis. An extension of the 3D hyperelastic model would include having $\kappa_{i,\mathrm{ref}}$ and M_{GP} dependent on E_{bulk}. This is discussed further in Chapter 6 of this thesis.

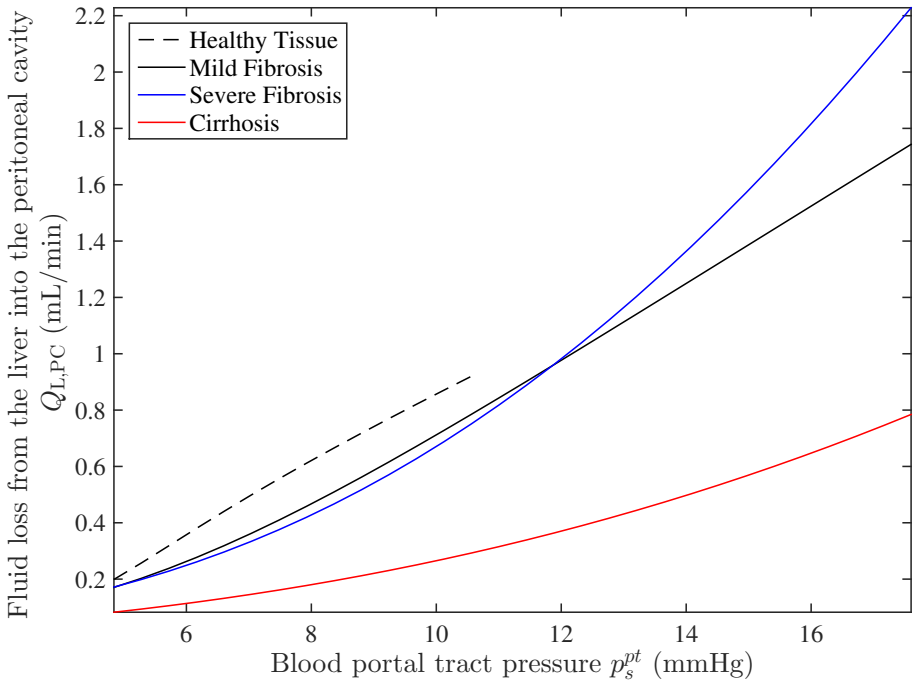


Figure 4.18: Effect of increased blood portal tract pressure p_s^{pt} (portal hypertension) on the fluid loss from the liver into the peritoneal cavity $Q_{\mathrm{L,PC}}$ in the healthy case, mild fibrotic case, severe fibrotic case and cirrhotic case.

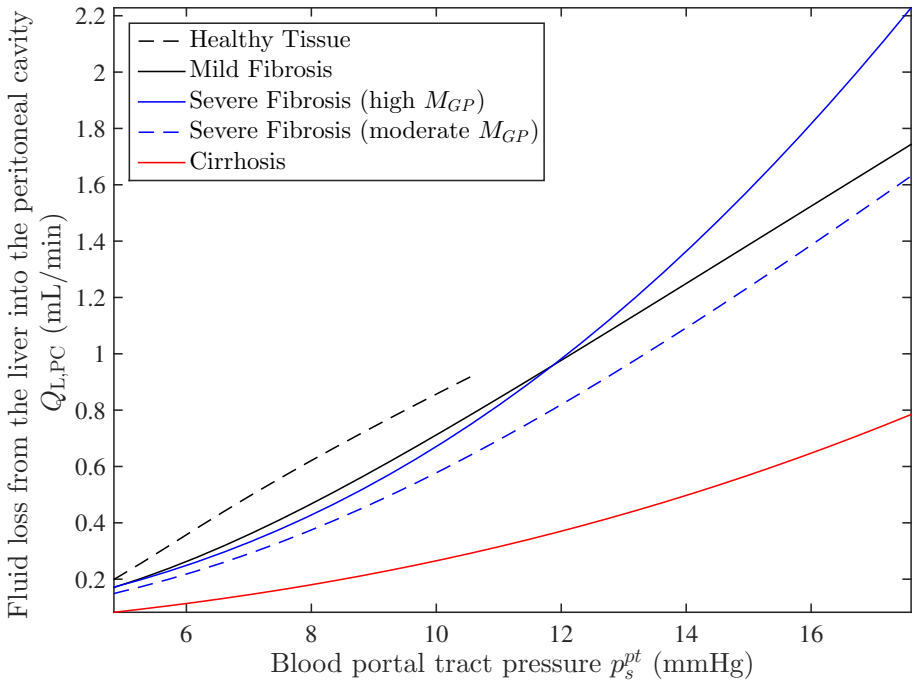


Figure 4.19: Effect of increased blood portal tract pressure p_s^{pt} (portal hypertension) on the fluid loss from the liver into the peritoneal cavity $Q_{\mathrm{L,PC}}$ in the healthy case, mild fibrotic case, severe fibrotic case (with high $M_{GP} = 5M_{GP,0}$ and moderate $M_{GP} = 1.5M_{GP,0}$) and cirrhotic case. $M_{GP,0}$ is the physiological conductivity of the Glissonian–peritoneal membrane.

4.5 Summary and Conclusion

In this chapter, we made use of the 3D poro-hyperelastic model of the liver tissue developed in Chapter 3 to study the fluid flow and deformation profiles in the diseased liver, with marked tissue fibrosis and portal hypertension. We compared the results of a healthy tissue and fibrotic tissue with different gradings: mild, severe and advanced (cirrhotic). This was achieved by increasing the bulk tissue stiffness E_{bulk}, decreasing the permeability of the interstitial space $\kappa_{i,\text{ref}}$ and increasing the conductivity of the Glissonian–peritoneal membrane M_{GP}. Results showed a significant decrease in all the parameters estimated, including volume change ratio, blood and interstitial fluid velocities, blood flux and lymphatic uptake rate with increased fibrosis progression. This explains why a higher blood portal pressure is required by the body in order to filter the same volume of blood done under the normal healthy case. As the stage of fibrosis increases, a higher blood portal pressure is also required to filter the same volume of blood as in the healthy case. Changes in fluid loss from the liver into the peritoneal cavity vary depending on $\kappa_{i,\text{ref}}$ and M_{GP}. The lowest values obtained, in the cirrhotic case, were when $\kappa_{i,\text{ref}}$ was minimum and M_{GP} was maximum. In Chapter 5, we develop a mathematical model of the peritoneal cavity in order to study the role played by the diseased liver, through fluid loss via the Glissonian–peritoneal membrane, on the development of ascites.

Part III

Development of Ascites

Chapter 5

Mathematical Model of the Peritoneal Cavity

5.1 Introduction

This chapter details the mathematical model of the peritoneal cavity developed in order to study the effect of liver disease on the development of ascites, which is the abnormal accumulation of fluid in the peritoneal cavity. We study the volume–pressure behaviour of the cavity, rate of fluid absorption and explore the sources and drains of fluid from the cavity, all under normal physiological pressure conditions. This model is then later used to study the effect of increased fluid loss from the surface of the liver, as a consequence of liver disease, on the volume of fluid accumulating in the peritoneal cavity and hence, progression of ascites.

5.2 Volume–Pressure Relationship

In this section, we obtain the equations of steady state pressure within the peritoneal cavity, P_{PC}, against peritoneal fluid volume, V_{PC}. We begin by analysing experimental data obtained from current literature, as a first step towards understanding the relationship between fluid accumulation and the mechanical expansion of the peritoneal cavity.

5.2.1 Experimental Data From Literature

Peritoneal dialysis is a method of draining excess fluid from the peritoneal cavity of ascitic patients via catheters inserted through the abdominal wall. However, these catheters can also be used to increase the volume of fluid in the cavity, using commercially available dialysate fluid, and measure the resultant pressure in the cavity using a manometer. Experimental measurements performed on patients already undergoing peritoneal dialysis have shown that

the pressure within the peritoneal cavity increases linearly with increase in dialysate volume of up to 5 L (Durand et al., 1994; Fischbach et al., 2003; Gotloib et al., 1981; Twardowski et al., 1983, 1986). However, the data obtained from these experiments varied significantly depending on the patients (male or female, children or adults; Fischbach et al., 2003), the position in which the patient was in (supine, upright or sitting; Twardowski et al., 1983), during normal daily activities (e.g. walking, jogging and lifting; Twardowski et al., 1986) and the measurement technique. Studies performed by Gotloib et al. (1981) and Twardowski et al. (1983) made use of the same measurement device, referenced at the same point in the abdomen, and yet obtained results with different slopes and intercepts for patients in the supine position. Gotloib et al. (1981) obtained a positive pressure of 0.7 mmHg when the cavity was empty, while Twardowski et al. (1983) obtained a negative pressure of -0.8 mmHg.

For the purpose of our model, we shall assume that the subject is in a supine position and take $P_{PC} = 0$ to be our reference point. We also require the volume in the cavity to be non-negative at $P_{PC} = 0$, hence, making the data obtained by Twardowski et al. (1983) the preferred option for parameter estimation. The experimental data suggest that the fluid volume, V_{PC}, and pressure, P_{PC}, of the peritoneal cavity can be related by a straight line graph (see Figure 5.1[a]), and so we represent the behaviour of the peritoneal cavity by a constant compliance model, described in Section 5.2.2.

Note that the experimental data by Twardowski et al. (1983) might not have accurately captured the behavior of the peritoneal cavity at very low volumes ($\sim$ 20 ml and less). In particular, the fact that the cavity is never completely empty (Guyton and Hall, 2015), whereas the models of both Twardowski et al. (1983) and Gotloib et al. (1981) formally predict zero or negative volumes if extrapolated to negative pressures. This is because these studies were focused only on the case of abnormally large volumes of fluid, and did not seek to reproduce the behaviour under normal physiological conditions. We base the present model on their data since our aim is also to study these abnormally large fluid volumes. Therefore it is sufficient for us to have a constant compliance model for low fluid volumes. On the other hand, as there are no data available for high pressures and volumes, and since it is unlikely that the behaviour will remain linear in this regime, we extend our model by considering a sac model, described in Section 5.2.3.

[a]Figure obtained from Twardowski et al. (1983).

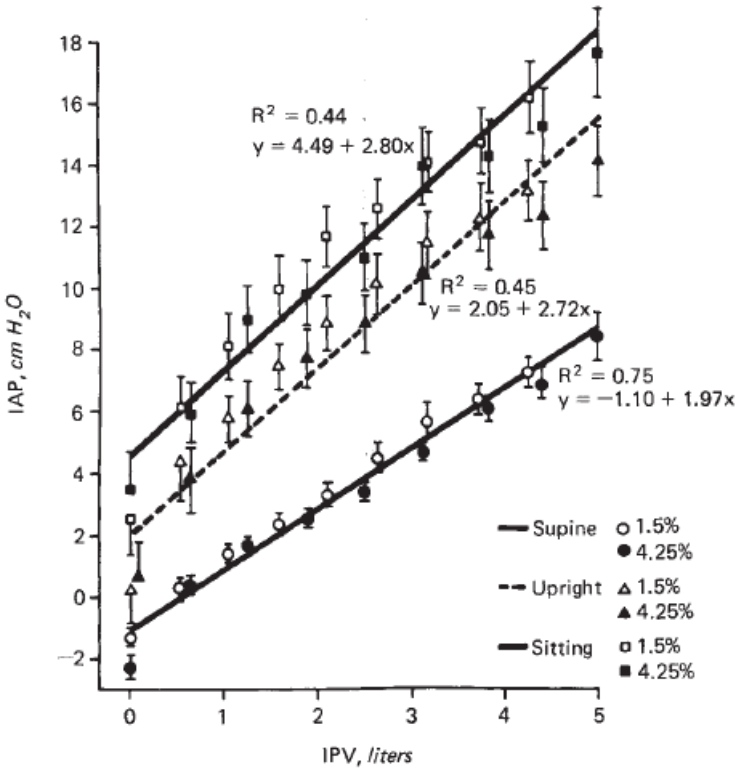


Figure 5.1: Graphs of intra-peritoneal pressure (IAP) measured against intra-peritoneal fluid volume (IVP) of 1.5% and 4.25% glucose solutions from the experiments by Twardowski et al. (1983). Results show an approximate linear relation between pressure and volume obtained in supine, upright and sitting patient positions.

5.2.2 Constant Compliance Model

The compliance, C_{PC}, of the peritoneal cavity is defined as the rate of change of the fluid volume in cavity with respect to change in fluid pressure:

$$C_{PC} = \frac{\mathrm{d}V_{PC}}{\mathrm{d}P_{PC}}, \tag{5.1}$$

which, assuming $C_{PC} = C_0$ is constant, yields

$$V_{PC} = V_{PC,\mathrm{ref}} + C_0 \left(P_{PC} - P_{PC,\mathrm{ref}}\right), \tag{5.2}$$

where $V_{PC,\mathrm{ref}}$ and $P_{PC,\mathrm{ref}}$ are a measured reference volume and pressure of the cavity.

Although a linear volume–pressure relationship provides a good approximation of the behaviour of the cavity for fluid volume increases up to 5 L, it could be unrealistic at volumes larger than this, such as might occur in extreme cases of ascites, as both the wall properties and the interaction with neighbouring organs might change. In Section 5.2.3 we extend this model to account for the expected nonlinear behaviour for large volumes due to changes in the mechanical properties of the peritoneum.

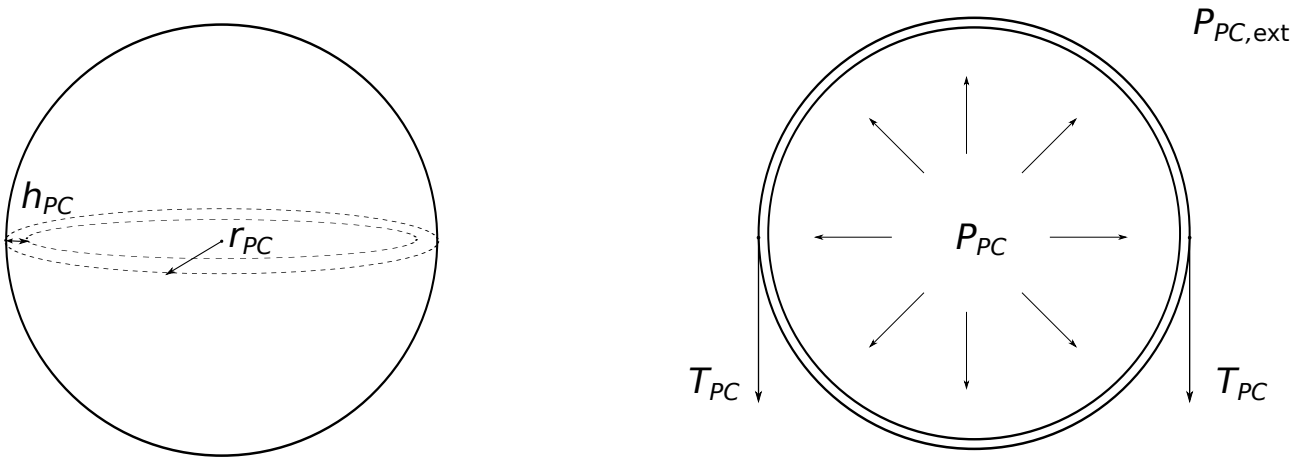


Figure 5.2: Schematic diagram of a linearly elastic peritoneal cavity. Left: Spherical, inflated peritoneal cavity with radius, r_{PC}, and membrane thickness, h_{PC}; Right: Cross section of inflated cavity with internal and external pressures, P_{PC} and $P_{PC,\text{ext}}$, respectively, and membrane stress T_{PC}.

5.2.3 Combination Model: Linear and Nonlinear Behaviour

As long as the volume of fluid in the peritoneal cavity is lower than a certain critical value, $V_{PC,\text{crit}}$, with corresponding pressure $P_{PC,\text{crit}}$, we make use of the constant compliance model, with compliance C_0. For larger volumes we use a simplified membrane model to determine the pressure–volume relationship.

A suitable physiological value of the critical point $V_{PC,\text{crit}}$ is difficult to determine and likely to vary between patients. As a first estimate we make use of $V_{PC,\text{crit}} = 5\,\text{L}$, which is the maximum recorded volume and the volume at which most patients experienced pain or discomfort in the experiments by Twardowski et al. (1983), giving $P_{PC,\text{crit}} = 0+(5-0.56)/0.69 = 6.4\,\text{mmHg}$ using the parameter values in Table 5.1 on page 168.

Now for $V_{PC} > V_{PC,\text{crit}}$, and only for the purposes of deriving the pressure–volume relationship, we represent the peritoneal cavity as a spherical sac with radius $r_{PC} = (3V_{PC}/(4\pi))^{1/3}$ surrounded by a thin elastic membrane (i.e. the peritoneum) of thickness $h_{PC} \ll r_{PC}$ (see Figure 5.2). We let $r_{PC,\text{crit}}$ and $h_{PC,\text{crit}}$ be the values of r_{PC} and h_{PC} when $V_{PC} = V_{PC,\text{crit}}$. The law of Laplace (see e.g. Guyton and Hall, 2015) gives

$$T_{PC} = \frac{(P_{PC} - P_{PC,\text{ext}})r_{PC}}{2h_{PC}}, \tag{5.3}$$

where T_{PC} is the normal stress in the membrane (membrane tension divided by membrane thickness) and $P_{PC,\text{ext}}$ is the uniform pressure outside the cavity. Assuming the membrane is incompressible, its volume must always remain constant such that

$$V_{\text{membrane}} = 4\pi r_{PC}^2 h_{PC} = 4\pi r_{PC,\text{crit}}^2 h_{PC,\text{crit}}. \tag{5.4}$$

This allows us to eliminate h_{PC} from Equation (5.3):

$$T_{PC} = \frac{(P_{PC} - P_{PC,\text{ext}})r_{PC}^3}{2h_{PC,\text{crit}}r_{PC,\text{crit}}^2}. \tag{5.5}$$

Treating the membrane tissue as a linearly elastic isotropic material, and using the generalised Hooke's law for a spherical membrane (Rees, 2000) gives

$$T_{PC} = \frac{E_{PC}}{1 - \nu_{PC}}\epsilon_{PC}, \tag{5.6}$$

where E_{PC} is the Young's modulus, ν_{PC} is the Poisson's ratio (assumed to be 0.5, representing an incompressible material) and ϵ_{PC} is the strain, given by

$$\epsilon_{PC} = \frac{r_{PC} - r_0}{r_0}, \tag{5.7}$$

where V_0 is the unknown volume at which the transmural pressure would be zero if this law were followed in that regime, and $r_0 = (3V_0/(4\pi))^{1/3}$.

Combining Equations (5.5), (5.6) and (5.7) leads to

$$\begin{aligned} P_{PC} - P_{PC,\text{ext}} =& \frac{2E_{PC}h_{PC,\text{crit}}r_{PC,\text{crit}}^2(r_{PC} - r_0)}{(1 - \nu_{PC})r_{PC}^3 r_0} \\ =& 2\left(\frac{4\pi}{3}\right)^{1/3} \frac{E_{PC}h_{PC,\text{crit}}V_{PC,\text{crit}}^{2/3}}{(1 - \nu_{PC})} \left(\frac{V_{PC}^{1/3} - V_0^{1/3}}{V_{PC}V_0^{1/3}}\right), \end{aligned} \tag{5.8}$$

where we substituted for r_{PC}, r_0 and $r_{PC,\text{crit}}$.

Combining this with Equation (5.2),

$$P_{PC} = \begin{cases} P_{PC,\text{ref}} + \dfrac{V_{PC} - V_{PC,\text{ref}}}{C_0} & \text{for } V_{PC} \leq V_{PC,\text{crit}}, \\ P_{PC,\text{ext}} + 2\left(\dfrac{4\pi}{3}\right)^{1/3} \dfrac{E_{PC}h_{PC,\text{crit}}V_{PC,\text{crit}}^{2/3}}{(1 - \nu_{PC})} \left(\dfrac{V_{PC}^{1/3} - V_0^{1/3}}{V_{PC}V_0^{1/3}}\right) & \text{for } V_{PC} > V_{PC,\text{crit}}, \end{cases} \tag{5.9}$$

and (5.1) gives the compliance as

$$C_{PC} = \begin{cases} C_0 & \text{for } V_{PC} \leq V_{PC,\text{crit}}, \\ \dfrac{3^{4/3}(1 - \nu_{PC})V_0^{1/3}V_{PC}^2}{4^{5/6}\pi^{1/3}E_{PC}h_{PC,\text{crit}}V_{PC,\text{crit}}^{2/3}\left(3V_0^{1/3} - 2V_{PC}^{1/3}\right)} & \text{for } V_{PC} > V_{PC,\text{crit}}. \end{cases} \tag{5.10}$$

Note that $C_{PC}(r)$ has a singularity at $V_{PC} = 27V_0/8$, which we estimate to be the maximum possible cavity volume in this model.

5.2.3.1 Parameter Estimation

We estimate suitable values of the unknowns $E_{PC}, h_{PC,\text{crit}}$ and V_0 for the cavity membrane by requiring the pressure and compliance to be continuous at $V_{PC} = V_{PC,\text{crit}}$, giving

$$P_{PC,\text{crit}} = P_{PC,\text{ext}} + 2\left(\frac{4\pi}{3}\right)^{1/3} \frac{E_{PC} h_{PC,\text{crit}} V_{PC,\text{crit}}^{2/3}}{(1-\nu_{PC})} \left(\frac{V_{PC,\text{crit}}^{1/3} - V_0^{1/3}}{V_{PC,\text{crit}} V_0^{1/3}}\right),$$

$$C_0 = \frac{3^{4/3}(1-\nu_{PC}) V_0^{1/3} V_{PC,\text{crit}}^2}{4^{5/6}\pi^{1/3} E_{PC} h_{PC,\text{crit}} V_{PC,\text{crit}}^{2/3} \left(3V_0^{1/3} - 2V_{PC,\text{crit}}^{1/3}\right)},$$

which means that

$$V_0 = \left(\frac{3V_{PC,\text{crit}} + 2(P_{PC,\text{crit}} - P_{PC,\text{ext}})C_0}{3V_{PC,\text{crit}} + 3(P_{PC,\text{crit}} - P_{PC,\text{ext}})C_0}\right)^3 V_{PC,\text{crit}} \approx 3.0\,\text{L}, \tag{5.11}$$

and

$$\begin{aligned} E_{PC} h_{PC,\text{crit}} &= \frac{3^{1/3}\,(1-\nu_{PC})\, V_{PC,\text{crit}}^{1/3}\,(3V_{PC,\text{crit}} + 2(P_{PC,\text{crit}} - P_{PC,\text{ext}})C_0)}{4^{5/6}\pi^{1/3} C_0} \\ &\approx 9.2\,\text{mmHg}\cdot\text{m}. \end{aligned} \tag{5.12}$$

The average measured thickness of the human peritoneum depends on time spent on dialysis and ranges between $370 - 660\,\mu$m (Duman et al., 2007). Using $h_{PC,\text{crit}} = 370\,\mu$m, i.e. with minimum time spent on dialysis, and Equation (5.12), we can also estimate the Young's modulus of the peritoneal cavity wall, which we find to be approximately $E_{PC} = 3.3\,$MPa. This value lies within the acceptable values of elastic constants for biological membranes (Akhtar et al., 2011).

The equation of pressure–volume in the peritoneal cavity thus becomes

$$P_{PC} = \begin{cases} P_{PC,\text{ref}} + \dfrac{V_{PC} - V_{PC,\text{ref}}}{C_0} & \text{for } V_{PC} \le V_{PC,\text{crit}}, \\ P_{PC,\text{ext}} + \left(\dfrac{3}{C_0}V_{PC,\text{crit}} + 3\,(P_{PC,\text{crit}} - P_{PC,\text{ext}})\right)\left(\dfrac{V_{PC,\text{crit}}}{V_{PC}}\right)^{2/3} & \\ \qquad - \left(\dfrac{3}{C_0}V_{PC,\text{crit}} + 2(P_{PC,\text{crit}} - P_{PC,\text{ext}})\right)\left(\dfrac{V_{PC,\text{crit}}}{V_{PC}}\right) & \text{for } V_{PC} > V_{PC,\text{crit}}. \end{cases} \tag{5.13}$$

Symbol	Description	Default Value	Reference
$P_{PC,\text{ref}}$	Reference pressure of peritoneal cavity	0 mmHg	Assumed
$V_{PC,\text{ref}}$	Fluid volume of peritoneal cavity at reference pressure	0.56 L	Twardowski et al. (1983)
C_0	Compliance constant of peritoneal cavity	0.69 L/mmHg	Twardowski et al. (1983)
$V_{PC,\text{crit}}$	Critical fluid volume of peritoneal cavity	5 L	See Section 5.2.3
$P_{PC,\text{crit}}$	Peritoneal cavity pressure at critical fluid volume	6.4 mmHg	See Section 5.2.3
$P_{PC,\text{ext}}$	Pressure external to peritoneal cavity	0 mmHg	Assumed
$E_{PC}h_{\text{crit}}$	Tension in the peritoneal cavity wall at the critical volume	9.2 mmHg · m	See Section 5.2.3
ν_{PC}	Poisson's ratio for the peritoneum	0.5	Assumed incompressible

Table 5.1: List of parameter values used for the volume–pressure equations in peritoneal cavity model, together with references.

5.2.4 Results and Discussion

The equations of the volume–pressure relationship of the peritoneal cavity developed above are plotted using Matlab, together with the parameter values listed in Table 5.1, and are presented in this section.

Figure 5.3 shows the graph of peritoneal cavity pressure against fluid volume increase using the combination model. The figure also highlights how the constant compliance and the linearly elastic models are used in the combination model. The experimental measurements by Twardowski et al. (1983) were only carried out for peritoneal volumes of up to around 5 L, whereas in reality volumes of up to 10 L are not uncommon in ascites patients. The behaviour for volumes of up to 10 L is shown, indicating the difference between the constant compliance and combination models at large volumes. The combination model is also more representative of the physiological volume–pressure behaviour of large tissue spaces agreeing with Wiig and Swartz (2012). Also, since the critical volume $V_{PC,\text{crit}}$ was chosen arbitrarily, in Figure 5.4 we compare the volume–pressure relationship for a range of values of $V_{PC,\text{crit}}$. Increasing the value of $V_{PC,\text{crit}}$ simply increases the maximum pressure within the peritoneal cavity attained in the combination model, with an approximate 2 mmHg rise in maximum pressure for each 1 L increase in $V_{PC,\text{crit}}$.

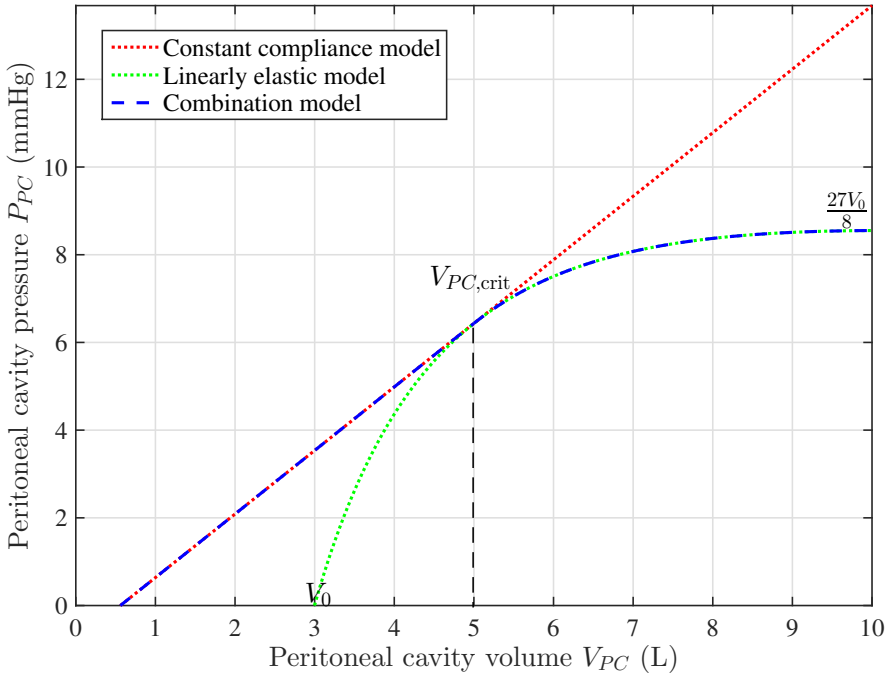


Figure 5.3: Graph of steady state pressure in the peritoneal cavity P_{PC} against fluid volume V_{PC} for the constant compliance model (dotted red line), linearly elastic Hooke's law model (dotted green line) and combination model (dashed blue line).

Having presented the results of the volume–pressure relationship of the peritoneal cavity above, we now look at the role played by some of the surrounding organs and tissues in regulating the net fluid volume within the cavity.

5.3 Fluid Exchange in the Peritoneal Cavity

In this section, we develop a mathematical model of fluid exchange between the peritoneal cavity and some of the surrounding organs, namely: the liver, spleen, diaphragm and abdominal wall. We first begin by analysing the net absorption rate data of the peritoneal cavity obtained from literature, and then quantifying the individual flux contributions from each of the organs/tissues named above using a compartmental model of fluid flow.

5.3.1 Absorption Rate Coefficient of the Peritoneal Cavity

The fluid absorption rate within the peritoneal cavity can be estimated from experimental studies conducted by Zink and Greenway (1977). These authors introduced fluid into the peritoneal cavity of anaesthetised cats, via a thin catheter inserted through the abdominal wall, until the pressure reached a prescribed value. The entire abdomen was enclosed in a plaster cast

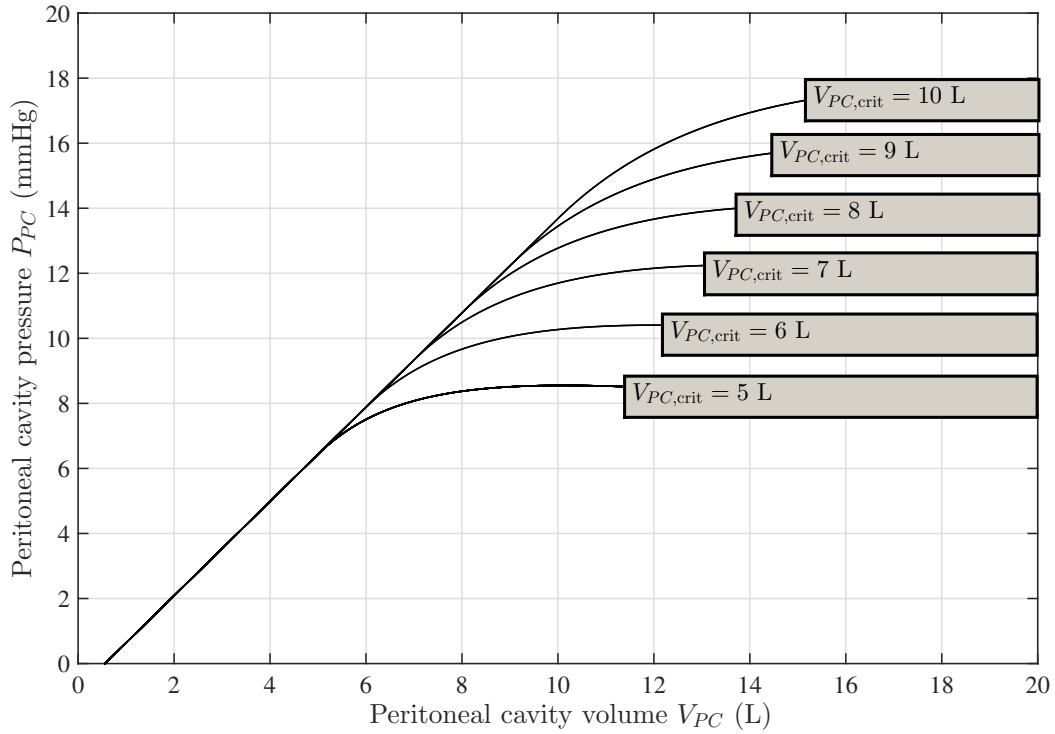


Figure 5.4: Graph of pressure in the peritoneal cavity, P_{PC}, against change in fluid volume, V_{PC}, at steady state for different values of the critical volume $V_{PC,\text{crit}}$.

to prevent the distension of the abdominal wall with increase in pressure. While maintaining the pressure at this level, the volume change over time was recorded until it reached a steady state. Their results suggest that the rate of fluid volume change, $\mathrm{d}V_{PC}/\mathrm{d}t$, and intraperitoneal pressure, P_{PC}, have an approximately linear dependence

$$\frac{\mathrm{d}V_{PC}}{\mathrm{d}t} = -k_{PC}(P_{PC} - P_{PC,0}), \tag{5.14}$$

where $k_{PC} = 0.02\,\mathrm{mL/min/mmHg}$ (for cats) is the absorption rate coefficient and $P_{PC,0}$ is the steady state pressure in the peritoneal cavity.

5.3.1.1 Parameter Estimation

To obtain an estimate of k_{PC} for humans, we assume that surface areas, and thus also volumetric fluxes, scale as body mass ratio raised to the power 2/3. Using the estimated human and cat masses of 70 kg and 2.6 kg (Zink and Greenway, 1977) gives $k_{PC} = (70/2.6)^{2/3} \times 0.02\,\mathrm{mL/min/mmHg} \approx 0.18\,\mathrm{mL/min/mmHg}$ for humans. We also estimate the equilibrium pressure $P_{PC,0} = -0.8\,\mathrm{mmHg}$ (Twardowski et al., 1983), corresponding to a fluid volume of $\sim 8\,\mathrm{mL}$ using Equation (5.2).

5.3.1.2 Timescale to Equilibrium Fluid Volume

Using the absorption rate coefficient above, we can make a few deductions on the timescale over which a steady state volume is reached within the peritoneal cavity using our volume–pressure equations from Section 5.2. Let the peritoneal cavity fluid volume be $V_{PC,0} \leq V_{PC,\text{crit}}$ at the initial time $t = 0$. Equations (5.13) and (5.14) imply that

$$V_{PC} = V_{PC,\text{ref}} + C_0(P_{PC,0} - P_{PC,\text{ref}}) + (V_{PC,0} - V_{PC,\text{ref}} - C_0(P_{PC,0} - P_{PC,\text{ref}}))\, \mathrm{e}^{-(k_{PC}/C_0)t}, \quad (5.15)$$

and

$$P_{PC} = P_{PC,0} + \left(\frac{V_{PC,0} - V_{PC,\text{ref}}}{C_0} - (P_{PC,0} - P_{PC,\text{ref}}) \right) \mathrm{e}^{-(k_{PC}/C_0)t}, \quad (5.16)$$

where $C_0/k_{PC} \approx 2.7$ days, using the values of C_0 and k_{PC} from Table 5.1, is the timescale over which the peritoneal cavity volume approaches equilibrium. If the initial volume is larger, $V_{PC,0} > V_{PC,\text{crit}}$, the model also predicts convergence to the same equilibrium state, but at first the volume and pressure drop faster than the exponential behaviours of (5.15) and (5.16), until the volume goes below $V_{PC,\text{crit}}$, after which the behaviour follows (5.15) and (5.16). Note that Equation (5.14), and thus also Equations (5.15) and (5.16), are only expected to be valid in the particular case of a healthy patient in which no abdominal expansion occurs. We consider the case of a healthy patient with normal abdominal expansion in Section 5.3.3.4.

5.3.2 Compartmental Model of Fluid Exchange

Here, we develop a compartmental model of fluid flow between the peritoneal cavity and the liver, spleen, diaphragm and abdominal wall. Let $Q_{L,PC}$ and $Q_{Sp,PC}$ denote the net volumetric fluid fluxes from the liver and spleen, respectively, into the peritoneal cavity, and $Q_{PC,D}$ and $Q_{PC,AW}$ denote the net volumetric fluid fluxes from the peritoneal cavity into the diaphragm and abdominal wall, respectively, as illustrated in Figure 5.5. By making use of volume conservation and Equation (5.14),

$$\frac{\mathrm{d}V_{PC}}{\mathrm{d}t} = Q_{L,PC} + Q_{Sp,PC} - Q_{PC,D} - Q_{PC,AW} = -k_{PC}(P_{PC} - P_{PC,0}). \quad (5.17)$$

and hence at steady state (i.e. when $P_{PC} = P_{PC,0}$),

$$Q_{L,PC} + Q_{Sp,PC} - Q_{PC,D} - Q_{PC,AW} = 0. \quad (5.18)$$

In the next section, we derive the expressions for each of the individual organ fluxes above.

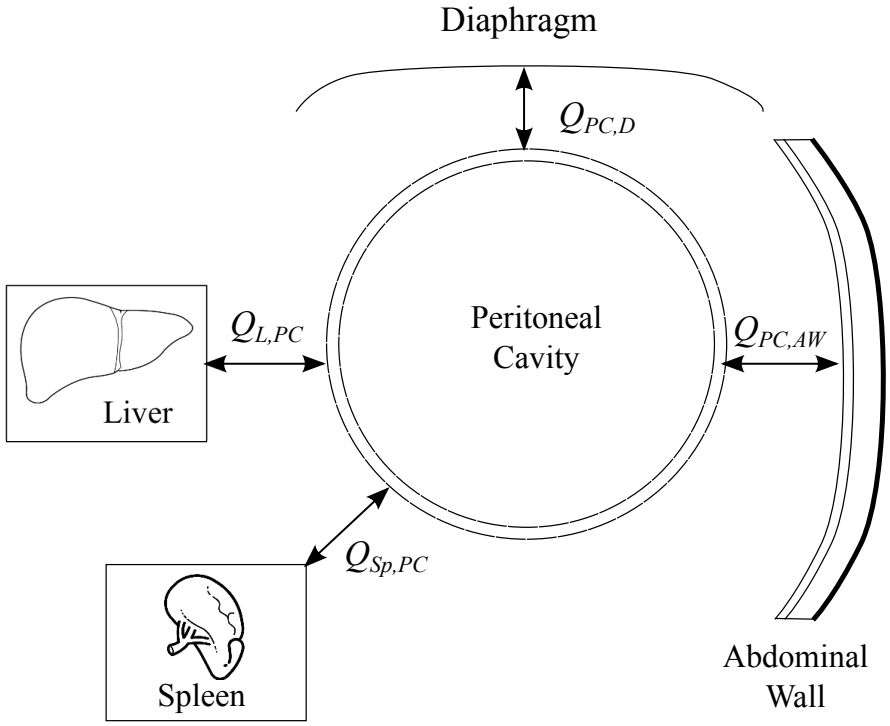


Figure 5.5: Schematic diagram of the compartment model of fluid exchange in the peritoneal cavity, where $Q_{i,PC}$ ($Q_{PC,i}$) denotes fluid flux from (into) tissue i into (from) the peritoneal cavity.

5.3.3 Fluid Flux Across Individual Organs/Tissue Adjacent to the Peritoneal Cavity

5.3.3.1 Liver Flux

Fluid loss from the liver into the peritoneal cavity, and vice versa, occurs across the Glissonian–peritoneal surface of the liver. The equation of fluid flow across the Glissonian–peritoneal surface was defined in Section 3.7.3, for the 3D hyperelastic liver model developed in Chapter 3. The equation is given by

$$Q_{\mathrm{L,PC}} = \tilde{A}_{\mathrm{L,GP}} \int_{\text{Outer surface}} M_{GP}(p_i - P_{PC}) \, \mathrm{d}A, \tag{5.19}$$

where $\tilde{A}_{\mathrm{L,GP}}$ is a constant, M_{GP} is the hydraulic conductivity of the Glissonian–peritoneal membrane and p_i is the interstitial fluid pressure within the liver, all defined in Chapter 3. The integral is taken over the outer surface of the liver lobule lattice shown in Figure 2.1 (Chapter 2).

5.3.3.2 Spleen Flux

We assume that the flow from the spleen into the peritoneal cavity is proportional to the pressure drop across the membrane surrounding the spleen, such that

$$Q_{Sp,PC} = A_{Sp} M_{Sp} (P_{Sp} - P_{PC}), \tag{5.20}$$

where A_{Sp} is the surface area of the spleen adjacent to the peritoneal cavity, M_{Sp} is the hydraulic conductivity of the spleen membrane and P_{Sp} is the average interstitial fluid pressure within the interior surface of the spleen.

Parameter Estimation

The values of M_{Sp} and A_{Sp} could not be found in the literature. Since the spleen has a similar fibrous membrane to that of the liver, we shall assume its membrane hydraulic conductivity equals that of the Glissonian–peritoneal membrane, $M_{Sp} = M_{GP}$. Although Rubin et al. (1988a) provide the surface areas of many of the organs in the human body, they do not provide that of the spleen, and thus to find an estimate of A_{Sp} we use the area measurement $8 \pm 0.3\,\mathrm{cm}^2$ of the rat spleen by Rubin et al. (1988a) and scale it by the body mass ratio raised to the power 2/3, i.e.

$$\left(\frac{\text{mass of human body}}{\text{mass of rat body}}\right)^{2/3} \times \text{surface area of rat spleen} \approx 250\,\mathrm{cm}^2,$$

using the typical rat and human masses 400 g and 70 kg, respectively. The value obtained above is within the range estimated by Pawlaczyk et al. (1996) for the surface area of the spleen as a percentage of the total peritoneal surface area. As a first approximation, we take $P_{Sp} = 2\,\mathrm{mmHg}$.

A summary of all the parameters used for the spleen flux and their physiological values is given in Table 5.2 on page 184.

5.3.3.3 Diaphragm Flux

Fluid uptake by the diaphragm depends on the pressure difference between the peritoneal cavity and the underlying diaphragmatic lymphatics (Negrini et al., 1992) as well as the density of stomata present on its surface (Negrini et al., 1991), and so we assume a linear dependence, giving

$$Q_{PC,D} = A_D D_{\text{stoma}} G_{\text{stoma}} (P_{PC} - P_{\text{stoma}}), \tag{5.21}$$

where A_D is the surface area of the diaphragm adjacent to the peritoneal cavity, D_{stoma} is the average density of a stoma, G_{stoma} is the average hydraulic conductivity of a stoma and P_{stoma} is the average pressure within the stomata. Note that this makes $M_{\text{stoma}} = D_{\text{stoma}} G_{\text{stoma}}$ the total hydraulic conductivity of the stomata.

Parameter Estimation

Estimated values of A_D and D_{stoma} were found in studies by Rubin et al. (1988a) and Negrini et al. (1991). The values of G_{stoma} and P_{stoma} could not be found in the literature, and so we estimate them a posteriori from the model. This is achieved by finding $Q_{PC,D}$ such that

$$Q_{PC,D} = -(Q_{L,PC} + Q_{Sp,PC} - Q_{PC,AW}) - k_{PC}(P_{PC} - P_{PC,0}), \tag{5.22}$$

holds for all values of P_{PC}. A summary of the parameters used for the diaphragm flux and their resultant values is given in Table 5.3 on page 184.

5.3.3.4 Abdominal Wall

The equations governing fluid flow and pressure distribution across the abdominal wall are based on a mathematical model by Stachowska-Pietka et al. (2004, 2006). The model by Stachowska-Pietka et al. (2004, 2006) is extended to include a subcutaneous sublayer within the abdominal wall, which is summarised below.

According to Stachowska-Pietka et al. (2004), the governing equation for the interstitial fluid volume fraction in the abdominal wall θ_{aw} is given by

$$\frac{\partial \theta_{aw}}{\partial t} = \frac{\partial p_{aw}}{\partial t}\frac{\partial \theta_{aw}}{\partial p_{aw}} = -\frac{\partial j_{aw}}{\partial x} + q_{c,aw} - q_{l,aw}, \tag{5.23}$$

where x is distance into the wall tissue, j_{aw} is volumetric flux per unit area into the wall, $q_{c,aw}$ and $q_{l,aw}$ are the local rate of net fluid absorption from the tissue into the blood capillaries and lymphatics, respectively. Fluid absorption by the capillaries is given by Starling's law:

$$q_{c,aw} = L_p a \left(p_b - p_{aw} - \sigma_\Pi \left(\Pi_b - \Pi_i\right)\right), \tag{5.24}$$

where L_p is the hydraulic conductivity of the capillary wall, a is the surface area of capillaries per unit volume of tissue, p_b and Π_b are blood mechanical and oncotic pressures, respectively, σ_Π is capillary wall reflection coefficient, and Π_i is local oncotic pressure in the interstitium. $L_p a$, p_b, σ_Π, Π_b and Π_i are treated as constants in the model. The uptake by lymphatic vessels is defined by

$$q_{l,aw} = q_{l0,aw} + q_{l1,aw}(p_{aw} - p_{aw,0}), \tag{5.25}$$

where $q_{l0,aw}$ is the rate of lymphatic absorption in the steady state, $q_{l1,aw}$ is the sensitivity of lymphatic absorption to increase in pressure and $p_{aw,0}$ is the interstitial fluid equilibrium pressure. We also treat q_{l0}, $q_{l1,aw}$ and $p_{aw,0}$ as constants.

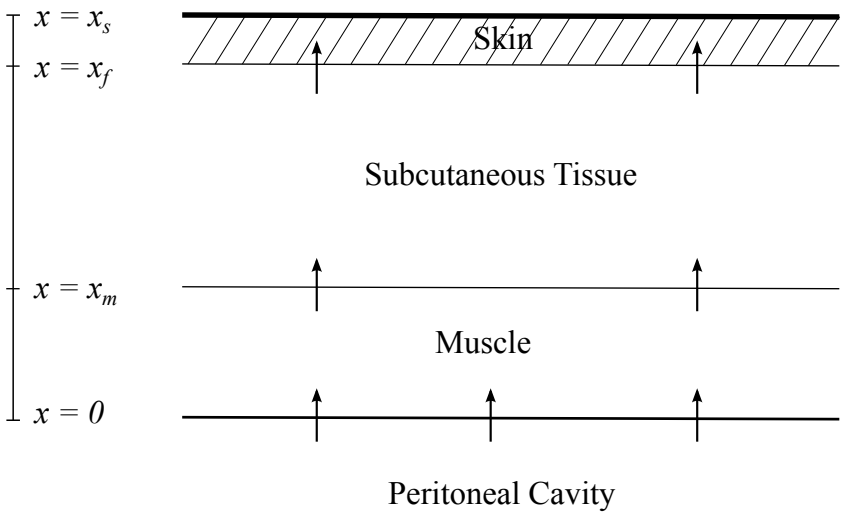


Figure 5.6: Schematic diagram of abdominal wall cross section showing the 3 layers: muscle; subcutaneous tissue and skin. Arrows show the direction of fluid flow, i.e. from the peritoneal cavity into the abdominal wall, in the normal physiological case.

The tissue is modelled as a porous medium with hydraulic conductivity K_{aw}, leading to

$$j_{aw} = -K_{aw}\frac{\partial p_{aw}}{\partial x}. \tag{5.26}$$

The interstitial fluid void volume fraction θ_{aw} is dependent on the local interstitial fluid pressure p_{aw} and can be obtained empirically from experimental results as shown by Stachowska-Pietka et al. (2004, 2006). However, since we are only interested in steady state solutions of the system (i.e. when $\partial p_{aw}/\partial t = 0$), Equation (5.23) simplifies to

$$\frac{\partial}{\partial x}\left(K_{aw}\frac{\partial p_{aw}}{\partial x}\right) + q_{c,aw} - q_{l,aw} = 0. \tag{5.27}$$

Furthermore, the abdominal wall can be divided into three distinct layers; an inner muscle layer, a middle subcutaneous tissue (fat) layer and an outer skin layer (see Figure 5.6). We denote $x = x_m$ as the boundary between the muscle and subcutaneous tissue layers, and $x = x_f$ as the boundary between the subcutaneous and skin layers, with the muscle in $0 \leq x \leq x_m$, the subcutaneous tissue in $x_m < x \leq x_f$ and the skin in $x_f < x \leq x_s$. The filtration coefficient of the capillaries $L_p a$, sensitivity of lymphatic absorption to pressure increases $q_{l1,aw}$ and hydraulic conductivity of the tissue K_{aw} take different values in the three layers. In addition the hydraulic conductivities of the tissue depend on local compression, which in turn depends on the mechanical pressure (Levick, 1987). Zakaria et al. (1997) showed that the relationship between hydraulic conductivity and pressure is approximately linear, and following Stachowska-

Pietka et al. (2004, 2006), we use

$$K_{aw} = \begin{cases} a_K, & \text{for } p_{aw} \leq 1.2\text{mmHg}, \\ a_K + b_K(p_{aw} - 1.2), & \text{for } p_{aw} > 1.2\text{mmHg}, \end{cases} \tag{5.28}$$

where a_K and b_K are constants that both take different values in the muscle, subcutaneous and skin layers.

Equations (5.27)–(5.28) applied to all 3 layers constitute a system of nonlinear second-order ODEs. Together with imposed boundary conditions of pressure continuity at the boundary with the peritoneal cavity (i.e. at $x = 0$); pressure and flow continuity at $x = x_m$ and $x = x_f$; and no fluid flow across the outer (skin) boundary at $x = x_s$, the system can be solved numerically to find the pressure distribution p_{aw}. Substituting into Equation (5.26) enables j_v to be found, and the flux at $x = 0$ multiplied by the surface area of the abdominal wall A_{AW} gives the volume of fluid entering the wall per unit time $Q_{PC,AW}$.

Since Zink and Greenway (1977) performed experiments on cats whose abdomens were encased in a cast, we assume this to mean that the abdominal wall does not expand and so $K_{aw} = a_K$ does not depend on the local pressure. Hence, in the case of a constant K_{aw}, the pressure distribution can be found analytically, which leads to the volume flow rate

$$Q_{PC,AW} = A_{AW} M_{AW} \left(P_{PC} - p_{aw,0} \right), \tag{5.29}$$

where M_{AW} is a constant.

Parameter Estimation

All the parameter values associated with the abdominal wall model were readily available in literature, except the capillary wall filtration coefficient, $L_p a$, and the sensitivity of the lymphatic absorption to increase in pressure , $q_{l1,aw}$, in both the subcutaneous tissue and skin. $L_p a$ of the subcutaneous tissue and skin were assumed to be the same as that of the muscle, since all three layers have the same type of *continuous* blood capillaries (Levick, 2013).

The hydraulic conductivity K_{aw} of the subcutaneous tissue and skin were found to be 0.4 and 0.35 times that of the muscle, respectively (Swartz and Fleury, 2007). Following Stachowska-Pietka et al. (2004), $q_{l1,aw}$ of the subcutaneous tissue and skin were scaled in the same ratio, in relation to the muscle, as that of the hydraulic conductivity (i.e. 0.4 and 0.35, respectively).

The thickness of the muscle, subcutaneous tissue and skin layer of the human abdominal wall were found to vary widely between $2.81 - 11.38\,\text{mm}$ (Dong et al., 2015), $10.89 - 19.71\,\text{mm}$ (Dong et al., 2015) and $0.75 - 1.16\,\text{mm}$ (Alexander and Miller, 1979), respectively. An averaged value of thickness for each of the sublayers was used in our numerical simulations.

A summary of all the parameters used in the abdominal wall model and their physiological

values is also given in Table 5.4 on page 185.

5.3.4 Results and Discussion

5.3.4.1 Fluid Contributions to the Peritoneal Cavity

The results of simulating the flux equations that were defined in Sections 5.3.3.1–5.3.3.4 are presented in this section. We also plot the result of the net volume flux in the peritoneal cavity in two cases. Firstly, in the case of a constant hydraulic conductivity in the abdominal wall (i.e. no abdominal expansion) as in the studies by Zink and Greenway (1977) and secondly, in the case of the abdominal wall hydraulic conductivity increasing with abdominal wall pressure (i.e. allowing for abdominal expansion).

Figure 5.7 shows the volumetric fluxes predicted by the model from each of the organs/tissue into the peritoneal cavity with changes in peritoneal cavity pressure, while Figure 5.8 shows the net volume change in the peritoneal cavity, defined in Equation (5.17), as the sum of these fluxes. Both figures also show the case of constant hydraulic conductivity in the abdominal wall (dashed lines) and the case in which the hydraulic conductivity is given by Equation (5.28) (solid lines), which only makes a difference in the case of the flux into the abdominal wall and the total absorption rate.

Net flow from the liver and spleen is into the peritoneal cavity for pressures $P_{PC} < 3.65\,\text{mmHg}$ and $P_{PC} < 2\,\text{mmHg}$, respectively, and out of the peritoneal cavity for larger pressures. Net flow from the peritoneal cavity into the diaphragm is positive for all pressures considered, whilst the abdominal wall flow is positive for $P_{PC} > -0.7\,\text{mmHg}$. With pressure-dependent hydraulic conductivity, and for $P_{PC} = 10\,\text{mmHg}$, uptake by the abdominal wall is more than twice that of the case of constant hydraulic conductivity, suggesting it is important to include this feature at high pressures. Correspondingly, the total absorption rate is significantly higher at larger pressures in the case of pressure-dependent hydraulic conductivity.

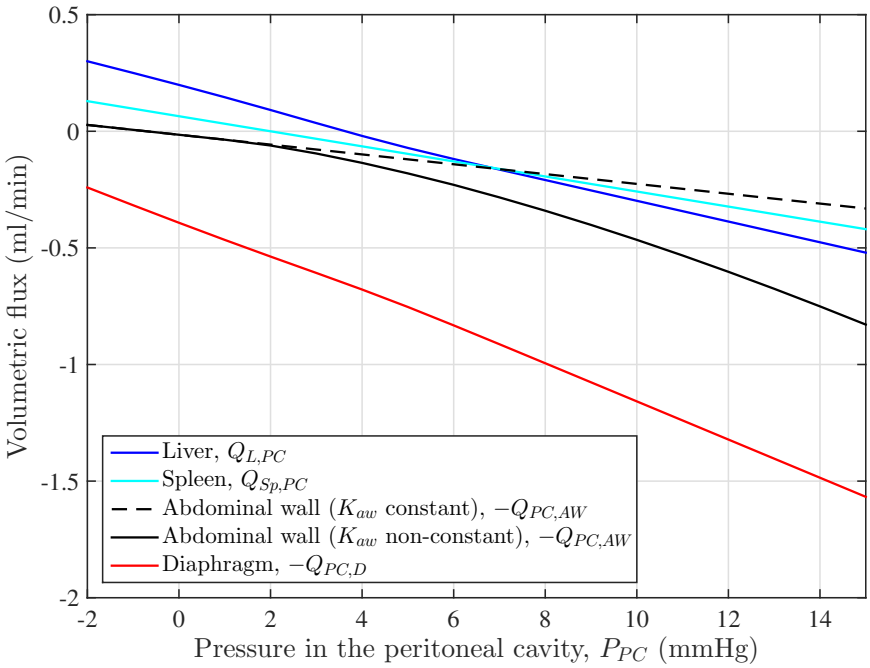


Figure 5.7: Volumetric fluxes from each organ into the peritoneal cavity. Dark blue: liver, $Q_{L,PC}$; Light blue: spleen, $Q_{Sp,PC}$; Black: abdominal wall, $-Q_{PC,AW}$; Red: diaphragm, $-Q_{PC,D}$. In the case of the abdominal wall, the dashed line shows the case with constant hydraulic conductivity and the solid line indicates the case with pressure-dependent hydraulic conductivity given by Equation (5.28).

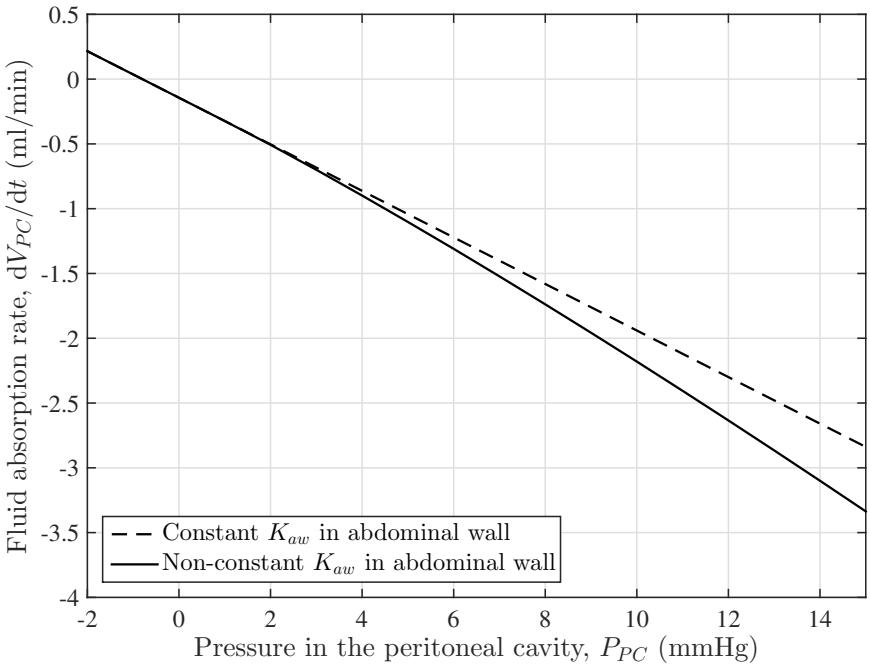


Figure 5.8: Total fluid absorption rate from the peritoneal cavity dV_{PC}/dt given by Equation (5.17), against change in intraperitoneal pressure. The dashed line shows the case with constant hydraulic conductivity and the solid line indicates the case with pressure-dependent hydraulic conductivity given by (5.28).

5.3.4.2 Parameter Estimates

In this section, we investigate the values of the diaphragmatic parameters G_{stoma} and P_{stoma}, which we estimated from our model, and also investigate the relative errors of some of the parameter values associated with the spleen flux and the abdominal wall flux. These parameters, discussed below, are selected for analysis as their values are less certain than others. An extensive parameter sensitivity analysis of the liver flux was done by both Siggers et al. (2014) and also in Chapters 2–4 of this thesis. The diaphragm flux was obtained from the sum of the other organ fluxes using mass conservation (Section 5.3.3.3) and so changed accordingly.

Parameters Associated with the Diaphragm

Since the physiological parameters values of G_{stoma} and P_{stoma} were not readily available in the literature, we had to deduce them a priori from our model using the process described in Section 5.3.3.3. Furthermore, as mentioned Section 5.3.3.4, since in the experiments by Zink and Greenway (1977) the entire abdomen of the cats was enclosed in a cast to prevent expansion of the abdominal wall, instead of using Equation (5.28) we use $K_{aw} = a_K$ for all p_{aw}. Substituting into Equation (5.22), and requiring the equation to hold for all values of P_{PC}, we can find estimated values of G_{stoma} and P_{stoma}.

Note, however, as we can see from Figure 5.7 (red line), flux across the diaphragm predicted by our model increases slightly non-linearly with increasing peritoneal cavity pressure. This is due to the fact that the liver flux obtained using the 3D hyperelastic is non-linear (dark blue line in Figure 5.7), and by volume conservation, so is the diaphragm flux since both spleen and abdominal wall fluxes are linear in the case of $K_{aw} = a_K$, for all p_{aw}. This means that the parameter G_{stoma} is possibly non-constant. So we let $G_{\text{stoma}} = G_0 + G_1 P_{PC}$, where G_0 and G_1 are constants to be found. Using parameter fitting analysis, we find that G_{stoma} does increase with increase in P_{PC}, with approximate estimates of $G_0 = 4.49 \times 10^{-9}\,\text{mL/min/mmHg}$, $G_1 = 2.92 \times 10^{-11}\,\text{mL/min/mmHg}^2$ and $P_{\text{stoma}} = -5.57\,\text{mmHg}$. The ratio $G_1/G_0 = 0.0065$ gives us a measure of the increase in average hydraulic conductivity of the stoma with each increase in peritoneal cavity pressure, which is relatively small. Also, we can deduce that at steady state pressure within the peritoneal cavity (i.e. at $P_{PC} = -0.8\,\text{mmHg}$), the average hydraulic conductivity of the stoma is given by $G_{\text{stoma}} = 4.63 \times 10^{-9}\,\text{mL/min/mmHg}$ and the total hydraulic conductivity of the stomata per unit area is given by $M_{\text{stoma}} = D_{\text{stoma}} G_{\text{stoma}} = 1.16 \times 10^{-6}\,\text{m/min/mmHg}$.

Miserocchi et al. (1989) experimentally estimated the hydraulic conductivity across the tendinous part of a rabbit diaphragm by applying a forced pressure drop of between 0 mmHg and $-7\,\text{mmHg}$ between the pleural cavity and the peritoneal cavity (with the pressure in the peritoneal cavity being the higher of the two), and obtained an estimate of $2.0 \times 10^{-5}\,\text{m/min/mmHg}$ for the mean hydraulic conductivity per unit area, which is much higher than our value. As stated in the discussion of experimental limitations in their paper, their experiments could not

clearly distinguish whether the fluid from the peritoneal side of the diaphragm flowed directly into the diaphragmatic lymphatics within the stomata, or whether it crossed the diaphragm and flowed into the pleural cavity, or whether there was a combination of both these flows. Moriondo et al. (2007) carried out a more recent study in which radioactive markers were placed in the peritoneal fluid of sedated rats, which were traced to lymphatic vessels both on the surface of and within the diaphragm, but were not found in the pleural cavity, both in normal and in ascites-induced conditions. A possible explanation of the difference between the hydraulic conductivity per unit area predicted by our model and that found by Miserocchi et al. (1989) is that there was drainage through both pathways in their experiment, due to the high pressures and experimental techniques used, but under normal physiological conditions there would only be drainage into the diaphragmatic lymphatics and not directly into the pleural cavity.

The uptake rates predicted by the model suggest that, for example, in the normal measured physiological range of $2.9 - 3.7\,\text{mmHg}$, flow into the diaphragmatic lymphatics is between $0.60 - 0.66\,\text{ml/min}$, which agrees with direct measurements of flow rates in lymphatic vessels draining the peritoneal cavity by Tran et al. (1993a,b). This value represents around 80% of fluid uptake from the cavity in our model. Note that the studies by Tran et al. (1993a,b) were conducted on sheep. In a separate study conducted by Heimbürger et al. (1995) on human patients already undergoing peritoneal dialysis, a colloid tracer dissolved in a hypertonic fluid was used to estimated the rate of fluid loss from the peritoneal cavity. At peritoneal cavity pressures of $6 - 8\,\text{mmHg}$ (supine), the tracer disappearance rate from the cavity was found to be between $1.03 - 1.15\,\text{ml/min}$ while the rate of reappearance in blood plasma was at a lower value of $0.15 - 0.17\,\text{ml/min}$. At similar peritoneal cavity pressures, our model predicts a rate of uptake by the diaphragmatic lymphatics of $0.83 - 0.99\,\text{ml/min}$, which lies between the two extremes of the values estimated by Heimbürger et al. (1995).

Note, however, that we did not account for pressure variations due to normal movements of the diaphragm during breathing, which could affect the flows. A rough estimate can be obtained from the results of Miserocchi et al. (1989) who measured the pressure in both the the pleural cavity and in the peritoneal cavity of rabbits during inspiration. The pressures increased from $-3.7\,\text{mmHg}$ to $-8.3\,\text{mmHg}$ and from $-2.7\,\text{mmHg}$ to $-3.2\,\text{mmHg}$ during inspiration for the two cavities, respectively. Thus the pressure variation in the peritoneal cavity during breathing is around $0.5\,\text{mmHg}$, corresponding to a flux difference into the diaphragm of around $0.04\,\text{ml/min}$. Changes in respiratory pattern and posture are also likely to have an effect on the rate of fluid drainage through the diaphragmatic lymphatics. However, these changes are outside the scope of this research and can be considered as part of future studies.

Parameters Associated with the Abdominal Wall

The capillary wall filtration coefficients $L_p a$ of the subcutaneous tissue and skin were assumed to be the same as that of the muscle, i.e. 5.3×10^{-5} /min/mmHg (see Table 5.4). Doubling or halving the value of $L_p a$ in the subcutaneous tissue and skin sublayers has a negligible effect on the volumetric flux into the abdominal wall at different peritoneal cavity pressures, with less than 3% change, respectively.

The sensitivity of the lymphatic absorption to increase in pressure q_{l1} of the subcutaneous tissue and skin were scaled in the same ratios, in relation to the muscle, as those of the hydraulic conductivity (i.e. 0.4 and 0.35, respectively). Similarly, doubling or halving these values had a negligible effect on the volumetric flux into the abdominal wall at different peritoneal cavity pressures ($< 2\%$ change).

The thickness of the muscle, subcutaneous tissue and skin layers of the human abdominal wall were found to vary widely between $2.81 - 11.38$ mm (Dong et al., 2015), $10.89 - 19.71$ mm (Dong et al., 2015) and $0.75 - 1.16$ mm (Alexander and Miller, 1979), respectively. We made use of the average value from each set of measurements of the individual sublayers for the abdominal wall model (muscle = 7.53 mm; subcutaneous tissue = 14.98 mm; skin = 1.01 mm; see Table 5.4). Increasing the thickness of the muscle layer resulted in up to 9.5% increase in the volumetric flux across the wall in the case with K_{aw} constant and 17.6% increase in the volumetric flux in the case with K_{aw} as a linear function of pressure (see Figure 5.9). The muscle layer takes up fluid at a higher rate than the other tissue layers, which is why increasing its thickness results in the overall increased uptake of fluid by the abdominal wall. But the uptake rate approaches a constant value if the muscle layer is thick enough, as most of the uptake happens near the wall of the peritoneal cavity. Varying the thickness of the subcutaneous tissue and skin layers had a negligible effect on the volumetric fluid flux ($< 0.1\%$ change).

Parameters Associated with the Spleen

To create Figure 5.7, we assumed that the hydraulic conductivity of the spleen membrane is the same as that of the Glissonian–peritoneal membrane (i.e. $M_{Sp} = M_{GP}$). Decreasing the value of M_{Sp} simply decreases the gradient of the spleen flux, as shown in Figure 5.10. This in turn increases the gradient of the fluid flux into the diaphragm (see Figure 5.11). For example, when we increase the values of M_{Sp} from 0 to M_{GP}, as in Figure 5.10, the estimated value of the base hydraulic conductivity of the stoma G_0 increases from 4.49×10^{-9} mL/min/mmHg to 6.65×10^{-9} mL/min/mmHg, while the sensitivity of the hydraulic conductivity of the stoma to peritoneal cavity pressure increase G_1 remained constant at 2.92×10^{-11} mL/min/mmHg^2 for all variations of M_{Sp}. The average pressure within the stoma P_{stoma} also increased from -5.57 mmHg to -3.14 mmHg. In all cases, the value of P_{stoma} obtained is within the expected range, given that experimental measurements of the underlying diaphragmatic interstitial fluid and lymphatic lacunae had pressures ranging between 2 to -10 mmHg and -25 to -35 mmHg,

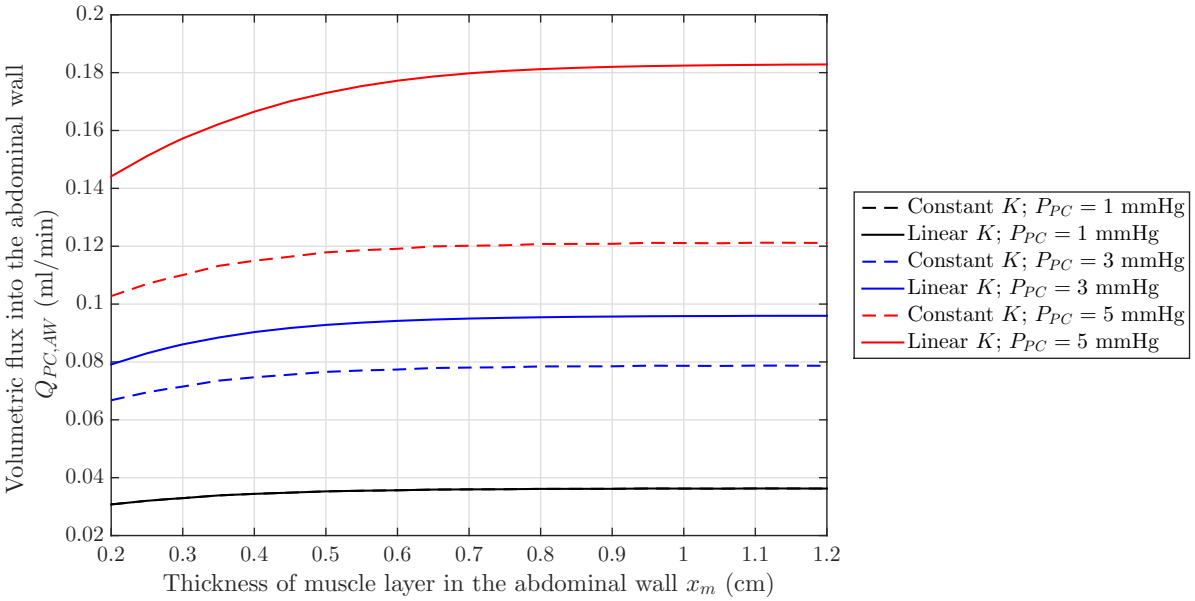


Figure 5.9: Graph of volumetric flux from the peritoneal cavity into the abdominal wall against change in abdominal muscle thickness for different values of peritoneal cavity pressure. The dashed lines show the case with constant hydraulic conductivity and the solid lines indicate the case with pressure-dependent hydraulic conductivity given by Equation (5.28). The thicknesses of the subcutaneous tissue and skin layers, as well as all the other parameters except x_m and P_{PC}, are held fixed at the values in Table 5.4. The black solid line overlaps the black dashed line since the pressure-dependent hydraulic conductivity is constant for pressures ≤ 1.2 mmHg.

respectively, during normal breathing cycles (Negrini and Moriondo, 2011). The lacunae are embedded deep within the diaphragm, and as expected, have a much lower pressure than P_{stoma} in order to drive fluid flow from the stomata into the lacunae. According to our modelling assumptions, the liver and abdominal fluxes are not affected by the variation of the spleen membrane hydraulic conductivity.

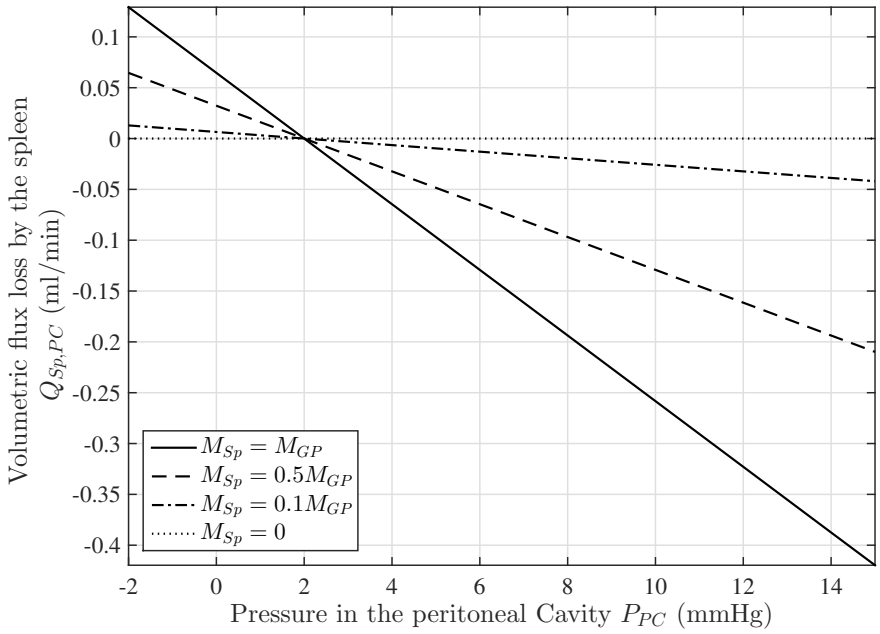


Figure 5.10: Graph of volumetric flux from the spleen into the peritoneal cavity $Q_{Sp,PC}$ against change in peritoneal cavity pressure for different values of the membrane conductivity of the spleen M_{Sp}.

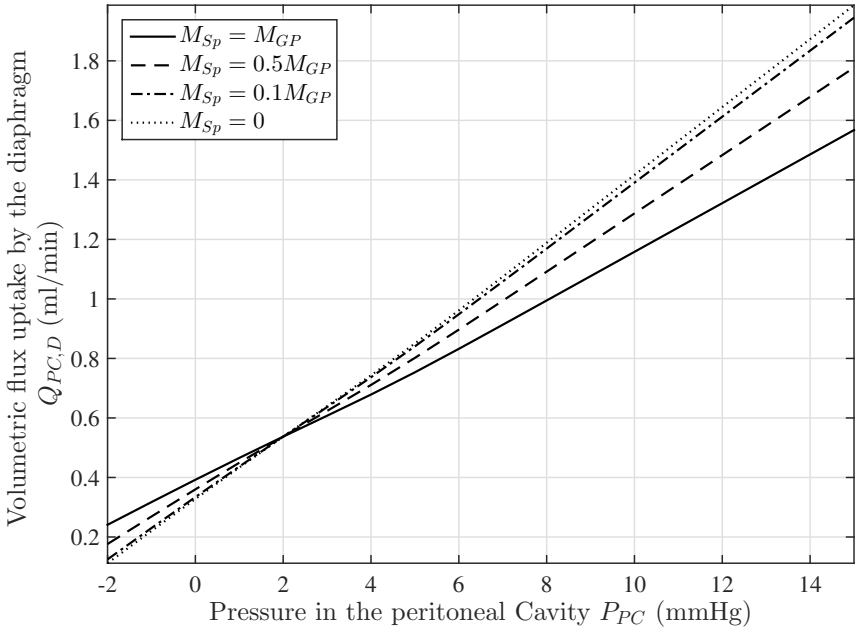


Figure 5.11: Graph of volumetric flux from the peritoneal cavity into the diaphragm $Q_{PC,D}$ against change in peritoneal cavity pressure for different values of the membrane conductivity of the spleen M_{Sp}.

Table 5.2: List of parameter values used to estimate fluid flux from the spleen, together with references.

Symbol	Description	Default Value	Reference
A_{Sp}	Surface area of the spleen adjacent to the peritoneal cavity	$250\,\text{cm}^2$	See Section 5.3.3.2
M_{Sp}	Hydraulic conductivity of spleen membrane per unit area	M_{GP}	See Section 5.3.3.2
P_{Sp}	Average interstitial fluid mechanical pressure at the interior surface of the spleen	2 mmHg	Assumed

Table 5.3: List of parameter values used to estimate fluid flux through the diaphragm, together with references.

Symbol	Description	Default Value	Reference
A_D	Surface area of the diaphragm adjacent to the peritoneal cavity	$620\,\text{cm}^2$	Rubin et al. (1988a)
D_{stoma}	Density of diaphragmatic stomata	$25,000\,/\text{cm}^2$	Negrini et al. (1991)
G_0	Average base hydraulic conductivity of a diaphragmatic stoma	4.49×10^{-9} mL/min/mmHg	See Section 5.3.4.2
G_1	Sensitivity of the hydraulic conductivity of the average diaphragm stoma to increase in peritoneal cavity pressure	2.92×10^{-11} mL/min/mmHg^2	See Section 5.3.4.2
P_{stoma}	Average pressure within the stoma	-5.57 mmHg	See Section 5.3.4.2

Table 5.4: List of parameter values used in the abdominal wall model, together with references.

Symbol	Description	Default Value	Reference
A_{AW}	Surface area of the abdominal wall adjacent to the peritoneal cavity	$840\,\text{cm}^2$	Rubin et al. (1988a)
x_m	Width of muscle layer within the abdominal wall	7.53 mm	Dong et al. (2015)
$x_f - x_m$	Width of subcutaneous tissue layer within the abdominal wall	14.98 mm	Dong et al. (2015)
$x_s - x_f$	Width of skin layer within the abdominal wall	1.01 mm	Alexander and Miller (1979)
$(a_K)_m$	Basic hydraulic conductivity level per unit depth (*muscle*)	$9 \times 10^{-6}\,\text{cm}^2/\text{min/mmHg}$	Zakaria et al. (1997)
$(a_K)_f$	Basic hydraulic conductivity level per unit depth (*subcutaneous tissue*)	$0.4a_{Km}$	Swartz and Fleury (2007)
$(a_K)_s$	Basic hydraulic conductivity level per unit depth (*skin*)	$0.35a_{Km}$	Swartz and Fleury (2007)
$(b_K)_m$	Sensitivity of hydraulic conductivity to increase in pressure per unit depth (*muscle*)	$5.6 \times 10^{-6}\,\text{cm}^2/\text{min/mmHg}^2$	Zakaria et al. (1997)
$(b_K)_f$	Sensitivity of hydraulic conductivity to increase in pressure per unit depth (*subcutaneous tissue*)	$0.4b_{Km}$	See Section 5.3.3.4
$(b_K)_s$	Sensitivity of hydraulic conductivity to increase in pressure per unit depth (*skin*)	$0.35b_{Km}$	See Section 5.3.3.4
$(L_pa)_m$	Capillary wall filtration coefficient (*muscle*)	$5.3 \times 10^{-5}\,/\text{min/mmHg}$	Xie et al. (1995)
$(L_pa)_f$	Capillary wall filtration coefficient (*subcutaneous tissue*)	$(L_pa)_m$	See Section 5.3.3.4
$(L_pa)_s$	Capillary wall filtration coefficient (*skin)*	$(L_pa)_m$	See Section 5.3.3.4
p_b	Blood mechanical pressure	11.0 mmHg	Xie et al. (1995)
Π_b	Blood oncotic pressure	25.9 mmHg	Xie et al. (1995)
Π_0	Eq'm interstitial fluid oncotic pressure	14.7 mmHg	Xie et al. (1995)
σ_Π	Capillary wall reflection coefficient	0.99	Xie et al. (1995)
$p_{aw,0}$	Eq'm interstitial mechanical pressure	-0.7 mmHg	Xie et al. (1995)
q_{l0}	Rate of lymphatic absorption in the steady state of the system	$3.3 \times 10^{-5}\,/\text{min}$	Xie et al. (1995)
$(q_{l1})_m$	Sensitivity of lymphatic absorption to increase in pressure (*muscle*)	$(0.6\,/\text{mmHg})q_{l0}$	Xie et al. (1995)
$(q_{l1})_f$	Sensitivity of lymphatic absorption to increase in pressure (*subcutaneous tissue*)	$0.4(q_{l1})_m$	See Section 5.3.3.4
$(q_{l1})_s$	Sensitivity of lymphatic absorption to increase in pressure (*skin*)	$0.35(q_{l1})_m$	See Section 5.3.3.4
M_{AW}	Rate of fluid uptake by the abdominal wall per unit area, in the case with no abdominal wall expansion	$2.51\times10^{-9}\,\text{m/min/mmHg}$	See Section 5.3.3.4

5.4 Development of Ascites due to Liver Disease

Abnormal accumulation of fluid in the peritoneal cavity, as observed in ascites patients, suggests a significant imbalance in the rate of fluid turnover within the cavity. Such large fluid build up will only occur if the rate of fluid flow into the peritoneal cavity is much higher than the rate of drainage, over a prolonged period of time. In this section, we will make use of the compartmental model of fluid exchange in the peritoneal cavity developed in Section 5.3 to study the role played by the diseased liver, presented in Chapter 4, in the accumulation of abnormal fluid in the peritoneal cavity.

Based on the results in Chapter 4, we know that portal hypertension is the driving force for increased fluid loss from the liver into the peritoneal cavity. However, the different stages of liver fibrosis also produce different degrees of fluid loss. Hence, we will study the effects of combined portal hypertension and tissue fibrosis, and make use of the 5 tissue types defined in Section 4.4. Listed in progressive diseased stages, these are the: healthy liver tissue, mild fibrotic tissue, severe fibrotic tissue with little membrane damage (moderate M_{GP}), severe fibrotic tissue with severe membrane damage (high M_{GP}) and cirrhotic tissue with advanced membrane damage, where M_{GP} is the conductivity of the Glissonian–peritoneal membrane.

For each tissue type, the steady state pressure in the peritoneal cavity following portal hypertension is obtained by estimating the average fluid loss from the Glissonian–peritoneal liver surface into the peritoneal cavity, $Q_{\mathrm{L,PC}}$, at different peritoneal cavity pressures, P_{PC}, and then finding the steady state pressure where the rate of fluid volume change equals zero, i.e. $\mathrm{d}V_{PC}/\mathrm{d}t = 0$. Having obtained the steady state peritoneal cavity pressure, we then make use of the volume–pressure equations derived in Section 5.2.3 to obtain the steady state fluid volume in the peritoneal cavity, in each tissue type, as the blood sinusoidal portal pressure increases.

The resulting pressure against liver sinusoidal portal hypertension for the different tissue types is shown in Figure 5.12. Note that for all tissue types, the steady state pressure follows a similar profile to that of fluid loss from the liver surface $Q_{\mathrm{L,PC}}$, shown in Figure 4.19 of Section 4.4, i.e. it increases non-linearly with increase in blood portal tract pressure. Also, the more advanced the fibrosis stage, the less increase in steady state peritoneal cavity pressure there is for each unit rise in blood portal tract pressure. For the healthy liver tissue in Figure 5.12, blood portal tract pressure is capped at about 13 mmHg, which is when the volume change ratio of the tissue $J = 1.45$. As explained in Section 4.4, this limit on J is imposed as we do not expect the liver tissue to expand beyond this value, especially in the healthy case. For the mild fibrotic case, this cap is placed at a blood portal tract pressure of about 18 mmHg. The blood portal tract pressures of the severe fibrotic and cirrhotic tissues were not capped since the volume change ratio did not reach the value of 1.45 for all blood portal tract pressures considered (up to 22 mmHg). However, note that in the case of the severe fibrotic tissue with severe membrane damage (high M_{GP}), the steady state peritoneal cavity pressure result in Figure 5.12 goes up to 8.4 mmHg, which is just below the ≈ 8.5 mmHg limit of the combination model of the

volume–pressure relationship of the peritoneal cavity (see Figure 5.3 in Section 5.2.3).

The fluid volume accumulation in the peritoneal cavity corresponding to the steady state pressures in Figure 5.12 is shown in Figure 5.13. As expected, fluid volume accumulation in the peritoneal cavity also increases non-linearly with increase in blood portal pressure, but with a smaller gradient for each progressive stage of fibrosis. The cirrhotic liver tissue had the least accumulation of fluid volume per unit rise in blood portal tract pressure. Note that both the healthy tissue and the mild fibrotic tissue have the same caps in blood portal tract pressures as that of the steady state peritoneal cavity pressure (at 13 mmHg and 18 mmHg, respectively), for the same reason as detailed in the paragraph above. Note, also that for all blood portal tract pressures considered in Figure 5.13 (up to 22 mmHg), fluid volume accumulation in the peritoneal cavity using the healthy tissue, mild fibrotic tissue and cirrhotic tissue was below the assigned critical fluid volume of the peritoneal cavity ($V_{PC,\text{crit}} = 5\,\text{L}$) and so stayed within the linear regime of the volume–pressure relationship. Only the severe fibrotic liver tissue resulted in volumes above 5 L, and so captured the linearly elastic regime of volume–pressure relationship above $V_{PC,\text{crit}}$. In particular, the severe fibrotic tissue with severe membrane damage (high M_{GP}) best highlights the exponential rise in fluid volume accumulation, above $V_{PC,\text{crit}}$, as the blood portal tract pressure increases.

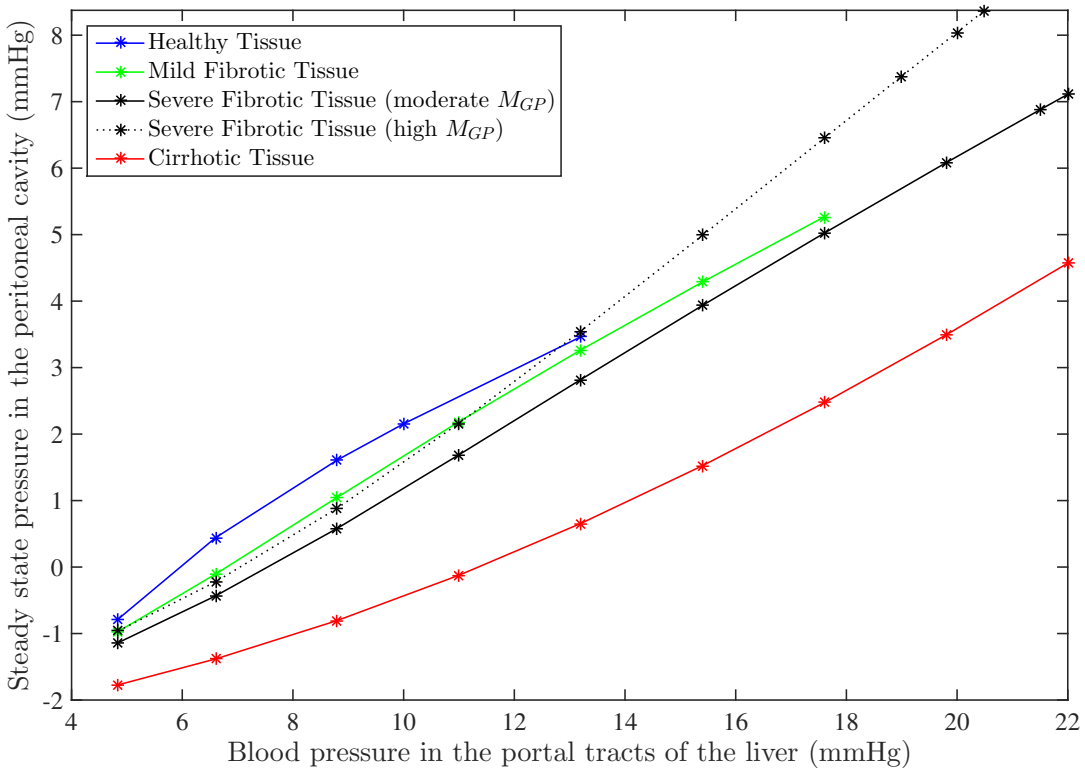


Figure 5.12: Fluid pressure in the peritoneal cavity against increase in blood pressure in the portal tracts of the liver for the different liver tissue types, as defined in Section 4.4.

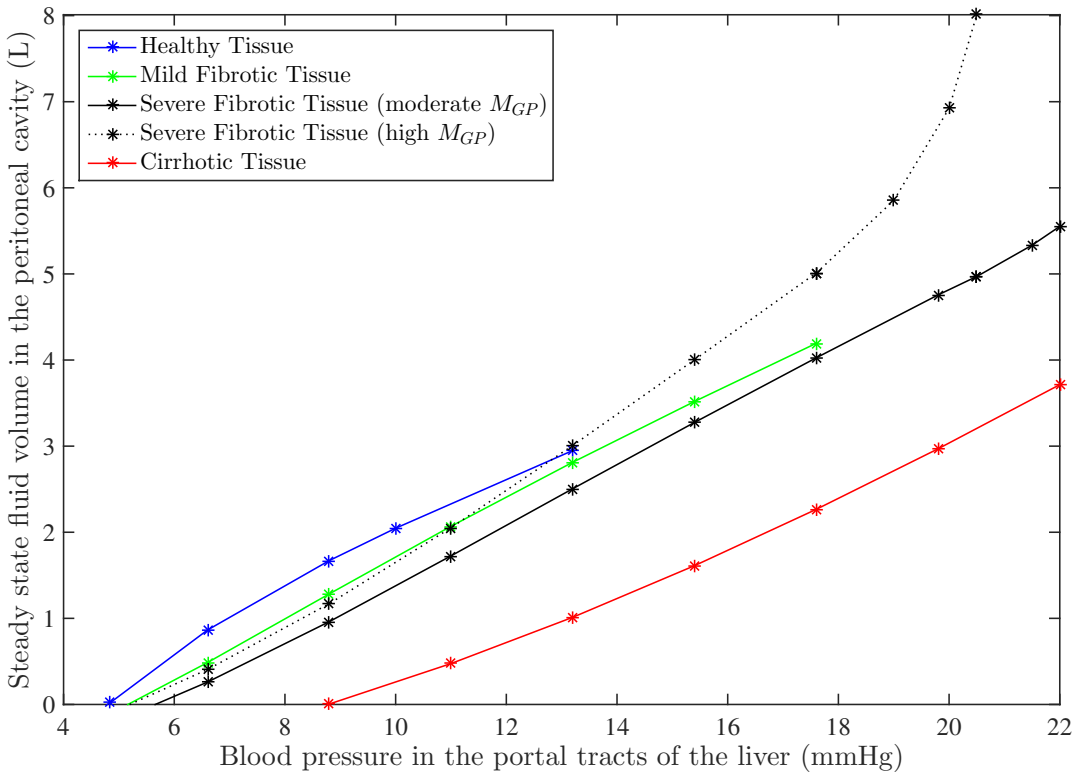


Figure 5.13: Fluid volume accumulation in the peritoneal cavity against increase in blood pressure in the portal tracts of the liver for the different liver tissue types, as defined in Section 4.4.

Note that the model predicts negative volumes for pressures < -0.8 mmHg (physiological steady state pressure) as a consequence of the fact that the pressure–volume relationship does not capture correctly what happens at higher negative pressures (since we are not interested in these values for the purposes of this research).

5.4.1 Predicting Severity of Ascites

The International Ascites Club has produced guideline volumes of fluid in the peritoneal cavity in order to classify the severity of ascites and method of detection, which are shown in Table 5.5. Based on Figure 5.13 and Table 5.5, we can deduce the following from our peritoneal cavity model:

Healthy Case

- Even in the case of a healthy liver tissue, prolonged portal hypertension is likely to lead to the accumulation of abnormal fluid volumes in the peritoneal cavity. Over time, a 1 mmHg rise in blood portal tract pressure (i.e. $p_s^{pt} = 5.8$ mmHg, about 20% higher than its normal physiological value) can lead to a fluid volume increase classed as Grade 1 ascites. Grade 2 ascites would occur if p_s^{pt} increase is between 20% and 75% of its normal physiological value (i.e. 5.8 mmHg and 8.4 mmHg, respectively) and Grade 3 ascites if p_s^{pt} increase is greater than 75% of its normal physiological value (8.4 mmHg). Note however

that such variation in portal tract pressures are unlikely to occur without causing other damage to the liver tissue.

Diseased Cases

- Grade 1 ascites develops when the blood portal tract pressure becomes higher than 5.3 mmHg in the mild fibrotic tissue, 5.9 mmHg in the severe fibrotic tissue and 9.0 mmHg in the cirrhotic tissue. This supports medical data that shows that patients with severe cirrhosis but without portal hypertension do not develop ascites, and that a sinusoidal portal pressure greater than 9.3 mmHg is required before ascites can be detected in cirrhotic patients (Morali et al., 1992).
- Grade 2 ascites develops when the blood portal tract pressures are between 5.3 mmHg and 9.4 mmHg in the mild fibrotic case, 5.9 mmHg and 10.4 mmHg in the severe fibrotic case and 9.0 mmHg and 15.0 mmHg in the cirrhotic case.
- Finally, Grade 3 ascites develops when the blood portal tract pressure is higher than 9.4 mmHg in the mild fibrotic case, 10.4 mmHg in the severe fibrotic case and 15.0 mmHg in the cirrhotic case.

Grade	Fluid Volume	Description
1	< 500 ml	Mild ascites detectable only by ultrasound
2	$500 - 1500$ ml	Moderate ascites manifested by moderate symmetrical distension of the abdomen
3	> 1500 ml	Large ascites with marked abdominal distension

Table 5.5: Classification of the severity of ascites by the International Ascites Club (Moore et al., 2003).

Given that the volume of ascitic fluid could be easily measured using an ultrasound and the stage of fibrosis determined by liver elastography, the estimates of the sinusoidal blood portal pressures obtained above for the different grades of ascites could perhaps be useful in informing treatment strategies, e.g. by acting as a guide for the placement of portal venous stents used to treat portal hypertension, and hence, limit the further progression of ascites.

5.5 Summary and Conclusion

We began this chapter by studying the effect of increased fluid volume on pressure within the peritoneal cavity. Based on experiments by Twardowski et al. (1983), we modelled the cavity as having a linear relationship between pressure and fluid volumes up to 5 L. For fluid volumes

$> 5\,\mathrm{L}$, we modelled the peritoneum as a thin linearly elastic membrane, which resulted in a non-linear volume–pressure behaviour representative of biological potential spaces, with a higher compliance at higher fluid volumes. The maximum fluid volume allowed by the model gave an indication of the maximum possible expansion and pressure within the cavity, thus, providing a first approximation of the true peritoneal cavity dynamics.

Then, we developed a compartmental model of fluid exchange between the peritoneal cavity and some of the adjacent tissues/organs, namely: liver, spleen, diaphragm and abdominal wall. For each adjacent tissue/organ, we defined equations to quantify the fluid volume flux from the organ to the peritoneal cavity, and vice versa. We then made use of the model to predict the rates of fluid production and drainage by the adjacent tissues/organs, for different peritoneal cavity pressures. For example, at $P_{PC} = P_{\mathrm{ref}} = 0\,\mathrm{mmHg}$, the liver is estimated to produce 75% of the fluid input into the peritoneal cavity, with the remainder coming from the spleen, while 96% of the drainage goes into the diaphragm with the remaining 4% going into the abdominal wall (for both the cases of constant and non-constant K_{aw}). As P_{PC} increases from zero, a gradually higher proportion of the outflow enters the abdominal wall. Note that if we remove the spleen contribution from our model, only the liver acts as a source of fluid into the peritoneal cavity, and for example at $P_{PC} = P_{\mathrm{ref}} = 0\,\mathrm{mmHg}$, about 95% of the drain is still through the diaphragm, while the remainder is into the abdominal wall. Note also that in the model, we neglected any production or drainage by the hollow viscera.

Finally, we made use of the compartmental model of fluid exchange developed and the volume–pressure equations derived for the peritoneal cavity to study the effect of increased fluid flux from the liver, as a result of liver fibrosis and portal hypertension, on the development of ascites. Fluid accumulation in the peritoneal cavity increased with increase in portal hypertension, but decreased with progressive fibrosis stages. The general pattern observed was that the further the progression of fibrosis stage, the higher the blood portal tract pressure necessary to generate fluid accumulation in the peritoneal cavity. This is in agreement with the rest of the results obtained in this thesis, since progressive fibrosis reduces the permeability of the interstitial space, and hence the filtration capability of the sinusoids, so that less interstitial fluid is able to flow from the interior liver tissue, towards the liver surface and into the peritoneal cavity. On the other hand, the Glissonian–peritoneal membrane also plays an important role in the regulation of fluid volume accumulation in the peritoneal cavity. This fact is highlighted when we compare the results of the severe fibrotic tissue with different membrane conductivities (moderate M_{GP} and high M_{GP}). The higher membrane conductivity value (high M_{GP}), representing a more severe membrane damage, showed an even higher fluid volume accumulation in the peritoneal cavity than all the other stages of tissue fibrosis considered. This tells us that before the diseased liver reaches the terminal cirrhotic stage, the liver surface membrane might be key to limiting the accumulation of fluid in the peritoneal cavity and that more research is required into the disease progression of the Glissonian–peritoneal membrane itself and how it relates to the different fibrotic staging of the interior liver tissue.

Part IV

Conclusion

Chapter 6

Thesis Summary and Conclusion

6.1 General Summary/Discussion

The primary aim of this thesis was to develop a more robust mathematical model of micro-circulation in the liver, so as to study the effect of liver diseases on blood perfusion and the resultant development of ascites in the peritoneal cavity. This involved extending the current rigid double-porous media model by Siggers et al. (2014) to include tissue compliance, through modelling the liver as a homogeneous double poro-elastic solid. The inherent assumption in our modelling was that increase in blood sinusoidal portal pressure translated to a normal pressure stress that resulted in the expansion of the pore networks, and hence, deformation of the tissue to accommodate changes in blood and interstitial fluid volume. With that in mind, we worked in terms of blood and interstitial fluid pressures referenced against their values in the normal physiological case, also termed the undeformed liver. The coupling between fluid flow and solid deformation was achieved through the individual hydraulic conductivities of the fluid networks, which was made dependent on the deformation gradient of the respective pore networks.

As a first approximation, the liver tissue was modelled as a 2D linearly elastic solid using small strain deformation theory in Chapter 2. This allowed us to obtain blood and interstitial fluid flow profiles, as well as tissue displacement following, for example, a 10% increase in blood sinusoidal portal tract pressure. We studied the results of both a single lobule and that of a lattice arrangement of lobules close to the liver surface. The model also allowed us to make estimates of important parameters, including the tissue expansion, total blood flux into the liver, lymphatic uptake rate and fluid loss via the outer surface of the liver, against changes in blood sinusoidal portal tract pressure. The results obtained showed a significant difference between the linear elastic model and the current rigid model of the liver by Siggers et al. (2014), with the former giving much lower values of the parameter estimates with increase in blood sinusoidal portal tract pressure, which highlights the importance of incorporating tissue compliance in our liver model.

The linearly elastic model was only valid for strains up to 10%, while the liver tissue is

capable of expanding up to 40% (Chui et al., 2004). In Chapter 3, we extended the 2D linear elastic model into a 3D hyperelastic model, which is more representative of the non-linear stress–strain behaviour of the liver tissue. The 3D hyperelastic model gave the same results as that of the 2D linear elastic model up to a liver volume increase of about 10%, which is expected since the hyperelastic equations become approximately linear under small strain. However, above the 10% liver volume increase, the 3D hyperelastic model gave higher results for all other parameters estimated, including the total blood flux into the liver, lymphatic uptake rate and the fluid loss from the liver into the peritoneal cavity, highlighting the slight underestimation given by the 2D linear elastic model at higher blood sinusoidal portal tract pressures. For this reason, we make use of the 3D hyperelastic model to study the effect of liver diseases.

In Chapter 4, we looked at the effect of different stages of tissue fibrosis, including mild, severe and advanced (cirrhotic), which are consequences of progressive liver disease, and portal hypertension on fluid flow and deformation of the liver tissue. The different stages of tissue fibrosis were modelled using increased bulk tissue stiffness, decrease in interstitial space permeability and increase in conductivity of the Glissonian–peritoneal membrane, respectively, in order to capture the changes in tissue structure that occur within each progressive stage. All the parameter estimates investigated, including tissue expansion, average blood and interstitial fluid velocities, total blood flux into the liver, lymphatic uptake and fluid loss into the peritoneal cavity, decreased with each progressive stage of fibrosis. This highlights the significant decrease in blood perfusion present in a diseased liver. The further the progression of fibrosis, the higher the blood portal pressure (and by relation sinusoidal portal tract pressure) required to filter the same volume of blood in the body. This was all successfully captured by the 3D hyper-poroelastic model.

In Chapter 5, we developed a mathematical model of the peritoneal cavity, which included both deriving equations for the fluid volume–pressure behaviour of the peritoneal cavity, and also developing a compartmental model of fluid exchange between the peritoneal cavity and the liver, spleen, diaphragm and abdominal wall. The volume–pressure relationship served as a first approximation towards understanding the fluid dynamics of the cavity, while the compartmental model allowed us to quantify the fluid flux across the sources (liver and spleen) and the drains (diaphragm and abdominal wall) of the peritoneal cavity. Finally, we made use of the peritoneal cavity model to investigate the contribution of the diseased liver, with different stages of fibrosis and portal hypertension, towards the accumulation of abnormal fluid volumes in the peritoneal cavity. We found out that portal hypertension is the driving force for fluid loss from the liver into the peritoneal cavity. However, portal hypertension rarely occurs without prior damage to the tissue, i.e. fibrosis. The more severe the degree of fibrosis, the less interstitial fluid is lost through the liver surface as a result of portal hypertension. With our results, we were also able to predict the severity of ascites, depending on the stage of fibrosis, at different blood sinusoidal portal pressures. This could be a useful tool in future diagnostics of liver diseases and could aid in informing treatment strategies for ascites patients. Further

experimental validation of the model on human subjects would need to be performed for this to be achieved. For example, the volume of fluid loss across the Glissonian–peritoneal membrane, and into the peritoneal cavity, can be estimated by increasing the blood pressure into the portal vein and measuring the resultant fluid loss across the liver. This experiment can be carried out for various degrees of blood pressure increase, and also using diseased livers at different stages of fibrosis. The results obtained can be compared to those obtained within this theses, and if necessary, used to recalibrate some of the parameters used.

6.2 Future Work

As the summary above shows, we have achieved the aims and objectives of this research as set out in Chapter 1 of this thesis. Using both the liver models and the peritoneal cavity model, we obtained numerical results that were comparable to experimental data, where available. However, as with all mathematical models, there is always room for improvement. In this final section, we discuss some of the limitations of our models and provide some suggestions for future work that can be undertaken to extend and improve them, which are currently beyond the scope of this research.

6.2.1 3D Hyperelastic Liver Model

Modelling Blood Flow Across the Vascular Septa

Whilst the flow of blood has been restricted to individual lobules within this thesis, studies by Debbaut et al. (2014) and Lettmann and Hardtke–Wolenski (2014) have shown that incorporating blood flow across neighbouring lobules can make a significant difference to blood perfusion in the liver. In both cases, blood perfusion was found to be more homogenous across the lobule with flux across the vascular septa compared with simulations with no flux across the vascular septa. Thus, the effect of blood flow across the vascular septa should be considered in future studies of the poroelastic liver.

Incorporating Anisotropy in Tissue Permeability and Deformation for the Healthy Liver

One of the assumptions made in this thesis about fluid flow in the liver lobule is that it is isotropic, i.e. has the same permeability properties in all three principal directions. In the study by Bonfiglio et al. (2010), it was shown that incorporating anisotropic permeability in a 2D linear elastic model of blood flow in the liver lobule had a small effect on flow and pressure distribution. However, this might not be true in the case of a 3D hyperelastic lobule, as shown in Debbaut et al. (2012) and Peeters et al. (2015), especially under large deformations. Hence, the

potential effect of anisotropic permeability should be considered in any future work. Similarly, we also assumed that deformation of the 3D lobule tissue is orthotropic, i.e. occurs uniformly in all three principal directions. Experimental compression/elongation measurements conducted on liver tissue have shown it to be transversely isotropic, with the tissue being stiffer in the axial direction compared to the transverse direction (Chui et al., 2007). A future extension of the liver model should make use of a transversely isotropic strain energy function (Chui et al., 2007), rather than the fully isotropic function used in this thesis, in order to capture the anisotropic deformation behaviour of the 3D tissue.

Modelling the Glissonian–Peritoneal Membrane as a Hyperelastic Material

The Glisson's capsule of the liver is actually stiffer than the interior parenchyma of the liver tissue (Umale et al., 2011), whereas we have modelled them both to have the same material constants (c_1, c_2, c_3, c_4 and c_5) and bulk tissue stiffness (E_{bulk}). In future work, the Glissonian–peritoneal membrane should be modelled as a hyper-poroelastic tissue, with its own strain energy function (Umale et al., 2011). It would then have its own coupling between the conductivity of the membrane M_{GP} and deformation $\mathbf{u}$, rather than having the constant value of M_{GP} used in this thesis.

Modelling Fibrotic Tissue as Anisotropic Fibres

Rather than making use of a general bulk tissue stiffness (E_{bulk}) to represent the presence of fibrosis, fibrotic tissue itself can be modelled as localised regions of anisotropic fibres within the liver tissue. This is an extension of the model that is currently being done in collaboration with Fillipo Recrosi (Gran Sasso Science Institute), Rodolfo Repetto (University of Genoa) and Amabile Tatone (University of L'Aquila).

Incorporating a Fibrosis-Dependent Tissue Permeability

As highlighted in Section 4.4, decrease in the reference permeability of the interstitial space $\kappa_{i,\text{ref}}$ in the diseased liver was chosen arbitrarily in declining order to correspond with the progressive stages of fibrosis. To make the model more robust, a fibrosis-dependent $\kappa_{i,\text{ref}}$ should be used in the future. Since this cannot be measured experimentally, one way around this would be to make use of the model of localised fibrotic tissue mentioned above to estimate the permeability of the liver lobule. For progressive degrees of localised fibrotic tissue, the resultant fibrosis-dependent permeability can be estimated using a fixed blood volume flux and pressure drop across the lobule.

Incorporating a Model of the Larger Blood and Lymphatic Vessels

Incorporating a network model of the larger blood vessels in the liver will enable us to study the effects of blood pressure changes in the portal vein on the portal tract pressures of the lobules, i.e. obtain a direct relationship between the larger blood vessels and their terminal endings within the liver. This will lead to a better understanding of portal hypertension in the fibrotic liver and should be included in future studies. A model of the larger lymphatic vessels in the liver should also be considered in future studies in order to study the effect of vasodilation on lymphatic drainage.

Modelling Sinusoidal Capillarization in Cirrhotic Tissue

The presence of advanced fibrotic and cirrhotic tissue within the liver has been modelled in this thesis as a global increase in tissue stiffness and the decrease in interstitial space permeability. Another consequence of advanced fibrosis and cirrhosis is sinusoidal capillarization, which is the transformation of hepatic sinusoids into capillaries. Capillarization leads to the decrease in fenestrations of the sinusoids, and hence blood porosity of the liver, and global vascular resistance (Bhunchet and Fujieda, 1993). This phenomenon should be considered in future extensions of the model.

6.2.2 Peritoneal Cavity Model

Modelling the Peritoneum as a Hyperelastic Material

We note that the assumptions used to develop the non-linear volume–pressure relationship of the peritoneal cavity are simplified, and it would be preferable to use a relationship based on experimental data or alternatively, to account more accurately for the non-linear stress–strain behaviour of the peritoneum. Until the availability of further experimental data, the peritoneum can be modelled as a hyperelastic material in the future, which is more representative of the behaviour of biological tissues.

Incorporating a Model of Sodium Transport and Impairment

The peritoneal cavity model presented in this thesis does predict significant accumulation of fluid in the peritoneal cavity for raised, but physiologically realistic, portal tract pressures. However, the very large volumes that are sometimes seen in cirrhotic patients (up to 10 L) are not predicted by this model for the physiological variations that we considered. One improvement that might increase the peritoneal cavity volume to such levels is by incorporating the transport and imbalance of sodium in the model. The reasoning is that expansion of the blood pore network predicted by the compliant model of the liver (more commonly known as

vasodilation) also leads to systemic vasodilation in the rest of the body, leading to reduced systemic vascular resistance and decreased arterial blood pressure (Ginès et al., 2004). One of the homeostatic response provided by the kidneys is vasoconstriction to maintain normal blood pressure. This in turn results in a decreased filtration rate and excretion of sodium, and eventually renal impairment. Sodium is retained in the renal blood stream causing a sodium imbalance in the rest of the body. This leads to water retention and expansion of the body's extracellular fluid space (Ginès et al., 2004). Therefore, incorporating a model of sodium transport and impairment in our model will increase the rate of fluid accumulation in the peritoneal cavity.

In relation to this, a model of fluid transport in the kidneys could also be incorporated into the peritoneal cavity model. This would allow the studies of another secondary consequence of liver disease known as Hepatorenal syndrome, which is the impairment of kidney functions observed in patients with liver cirrhosis.

Appendix A

Parameter Sensitivity Analysis

A number of estimated physiological parameters were used in the mathematical modelling of liver microcirculation in this thesis, and were listed in Sections 2.9 and 3.8. Most of these parameters were common to both the 2D linear poroelastic model and the 3D hyper-poroelastic model. In this chapter, we perform parameter sensitivity analysis to see the effect of varying some of these parameters by ±20% of their physiological values on our numerical results. For each parameter, we consider the relative error associated with its variation on volume change J, average displacement magnitude $|\mathbf{u}|$, average blood Darcy velocity $\mathbf{v}_s$ and average interstitial fluid Darcy velocity $\mathbf{v}_i$. This is because a lot of the other defined variables in the thesis are either dependent on J or the gradient of $\mathbf{u}$, whereas looking at blood and interstitial fluid velocities give us a measure of the change in perfusion within the tissue. Relative errors less than 5% are considered to be negligible. This analysis is performed on 3 groups of parameters; those associated with the geometry, the fluid properties and the solid tissue.

A.1 Geometrical Parameters

In this section, we perform sensitivity analysis on the parameters associated with the geometry of the lobule. These include the side length of the lobule ($l_{\text{lob}} = 500\,\mu$m), the diameter of the central vein ($d_{cv} = 75\,\mu$m) and the diameter of the portal tracts ($d_{pt} = 50\,\mu$m). The effect of variation of the height of the 3D lobule has already been performed in Section 3.9.5.1.

In separate simulations, the length of the side of the lobule was varied between $400\,\mu\text{m} - 600\,\mu$m, the diameter of the central vein was varied between $60\,\mu\text{m} - 90\,\mu$m and the diameter of the portal tracts was varied between $40\,\mu\text{m} - 60\,\mu$m. The variation had a negligible effect on the volume change ratio J, with relative error being $< 0.2\%$ for all 3 parameters, using both the 2D linear elastic and 3D hyperelastic models. In the 2D linear elastic model, average displacement magnitude $|\mathbf{u}|$ increased significantly with increase in l_{lob}, up to 60%. Increase in $|\mathbf{u}|$ was negligible with increase in d_{pt} ($< 2\%$), while $|\mathbf{u}|$ decreased only slightly with increase in d_{cv} ($< 6\%$). For the 3D hyperelastic model, $|\mathbf{u}|$ also increased significantly with increase in l_{lob},

up to 62%. It had a negligible decrease with increase in d_{pt} ($< 3\%$) and also decreased with increase in d_{cv} ($< 6\%$). These are all shown in Figure A.1.

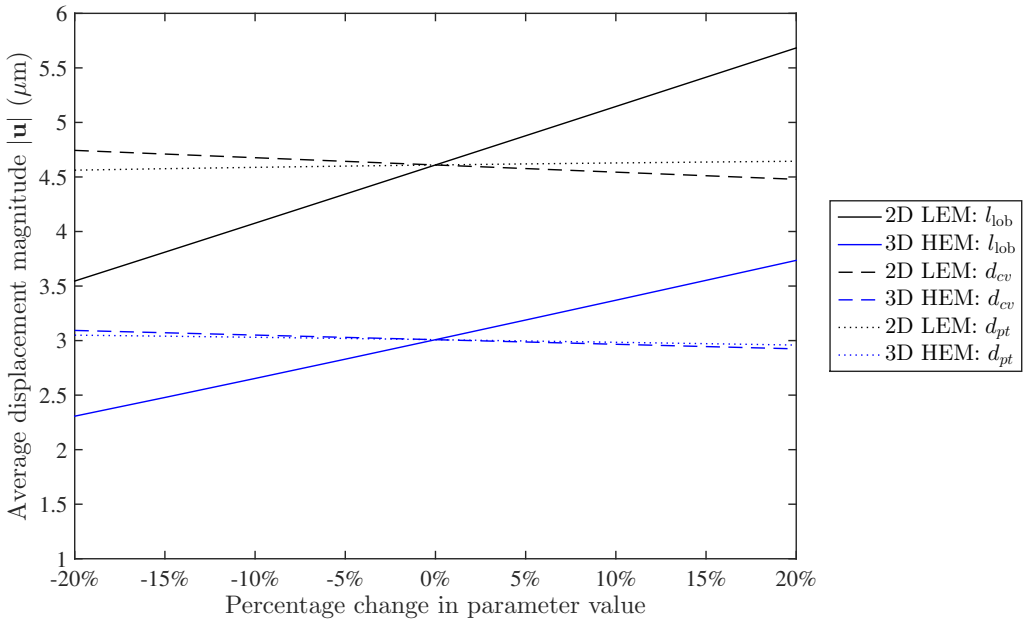


Figure A.1: Effect of changes in geometrical parameters: side length of lobule (l_{lob}), diameter of central vein (d_{cv}) and diameter of portal tracts (d_{pt}) on the average displacement magnitude of the lobule $|\mathbf{u}|$. Black lines denote the 2D linear elastic model (LEM) while blue lines denote the 3D hyperelastic model (HEM).

As for fluid perfusion, blood Darcy velocity $\mathbf{v}_s$ decreases non-linearly by about 42% in the rigid liver (Siggers et al., 2014), the 2D linear elastic model and the 3D hyperelastic model with increase in l_{lob}. For all 3 models, $\mathbf{v}_s$ increased by about 10% with increase in d_{cv} and increased by less than 5% with increase in d_{pt}. These are shown in Figure A.2. Blood Darcy velocity decreases with increase in l_{lob} because of the added distance travelled by blood across the lobule. On the other hand, blood Darcy velocity increases with increase in d_{pt} and d_{cv} because of the added flux of blood due to the increased surface area in the portal tracts and central vein, respectively.

Interstitial fluid Darcy velocity $\mathbf{v}_i$ increased by about 10% in the 2D rigid model (Siggers et al., 2014) and about 23% in both the 2D linear elastic and the 3D hyperelastic models with increase in l_{lob}, respectively. In all 3 models, $\mathbf{v}_i$ increased by about 8% with increase in d_{cv} and increased by less than 5% with increase in d_{pt}. For all 3 parameters, increase in $\mathbf{v}_i$ is seen to be nonlinear. This is shown in Figure A.3.

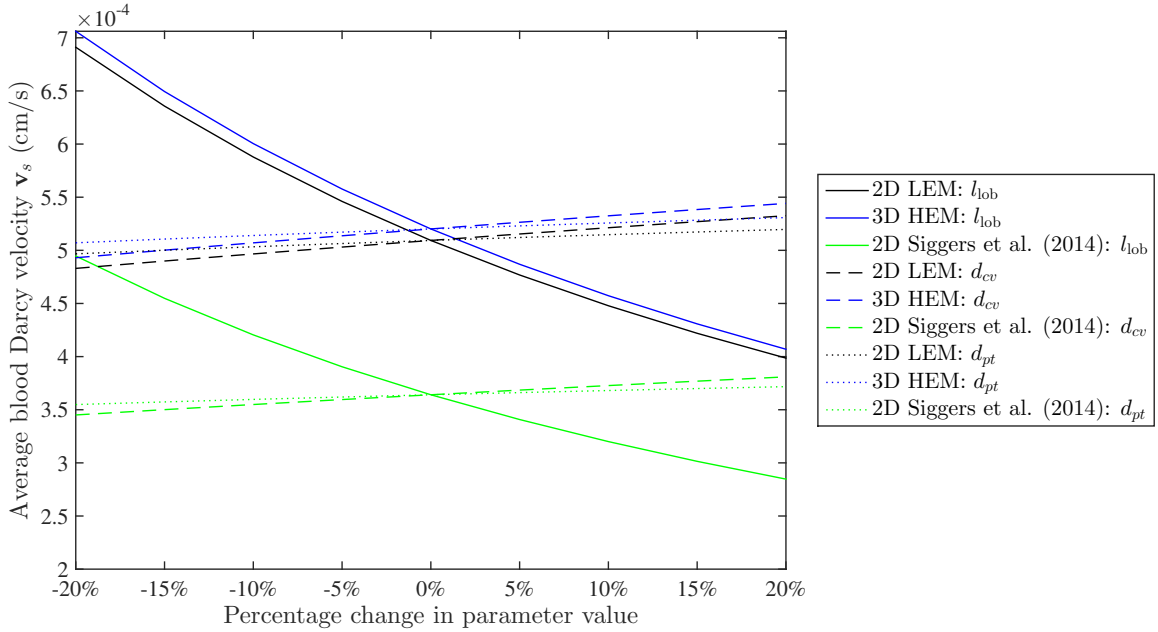


Figure A.2: Effect of changes in geometrical parameters: side length of lobule (l_{lob}), diameter of central vein (d_{cv}) and diameter of portal tracts (d_{pt}), on the average blood Darcy velocity within the lobule $\mathbf{v}_s$. Black lines denote the 2D linear elastic model (LEM), blue lines denote the 3D hyperelastic model (HEM), while green lines denote the rigid model by Siggers et al. (2014).

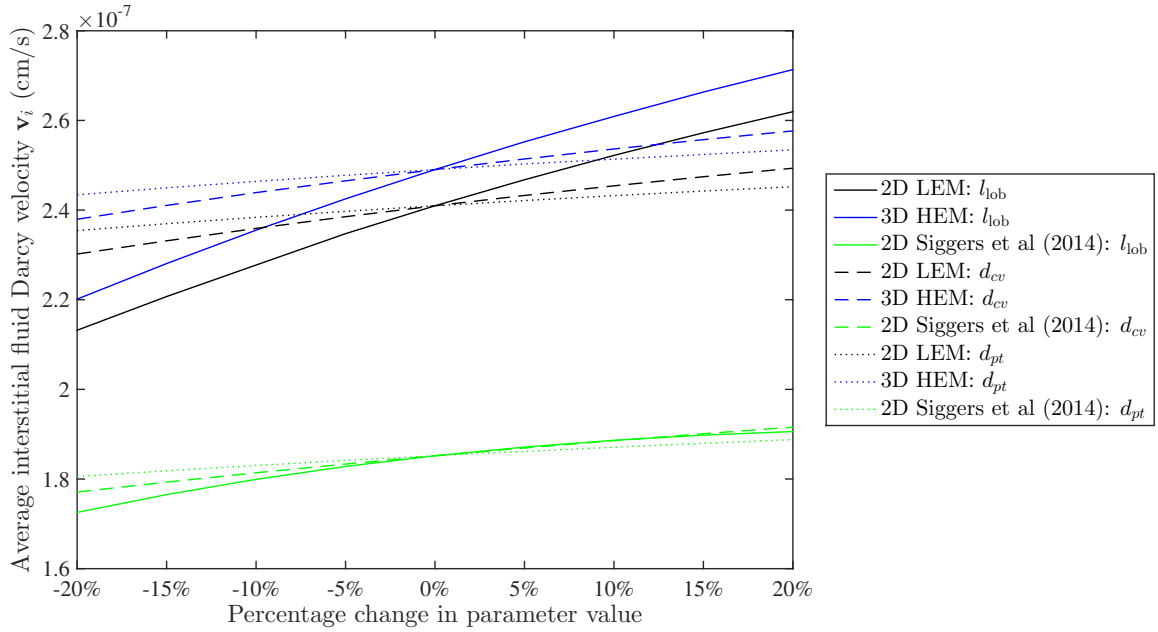


Figure A.3: Effect of changes in geometrical parameters: side length of lobule (l_{lob}), diameter of central vein (d_{cv}) and diameter of portal tracts (d_{pt}), on the average interstitial fluid Darcy velocity within the lobule $\mathbf{v}_i$. Black lines denote the 2D linear elastic model (LEM), blue lines denote the 3D hyperelastic model (HEM), while green lines denote the 2D rigid model by Siggers et al. (2014).

Based on the above results, we can conclude that neither changes in l_{lob}, d_{cv} nor d_{pt} have an effect on the average volume change ratio of the lobule. However, increase in l_{lob} can lead to a linear increase in the observed average displacement magnitude of the lobule. Secondly, changes in blood and interstitial fluid velocity are approximately the same across the 2D rigid model by Siggers et al. (2014), 2D linear elastic model and 3D hyperelastic model with changes in l_{lob}, d_{cv} and d_{pt}. Thirdly, while increase in l_{lob} reduces the average blood velocity in the lobule, increases in d_{cv} and d_{pt} will increase the average blood velocity in the lobule.

A.2 Fluid Flow Parameters

In this section, we look at the effect of variation on some of the parameters associated with fluid flow listed in Table 2.2 (Chapter 2). These include the reference permeabilities of the sinusoidal and interstitial spaces, $\kappa_{s,\text{ref}}$ and $\kappa_{s,\text{ref}}$, respectively, the effective dynamic viscosities of blood and interstitial fluid, μ_s and μ_i, respectively, the hepatic filtration coefficient C_f, the conductance of lymphatic vessels C_l and the average pressure within the flowing lymphatic vessels p_0.

A.2.1 Permeabilities of Pore Spaces

The permeability of the sinusoids in the undeformed liver case $\kappa_{s,\text{ref}} = 1.56 \times 10^{-14}\,\text{m}^2$ was varied by $\pm 20\%$ ($1.25 \times 10^{-14}\,\text{m}^2 - 1.87 \times 10^{-14}\,\text{m}^2$). This variation had no effect on the volume change ratio J of the liver lobule and a negligible effect on the average displacement magnitude $|\mathbf{u}|$ ($< 0.01\%$). Changes in interstitial fluid Darcy velocity $\mathbf{v}_i$ were negligible in the 2D linear elastic model ($< 0.01\%$), while $\mathbf{v}_i$ increased slightly in the 3D hyperelastic model ($\approx 4\%$). The parameter with the most significant increase was the blood Darcy velocity $\mathbf{v}_s$. A 50% increase in $\kappa_{s,\text{ref}}$ lead to a 50% increase in $\mathbf{v}_s$ in both 2D linear elastic and 3D hyperelastic models (see Figure A.4). This is expected since permeability is proportional to Darcy velocity according to Darcy's law (see Equation (1.1)). These results tell us that this proportionality is one-to-one.

The permeability of the interstitial space in the undeformed liver case $\kappa_{i,\text{ref}} = 3.12 \times 10^{-17}\,\text{m}^2$ was also varied by $\pm 20\%$ ($2.50 \times 10^{-17}\,\text{m}^2 - 3.74 \times 10^{-17}\,\text{m}^2$). Just like $\kappa_{s,\text{ref}}$, the variation in $\kappa_{i,\text{ref}}$ had no effect on the volume change ratio J of the liver. Changes in the average displacement magnitude $|\mathbf{u}|$ were negligible ($< 0.01\%$), as well as changes in blood Darcy's velocity $\mathbf{v}_s$ ($< 0.02\%$). Interstitial fluid Darcy velocity $\mathbf{v}_i$ increased linearly with increase in $\kappa_{i,\text{ref}}$, up to 4%. These results hold for both the 2D linear elastic and 3D hyperelastic models.

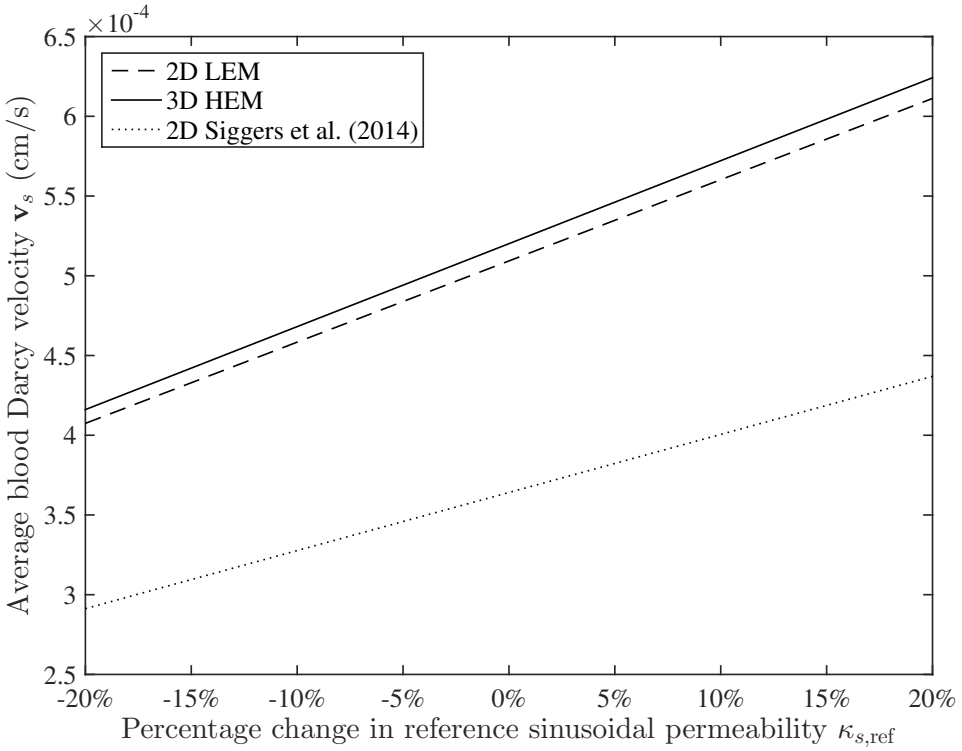


Figure A.4: Effect of variation of the reference sinusoidal space permeability $\kappa_{s,\text{ref}}$ on the average blood Darcy velocity within the lobule $\mathbf{v}_s$. Dashed line denotes the 2D linear elastic model (LEM), solid line denotes the 3D hyperelastic model (HEM), while dotted line denotes the 2D rigid model by Siggers et al. (2014).

A.2.2 Effective Dynamic Viscosities

The effective dynamic viscosity of blood $\mu_s = 0.0024\,\text{Pa}\cdot\,\text{s}$ was varied by $\pm 20\%$, which fell within the range of $0.0019\,\text{Pa}\cdot\,\text{s} - 0.0029\,\text{Pa}\cdot\,\text{s}$. This variation had no effect on the volume change ratio J of the liver lobule and the average displacement magnitude $|\mathbf{u}|$. A 50% increase in μ_s lead to a 33% decrease in blood Darcy velocity $\mathbf{v}_s$, in both 2D linear elastic and 3D hyperelastic models (see Figure A.5). This result is expected since viscosity is inversely proportional to Darcy velocity according to Darcy's law (see Equation (1.1)). Finally, changes in μ_s had a negligible effect on interstitial fluid Darcy velocity $\mathbf{v}_i$ ($< 0.01\%$), in both 2D linear elastic and 3D hyperelastic models.

The effective dynamic viscosity of interstitial space $\mu_i = 0.0018\,\text{Pa}\cdot\,\text{s}$ was also varied by $\pm 20\%$, which fell within the range of $0.0014\,\text{Pa}\cdot\,\text{s} - 0.0022\,\text{Pa}\cdot\,\text{s}$. This variation had no effect on the volume change ratio J of the liver lobule, while changes in the average displacement magnitude $|\mathbf{u}|$ were negligible ($\approx 1\%$). Changes in blood Darcy velocity $\mathbf{v}_s$ were also negligible ($< 0.02\%$). Increase in μ_i lead to a slight decrease in interstitial fluid Darcy velocity $\mathbf{v}_i$ ($< 4\%$), in both 2D linear elastic and 3D hyperelastic models.

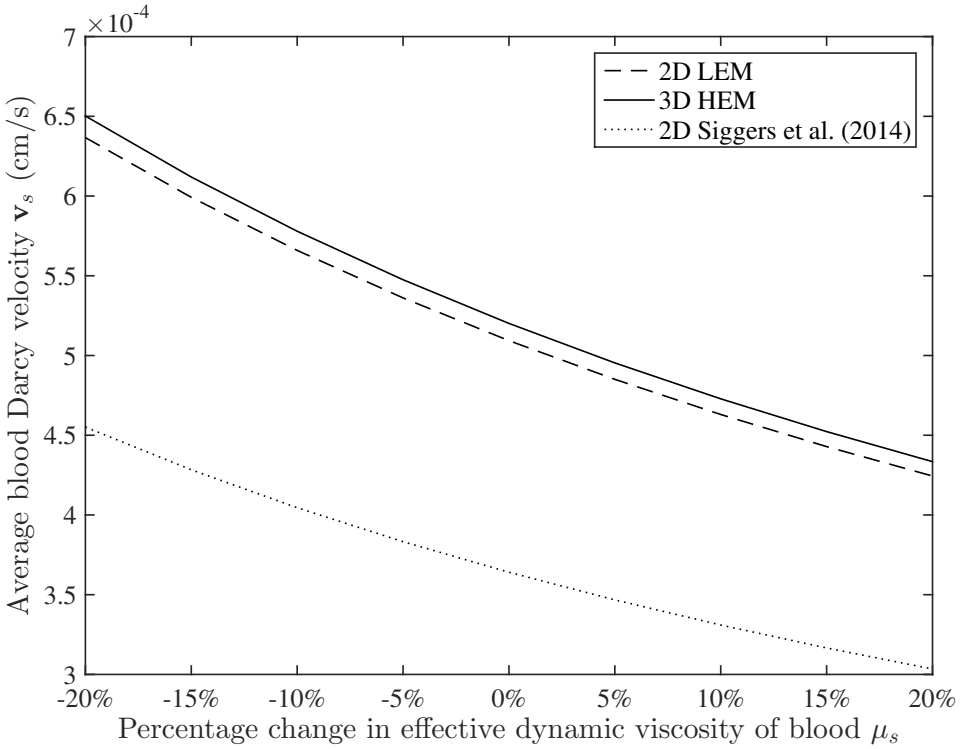


Figure A.5: Effect of variation of the effective dynamic viscosity of blood μ_s on the average blood Darcy velocity within the lobule $\mathbf{v}_s$. Dashed line denotes the 2D linear elastic model (LEM), solid line denotes the 3D hyperelastic model (HEM), while dotted line denotes the 2D rigid model by Siggers et al. (2014).

A.2.3 Hepatic Filtration Coefficient

The hepatic filtration coefficient of the liver sinusoids $C_f = 5.3\times10^{-5}\,\mathrm{s}^{-1}\,\mathrm{mmHg}^{-1}$ was varied by $\pm20\%$ ($4.24\times10^{-5}\,\mathrm{s}^{-1}\,\mathrm{mmHg}^{-1} - 6.36\times10^{-5}\,\mathrm{s}^{-1}\,\mathrm{mmHg}^{-1}$). The variation had a negligible effect on both volume change ratio J of the liver ($< 0.01\%$) and the average displacement magnitude $|\mathbf{u}|$ ($< 1.5\%$). Changes in average blood Darcy velocity $\mathbf{v}_s$ were also negligible ($< 0.03\%$). However, average interstitial fluid Darcy velocity $\mathbf{v}_i$ did increase as C_f was increased, up to about 44%, in both 2D linear elastic and 3D hyperelastic models (see Figure A.6). This is due to the increased filtration of plasma fluid from sinusoidal vessel walls into the surrounding space of Disse.

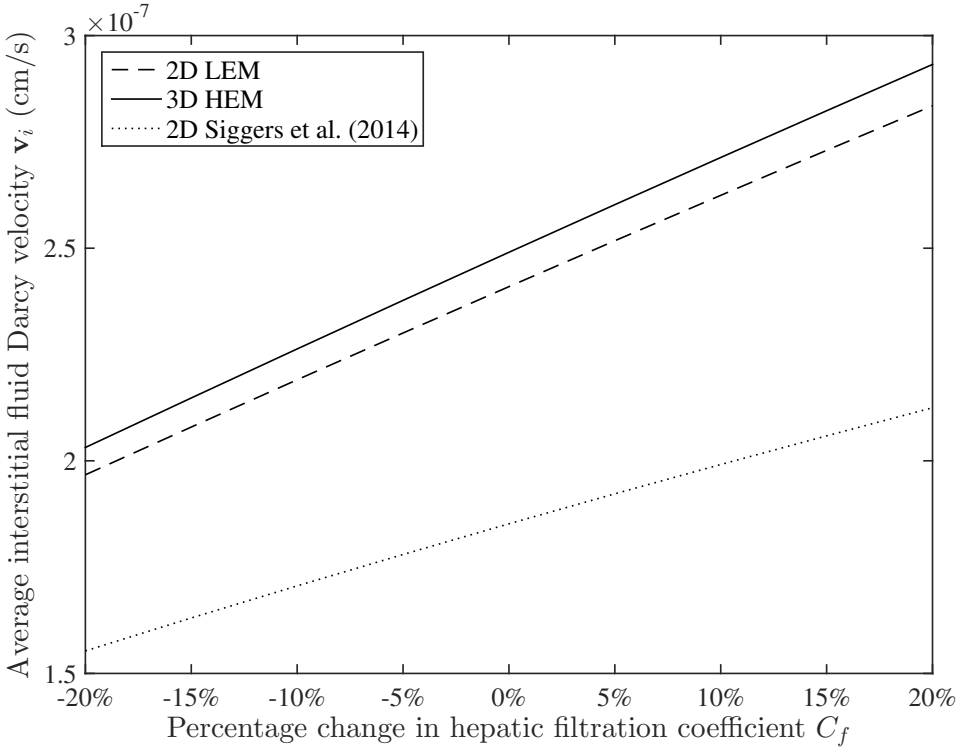


Figure A.6: Effect of variation of the hepatic filtration coefficient C_f on the average interstitial fluid Darcy velocity within the lobule $\mathbf{v}_i$. Dashed line denotes the 2D linear elastic model (LEM), solid line denotes the 3D hyperelastic model (HEM), while dotted line denotes the 2D rigid model by Siggers et al. (2014).

A.2.4 Conductance of Lymphatic Vessels

The conductance of lymphatic vessels within the liver lobules $C_l = 5.9 \times 10^{-7}\,\mathrm{s}^{-1}\,\mathrm{mmHg}^{-1}$ was varied by $\pm 20\%$ ($4.72 \times 10^{-7}\,\mathrm{s}^{-1}\,\mathrm{mmHg}^{-1} - 7.08 \times 10^{-7}\,\mathrm{s}^{-1}\,\mathrm{mmHg}^{-1}$). The variation had a negligible effect on the volume change ratio J of the liver ($< 0.01\%$), the average displacement magnitude $|\mathbf{u}|$ of the lobule ($< 0.3\%$), the average blood Darcy velocity $\mathbf{v}_s$ ($< 0.01\%$) and the average interstitial fluid Darcy velocity $\mathbf{v}_i$ ($< 0.1\%$). These results hold for both 2D linear elastic and 3D hyperelastic models. The only other parameter that changed with variation in C_l in our model was the total lymphatic uptake Q_{lymph} of the liver. The latter increased by about 49% with a 50% increase in C_l (see Figure A.7). This result is expected since Q_{lymph} has been defined to be directly proportional to C_l in our models (see Equations (2.57) and (3.64) for the 2D linear elastic and 3D hyperelastic models, respectively).

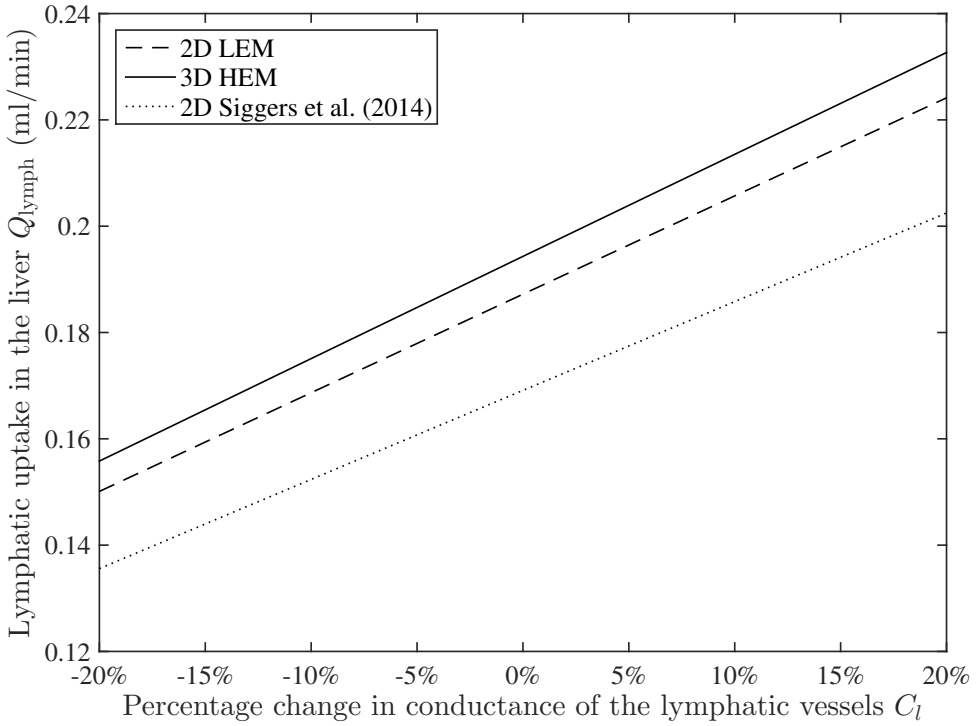


Figure A.7: Effect of variation of the conductance of lymphatic vessels C_l on the total lymphatic fluid uptake of the liver Q_{lymph}. Dashed line denotes the 2D linear elastic model (LEM), solid line denotes the 3D hyperelastic model (HEM), while dotted line denotes the 2D rigid model by Siggers et al. (2014).

A.2.5 Pressure Within Flowing Lymphatic Vessels

The pressure within flowing lymphatic vessels $p_0 = 0\,\text{mmHg}$ was varied between $\pm 2\,\text{mmHg}$. This variation had a negligible effect ($< 0.05\%$) on the volume change ratio J, average displacement magnitude $|\mathbf{u}|$, blood and interstitial fluid Darcy's velocities $\mathbf{v}_s$ and $\mathbf{v}_i$, respectively, for both the 2D linear elastic and 3D hyperelastic models. The only parameter in our model that is affected by a variation in p_0 is the total rate of fluid uptake by the lymphatics in the liver Q_{lymph}. Lymphatic uptake Q_{lymph} decreased by about 70% with the variation in p_0 considered, for both the 2D linear elastic and 3D hyperelastic models. This is shown in Figure A.8.

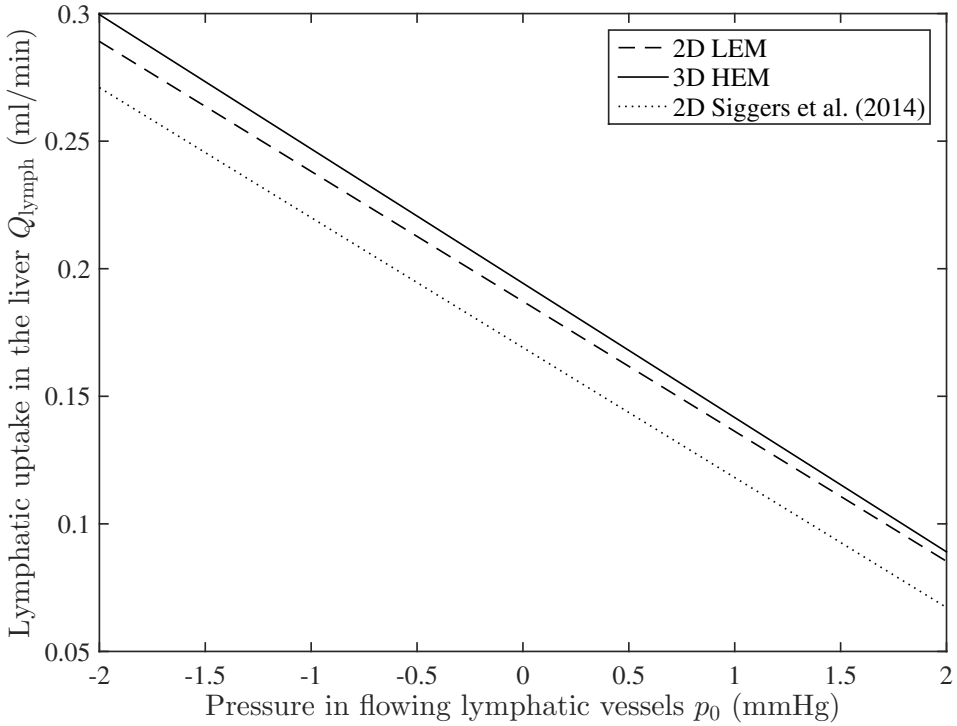


Figure A.8: Effect of variation of the pressure within flowing lymphatic vessels p_0 on the total lymphatic fluid uptake of the liver Q_{lymph}. Dashed line denotes the 2D linear elastic model (LEM), solid line denotes the 3D hyperelastic model (HEM), while dotted line denotes the 2D rigid model by Siggers et al. (2014).

A.3 Solid Material Parameters

The list of parameters associated with the solid liver tissue include the poisson ratio $\nu_L = 0.43$, the elastic constant $E_L = 1185\,\text{Pa}$, the bulk modulus $E_{\text{bulk}} = 2821\,\text{Pa}$, the porosity of the sinusoids and interstitial space in the undeformed liver $\varphi_{s,\text{ref}} = 0.12$ and $\varphi_{i,\text{ref}} = 0.025$, respectively, and the material constants of the 5-constant Mooney–Rivlin polynomial $c_1 = 286.9\,\text{Pa}$, $c_2 = -96.8\,\text{Pa}$, $c_3 = 1926.0\,\text{Pa}$, $c_4 = -4164.4\,\text{Pa}$, $c_5 = 2649.1\,\text{Pa}$. The bulk modulus is related to the poisson ratio and elastic constant via the relationship $E_{\text{bulk}} = E_L/(3(1-2\nu_L))$ (see Section 3.8), and since the variation in E_{bulk} has been studied extensively in Chapter 4, we neglect these 3 parameters in this section of the parameter sensitivity analysis.

A.3.1 Porosity Constants

The reference blood and interstitial fluid porosities, $\varphi_{s,\text{ref}}$ and $\varphi_{i,\text{ref}}$, were varied by $\pm 20\%$, which fell within the ranges of $0.096 - 0.144$ and $0.02 - 0.03$, respectively. Changes in both porosities had a negligible effect on volume change ratio J ($< 0.2\%$), in both the 2D linear elastic and 3D hyperelastic models. Average displacement magnitude $|\mathbf{u}|$ decreased by less

than 7% with increase in $\varphi_{s,\text{ref}}$ and decreased by less than 1.5% with increase in $\varphi_{i,\text{ref}}$, in both 2D linear elastic and 3D hyperelastic models. Increase in $\varphi_{s,\text{ref}}$ led to a linear decrease in blood Darcy velocity ($\approx 9\%$), yet had a negligible effect on interstitial fluid Darcy velocity ($\approx 1\%$) for both 2D linear elastic and 3D hyperelastic models. On the other hand, increase in $\varphi_{i,\text{ref}}$ had a negligible effect on blood Darcy velocity ($< 0.1\%$) and led to a slight decrease in interstitial fluid velocity ($< 3.5\%$).

In summary, increase in blood porosity causes a decrease in blood velocity, while increase in interstitial space porosity causes a decrease in interstitial fluid velocity. However, for a 50% increase in both porosities, changes in their respective fluid velocities were less than 10% in both 2D linear elastic and 3D hyperelastic models.

A.3.2 Shear Deformation Constants

The 5-constant Mooney–Rivlin polynomial was chosen to account for the shear deformation behaviour of our 3D hyperelastic liver model. Variation of the material constants c_1, c_2, c_3, c_4, and c_5 by $\pm 20\%$ resulted in a change of the steepness of the experimental stress–strain behaviour, as shown in Figure A.9.

The variation had a negligible effect on the volume change ratio J of the tissue ($< 0.1\%$) and only resulted in $\approx 3\%$ increase in average displacement magnitude $|\mathbf{u}|$. Change in blood Darcy velocity was also negligible ($< 0.7\%$), as well as interstitial fluid Darcy velocity ($< 0.3\%$). These results tell us that a $\pm 20\%$ change in our choice of 5 Mooney–Rivlin constants have a negligible effect on our numerical solutions of the 3D hyperelastic liver model.

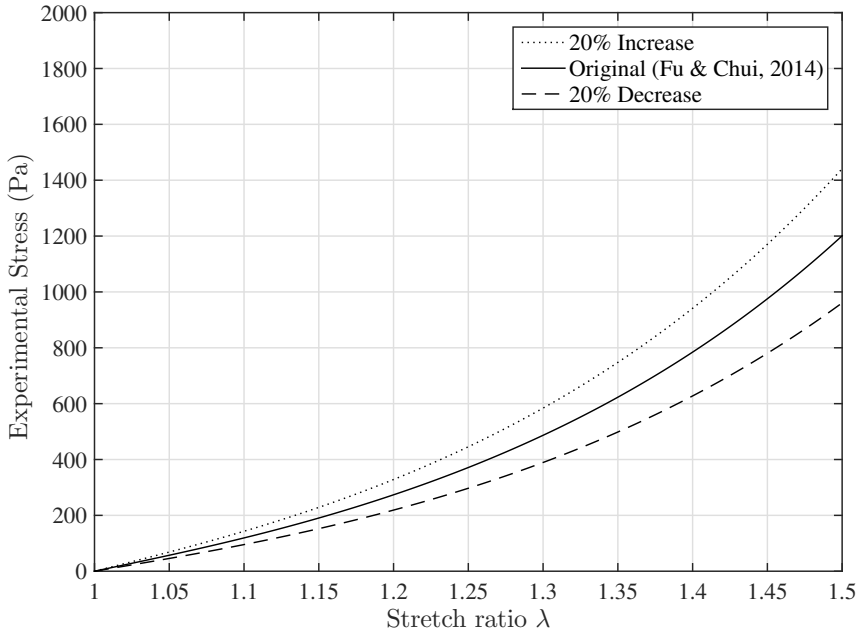


Figure A.9: Effect of the variation of the 5-constant Mooney–Rivlin polynomial constants by $\pm 20\%$ on the experimental stress-strain behaviour of the liver paranchyma.

Bibliography

M. F. Abu-Hijleh, O. A. Habbal, and S. T. Moqattash. The role of the diaphragm in lymphatic absorption from the peritoneal cavity. *Journal of anatomy*, 186(Pt 3):453, 1995.

R. Akhtar, M. J. Sherratt, J. K. Cruickshank, and B. Derby. Characterizing the elastic properties of tissues. *Materials Today*, 14(3):96–105, 2011.

M. C. M. Aletti. *Mathematical modelling and simulations of the hemodynamics in the eye*. PhD thesis, Université Pierre et Marie Curie (UPMC Paris 6), 2017.

H. Alexander and D. L. Miller. Determining skin thickness with pulsed ultra sound. *Journal of Investigative Dermatology*, 72(1):17–19, 1979.

D. H. Alpers, A. N. Kalloo, N. Kaplowitz, C. Owyang, and D. W. Powell. *Textbook of gastroenterology*. John Wiley & Sons, 2011.

M. Argungu and J. H. Tweedy. Microcirculation of blood and interstitial fluid in a poroelastic model of the liver. In *Poromechanics VI*, pages 1126–1134. American Society of Civil Engineers, 2017.

J. Bear. *Dynamics of fluids in porous media*. Courier Corporation, 2013.

L. Berger, D. Kay, K. Burrowes, V. Grau, S. Tavener, and R. Bordas. A poroelastic model of the lung. *arXiv preprint arXiv:1411.1491*, 2014.

L. Berger, R. Bordas, K. Burrowes, V. Grau, S. Tavener, and D. Kay. A poroelastic model coupled to a fluid network with applications in lung modelling. *International journal for numerical methods in biomedical engineering*, 32(1), 2016.

E. Bhunchet and K. Fujieda. Capillarization and venularization of hepatic sinusoids in porcine serum-induced rat liver fibrosis: a mechanism to maintain liver blood flow. *Hepatology*, 18 (6):1450–1458, 1993.

A. Bonfiglio, K. Leungchavaphongse, R. Repetto, and J. H. Siggers. Mathematical modeling of the circulation in the liver lobule. *Journal of Biomechanical Engineering*, 132(11):111011, 2010.

J. L. Boyer. Bile formation and secretion. *Comprehensive physiology*, 2013.

C. G. Caro, T. J. Pedley, and W. A. Seed. Mechanics of the circulation. *Cardiovascular physiology.*, 1974.

P. Causin, G. Guidoboni, A. Harris, D. Prada, R. Sacco, and S. Terragni. A poroelastic model for the perfusion of the lamina cribrosa in the optic nerve head. *Mathematical biosciences*, 257:33–41, 2014.

D. Chapelle, J.-F. Gerbeau, J. Sainte-Marie, and I. E. Vignon-Clementel. A poroelastic model valid in large strains with applications to perfusion in cardiac modeling. *Computational Mechanics*, 46(1):91–101, 2010.

D. Chou, J. C. Vardakis, and Y. Ventikos. Multiscale modelling for cerebrospinal fluid dynamics: multicompartmental poroelacticity and the role of aqp4. *Journal of Biosciences and Medicines*, 2(02):1, 2014.

C. Chui, E. Kobayashi, X. Chen, T. Hisada, and I. Sakuma. Combined compression and elongation experiments and non-linear modelling of liver tissue for surgical simulation. *Medical and Biological Engineering and Computing*, 42(6):787–798, 2004.

C. Chui, E. Kobayashi, X. Chen, T. Hisada, and I. Sakuma. Transversely isotropic properties of porcine liver tissue: experiments and constitutive modelling. *Medical & biological engineering & computing*, 45(1):99–106, 2007.

U. Dahmen, C. A. Hall, N. Madrahimov, V. Milekhin, and O. Dirsch. Regulation of hepatic microcirculation in stepwise liver resection. *Acta gastro-enterologica Belgica*, 70(4):345–351, 2007.

H. Dancygier. *Clinical hepatology: Principles and practice of hepatobiliary diseases*, volume 1. Springer Science & Business Media, 2009.

C. Debbaut, D. Monbaliu, C. Casteleyn, P. Cornillie, et al. From vascular corrosion cast to electrical analog model for the study of human liver hemodynamics and perfusion. *IEEE Transactions on Bio-medical Engineering*, 58(1):25–35, 2011.

C. Debbaut, J. Vierendeels, C. Casteleyn, P. Cornillie, D. Van Loo, P. Simoens, L. Van Hoorebeke, D. Monbaliu, and P. Segers. Perfusion characteristics of the human hepatic microcirculation based on three-dimensional reconstructions and computational fluid dynamic analysis. *Journal of Biomechanical Engineering*, 134(1):011003, 2012.

C. Debbaut, J. Vierendeels, J. H Siggers, R. Repetto, D. Monbaliu, and P. Segers. A 3D porous media liver lobule model: the importance of vascular septa and anisotropic permeability for homogeneous perfusion. *Computer Methods in Biomechanics and Biomedical Engineering*, 17(12):1295–1310, 2014.

D-H. Dong, W-Y. Liu, H-B. Feng, Y-L. Fu, S. Huang, J-X. Xiang, and Y. Lyu. Study of individual characteristic abdominal wall thickness based on magnetic anchored surgical instruments. *Chinese medical journal*, 128(15):2040, 2015.

R. Drake, A. W. Vogl, A. W. M. Mitchell, R. Tibbitts, and P. Richardson. *Gray's Atlas of Anatomy E-Book*. Elsevier Health Sciences, 2014.

S. Duman, S. Ozbek, E. Gunay, D. Bozkurt, G. Asci, S. Sipahi, F. Kirçelli, M. Ertilav, M. Ozkahya, and E. Ok. What does peritoneal thickness in peritoneal dialysis patients tell us? *Advances in Peritoneal Dialysis*, 23:28–33, 2007.

P. Y. Durand, J. Chanliau, J. Gamberoni, D. Hestin, and M. Kessler. Apd: clinical measurement of the maximal acceptable intraperitoneal volume. *Advances in peritoneal dialysis*, 10:63–63, 1994.

P. W. Dykes and J. H. Jones. Albumin exchange between plasma and ascitic fluid. *Clinical Science*, 34(1):185–197, 1968.

C. Eipel, K. Abshagen, and B. Vollmar. Regulation of hepatic blood flow: the hepatic arterial buffer response revisited. *World Journal of Gastroenterology: WJG*, 16(48):6046, 2010.

J. R. Elk, R. E. Drake, J. P. Williams, J. C. Gabel, and G. A. Laine. Lymphatic function in the liver after hepatic venous pressure elevation. *American Journal of Physiology–Gastrointestinal and Liver Physiology*, 254:G748–G752, 1988.

C. R. Ethier and C. A. Simmons. *Introductory biomechanics: from cells to organisms*. Cambridge University Press, 2007.

M. Fischbach, J. Terzic, V. Laugel, B. Escande, C. L. Dangelser, and A. Helmstetter. Measurement of hydrostatic intraperitoneal pressure: a useful tool for the improvement of dialysis dose prescription. *Pediatric Nephrology*, 18(10):976–980, 2003.

M. F. Flessner, R. L. Dedrick, and J. S. Schultz. A distributed model of peritoneal-plasma transport: theoretical considerations. *American Journal of Physiology-Regulatory, Integrative and Comparative Physiology*, 246(4):R597–R607, 1984.

M. F. Flessner, R. L. Dedrick, and J. S. Schultz. A distributed model of peritoneal-plasma transport: analysis of experimental data in the rat. *American Journal of Physiology-Renal Physiology*, 248(3):F413–F424, 1985a.

M. F. Flessner, J. D. Fenstermacher, R. L. Dedrick, and R. G. Blasberg. A distributed model of peritoneal-plasma transport: tissue concentration gradients. *American Journal of Physiology-Renal Physiology*, 248(3):F425–F435, 1985b.

Y. B. Fu and C. K. Chui. Modelling and simulation of porcine liver tissue indentation using finite element method and uniaxial stress–strain data. *Journal of biomechanics*, 47(10):2430–2435, 2014.

P. Ginès, A. Cárdenas, V. Arroyo, and J. Rodés. Management of cirrhosis and ascites. *New England Journal of Medicine*, 350(16):1646–1654, 2004.

R. Gokal. *Textbook of Peritoneal Dialysis*. Springer, 2000.

F. D. Gordon. Ascites. *Clinics in Liver Disease*, 16(2):285–299, 2012.

L. Gotloib, M. Mines, L. Garmizo, and I. Varka. Hemodynamic effects of increasing intraabdominal pressure in peritoneal dialysis. *Peritoneal Dialysis International*, 1(4):41–43, 1981.

T. Grabowski and G. Tortora. *Principles of Anatomy and Physiology*. John Wiley & Sons, 2003.

A. C. Guyton and J. E. Hall. *Textbook of Medical Physiology*. Elsevier Health Sciences, 2015.

O. Heimbürger, J. Waniewski, A. Werynski, M. S. Park, and B. Lindholm. Lymphatic absorption in capd patients with loss of ultrafiltration capacity. *Blood purification*, 13(6):327–339, 1995.

H. Ho, K. Sorrell, A. Bartlett, and P. Hunter. Modeling the hepatic arterial buffer response in the liver. *Medical Engineering and Physics*, 35(8):1053–1058, 2013a.

H. Ho, K. Sorrell, L. Peng, Z. Yang, A. Holden, and P. Hunter. Hemodynamic analysis for transjugular intrahepatic portosystemic shunt (tips) in the liver based on a ct-image. *IEEE transactions on medical imaging*, 32(1):92–98, 2013b.

A. G. Holzapfel. *Nonlinear Solid Mechanics II*. John Wiley & Sons, Inc., 2000.

G. A. Holzapfel and R. W. Ogden. *Biomechanical modelling at the molecular, cellular and tissue levels*, volume 508. Springer Science & Business Media, 2009.

J. Hu, S. Lü, S. Feng, and M. Long. Flow dynamics analyses of pathophysiological liver lobules using porous media theory. *Acta Mechanica Sinica*, 33(4):823–832, 2017.

L. Jerby, T. Shlomi, and E. Ruppin. Computational reconstruction of tissue-specific metabolic models: application to human liver metabolism. *Molecular systems biology*, 6(1):401, 2010.

E. B. Keeffe and L. S. Friedman. *Handbook of Liver Disease*. Elsevier, 2004.

P. R. Kvietys and D. N. Granger. Role of intestinal lymphatics in interstitial volume regulation and transmucosal water transport. *Annals of the New York Academy of Sciences*, 1207(s1): E29–E43, 2010.

W. M. Lai, D. H. Rubin, E. Krempl, and D. Rubin. *Introduction to continuum mechanics*. Butterworth-Heinemann, 2009.

G. A. Laine, J. T. Hall, S. H. Laine, and J. Granger. Transsinusoidal fluid dynamics in canine liver during venous hypertension. *Circulation Research*, 45(3):317–323, 1979.

W. W. Lautt. Mechanism and role of intrinsic regulation of hepatic arterial blood flow: hepatic arterial buffer response. *American Journal of Physiology-Gastrointestinal and Liver Physiology*, 249(5):G549–G556, 1985.

K. A. Lettmann and M. Hardtke–Wolenski. The importance of liver microcirculation in promoting autoimmune hepatitis via maintaining an inflammatory cytokine milieu–a mathematical model study. *Journal of Theoretical Biology*, 348:33–46, 2014.

J. R. Levick. *An introduction to cardiovascular physiology*. Butterworth-Heinemann, 2013.

J.R. Levick. Flow through interstitium and other fibrous matrices. *Experimental Physiology*, 72(4):409–437, 1987.

G. Miserocchi, D. Negrini, S. Mukenge, P. Turconi, and M. Del Fabbro. Liquid drainage through the peritoneal diaphragmatic surface. *Journal of Applied Physiology*, 66(4):1579–1585, 1989.

H. H. Mitchell, T. S. Hamilton, F. R. Steggerda, and H. W. Bean. The chemical composition of the adult human body and its bearing on the biochemistry of growth. *Journal of Biological Chemistry*, 168:625–637, 1945.

K. L. Moore, A. M. R Agur, and A. F. Dalley. *Essential Clinical Anatomy*, volume 469. Lippincott Williams & Wilkins Philadelphia:, 2002.

K. P. Moore and G. P. Aithal. Guidelines on the management of ascites in cirrhosis. *Gut*, 55 (suppl 6):vi1–vi12, 2006.

K. P. Moore, F. Wong, P. Gines, M. Bernardi, A. Ochs, F. Salerno, P. Angeli, M. Porayko, R. Moreau, G. Garcia-Tsao, et al. The management of ascites in cirrhosis: report on the consensus conference of the international ascites club. *Hepatology*, 38(1):258–266, 2003.

G. A. Morali, K. W. Sniderman, K. I. Deitel, S. Tobe, H. Witt-Sullivan, M. Simon, J. Heathcote, and L. M. Blendis. Is sinusoidal portal hypertension a necessary factor for the development of hepatic ascites? *Journal of Hepatology*, 16(1):249–250, 1992.

A. Moriondo, A. Grimaldi, L. Sciacca, M. L. Guidali, C. Marcozzi, and D. Negrini. Regional recruitment of rat diaphragmatic lymphatics in response to increased pleural or peritoneal fluid load. *The Journal of physiology*, 579(3):835–847, 2007.

A. Moriondo, F. Boschetti, F. Bianchin, S. Lattanzio, C. Marcozzi, and D. Negrini. Tissue contribution to the mechanical features of diaphragmatic initial lymphatics. *The Journal of Physiology*, 588(20):3957–3969, 2010.

S. Mueller and L. Sandrin. Liver stiffness: a novel parameter for the diagnosis of liver disease. *Hepatic medicine: evidence and research*, 2:49, 2010.

D. Negrini and A. Moriondo. Lymphatic anatomy and biomechanics. *The Journal of Physiology*, 589(12):2927–2934, 2011.

D. Negrini, S. Mukenge, M. Del Fabbro, C. Gonano, and G. Miserocchi. Distribution of diaphragmatic lymphatic stomata. *Journal of Applied Physiology*, 70(4):1544–1549, 1991.

D. Negrini, M. Del Fabbro, C. Gonano, S. Mukenge, and G. Miserocchi. Distribution of diaphragmatic lymphatic lacunae. *Journal of Applied Physiology*, 72(3):1166–1172, 1992.

National Health Service (NHS). Liver disease. `https://www.nhs.uk/conditions/liver-disease/`. Accessed: 30 February 2016.

A. Ochs. Transjugular intrahepatic portosystemic shunt. *Digestive diseases*, 23(1):56–64, 2005.

O. Ohtani and Y. Ohtani. Lymph circulation in the liver. *The Anatomical Record*, 291(6): 643–652, 2008.

K. Pawlaczyk, M. Kuzlan, K. Wieczorowska-Tobis, H. Pawlik-Juzkow, A. Breborowicz, J. Knapowski, and D. G. Oreopoulos. Species dependent topography of the peritoneum. *Advances in Peritoneal Dialysis*, 12:3–6, 1996.

G. Peeters, C. Debbaut, P. Cornillie, T. De Schryver, D. Monbaliu, W. Laleman, and P. Segers. A multilevel modeling framework to study hepatic perfusion characteristics in case of liver cirrhosis. *Journal of biomechanical engineering*, 137(5):051007, 2015.

G. Peeters, C. Debbaut, W. Laleman, D. Monbaliu, I. Vander Elst, J. R. Detrez, T. Vandecasteele, T. De Schryver, L. Van Hoorebeke, K. Favere, et al. A multilevel framework to reconstruct anatomical 3d models of the hepatic vasculature in rat livers. *Journal of anatomy*, 230(3):471–483, 2017.

Public Health England (PHE). Research and analysis, chapter 2: Major causes of death and how they have changed. `https://www.gov.uk/government/publications/health-profile-for-england/chapter-2-major-causes-of-death-and-how-they-have-changed`, Published 13 July 2017. Accessed: 03 March 2018.

G. Puhl, K. D. Schaser, B. Vollmar, M. D. Menger, and U. Settmacher. Noninvasive in vivo analysis of the human hepatic microcirculation using orthogonal polorization spectral imaging. *Transplantation*, 75(6):756–761, 2003.

H. P. Rani, Tony W. H. Sheu, T. M. Chang, and P. C. Liang. Numerical investigation of non–newtonian microcirculatory blood flow in hepatic lobule. *Journal of Biomechanics*, 39 (3):551–563, 2006.

D. W. A. Rees. *Mechanics of solids and structures*. Imperial College Press, 2000.

R. Repetto, A. Tatone, A.and Testa, and E. Colangeli. Traction on the retina induced by saccadic eye movements in the presence of posterior vitreous detachment. *Biomechanics and Modeling in Mechanobiology*, 10(2):191–202, 2011.

T. Ricken, U. Dahmen, and O. Dirsch. A biphasic model for sinusoidal liver perfusion remodeling after outflow obstruction. *Biomechanics and Modeling in Mechanobiology*, 9(4):435–450, 2010.

T. Ricken, D. Werner, H. G. Holzhütter, M. König, U. Dahmen, and O. Dirsch. Modeling function–perfusion behavior in liver lobules including tissue, blood, glucose, lactate and glycogen by use of a coupled two–scale PDE–ODE approach. *Biomechanics and Modeling in Mechanobiology*, pages 1–22, 2014.

T. Ricken, N. Waschinsky, and D. Werner. Simulation of steatosis zonation in liver lobule–a continuum mechanical bi-scale, tri-phasic, multi-component approach. In *Biomedical Technology*, pages 15–33. Springer, 2018.

J. Rubin, M. Clawson, A. Planch, and Q. Jones. Measurements of peritoneal surface area in man and rat. *The American Journal of the Medical Sciences*, 295(5):453–458, 1988a.

J. Rubin, Q. Jones, A. Planch, and J. D. Bower. The minimal importance of the hollow viscera to peritoneal transport during peritoneal dialysis in the rat. *ASAIO Journal*, 34(4):912–915, 1988b.

R. Shah. Ascites. `http://emedicine.medscape.com/article/170907-overview`, 2016. Accessed: 17 March 2016.

J. H. Siggers, K. Leungchavaphongse, C. H. Ho, and R. Repetto. Mathematical model of blood and interstitial flow and lymph production in the liver. *Biomechanics and Modeling in Mechanobiology*, 13(2):363–378, 2014.

J. E. Skandalakis, G. L. Colborn, T. A. Weidman, et al. *Skandalakis' Surgical Anatomy*. McGraw-Hill Companies, 2004a.

J. E. Skandalakis, L. J. Skandalakis, P. N. Skandalakis, and P. Mirilas. Hepatic surgical anatomy. *Surgical Clinics*, 84(2):413–435, 2004b.

H. Sönnerlind. Why all these stresses and strains? `https://www.comsol.se/blogs/why-all-these-stresses-and-strains`, 2013.

H. Sönnerlind. What is geometric nonlinearity? `https://www.comsol.co.in/blogs/what-is-geometric-nonlinearity`, 2015.

L. S. Srinath. *Advanced mechanics of solids*. Tata McGraw-Hill Education, 2009.

J. Stachowska-Pietka and J. Waniewski. *Distributed Models of Peritoneal Transport*. INTECH Open Access Publisher, 2011.

J. Stachowska-Pietka, J. Waniewski, M. F. Flessner, and B. Lindholm. A mathematical model of peritoneal fluid absorption in tissue. In *Advances in Peritoneal Dialysis. Conference on Peritoneal Dialysis*, volume 21, pages 9–12, 2004.

J. Stachowska-Pietka, J. Waniewski, M. F. Flessner, and B. Lindholm. Distributed model of peritoneal fluid absorption. *American Journal of Physiology–Heart and Circulatory Physiology*, 291(4):H1862–H1874, 2006.

M. A. Swartz and M. E. Fleury. Interstitial flow and its effects in soft tissues. *Annual Review of Biomedical Engineering*, 9:229–256, 2007.

E. B. Tadmor, R. E. Miller, and R. S. Elliott. *Continuum mechanics and thermodynamics: from fundamental concepts to governing equations*. Cambridge University Press, 2012.

L. Tran, H. Rodela, N. J. Abernethy, Z. Y. Yuan, J. B. Hay, D. Oreopoulos, and M. G. Johnston. Lymphatic drainage of hypertonic solution from peritoneal cavity of anesthetized and conscious sheep. *Journal of Applied Physiology*, 74(2):859–867, 1993a.

L. Tran, H. Rodela, J. B. Hay, D. Oreopoulos, and M. G. Johnston. Quantitation of lymphatic drainage of the peritoneal cavity in sheep: comparison of direct cannulation techniques with indirect methods to estimate lymph flow. *Peritoneal Dialysis International*, 13(4):270–279, 1993b.

B. Tully and Y. Ventikos. Coupling poroelasticity and cfd for cerebrospinal fluid hydrodynamics. *IEEE Transactions on Biomedical Engineering*, 56(6):1644–1651, 2009.

B. Tully and Y. Ventikos. Cerebral water transport using multiple-network poroelastic theory: application to normal pressure hydrocephalus. *Journal of Fluid Mechanics*, 667:188–215, 2011.

Z. J. Twardowski, B. F. Prowant, K. D. Nolph, A. J. Martinez, and L. M. Lampton. High volume, low frequency continuous ambulatory peritoneal dialysis. *Kidney international*, 23 (1):64–70, 1983.

Z. J. Twardowski, R. Khanna, K. D. Nolph, A. Scalamogna, M. H. Metzler, T. W. Schneider, B. F. Prowant, and L. P. Ryan. Intraabdominal pressures during natural activities in patients treated with continuous ambulatory peritoneal dialysis. *Nephron*, 44(2):129–135, 1986.

J. H. Tweedy. BE3-MPFM Physiological fluid mechanics lecture notes, Imperial College London, 2017.

S. Umale, S. Chatelin, N. Bourdet, C. Deck, M. Diana, P. Dhumane, L. Soler, J. Marescaux, and R. Willinger. Experimental in vitro mechanical characterization of porcine glisson's capsule and hepatic veins. *Journal of biomechanics*, 44(9):1678–1683, 2011.

S. Umale, C. Deck, N. Bourdet, P. Dhumane, L. Soler, J. Marescaux, and R. Willinger. Experimental mechanical characterization of abdominal organs: liver, kidney & spleen. *Journal of the mechanical behavior of biomedical materials*, 17:22–33, 2013.

A. Van Der Plaats, N. A. 't Hart, G. J. Verkerke, H. G. D. Leuvenink, P. Verdonck, R. J. Ploeg, and G. Rakhorst. Numerical simulation of the hepatic circulation. *The International Journal of Artificial Organs*, 27(3):222–230, 2004.

R. E. Wells and E. W. Merrill. Shear rate dependence of the viscosity of whole blood and plasma. *Science*, 133(3455):763–764, 1961.

C. Wex, S. Arndt, A. Stoll, C. Bruns, and Y. Kupriyanova. Isotropic incompressible hyperelastic models for modelling the mechanical behaviour of biological tissues: a review. *Biomedical Engineering/Biomedizinische Technik*, 60(6):577–592, 2015.

H. Wiig and M. A. Swartz. Interstitial fluid and lymph formation and transport: physiological regulation and roles in inflammation and cancer. *Physiological reviews*, 92(3):1005–1060, 2012.

H. A. Wynne, L. H. Cope, E. Mutch, M. D. Rawlins, K. W. Woodhouse, and O. F. W. James. The effect of age upon liver volume and apparent liver blood flow in healthy man. *Hepatology*, 9(2):297–301, 1989.

S. L. Xie, R. K. Reed, B. D. Bowen, and J. L. Bert. A model of human microvascular exchange. *Microvascular Research*, 49(2):141–162, 1995.

M. Yang, L. A. Taber, and E. B. Clark. A nonliner poroelastic model for the trabecular embryonic heart. *Journal of biomechanical engineering*, 116(2):213–223, 1994.

E. Zakaria, J. Lofthouse, and M. F. Flessner. In vivo hydraulic conductivity of muscle: effects of hydrostatic pressure. *American Journal of Physiology–Heart and Circulatory Physiology*, 273(6):H2774–H2782, 1997.

J. Zink and C. V. Greenway. Control of ascites absorption in anesthetized cats: effects of intraperitoneal pressure, protein, and furosemide diuresis. *Gastroenterology*, 73(5):1119–1124, 1977.